UNIVERSIDADE DE SÃO PAULO
Escola de Engenharia de São Carlos

Compact Models of Resonant Tunneling Diodes

Daniel Ricardo Celino

EESC · USP

UNIVERSIDADE DE SÃO PAULO
ESCOLA DE ENGENHARIA DE SÃO CARLOS
DEPARTAMENTO DE ENGENHARIA ELÉTRICA E DE COMPUTAÇÃO

Daniel Ricardo Celino

Compact Models of Resonant Tunneling Diodes

São Carlos
2024

UNIVERSIDADE DE SÃO PAULO
ESCOLA DE ENGENHARIA DE SÃO CARLOS
DEPARTAMENTO DE ENGENHARIA ELÉTRICA E DE COMPUTAÇÃO

Daniel Ricardo Celino

Compact Models of Resonant Tunneling Diodes

Tese de doutorado apresentada ao Programa de Engenharia Elétrica da Escola de Engenharia de São Carlos como parte dos requisitos para a obtenção do título de Doutor em Ciências.

Área de concentração: Telecomunicações

Orientador: Prof. Dr. Murilo Araujo Romero

São Carlos - SP
2024

Trata-se da versão corrigida da tese. A versão original se encontra disponível na EESC/USP que aloja o Programa de Pós-Graduação de Engenharia Elétrica.

Ficha catalográfica elaborada pela Biblioteca Prof. Dr. Sérgio Rodrigues Fontes da EESC/USP com os dados inseridos pelo(a) autor(a).

Celino, Daniel Ricardo
C392c Compact Models of Resonant Tunneling Diodes / Daniel Ricardo Celino; orientador Murilo Araujo Romero. São Carlos, 2024.

Tese (Doutorado) - Programa de Pós-Graduação em Engenharia Elétrica e Área de Concentração em Telecomunicações -- Escola de Engenharia de São Carlos da Universidade de São Paulo, 2024.

1. resonant tunneling diode. 2. compact model. 3. quantum well. 4. nanoelectronics. 5. RTD 2D-2D. 6. RTD 3D-2D . I. Título.

Eduardo Graziosi Silva - CRB - 8/8907

FOLHA DE JULGAMENTO

Candidato: Bacharel **DANIEL RICARDO CELINO**.

Título da tese: "Modelos Compactos de Diodos de Tunelamento Ressonante".

Data da defesa: 02/08/2024.

Comissão Julgadora	**Resultado**
Prof. Titular Murilo Araujo Romero (Orientador) (Escola de Engenharia de São Carlos/EESC-USP)	Aprovado
Prof. Dr. Helder Vinícius Avanço Galeti (Universidade Federal de São Carlos/UFSCar)	Aprovado
Prof. Dr. Joaquim Ferreira Martins Filho (Universidade Federal de Pernambuco/UFPE)	Aprovado
Prof. Dr. Luís Alberto Mijam Barêa (Universidade Federal de São Carlos/UFSCar)	Aprovado
Prof. Dr. Marcelo Antonio Pavanello (Faculdade de Engenharia Industrial/FEI)	Aprovado

Coordenador do Programa de Pós-Graduação em Engenharia Elétrica:
Prof Associado **Marcelo Andrade da Costa Vieira**

Presidente da Comissão de Pós-Graduação:
Prof. Titular **Carlos De Marqui Junior**

A você meu querido irmão, Darlan, dedico essa Tese. Muito obrigado pelo tempo que tivemos juntos nessa terra e por toda torcida, companheirismo, amizade e amor que demonstrou. Te amo, nos veremos novamente...

x

"I would rather have questions that can't be answered than answers that can't be questioned."

Richard Feynman

Agradecimentos

Agradeço primeiramente a Deus, por ter me concedido saúde, perseverança e dedicação para conclusão de mais esta etapa.

A CAPES, Coordenação de Aperfeiçoamento de Pessoal de Nível Superior, pelo fomento ao projeto de pesquisa.

Ao meu orientador, Prof. Dr. Murilo Araujo Romero, por ter me aceitado como seu orientando, pela paciência, pelas diretrizes, correções e conselhos.

A Profª. Dra. Regiane Ragi, pela dedicação, paciência e disponibilidade muito obrigado.

Aos meus pais Neilton e Ercília, por sempre me apoiarem, me amarem e ajudarem, por ser minha fortaleza quando mais preciso. Sem esse suporte nada disso seria possível.

A minha esposa Daniela, pela compreensão, pelo amor e carinho, pela paciência, amizade, companheirismo, enfim, por tudo, minha metade.

Ao meu irmão Danillo por sonhar comigo, por me amar, por ser família sempre.

A toda minha família Ricardo e Celino.

Aos meus colegas do laboratório, Adelcio e Caio pela parceria e colaboração durante esse período e pelas diversas publicações que daí resultaram.

Por fim, agradeço a todos os meus professores de doutorado, por todo conhecimento, experiência de vida e ensinamentos que levarei durante a minha carreira.

Resumo

CELINO, D. R. **Modelos Compactos de Diodos de Tunelamento Ressonante**. 2024. 174 f. Tese de Doutorado – Escola de Engenharia de São Carlos, Universidade de São Paulo, São Carlos, 2024.

Devido à crescente demanda por tecnologias capazes de operar na faixa de frequência de Terahertz (THz) o Diodo de Tunelamento Ressonante (RTD) teve seu interesse renovado por parte da comunidade acadêmica. O RTD é considerado um candidato promissor para aplicações digitais e analógicas, devido à sua característica intrínseca de resistência diferencial negativa (NDR), alta velocidade de comutação e requisitos de design flexíveis.

Neste cenário, esta tese de doutorado trata da modelagem compacta e analítica da característica corrente-tensão (I-V) de diodos de tunelamento ressonante de dupla barreira de potencial. Com este propósito, é necessário inicialmente calcular os níveis de energia dos auto-estados do poço quântico de altura finita, presente nas estruturas semicondutoras de RTDs. Todavia, a determinação de níveis de energia, para poços quânticos finitos, somente é possível por meio da resolução de equações transcendentais ou por algum tipo de solução numérica, não permitindo, portanto, solução analítica exata. Desta forma foram desenvolvidas soluções aproximadas totalmente analíticas para o cálculo dos níveis de energia em poços quânticos retangulares de altura finita, simétricos e assimétricos, sendo verificada excelente concordância.

Em seguida, tendo como ponto de partida o formalismo de Tsu-Esaki para descrever o transporte de portadores no RTD, considerou-se a distribuição geral do potencial elétrico no dispositivo semicondutor, incluindo a formação das regiões de carga espacial de acumulação no emissor, armazenamento de carga no poço quântico e formação de uma região depleção no coletor. Além disso, considerou-se o espalhamento experimentado pelos portadores durante o processo de tunelamento através da região de dupla barreira de potencial.

O modelo I-V desenvolvido contempla dois casos distintos. O primeiro caso descreve o tunelamento ressonante de elétrons em RTDs, nos quais, devido as características físicas, paramétricas e geométricas do dispositivo, a região do emissor apresenta densidade de estados tridimensional (3D) para os elétrons. O segundo caso

ocorre especialmente em RTDs com camadas espaçadoras com baixo nível de dopagem. Neste caso, forma-se no RTD uma região de acumulação, adjacente a região de dupla barreira, na qual os elétrons no emissor estão sujeitos a uma densidade de estado bidimensional (2D).

De posse do modelo analítico para o cálculo dos níveis de energia em poço quântico e do modelo desenvolvido para descrever a distribuição do perfil de potencial elétrico no RTD, foram desenvolvidos modelos compactos de característica I-V de RTDs 3D-2D e 2D-2D. Desta forma, este trabalho contribui para a modelagem compacta dos RTDs, com vistas ao futuro projeto de circuitos empregando estes dispositivos e considerando os principais fenômenos físicos relevantes na descrição das suas características elétricas e obtendo modelos totalmente analíticos e explícitos. Os modelos desenvolvidos foram validados com dados experimentais e numéricos e fornecendo concordância muito boa.

Palavras-chave: diodo de tunelamento ressonante, modelo compacto, poço quântico, nanoeletrônica, RTD 2D-2D, RTD 3D-2D

Abstract

CELINO, D. R. **Compact Models of Resonant Tunneling Diodes**. 2024. 174 p. Doctoral Thesis – São Carlos School of Engineering, University of São Paulo, São Carlos, 2024.

Due to the growing demand for technologies capable of operating in the Terahertz (THz) frequency range, the Resonant Tunneling Diode (RTD) has attracted renewed interest from the academic community. RTD is a promising candidate for digital and analog applications due to its intrinsic negative differential resistance (NDR) characteristics, high switching speed, and flexible design requirements.

In this framework, this doctoral thesis deals with the compact modeling of the current-voltage (I-V) characteristics of double potential barrier resonant tunneling diodes. For this purpose, it is initially necessary to calculate the energy levels of the eigenstates for the quantum well of finite height present in the semiconductor structures of RTDs. However, determining energy levels for finite quantum wells is only possible through the resolution of transcendental equations using some numerical routine, thereby not allowing an exact analytical solution. Thus, fully analytical approximate solutions were developed to calculate energy levels in rectangular quantum wells of finite height, symmetric and asymmetric, with excellent agreement to exact solutions.

Next, taking the Tsu-Esaki formalism as a starting point to describe carrier transport in the RTD, we consider the general distribution of the electrical potential in the semiconductor device, including the formation of the accumulation and depletion space charge regions, as well as the charge in the quantum well. Furthermore, the scattering experienced by the carriers during the tunneling process through the double potential barrier region was also considered.

The I-V model developed encompasses two distinct cases. The first case describes RTDs, in which, due to the physical, parametric and geometric characteristics of the device, electrons in the emitter have a three-dimensional (3D) density of states. The second case occurs particularly in RTDs employing spacer layers with low doping levels. In this case, the accumulation layer formed in the RTD, adjacent to the double barrier region, is such that the electrons in the emitter have a two-dimensional (2D) density of states

With the analytical model to calculate energy levels in a quantum well and the model developed to describe the distribution of the electrical potential profile in the RTD, compact I-V characteristic models of RTDs 3D-2D and 2D-2D were proposed. In this way, this work contributes to the compact modeling of RTDs, aiming to help on the design of integrated circuits using these devices and taking into account the main physical phenomena relevant in the description of the electrical characteristics of the RTD, thus obtaining fully analytical and explicit models. The developed models were validated with experimental and numerical data, providing very good agreement.

Keywords: resonant tunneling diode, compact model, quantum well, nanoelectronics, RTD 2D-2D, RTD 3D-2D

List of Symbols

$U(x)$	Potential Energy Profile
m^*	Carrier Effective Mass
m_0	Resting Electron Mass
$\hbar$	Reduced Planck Constant
$\Psi(x)$	Wave Function
E	Carrier Kinetic Energy
k	Wave Vectors
$\mathbf{T}$	Transmission Coefficient
$\mathbf{R}$	Reflection Coefficient
U_0	Potential Barrier Height Under Equilibrium
V_a	Applied External Bias
$\mathbf{W}$	Wronskian
ΔV_j	Electric Potential Drop
Φ_j	Electric Potential Barrier Height
κ_b	Barrier Dielectric Constant
κ_w	Quantum Well Dielectric Constant
$\mathbf{D}$	Electric Field Displacement Vector
$\mathbf{F}$	Electric Field Vector
ϵ	Permittivity
ϵ_0	Vacuum Permittivity
e	Elementary Charge
$\mathbf{T}_{WKB}$	Wentzel Kramers Brillouin Tunneling Coefficient
$\mathbf{T}_{DBQW}$	Double Barrier Quantum Well Tunneling Coefficient
$E_{sy,n}$	Eigenenergy Levels of Symmetric Finite Quantum Wells
L_w	Quantum Well Width
α_m	Parameter Accounting for the Differences in Effective Masses
N_{sy}	Allowed Energy Levels of the Symmetric Quantum Well
$\mathbf{M}_{sy}$	Symmetric Well Mapping Function

μ_m	Asymmetric Well Effective Masses Ratio
$E_{asy,n}$	Eigenenergy Levels of Asymmetric Finite Quantum Wells
$\mathbf{M}_{asy}$	Asymmetric Well Mapping Function
N_{asy}	Allowed Energy Levels of Asymmetric Finite Quantum Wells
$L_{Wasy,\min}$	Minimum Width of the Asymmetric Quantum Well
Γ	Resonance Linewidth
$\hat{\mathbf{H}}$	Hamiltonian Operator
$\|\Psi(x)\rangle$	Eigenstate of the System
E_C	Conduction Band
ΔE_C	Discontinuity in the Conduction Band
$V_{ef}(x)$	Effective Electrical Potential
$V\,(x)$	Hartree Electrical Potential
$V_{xc}\,(x)$	Exchange Correlation Electric Potential Term
$\rho\,(x)$	Charge Density
$N_d(x)$	Density of Impurities Donors
$N_d^+(x)$	Density of Ionized Donors
g	Degeneracy Factor
E_d	Donor Energy Level
E_F	Fermi Energy Level
k_B	Boltzmann Constant
$D(E)$	Density of States
$F(E)$	Fermi-Dirac Statistics
$n(x)$	Free Electron Density Distribution
$N_a^-(x)$	Ionized Acceptors Density
J	Current Density
$J_{R\rightarrow L}$	Current Density from Collector to Emitter
$J_{L\rightarrow R}$	Current Density from Emitter to Collector
$\mathbf{v}_g(\mathbf{k})$	Group Velocity
H_T	Total Hamiltonian of the System
H_e^0	Hamiltonian of the Emitter

H_w^0	Hamiltonian of the Well
H_c^0	Hamiltonian of the Collector
$a_{\mathbf{k}}$	Electron Creation Operator
$a_{\mathbf{k}}^\dagger$	Electron Annihilation Operator
Σ_w	Electron Self-Energy
$W(i \to f)$	Scattering Rate from Fermi's Golden Rule
H_{e-ph}	Electron-Phonons Hamiltonian
$\hbar\omega_{LO}$	Energy of the LO-phonon
$H_{_{Fr}}$	Fröhlich Hamiltonian
Γ_T	Total Resonance Width
τ_d	Dwell-Time
τ_m	Moment Relaxation Time
E_r	Resonant Energy Level
Λ	Debye Temperature
$E_{ac,m}$	Accumulation Layer Energy Level
Q_e	Charge in the Emitter
Q_w	Charge in the Quantum Well
Q_c	Charge in the Collector
$\mathbf{T}_L$	Transmission Coefficients for the Left Barrier
$\mathbf{T}_R$	Transmission Coefficients for the Right Barrier
L_{bL}	Left Barrier Width
L_{bR}	Right Barrier Width
V_L	Voltage Drop at the Left Potential Barrier
V_R	Voltage Drop at the Right Potential Barrier
V_w	Voltage Drop in the Well
V_{db}	Voltage Drop in the Double Barrier
V_s	Voltage Drop in the Spacer Layer
L_d	Depletion Region Width
L_{TF}	Thomas-Fermi Length
$n_a(V_a)$	Sheet Carrier Density

$E_{r,n}^{(0)}$	Resonant Energy Level in Equilibrium
$E_{r,n}^{(2)}$	Second-Order Correction for the Energy Level
Γ_s	Linewidth due to Scattering Effects
U_L	Effective left-barrier Height
U_R	Effective right-barrier Height
L_{acc}	Accumulation Region Width
V_{acc}	Voltage Drop in the Accumulation Region
C_i	Geometric Capacitances
G	Differential Conductance
L_Q	Tunneling Inductance
C_t	Total Geometric Capacitance
C_{QW}	Quantum Capacitance
C_{eq}	Overall Equivalent Capacitance
$f_{\max}$	Maximum Oscillation Frequency
$P_{\max}$	Maximum Output Power
I_v	Valley Current
I_p	Peak Current
V_v	Valley Voltage
V_p	Peak Voltage
R_c	Conductive Radius
R_S	Contact and Access Resistance
$L_{Wsy,\min}$	Symmetric Well Minimum Width
β_m	Second Asymmetric Well Effective Masses Ratio

List of Figures

List of Tables

Contents

Chapter 1

Introduction

1.1 Brief Historical Account

Quantum tunneling is a physical phenomenon described by quantum mechanics in which a subatomic particle crosses a potential barrier despite having a kinetic energy lower than the barrier height. Such a phenomenon is prohibited by the laws of classical mechanics, where overcoming a potential barrier by a particle requires sufficient kinetic energy to do so, that is, energy greater than the barrier height [1]- [3].

Radioactivity, discovered in 1896 by H. Becquerel, was the basis for developing the theory of quantum tunneling, mainly from the investigation of the decay of alpha particles [4]. As early as 1900, Rutherford introduced the idea of the half-life of radioactive elements, that is, the time it takes for a sample of radioactive material to have its atomic mass reduced by half [5]. In 1905, Schweidler demonstrated that the decay time of a nucleus of radioactive material can only be estimated statistically [6].

In this context, the phenomenon of quantum tunneling was first observed in 1927 by F. Hund [7]. When investigating the spectra of certain molecules, Hund observed that, in the specific case of a double well of quantum potential, the superposition of even and odd states results in a state that allows the tunneling of a subatomic particle from one well to the other [7]. This phenomenon was also observed in the same year independently by L. Mandelstam and M. Leontovich when they analyzed the implications of the formalism proposed by Schrödinger for a particle in a potential well with finite height [8].

One of the first applications of the wave formalism developed by Schrödinger consisted of the mathematical description for the decay of alpha particles, developed in 1928 by G. Gamow [9]- [10]. To explain the decay of alpha particles, Gamow solved the Schrödinger equation with an effective continuous potential that contemplates the interior and exterior of the nucleus, to which he imposed the boundary conditions for the outbound wave function [9]- [10]. Thus, in Gamow's formalism, the alpha particle must tunnel through the effective potential barrier to escape the nucleus. M. Born noted that the idea of tunneling presented by Gamow was not only applicable to nuclear physics but also to an intrinsic, general characteristic that should be present in other physical systems. Born realized that the cold emission of electrons from a metal surface may be another example of this phenomenon. With this assumption, Born generalized the phenomenon of quantum tunneling, not restricted to nuclear physics but a general result of quantum mechanics that applies to many different systems [3], [11].

Independently of Gamow, R. Gurney and E. Condon formalized a quantum tunneling-based explanation for alpha particle decay [12]. Gurney and Condon simultaneously solved the Schrödinger equation for a nuclear potential model and derived a relationship between particle half-life and emission energy, which is directly dependent on the tunneling probability coefficient.

A classic work on tunneling was published in 1928 by Oppenheimer, in which the author proposes a probabilistic quantum explanation for certain aperiodic phenomena, such as the scattering of alpha particles [13]. At the same time, Gurney formulated resonant tunneling, trying to explain how a particle with energy equal to one of the nucleus's self-energies can easily penetrate the potential barrier [14].

As far as solid-state devices are concerned, from the 1920s to the 1940s, there were many attempts to relate the electrical current in a metal-semiconductor rectifier device to the phenomenon of electron tunneling in solids [3]. In 1928, Fowler and Nordheim [15] developed a theory, based on the cold emission model, to describe the electron emission from the metal in a vacuum at low temperatures and subjected to intense electric fields. Later, Fowler and Nordheim derived an accurate expression for current density considering the probability of electrons tunneling through the potential barrier between the metal surface and the vacuum [15]. An excellent historical review of the earliest days of quantum tunneling can be found in [8].

After the invention of the transistor in 1947, electron tunneling returned to attract the interest of many researchers. By 1950, the fabrication of thin layers of semiconductors such as Ge and Si had advanced to the point where it was possible to manufacture semiconductor devices with satisfactory electric output characteristics [16].

In 1957, Esaki proposed the so-called tunnel diode, also known as the Esaki diode [17]. The tunnel diode is named after the inter-band tunneling between the valence and conduction bands. The device is composed of a heavily doped PN-junction. When investigating the proposed tunnel diode, Esaki and coworkers observed a physical phenomenon called negative differential resistance (NDR). Basically, as the applied bias increases, the current density decreases, which characterizes the NDR. The Esaki diode has applications in microwave technology and can be used as a frequency converter, oscillator and receiver [18]. However, its low power output limits the applications of the device.

Next, in 1964, Iogansen [19] theoretically investigated the control of resonant quantum tunneling by applying voltage in double potential barrier structures formed by layers of dielectrics in a metallic conductor [19]. In addition, throughout the 1960s, there was great research interest in quantum tunneling between superconductors and metals [20] and between superconductors separated by thin insulating layers [21].

Later, in 1970, Esaki and Tsu [22] proposed a novel type of one-dimensional periodic potential – an artificial superlattice. This structure consists of alternating sequence potential barriers and quantum wells formed by the successive deposition of different semiconductor layers or by the periodic variation of the alloy composition, such as the alloy $Al_xGa_{1-x}As$. In the article [22], the authors demonstrated that, when biasing the structure, the current-voltage (**I–V**) characteristics show an NDR similar to the one observed in the tunnel diodes [22]. However, unlike the tunnel diode, the negative resistance in superlettice originates from intra-band resonant tunneling.

During the 1970s, advances in epitaxial growth technologies such as MBE (Molecular Beam Epitaxy) and MOCVD (Metalorganic Chemical Vapor Deposition) increasingly allowed the growth of semiconductor heterostructures with a high level of precision and low density of unwanted impurities [23]. Thus, it became feasible to manufacture semiconductor structures with one or more dimensions comparable to the de Broglie wavelength, giving rise to quantization

phenomena. As a consequence, the physical properties of these reduced dimensionality structures are governed by quantum mechanics. In general, features associated with the carrier's wave nature reveal many macroscopic quantum effects [24]. With technological maturity, it was possible to manufacture structures based on III-V semiconductors and their respective alloys, since there are many material systems with compatible lattice parameters, for instance, GaAs/AIGaAs, InGaAs/InP, and InGaAs/AlInAs.

L. Esaki, I. Giaever and B. Josephson were awarded with the Nobel Prize, in 1973, because of their work on quantum tunneling [25]. Since then, many devices based on quantum tunneling have been proposed in the literature: a prominent example is the Double Barrier Resonant Tunneling Diode (DB-RTD).

1.2 The Resonant Tunneling Diode (RTD)

By using the current technology fabrication process, it is possible to manufacture semiconductor structures with characteristic features of a few tens of Angströns. One of these popular structures is the quantum wire. Theoretically, the concept of a quantum wire was pioneered by Sakaki in 1980 [26], but, only in the 1990s, did these structures become technologically feasible, due to the improvement in material growth techniques. In these structures, the electronic confinement is two-dimensional, while, the carriers are free to move in the remaining dimension, reducing the scattering effects and allowing the production of ultra-fast devices [27]- [30].

Another structure in which quantum effects can be macroscopically observed is the superlattice [22], [31]. Theoretically, the superlattice is formed by an infinite periodic structure of barriers and quantum wells, with a period shorter than the electron mean free path [31]. However, realistic structures comprise a finite number of periods with alternating semiconductor layers. Also, the electron mean free path in these realistic structures is relatively short. Moreover, heavily doped interfaces between the superlattice and terminal electrodes, including ohmic contacts, are unavoidable [31]. Under these circumstances, the transport properties between the terminal electrodes through the undoped periodic structure can be determined by considering the multi-barrier tunneling under bias voltage application [31]. This formalism takes into account two important quantum effects: quantum confinement and quantum tunneling. Also, the

superlattice form coupled electronic states inducing numerous quantum effects, such as quantum Hall effect, Bloch oscillations and negative resistance [32].

Among these heterostructure devices are resonant tunneling devices, such as RTD [33], which are characterized by the non-linearity in the current-voltage characteristic. In this context, the negative differential resistance of RTDs allows its deployment as an oscillator circuit. There are also applications in logic circuits and memory devices. Currently, resonant tunneling structures have a high degree of technological maturity, in which a large number of fabricated devices operate at room temperature [27]- [30], [34]- [47]. Fig. (1.1) shows a schematic illustration of a double potential barrier RTD composed of the GaAs/AlGaAs heterostructure, containing the different semiconductor layers and the conduction band profile.

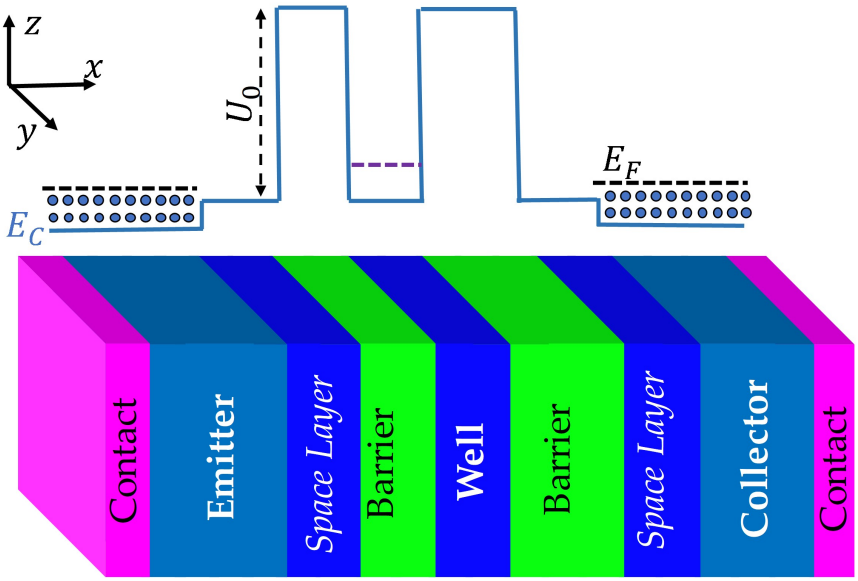

Figure 1.1: A schematic illustration of a typical bulk resonant tunneling diode structure depicting the different semiconductor layers that compose the device. The figure also contains a schematic illustration of the conduction band, depicting the double potential barrier region. The term, E_r, refers to the resonant energy in the quantum well.

From a historical point of view, one of the factors that boosted nanoelectronics in the mid-1980s was the work on resonant tunneling and semiconductor bandgap engineering with quantum wells and low-dimensional superlattices. The scientific community committed a great effort to developing these devices, which resulted in rapid progress in the physical understanding of the charge transport of mesoscopic structures. As a result, the RTD has become a focus of re-

search in nanoelectronics for analog and digital applications. Progress in epitaxial growth has improved the Peak-to-Valley Current ratio (PVCR) at room temperature beyond what is needed for many circuit applications. This temperature requirement is one of the most important characteristics any new technology must satisfy, and it distinguishes the RTD from other proposed interesting quantum devices, which demand cryogenic temperatures [34].

The increasing demand for high bandwidth services, such as 5G applications, artificial intelligence (AI), augmented reality (AR), virtual reality (VR), online gaming, IoT (Internet of Things), and stream platforms, is driving mobile communications towards the use of terahertz waves. In this context, 5G technology has been standardized to offer data rates up to tens of Gb/s operating in the millimeter-wave range (24.25 GHz to 52.6 GHz) [35]. However, despite the high spectral efficiency modulation formats employed, it is generally not possible to obtain data rates above 100 Gbps in this range. Since 6G mobile networks are expected to support peak data rates of 1 Tb/s, academia and industry turn their attention to the unlicensed and under-explored band from 300 GHz to 3 THz, as it provides a contiguous bandwidth of tens and up to hundreds of gigahertz [36], [37].

For this purpose, however, it is necessary to develop compact and low-cost THz transceivers, providing high enough output power. Among the available semiconductor technologies, transceivers based on RTDs are among the most efficient contenders for 6G applications [38], [43]. It is worth noting that the present record for the highest oscillation frequency of 1.92THz was obtained by an RTD oscillator [29]. Additionally, tunable RTDs were obtained by integrating a varactor with the resonant element [45]. Furthermore, the RTD demonstrated great versatility as a resonator across the entire frequency spectrum, with relatively high output power, 420 μW at a frequency of 550 GHz [46], $1\ \mathrm{mW}$ at $300\ \mathrm{GHz}$ and $5\ \mathrm{mW}$ at $160\ \mathrm{GHz}$ [47].

In particular, resonant tunneling devices in combination with silicon transistors are interesting for the semiconductor industry as they offer a way to extend the performance of existing technologies by increasing switching speed and decreasing power dissipation [48]. In this way, silicon RTTs (Resonant Tuneling Transistors) may be integrated with CMOS technology [49]. In short, RTDs and RTTs offer a wide range of applications in ADC (Analog-to-Digital Converter), frequency divider or multiplier, oscillator, and digital circuits with more than 2 bits [50].

The ongoing effort in modeling RTD quantum transport is motivated by the necessity to

fully understand its the main electrical characteristics. Furthermore, the modeling provides valuable knowledge of the quantum aspects of electron transport in mesoscopic systems [51]. For conventional devices, such as the MOSFET and the BJT (Bipolar Junction Transistor) with geometric dimensions in the micrometers range, the carrier transport models based on Boltzmann semi-classical formalism, in its simplest formulation, the drift-diffusion formulation, satisfactorily describe their electrical characteristics. However, Boltzmann formalism becomes inadequate with the downscaling of semiconductor devices reaching the nanometric scale. The formalism becomes invalid since the classical concepts of charge carrier transport neglect the effects of quantum interference which arise from the wave treatment of the physical principle of operation of the device. Thus, a device model which can adequately treat quantum transport phenomena between macroscopic and microscopic scales is necessary for nanostructures. In this sense, even in bulk RTDs, because the thickness of the barriers and the quantum well layers is of in a few nanometers, it becomes necessary to employ Schrödinger wave quantum formalism to describe carrier transport dynamics [51].

Compact models can be summarized into basically three types:

1. Table-based models, where empirical models are obtained from tabulated data arising from experimental characterizations or more complex simulations, such as atomistic simulations

2. Semi-empirical models, in which one or more physical parameters are adjusted to fit experimental data

3. Physics-based models

Considering the above discussion, compact models are employed over other numerical approaches for circuit simulators due to the lower computational effort, which allows a quick evaluation of the circuit electrical characteristics [51]. Physics-based compact models are widely used to describe semiconductor devices in electrical circuit simulators. The objective of such models is to relate the device parameters, such as the thickness of the semiconductor layers, the potential profile, and its semiconductor material composition, among others, to the output electrical characteristics. Unlike sophisticated numerical methods, compact models quickly evaluate the output characteristics of the device while keeping most of the physical insights required

for optimization. Therefore, they fashion an essential instrument to enable the development of next-generation devices applications.

As a requirement, compact models must allow a wide range of input parameters, to provide versatility, take into account the main physical characteristics of the device and have a fast convergence in circuit simulators [51], [52]. In this sense, the accuracy of a compact model depends mainly on the number of physical parameters used and on the simplifications and assumptions used to reach the compact expressions. For instance, modeling the I-V characteristic of RTDs requires a formalism based on quantum mechanics. Therefore, accurate compact models must include several physical effects, such as charge quantization, coherent resonant tunneling, sequential resonant tunneling, and quantum scattering effects, among other mechanisms, which influence the electrical characteristics of the device.

The number of parameters used in the model must be small but sufficient to represent the main physical phenomena of the device. Usually, a compact model is characterized by a determined validity interval. However, in many cases, it is possible to extend the validity interval through additional equations. Also, a compact analytical model based on device physics can also be useful for selecting suitable materials for device design.

1.3 Objective

The goal is to develop robust analytical models allowing the analysis and design of RTD devices. Specifically, we aim to develop compact, analytical physics-based models to describe RTDs electrical characteristics. In order to achieve a fully analytical model it is necessary to analytically describe the eigenergies of a finite quantum well present in RTDs. However, to determine these energy levels requires solving transcendental equations, which do not have exact analytical solutions. Therefore, the first step is to develop analytical expressions to calculate the energy levels in rectangular quantum wells of finite height.

Next, the thesis deals with two distinct cases. In short, the first case describes the resonant tunneling of electrons in an RTD, in which, due to the device characteristics, electrons in the emitter have a 2D density of states. The second one occurs in RTDs where tunneling carriers from the emitter side possess a 3D density of states.

1.4 Thesis Outline

- In Chapter 2, we review useful analytical expressions to compute the quantum tunneling transmission coefficient across rectangular potential barriers, with and without applied bias. These expressions are valuable for a fully analytical RTD model.

- Chapter 3 presents original, accurate analytical expressions to compute the eigenenergies for finite rectangular quantum wells. We derived useful analytical expressions for nano-electronics and optoelectronics design purposes. The expressions are validated against numerical solutions of the energy levels transcendental equations. As a result, an agreement greater than 99% is achieved for the solution space investigated.

- Chapter 4 presents the physical principles of charge transport in RTDs and the origin of the negative differential resistance (NDR). Then, Tsu and Esaki pioneering work on electronic charge transport in RTDs is discussed. Also, we outline the relevant scattering mechanisms present in RTD. Finally, some numerical and analytical models found in the literature are analyzed.

- In Chapter 5, we develop a fully analytical model for the I-V characteristics of 2D-2D and 3D-2D RTD. We consider the overall electrical potential distribution in the device layer structure, including the quantized space charge region in the emitter layer, and account for the scattering effects. The developed model is validated against experimental and numerical data gathered from technical literature and TCAD simulation performed in this work.

- In Chapter 6, the contributions and perspectives offered by this work are discussed. Also, the scope for future work is outlined.

- In the Appendix, we provide on how to employ the approach, referred here as the mapping function, derived in Chap. 3, to obtain approximate solutions of transcendental equations.

Chapter 2

Quantum Tunneling

In this chapter, we review useful analytical expressions to compute the quantum tunneling transmission coefficient across rectangular potential barriers, with and without applied bias. Specifically, we analyze the double barrier quantum well (DBQW) structure present in RTD in which the phenomenon of resonant tunneling occurs. For the DBQW, the exact analytical expression and the Breit-Wigner Lorentzian approximation are also demonstrated [53]. We should highlight that the expressions provided, in this chapter, comprise the key ingredients toward a fully analytical model to describe RTD electrical output characteristics.

2.1 Rectangular Potential Barrier

From quantum mechanics, it is known that when the energy of an incident particle is less than the barrier height, its wavefunction decays exponentially within the barrier region [54]-[56]. As a consequence, for a barrier of infinite extension, no probability current density flows through the interface [18], i.e., the entire probability current density is reflected to the incident region. However, considering a narrow enough barrier width, the wavefunction does not completely decay to zero before reaching the second interface. In other words, the probability wavefunction has a non-zero value after passing through the barrier. Classically, there is no difference in whether the potential barrier is finite or infinite spatial extent. In both cases, the particle must be reflected by the barrier [57]. However, wavefunction transmission is possible in the quantum mechanics framework, referred to as quantum tunneling [3].

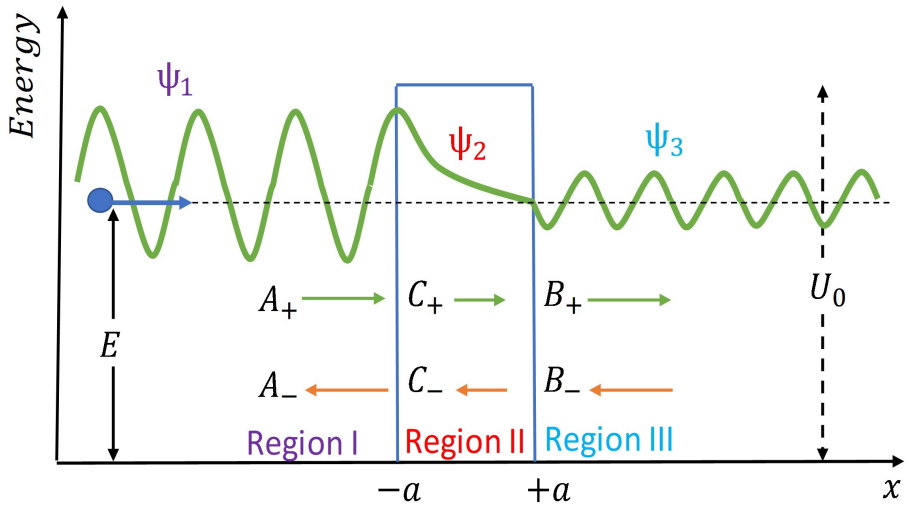

Figure 2.1: Schematic illustration of the wavefunction transmission through a symmetric rectangular potential barrier. The terms A_+, A_-, C_+, C_-, B_+ and B_- are the wavefunctions amplitudes of incident and reflected plane waves in each region.

Fig. (2.1) contains a schematic illustration of wavefunction transmission through the one-dimentional potential barrier. The potential energy profile can be written as

$$U(x) = \begin{cases} 0, & x < -a \\ U_0, & -a \leq x \leq a \\ 0, & x > a \end{cases} . \tag{2.1}$$

As usual, the one-dimensional Schrödinger equation is

$$-\frac{\hbar^2}{2m_i^*}\frac{d^2\Psi_i(x)}{dx^2} + U(x)\Psi_i(x) = E\Psi_i(x). \tag{2.2}$$

where m_i^* is the carrier effective mass in region i, $\hbar$ is the reduced Planck constant, $\Psi_i(x)$ is the wave function in region i and E is the energy of the carrier. For most practical cases in microelectronics, the carrier effective mass is the same in regions I and III and distinct in region II, i.e., different in the barrier region. Thus, for the three regions, we obtain

$$\begin{aligned} \Psi_1(x) &= A_+e^{ikx} + A_-e^{-ikx}, \quad x < -a \\ \Psi_2(x) &= C_+e^{-Kx} + C_-e^{Kx}, -a \leq x \leq a \\ \Psi_3(x) &= B_+e^{ikx} + B_-e^{-ikx}, \quad x > a \end{aligned} \tag{2.3}$$

where $A_+,\ A_-, C_+, C_-, B_+$ and B_- are the wavefunctions amplitudes of incident and reflected plane waves in each region (see Fig. (2.1)).

The wave vectors k and K are defined as

$$\begin{aligned} k &= \sqrt{\frac{2m_1^* E}{\hbar^2}}, \\ K &= \sqrt{\frac{2m_2^*(U_0 - E)}{\hbar^2}}. \end{aligned} \tag{2.4}$$

The boundary conditions at the interfaces are given by [1]:

$$\begin{aligned} \Psi_i(x) &= \Psi_j(x) \\ \frac{1}{m_i^*}\frac{\partial}{\partial x}\Psi_i(x) &= \frac{1}{m_j^*}\frac{\partial}{\partial x}\Psi_j(x), \end{aligned} \tag{2.5}$$

Applying the boundary conditions at the interfaces $x = -a$ and $x = a$, and setting $\beta_m = m_2^*/m_1^*$ yields

$$\begin{aligned} \begin{bmatrix} A_+ \\ A_- \end{bmatrix} = & \begin{bmatrix} \frac{1}{2}\left(\frac{k\beta_m + iK}{k\beta_m}\right) e^{a(ik+K)} & -\frac{1}{2}\left(\frac{-k\beta_m + iK}{k\beta_m}\right) e^{a(ik-K)} \\ -\frac{1}{2}\left(\frac{-k\beta_m + iK}{k\beta_m}\right) e^{-a(ik-K)} & \frac{1}{2}\left(\frac{k\beta_m + iK}{k\beta_m}\right) e^{-a(ik+K)} \end{bmatrix} \\ & \times \begin{bmatrix} \frac{1}{2}\left(\frac{K - ik\beta_m}{K}\right) e^{a(ik+K)} & \frac{1}{2}\left(\frac{K + ik\beta_m}{K}\right) e^{-a(ik-K)} \\ \frac{1}{2}\left(\frac{K + ik\beta_m}{K}\right) e^{a(ik-K)} & \frac{1}{2}\left(\frac{K - ik\beta_m}{K}\right) e^{-a(ik+K)} \end{bmatrix} \begin{bmatrix} B_+ \\ B_- \end{bmatrix}, \end{aligned} \tag{2.6}$$

writing Eq. (2.6) in the form

$$\begin{bmatrix} A_+ \\ A_- \end{bmatrix} = \underbrace{\begin{bmatrix} M_{11} & M_{12} \\ M_{21} & M_{22} \end{bmatrix}}_{\mathbf{M}} \begin{bmatrix} B_+ \\ B_- \end{bmatrix}, \tag{2.7}$$

where $\mathbf{M}$ is defined as the transfer matrix. This approach is best known in the literature as the Transfer Matrix Method (TMM) and can be generalized for multiple barriers structures [18], [56].

Knowing that $\cosh x = (e^x + e^{-x})/2$ and $\sinh x = (e^x - e^{-x})/2$ after some algebraic work, one obtains

$$\begin{aligned} M_{11} &= \left[\cosh(2Ka) - \tfrac{i}{2}\left(\tfrac{\beta_m^2 k^2 - K^2}{\beta_m kK}\right)\sinh(2Ka)\right] e^{i2ka}, \\ M_{21} &= -\tfrac{i}{2}\left(\tfrac{\beta_m^2 k^2 + K^2}{\beta_m kK}\right)\sinh(2Ka), \\ M_{22} &= M_{11}^*, \\ M_{12} &= M_{21}^*. \end{aligned} \tag{2.8}$$

The transmission coefficient is defined as the ratio between the transmitted probability current density, emerging from the right-side of the barrier, and the incident current density to the left-side of the barrier [1], [18]. Using Eq. (2.9), the current density for the incident wavefunction, J_{inc}, and transmitted, J_{tran}, is obtained assuming a zero incident current density to the barrier right-side, which means $B_- = 0$. Then, knowing that the current density can be written as [1]:

$$\vec{J} = \frac{\hbar}{2m^* i}\left(\Psi^* \vec{\nabla}\Psi - \Psi\vec{\nabla}\Psi^*\right), \tag{2.9}$$

we have J_{inc}, J_{tran}, and the current density reflected by the barrier, J_{ref}, as

$$J_{inc} = \frac{k\hbar}{m_1^*}\left|A_+^2\right|,\ J_{tran} = \frac{k\hbar}{m_1^*}\left|B_+^2\right|,\ J_{ref} = \frac{k\hbar}{m_1^*}\left|A_-^2\right|.$$

One can write the transmission, $\mathbf{T}$, and reflection, $\mathbf{R}$, coefficients as

$$\begin{aligned} \mathbf{T} &= \frac{J_{tran}}{J_{inc}} = \frac{\left|B_+^2\right|}{\left|A_+^2\right|}, \\ \mathbf{R} &= \frac{J_{ref}}{J_{inc}} = \frac{\left|A_-^2\right|}{\left|A_+^2\right|}, \end{aligned} \tag{2.10}$$

from Eq. (2.7) since $B_- = 0$, one gets

$$\frac{B_+}{A_+} = \frac{1}{M_{11}},\ \frac{A_-}{A_+} = \frac{M_{21}}{M_{11}}. \tag{2.11}$$

Next, by using the identity $\cosh^2 x = 1 + \sinh^2 x$ to simplify M_{11}, combining Eq. (2.11) with Eq. (2.10), we have:

$$\begin{aligned}\mathbf{T} &= \frac{1}{|M_{11}|^2} = \left[1 + \frac{\left(\beta_m^2 k^2 + K^2\right)^2}{4\beta_m^2 k^2 K^2}\sinh^2(2Ka)\right]^{-1}, \\ \mathbf{R} &= \frac{|M_{21}|^2}{|M_{11}|^2} = \frac{\left(\beta_m^2 k^2 + K^2\right)^2 \sinh^2(2Ka)}{\left(\beta_m^2 k^2 + K^2\right)^2 \sinh^2(2Ka) + 4\beta_m^2 k^2 K^2}.\end{aligned} \tag{2.12}$$

For the particular case in which $m_1^* = m_2^*$, replacing Eq. (2.4) in Eq. (2.12) yields:

$$\begin{aligned}\mathbf{T} &= \left[1 + \frac{V_0^2 \sinh^2(2Ka)}{4E(V_0 - E)}\right]^{-1}, \\ \mathbf{R} &= \left[1 + \frac{4E(V_0 - E)}{V_0^2 \sinh^2(2Ka)}\right]^{-1},\end{aligned} \tag{2.13}$$

From Eq. (2.13), when the term $\sinh^2(2Ka)$ vanishes, the transmission coefficient becomes equal to 1 and the reflection coefficient becomes equal to 0. As an example, consider a potential barrier with $U_0 = 1.0$ eV and width 20 Å. The electron effective mass in regions I and III is $m_1^* = 0.065m_0$, and in region II is $m_2^* = 0.15m_0$ where m_0 is the resting mass. Fig. (2.2) shows the transmission coefficient as a function of electron kinetic energy for both classical and quantum particles.

As it can be seen from Fig. (2.2), the transmission coefficient reaches its maximum value when the kinetic energy is approximately 1.632 eV. In addition, the transmission coefficient, although small, is non-zero for an incident electron with kinetic energy below U_0, thus, enabling quantum tunneling. It is interesting to note that the value of $\mathbf{T}$ drops significantly for $E > 1.632$ eV. This demonstrates that, even for electrons with kinetic energy greater than the barrier height there are specific values of E in which $\mathbf{T} \neq \mathbf{1}$. This is due to the transmission coefficient oscillatory behavior, tending to one for incident electrons with kinetic energy greater than barrier height. On the other hand, for a particle described by classical mechanics, whenever $E > U_0$, the transmission will occur [54].

2.2 Rectangular Barrier Under Applied Bias

Fig. (2.3) shows a schematic illustration of a rectangular potential barrier under applied bias. From Fig. (2.3) it is possible to notice potential slope ($-a \leq x \leq a$) due to the application

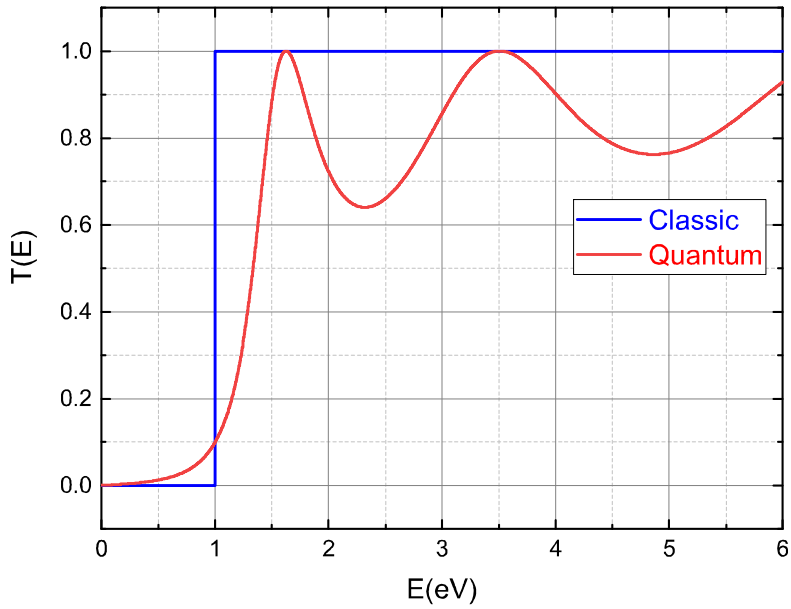

Figure 2.2: Transmission coefficient for a rectangular potential barrier as a function of incident kinetic energy.

of the external bias, $U_a = eV_a$. The applied electric potential modifies the solutions of the Schrödinger equation in regions II and III which become a function of the applied voltage.

As done in the previous section, for the region I, we have

$$\frac{d^2\Psi_1(x)}{dx^2} + k_1^2\Psi_1(x) = 0, \;\; k_1 = \sqrt{\frac{2m_1^* E}{\hbar^2}}, \tag{2.14}$$

with the solution given by

$$\Psi_1(x) = A_+ \exp(ik_1 x) + A_- \exp(-ik_1 x). \tag{2.15}$$

For the region II, we assume a constant electric field distribution as schematically illustrated in Fig. (2.3). Then, the electric potential in region II as a linear equation given by

$$V(x) = U_0 - \frac{U_a}{2} + \alpha x, \;\; \alpha = -\frac{U_a}{2a}.$$

Setting ρ_2 as

$$\rho_2\left(x\right) = \left(\frac{2m^*\alpha}{\hbar^2}\right)^{1/3}\left(x+\beta\right), \tag{2.16}$$

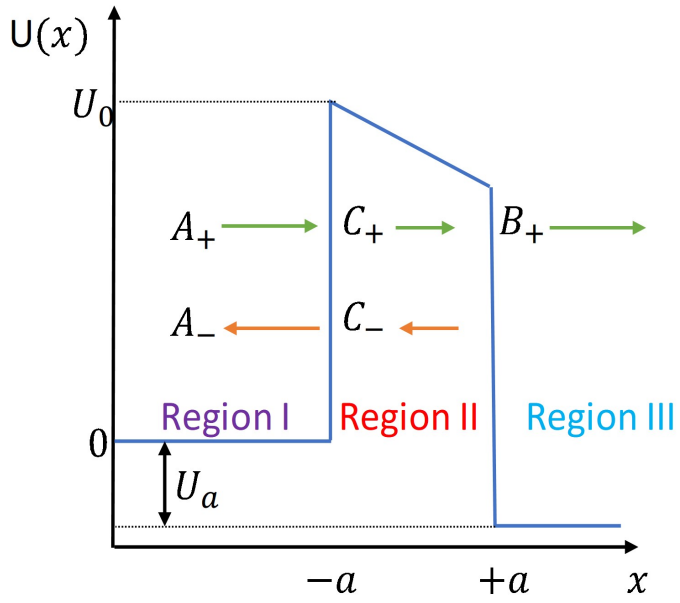

Figure 2.3: Schematic of a rectangular potential barrier under applied bias.

where $\beta = V_0 - V_a/2 - E/\alpha$, the Schrödinger equation can be written as

$$\frac{d^2\Psi_2(x)}{dx^2} - \left[\left(\frac{2m_2^*\alpha}{\hbar^2}\right)^{2/3}\left(\frac{2m_2^*\alpha}{\hbar^2}\right)^{1/3}(x+\beta)\right]\Psi_2(x) = 0. \tag{2.17}$$

One can write the relation

$$\frac{d^2}{dx^2} \rightarrow \left(\frac{d\rho_2}{dx}\right)^2\frac{d^2}{d\rho_2^2} = \left(\frac{2m_2^*\alpha}{\hbar^2}\right)^{2/3}\frac{d^2}{d\rho_2^2}. \tag{2.18}$$

Thus, the Schrödinger equation becomes an Airy-type differential equation:

$$\left(\frac{2m^*\alpha}{\hbar^2}\right)^{2/3}\frac{d^2\Psi_2}{d\rho_2^2} - \left(\frac{2m^*\alpha}{\hbar^2}\right)^{2/3}\rho_2\Psi_2 = 0. \tag{2.19}$$

The solution of the above equation is a linear combination of the Airy functions, Ai and Bi:

$$\Psi_2(x) = C_+ Ai\left[\rho_2(x)\right] + C_- Bi\left[\rho_2(x)\right]. \tag{2.20}$$

As usual, for region III, we have

$$\frac{d^2\Psi_3(x)}{dx^2} + k_3^2\Psi_3(x) = 0,\ k_3 = \sqrt{\frac{2m_3^*}{\hbar^2}(U_a + E)}, \tag{2.21}$$

The solution of Eq. (2.21) can be written as $\Psi_3(x) = B_+ \exp(ik_3x) + B_- \exp(-ik_3x)$.

By applying the boundary conditions, one can establish a relationship between the amplitudes of the incident and transmitted wave functions as

$$\begin{aligned}
\begin{bmatrix} A_+ \\ A_- \end{bmatrix} &= \begin{bmatrix} \frac{1}{2}\exp(ik_1a) & -\frac{im_1^*}{2k_1}\exp(ik_1a) \\ \frac{1}{2}\exp(-ik_1a) & -\frac{ik_1}{m_1^*}\exp(ik_1a) \end{bmatrix} \\
&\times \begin{bmatrix} Ai\left[\rho_2(-a)\right] & Bi\left[\rho_2(-a)\right] \\ \frac{1}{m_2^*}Ai'\left[\rho_2(-a)\right] & \frac{1}{m_2^*}Bi'\left[\rho_2(-a)\right] \end{bmatrix} \\
&\times \begin{bmatrix} \frac{1}{\mathbf{W}(Ai[\rho_2(a)],Bi[\rho_2(a)])}Bi'\left[\rho_2(a)\right] & -\frac{m_2^*}{\mathbf{W}(Ai[\rho_2(a)],Bi[\rho_2(a)])}Bi\left[\rho_2(a)\right] \\ -\frac{1}{\mathbf{W}(Ai[\rho_2(a)],Bi[\rho_2(a)])}Ai'\left[\rho_2(a)\right] & \frac{m_2^*}{\mathbf{W}(Ai[\rho_2(x_2)],Bi[\rho_2(x_2)])}Ai\left[\rho_2(a)\right] \end{bmatrix} \\
&\times \begin{bmatrix} \exp(ik_3a) & \exp(-ik_3a) \\ \frac{ik_3}{m_3^*}\exp(ik_3a) & -\frac{ik_3}{m_3^*}\exp(-ik_3a) \end{bmatrix} \begin{bmatrix} B_+ \\ B_- \end{bmatrix},
\end{aligned} \tag{2.22}$$

where $\mathbf{W}\left(Ai\left[\rho_2(a)\right], Bi\left[\rho_2(a)\right]\right)$, is the Wronskian of the Airy functions [58]- [59]:

$$\mathbf{W}\left(Ai\left[\rho_2(a)\right], Bi\left[\rho_2(a)\right]\right) = Ai\left[\rho_2(a)\right] Bi'\left[\rho_2(a)\right] - Ai'\left[\rho_2(a)\right] Bi\left[\rho_2(a)\right].$$

Assuming that the amplitude B_- is equal to zero, i.e., there is no reflection on the second interface ($x = a$), we have

$$\begin{bmatrix} A_+ \\ A_- \end{bmatrix} = \begin{bmatrix} M_{11} & M_{12} \\ M_{21} & M_{22} \end{bmatrix} \begin{bmatrix} B_+ \\ 0 \end{bmatrix}. \tag{2.23}$$

The transmission coefficient is given by

$$\mathbf{T} = \left(\frac{k_3m_1^*}{k_1m_3^*}\right)\frac{|B_+|^2}{|A_+|^2} = \left(\frac{k_3m_1^*}{k_1m_3^*}\right)\frac{1}{M_{11}^*M_{11}}. \tag{2.24}$$

After performing the matrix multiplications in Eq. (2.22) it is necessary to compute the matrix element M_{11}. After some algebraic manipulations and simplifications, one can write M_{11} as

$$\begin{aligned}
M_{11} &= \frac{\exp\left[i\left(k_3a + k_1a\right)\right]}{2\mathbf{W}\left(Ai\left[\rho_2(a)\right], Bi\left[\rho_2(a)\right]\right)} \\
&\times \left\{\left[\gamma_1 - \left(\frac{k_3}{k_1}\frac{m_1^*}{m_3^*}\right)\gamma_4\right] + i\left[\left(\frac{k_3}{m_3^*}m_2^*\right)\gamma_3 - \left(\frac{1}{k_1}\frac{m_1^*}{m_2^*}\right)\gamma_2\right]\right\},
\end{aligned} \tag{2.25}$$

where the constants are given by

$$\begin{aligned}
\gamma_1 &= \left[Ai\left[\rho_2(-a)\right] Bi^{'}\left[\rho_2(a)\right] - Bi\left[\rho_2(-a)\right] Ai^{'}\left[\rho_2(a)\right]\right], \\
\gamma_2 &= \left[Ai^{'}\left[\rho_2(-a)\right] Bi^{'}\left[\rho_2(a)\right] - Bi^{'}\left[\rho_2(-a)\right] Ai^{'}\left[\rho_2(a)\right]\right], \\
\gamma_3 &= \left[-Ai\left[\rho_2(-a)\right] Bi\left[\rho_2(a)\right] + Bi\left[\rho_2(-a)\right] Ai\left[\rho_2(a)\right]\right], \\
\gamma_4 &= \left[Ai^{'}\left[\rho_2(-a)\right] Bi\left[\rho_2(a)\right] - Bi^{'}\left[\rho_2(-a)\right] Ai\left[\rho_2(a)\right]\right],
\end{aligned} \tag{2.26}$$

besides, we have $\mathbf{W}\left(Ai\left[\rho_2(a)\right], Bi\left[\rho_2(a)\right]\right) = \pi^{-1}$ [60].

Finally, the transmission coefficient is obtained by replacing Eq. (2.25) in Eq. (2.24):

$$\begin{aligned}
\mathbf{T}\left(E, V_a\right) &= \left(\frac{k_3 m_1^*}{k_1 m_3^*}\right)\frac{\pi^2}{4} \\
&\times \left[\left|\gamma_1 - \left(\frac{k_3}{k_1}\frac{m_1^*}{m_3^*}\right)\gamma_4\right|^2 + \left|\left(\frac{k_3}{m_3^*}m_2^*\right)\gamma_3 - \left(\frac{1}{k_1}\frac{m_1^*}{m_2^*}\right)\gamma_2\right|^2\right]^{-1}.
\end{aligned} \tag{2.27}$$

Therefore, assuming a constant electric field distribution in the barrier, the transmission coefficient is expressed in terms of a linear combination of Airy functions. Because of the difficulties imposed by utilizing special functions such as Airy, in this work, aiming to derive, as simple as possible, analytical models, the exact solution given by Eq. (2.27) is used in our work to validate more simplified approximations.

2.3 Multiple Barriers Under Applied Bias

The multiple barrier structure is formed by alternating potential barriers separated by quantum wells, commonly referred to as superlattice [53], [61]. Superlattices are generally semiconductor structures consisting of a layers sequence composed of different semiconductor materials arranged periodically [53].

As a first step to compute the transmission coefficient for a multiple barrier structure, the electric potential energy profile $U(x)$ must be outlined. To do so, we assume a constant electric field distribution throughout the structure. Fig. (2.4) contains a schematic illustration of a multiple barrier structure composed of n barriers and $n-1$ quantum wells, under applied bias V_a.

The potential drop over the barriers and quantum well can be expressed as

$$eV_a = \Delta V_1 + \Delta V_2 + ... + \Delta V_n = \sum_{j=1}^{n} \Delta V_j, \tag{2.28}$$

where e represents the elementary charge. The terms ΔV_j in Eq. (2.28) accounts for the electrical potential energy drop over the barrier when j is even, and under the quantum well when j is odd, as illustrated in Fig. (2.4).

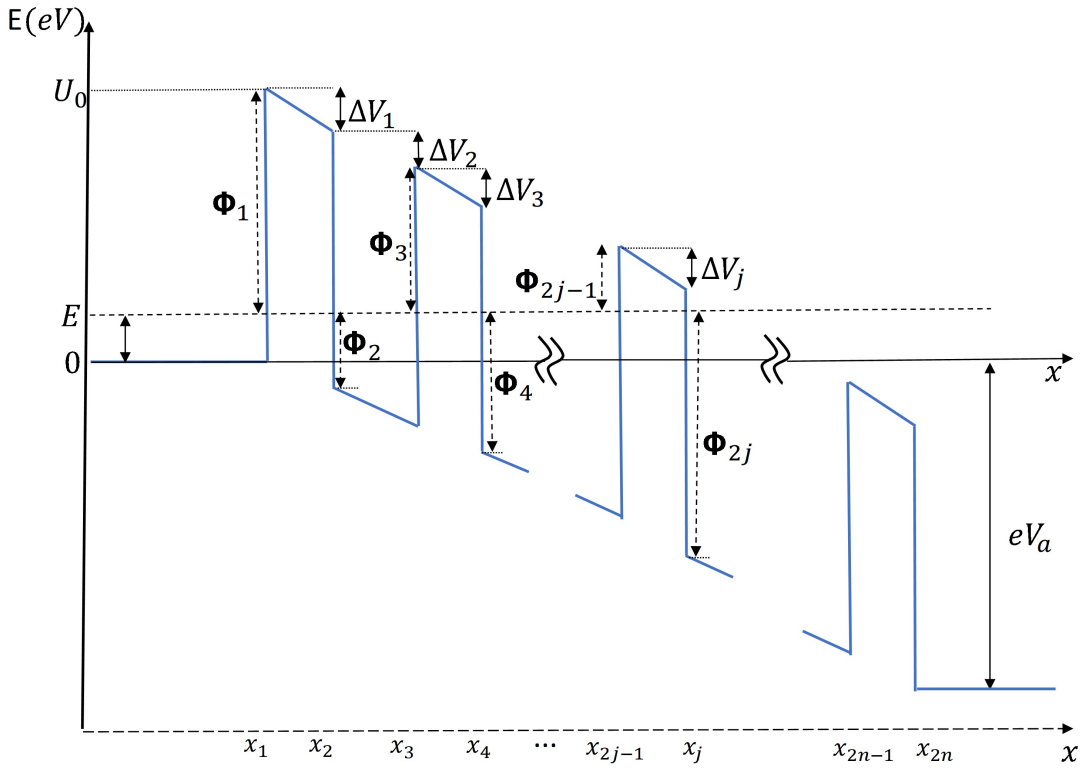

Figure 2.4: Schematic illustration of the electrical potential energy profile $U(x)$ of an artificial superlattice composed of n-barriers and n-1 quantum wells, under an applied bias V_a.

Throughout the calculations, κ_b and κ_w represent the dielectric constants for the barriers and quantum well regions, respectively. Applying the boundary condition at the interfaces, i.e., the continuity of electric field displacement vector, $\mathbf{D} = \epsilon \mathbf{F}$, yields:

$$\epsilon_{b_1} F_{b1} = \epsilon_{w1} F_{w1} = \epsilon_{b_2} F_{b2} = \epsilon_{w2} F_{w2} = ... = \epsilon_{wn-1} F_{wn-1} = \epsilon_{bn} F_{bn}, \tag{2.29}$$

where $\epsilon_{bi} = \kappa_{bi}\epsilon_0$ and $\epsilon_{wi} = \kappa_{wi}\epsilon_0$ are the permittivities in the barrier and in the well, respec-

tively. Where ϵ_0 is the vacuum permittivity. F_{bi} and F_{wi} are the electric field in the barrier and in the well [60]. Defying the barriers width as $L_{bj} = x_{2j} - x_{2j-1}$ and wells width as $L_{Wj} = x_{2j+1} - x_{2j}$. From Eq. (2.29), assuming a constant electric field, one can write

$$\epsilon_{b1}\frac{\Delta V_1}{e(x_2 - x_1)} = \epsilon_{w1}\frac{\Delta V_2}{e(x_3 - x_2)} = ... = \epsilon_{wn-1}\frac{\Delta V_{n-1}}{e(x_{2n-1} - x_{2n-2})} = \epsilon_{bn}\frac{\Delta V_n}{e(x_{2n} - x_{2n-1})}. \tag{2.30}$$

Using Eq. (2.30) we can write ΔV_j for $j \neq 1$ as a function of ΔV_1, hence, combining with Eq. (2.28), yields

$$V_a = \Delta V_1 \left\{ \begin{array}{c} 1 + \left[(x_4 - x_3)\frac{\epsilon_{b1}}{\epsilon_{b2}} + ... + (x_{2n} - x_{2n-1})\frac{\epsilon_{b1}}{\epsilon_{bn}}\right]\frac{1}{(x_2 - x_1)} + \\ \left[(x_3 - x_2)\frac{\epsilon_{b1}}{\epsilon_{w1}} + .. + (x_{2n-1} - x_{2n-2})\frac{\epsilon_{b1}}{\epsilon_{w2}}\right]\frac{1}{(x_2 - x_1)} \end{array} \right\},$$

isolating the term $(x_2 - x_1)$ and noticing that $F_{b1} = \Delta V_1/(x_2 - x_1)$, we have

$$F_{b1} = V_a \left[(x_2 - x_1) + \epsilon_{b_1}\sum_{j=2}^{n}\frac{1}{\epsilon_{bj}}(x_{2j} - x_{2j-1}) + \epsilon_{b_1}\sum_{j=1}^{n-1}\frac{1}{\epsilon_{wj}}(x_{2j+1} - x_{2j})\right]^{-1}. \tag{2.31}$$

For the particular case in which all quantum wells are made of the same semiconductor, $\epsilon_{wj} = \epsilon_w$. Similarly, if the barriers are composed of the same material, then yields $\epsilon_{bj} = \epsilon_b$. In this case, defining $F_b = F_{b1}$ and $F_{w1} = F_w$ and writing all the terms ΔV_j as a function of the electric field in the first barrier and the electric field in the first well, yields:

$$F_b = V_a \left[\sum_{j=1}^{n} L_{bj} + \left(\frac{\kappa_b}{\kappa_w}\right)\sum_{j=1}^{n-1} L_{Wj}\right]^{-1}. \tag{2.32}$$

Using Eq. (2.29) one gets $F_w = \epsilon_b F_b/\epsilon_w$. Hence, we can write the electrical potential energy drop ΔV_j as $\Delta V_j = ed_jF_j$, where $d_j = x_{j+1} - x_j$ and F_j is given by

$$F_j = \left\{ \begin{array}{l} F_w,\ j - even \\ F_b,\ j - odd \end{array} \right. .$$

Thus, to $j = 1, 2, ..., 2n - 1$, the potential energy within the region $x_j < x < x_{j+1}$ can be written as

$$U(x) = E + \Phi_j - eF_j(x - x_j) \tag{2.33}$$

where

$$\Phi_{2j} = -\sum_{j=1}^{2j-1} \Delta V_j - E, \tag{2.34}$$

$$\Phi_{2j-1} = U_0 - \sum_{j=1}^{2j-2} \Delta V_j - E, \tag{2.35}$$

After determining the electrical potential drop at each barrier and quantum well, one can compute the tunneling coefficient under an applied external voltage. Seeking an analytical approximation for the transmission coefficient in the particular case of double potential barrier, in the next section, the classical WKB method is presented.

2.4 The WKB Method

The WKB (Wentzel-Kramers-Brillouin) method, or simply WKB approximation, is a useful method for finding approximate solutions to linear differential equations with spatially varying coefficients [56]. For the case of interest here, consider an electron in a crystal structure, such as the semiconductor, subjected to an arbitrary potential energy profile $U(x)$ with slow spatial variation (in relation to de Broglie wavelength). The one-dimensional Schrödinger equation in the effective mass approximation is

$$\frac{d^2C(x)}{dx^2} = -\frac{2m^*}{\hbar^2}\left[E - U(x)\right]C(x) \tag{2.36}$$

where $C(x)$ is the envelope function in the crystalline medium [55]. The complete electron wave function is of the form $\Psi(x) \approx C(x)u_k(x)$, where $u_k(x)$ represents the Bloch function [55]. Using the WKB method, the solution of Eq. (2.36) is [55]:

$$C(x) \approx \frac{K_0}{\sqrt[4]{Q(x)}} e^{\pm \int_a^x \sqrt{Q(u)}du}, \tag{2.37}$$

where

$$Q(x) = -\frac{2m^*}{\hbar^2}\left[E - V(x)\right], \tag{2.38}$$

when $E > U(x)$, one can write $\sqrt{Q(x)} = ik(x)$, and, the wave vector can be written as $k(x) = \hbar^{-1}\sqrt{2m^*\left[E - U(x)\right]}$. Hence, the envelope function can be written as

$$C(x) \approx \frac{K_1}{\sqrt{k(x)}} e^{\pm i\int_a^x k(u)du}, \tag{2.39}$$

where K_1 is an arbitrary constant. One can interpret Eq. (2.39) as a plane wave in which the wavelength varies slowly in x-direction and also the amplitude decreases with increasing wave vector.

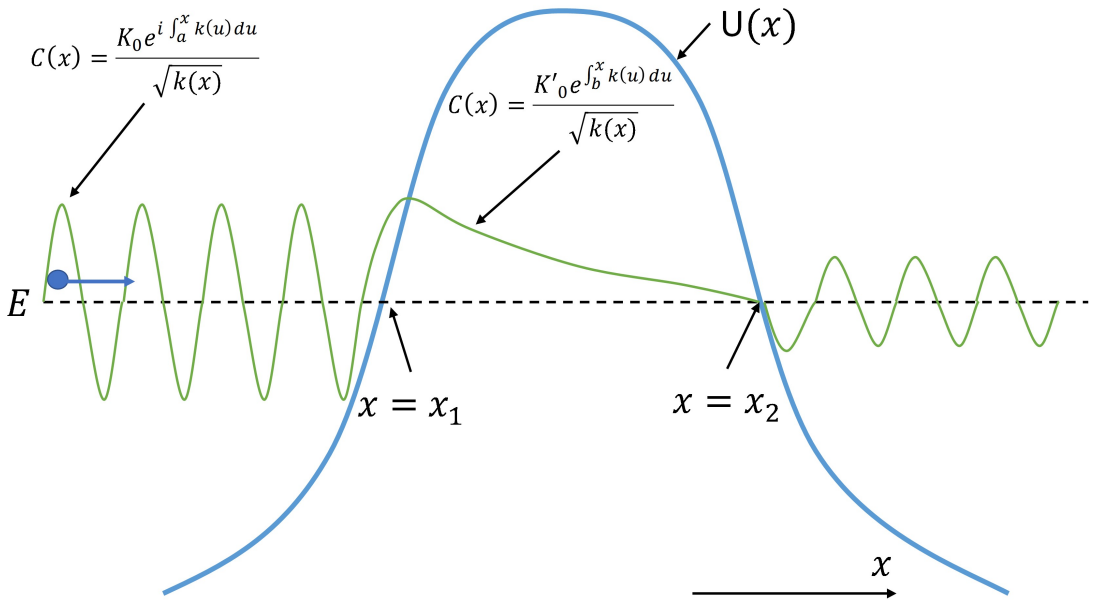

Figure 2.5: Schematic illustration of a particle tunneling through an arbitrary potential barrier.

Considering an electron incident at an electrical potential barrier with kinetic energy $E < U(x)$, as illustrated in Fig. (2.5). In this situation, we have $Q(x) = k^2(x) = -2m^*\left[E - U(x)\right]/\hbar^2 > 0$. Thus, the solution of Eq. (2.36) using the WKB method is given by

$$C(x) \approx \frac{K_0}{\sqrt{k(x)}} e^{\pm\int_a^x k(u)du}, \tag{2.40}$$

we neglect the term $(+)$ in the exponent of Eq. (2.40), since in this case, $C(x)$ would tend to infinite. Again, K_0 is a normalization constant of the wave function. Fig. (2.5) illustrates the classic turning points, $x = x_1$ and $x = x_2$, where the difference $E - U(x)$ tends to zero. In this

case, one can write the ratio between the envelope functions, at the turning points, by using Eq. (2.40):

$$\frac{C(x_2)}{C(x_1)} \approx \frac{e^{-\int_a^{x_2} k(u)du}}{e^{-\int_a^{x_1} k(u)du}} = e^{i\phi} e^{-\int_{x_1}^{x_2} k(u)du}, \tag{2.41}$$

where ϕ is the phase angle between the classic turning points [56]. Finally, we can calculate the tunneling coefficient using the WKB method, $\mathbf{T}_{WKB}(E)$, for the situation illustrated in Fig. (2.5), as [56]:

$$\mathbf{T}_{WKB}(E) \approx \left|\frac{C(x_2)}{C(x_1)}\right|^2 = \left|\exp\left(-\frac{2}{\hbar}\int_{x_1}^{x_2} \sqrt{2m^*\left[U(x)-E\right]}dx\right)\right|. \tag{2.42}$$

2.4.1 Calculation of $\mathbf{T}_{WKB}$ for a Rectangular Barrier With and Without Applied Bias

In this section, we apply the WKB method to calculate the transmission probability coefficient $\mathbf{T}_{WKB}(E)$ for a rectangular potential barrier with and without applied bias, as illustrated in Fig. (2.6). Fig (2.6-a) shows a schematic illustration of a barrier with height U_0 and width $2a$. Fig. (2.6-b) shows the barrier in the absence of applied bias, while Fig. (2.6-a) illustrates the barrier with applied bias U_1. Again, we assume a linear electrical potential energy $U(x)$ distribution in region defined by $x \in [-a, a]$. It is worth noting that the barrier shape illustrated in Fig. (2.6-b) is often used in the analytical modeling of the RTD output characteristics [18], [53].

In the absence of applied bias, by using Eq. (2.42) one gets

$$\mathbf{T}_{WKB}(E) = \left|\exp\left(-\frac{4a}{\hbar}\sqrt{2m_b^*\left(U_0-E\right)}\right)\right|. \tag{2.43}$$

As an example of transmitting an electron through a potential barrier, consider $U_0 = 1.0$ eV and width 20 Å, the electron effective mass in the barrier as $m_b^* = 0.15m_0$ and outside of the barrier region as $m_1^* = m_2^* = 0.065m_0$. Fig. (2.7) shows the transmission coefficient as a function of the kinetic energy by using Eq. (2.43) and also the exact solution obtained by Eq. (2.12). As it can be seen from Fig. (2.7), the first-order WKB approximation provides a good agreement for incident kinetic energy lower than the height of the barrier, that is, when $E < 1.0$ eV. For the cases where the electron kinetic energy is greater than the barrier height

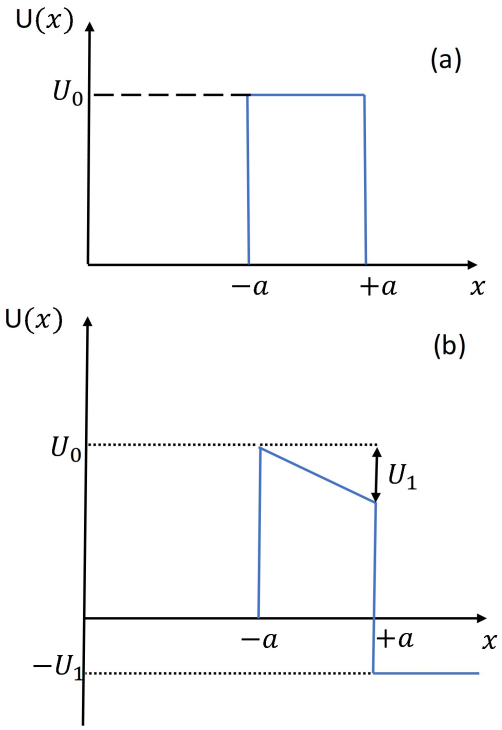

Figure 2.6: Part (a): Schematic illustration of a rectangular barrier U_0. Part (b): A schematic illustration of a barrier under applied voltage.

we have $\mathbf{T}_{WKB}(E) = 1$ resembling the classical behavior shown in Fig. (2.2), distinct from the oscillatory behavior given by Eq. (2.12) (red curve in Fig. (2.7)).

In the case of an external bias applied to the barrier, as depicted in Fig. (2.6-b), the electrical potential in the range $-a \leq x \leq a$ can be written as

$$U(x) = U_0 - \frac{U_1}{2}\left(1 + \frac{x}{a}\right), \quad -a \leq x \leq a \tag{2.44}$$

Applying the WKB method through Eq. (2.42) yields

$$\mathbf{T}_{WKB}(E) \approx \left| \exp\left(-\frac{2}{\hbar}\sqrt{2m_b^*} \int_{-a}^{a} \sqrt{-\frac{xU_1}{2a} + \left(U_0 - E - \frac{U_1}{2}\right)} dx \right) \right|,$$

making a change of variable, one can get

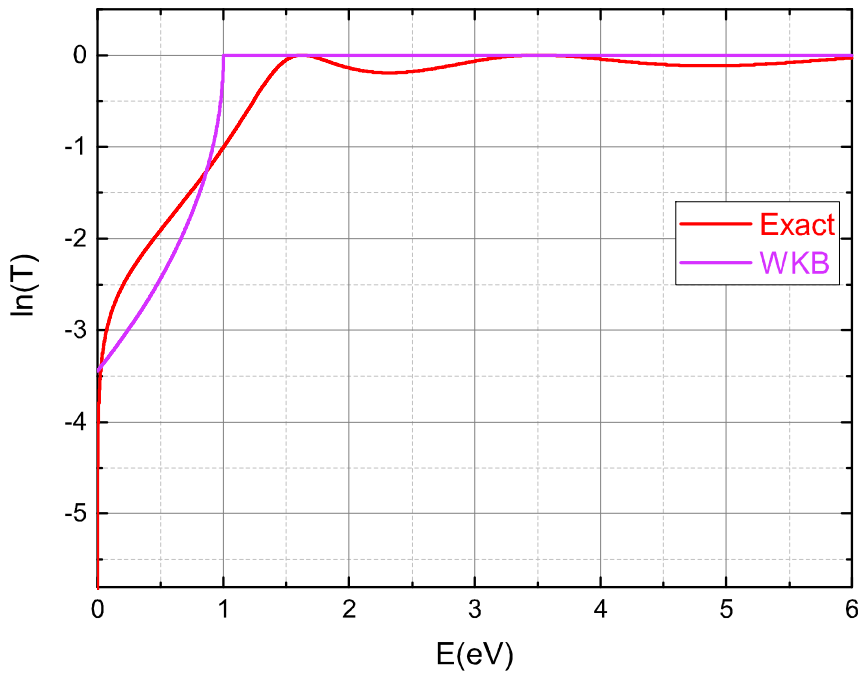

Figure 2.7: Exact and approximate transmission coefficient provided by the WKB method, for a rectangular potential barrier with $U_0 = 1.0$ eV and width 20 Å.

$$\begin{aligned} u &= -\frac{xU_1}{2a} + \left(U_0 - E - \frac{U_1}{2}\right), \\ dx &= \frac{-2a}{V_1} du, \end{aligned}$$

In this way, we have

$$\mathbf{T}_{WKB}(E) \approx \left| \exp\left(-\frac{1}{\hbar} \frac{-4a}{V_1} \sqrt{2m_b^*} \left[\frac{u^{3/2}}{3/2} \right]_{V_0-E}^{V_0-E-V_1} \right) \right|,$$

finally:

$$\mathbf{T}_{WKB}(E) \approx \left| \exp\left(-\frac{8a\sqrt{2m_b^*}}{3\hbar U_1} \left[(U_0 - E)^{3/2} - (U_0 - E - U_1)^{3/2} \right] \right) \right|. \tag{2.45}$$

Once more, as an example, consider a potential barrier with the following parameters: $U_0 = 1.0$ eV, barrier width 20 Å, $m_b^* = 0.15m_0$ and $m_1^* = m_2^* = 0.065m_0$. Fig. (2.8) shows the transmission coefficient as a function of the electron kinetic energy through Eq. (2.45) and the

exact solution given by Eq. (2.27) for an applied bias equivalent to $U_1 = 0.3\,\mathrm{eV}$. As it can be seen from Fig. (2.7) the first order WKB approximation shows a fair agreement for $E < 1.0$ eV.

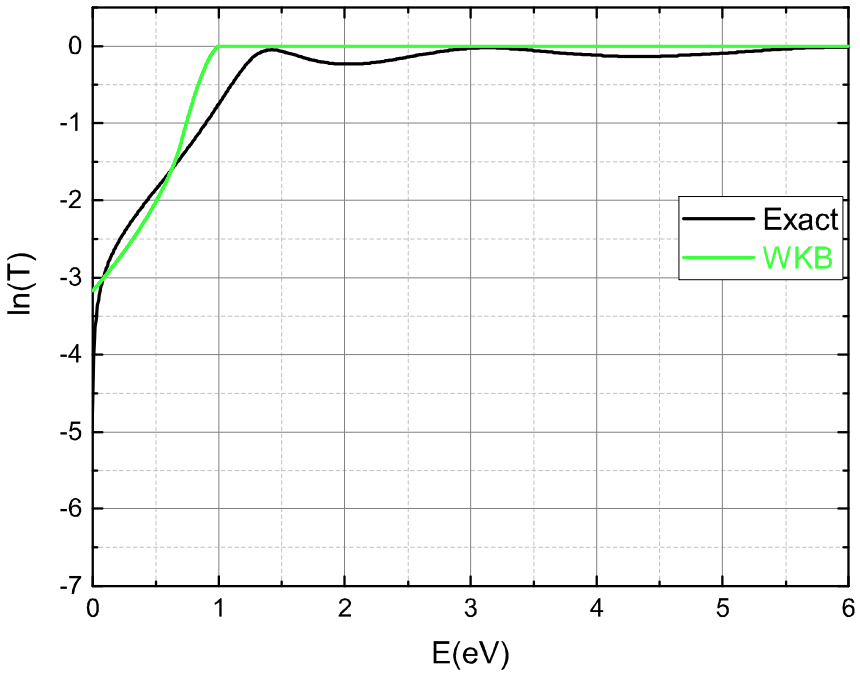

Figure 2.8: Exact and WKB approximate transmission coefficient for a rectangular potential barrier with $U_0 = 1.0$ eV and width 20 Å, under an applied external potential of $U_1 = -0.3\,\mathrm{eV}$.

We should point out that under an applied bias the barrier becomes asymmetrical. Indeed, by increasing the applied bias, the barrier assumes a more triangular shape than a trapezoidal one. Eventually, above a specific voltage, the barrier profile becomes completely triangular (in respect to an arbitrary incident energy E) [53]. Thus, for an electron with incident kinetic energy less than the barrier height, the WKB approximation provides a reasonable agreement with the exact solution. As we will demonstrate in the following chapters, the barrier profile sketched in Fig. (2.6-b) provides a satisfactory approximation for modeling the single barriers in RTD, under applied bias. In fact, the electrical output characteristics of RTD are more sensitive to the global tunneling, i.e., the transmission coefficient computed considering the double barrier structure rather than the individual transmission coefficient of each barrier.

In the next section, we investigate the electron tunneling through a double barrier quantum

well, characterized as resonant tunneling.

2.5 Double Barrier Quantum Well

In particular, the tunneling structure of interest in this work is the double barrier quantum well (DBQW), the basic building blocks in RTDs. Fig. (2.9) shows a schematic illustration of the DBQW. Semiconductor DBQWs can be fabricated through a layer sequence composed of different semiconductor materials, such as GaAs/$Ga_{1-x}Al_xAs$, InP/InAs, among others [51].

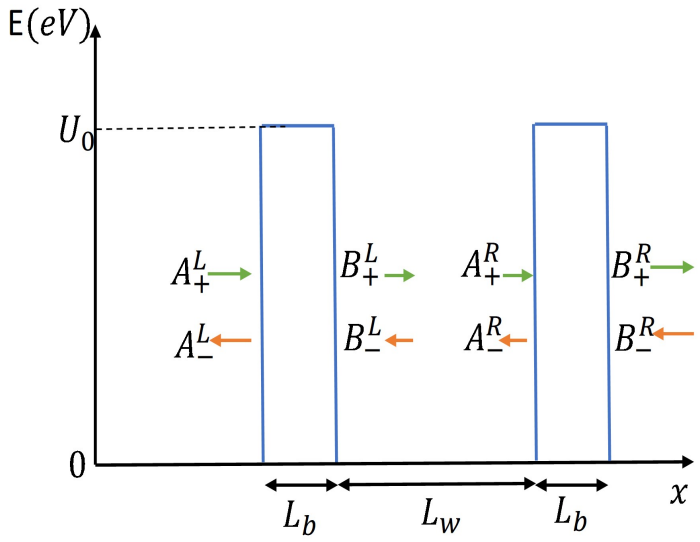

Figure 2.9: Schematic illustration of a double barrier quantum well. The terms B_+^L, B_-^L, A_+^R and A_-^R represent the incident and reflected waves propagating through the structure.

To calculate the tunneling coefficient for a DBQW, initially, we employ the transfer matrix formalism. The plane waves inside the well, B_+^L, B_-^L, A_+^R and A_-^R are under the same electrical potential, although defined in different regions. Thus, it can be considered that these waves experienced only phase shifting inside the quantum well. Hence, one can write

$$\begin{aligned} A_+^R &= e^{ikL_w} B_+^L, \\ A_-^R &= e^{-ikL_w} B_-^L, \end{aligned}$$

writing in matrix form

$$\begin{bmatrix} B_+^L \\ B_-^L \end{bmatrix} = \begin{bmatrix} e^{-ikL_w} & 0 \\ 0 & e^{ikL_w} \end{bmatrix} \begin{bmatrix} A_+^R \\ A_-^R \end{bmatrix} = \mathbf{P}_w \begin{bmatrix} A_+^R \\ A_-^R \end{bmatrix}, \tag{2.46}$$

so, we define $\mathbf{P}_w$ as the propagation matrix of the wave functions in the well. For the whole structure we can write

$$\begin{bmatrix} A_+^L \\ A_-^L \end{bmatrix} = \begin{bmatrix} M_{L11} & M_{L12} \\ M_{L21} & M_{L22} \end{bmatrix} \begin{bmatrix} e^{-ikL_w} & 0 \\ 0 & e^{ikL_w} \end{bmatrix} \begin{bmatrix} M_{R11} & M_{R12} \\ M_{R21} & M_{R22} \end{bmatrix} \begin{bmatrix} B_+^R \\ B_-^R \end{bmatrix},$$

$$\begin{bmatrix} A_+^L \\ A_-^L \end{bmatrix} = \mathbf{M}_L \mathbf{P}_w \mathbf{M}_R \begin{bmatrix} B_+^R \\ B_-^R \end{bmatrix},$$

writing $\mathbf{M}_T = \mathbf{M}_L \mathbf{P}_w \mathbf{M}_R$ and carrying out the calculations yields

$$\mathbf{M}_T = \begin{bmatrix} e^{-ikL_w} M_{L11} M_{R11} + e^{ikL_w} M_{L12} M_{R21} & e^{-ikL_w} M_{L11} M_{R12} + e^{ikL_w} M_{L12} M_{R22} \\ e^{-ikL_w} M_{L21} M_{R11} + e^{ikL_w} M_{L22} M_{R21} & e^{-ikL_w} M_{L21} M_{R12} + e^{ikL_w} M_{L22} M_{R22} \end{bmatrix}. \tag{2.47}$$

Thus, considering no wave incidence from right to left, leads to $B_-^L = 0$. Hence, we have $A_+^L = M_{T11} B_+^R$, where

$$M_{T11} = \left| \left(e^{-i(kL_w + 2\varphi)} m_{11}^2 + e^{i(kL_w)} M_{21}^2 \right)^2 \right|.$$

Since the barriers are identical, we can write M_{L11} and M_{R11} in a phasor form as

$$M_{L11} = M_{R11} = M_{11} = |m_{11}| \, e^{-i\varphi}$$

where the coefficients M_{11}, M_{12}, M_{21} and M_{22} are given by Eq. (2.8) setting $L_b = 2a$. Finally, we have

$$m_{11} = \sqrt{1 + \frac{\left(\beta_m^2 k^2 + K^2\right)^2}{4\beta_m^2 k^2 K^2} \sinh^2(KL_b)},$$

$$\varphi = \arctan\left[\left(\frac{K^2 - \beta_m^2 k^2}{2\beta_m k K} \right) \tanh(KL_b) \right],$$

where $\beta_m = m_b^*/m_w^*$, $k = \sqrt{2m_w^* E}/\hbar$ and $K = \sqrt{2m_b^*(U_0 - E)}/\hbar$. The term L_w refers to the quantum well width. The terms m_b^* and m_w^* account for the electron effective masses in the barrier and well regions, respectively.

The transmission coefficient is given by $\mathbf{T}_{DBQW}(E) = |M_{T11}|^{-2}$. After some algebraic manipulations, we get

$$|M_{T11}|^2 = \left(|m_{11}|^2 + |M_{21}|^2\right)^2 + 4\,|M_{11}|^2\,|M_{21}|^2 \cos^2\left[2\left(kL_w + \varphi\right)\right],$$

where the term $\left(|m_{11}|^2 + |M_{21}|^2\right)^2$ is equal to one, since it is the transfer matrix determinant, where the plane wave functions are normalized. Carrying out the calculations one obtain

$$\mathbf{T}_{DBQW}(E) = \frac{1}{|M_{T11}|^2} = \frac{1}{1 + 4\,|M_{11}|^2\,|M_{21}|^2 \cos^2\left[2\left(kL_w + \varphi\right)\right]}. \tag{2.48}$$

For a rectangular barrier the transmission and reflection coefficient are given by $\mathbf{T}_1 = |M_{11}|^{-2}$ and $\mathbf{R}_1 = |M_{21}|^2 / |M_{11}|^2$, respectively. Hence, Eq. (2.48) can be simplified to

$$\mathbf{T}_{DBQW}(E) = \frac{\mathbf{T}_1^2}{\mathbf{T}_1^2 + 4\mathbf{R}_1^2 \cos^2\left(kL_w - \theta\right)}. \tag{2.49}$$

As it can be seen in Eq. (2.49), the tunneling coefficient $\mathbf{T}_{DBQW}(E)$ depends on the barriers width, L_b, the well width, L_w, the electron effective masses and barrier height, U_0. Fig. (2.10) shows the tunneling coefficient for a DBQW with the following parameters: $L_b = 30\,\text{Å}$, $L_w = 50\,\text{Å}$, $m_b^* = 0.15m_0$, $m_w^* = 0.067m_0$ and $U_0 = 1.0\ \text{eV}$. In Fig. (2.10), it is possible to observe several peaks in the curve for $\ln(\mathbf{T}_{DBQW}(E))$. These peaks occurs for electron kinetic energy values less than the barriers height, i.e., in cases where $E < 1.0\ \text{eV}$. As it can be seen in Fig. (2.10), for energy greater than U_0, the tunneling coefficient tends to zero with an oscillatory behavior, which is equivalent to $\mathbf{T}_{DBQW}(E) \to 1$. The energy peaks shown in Fig. (2.10), marked by the blue and green dashed lines, can be interpreted as resonance energies, where $\mathbf{T}_{DBQW}(E)$ has maximum values, for this particular case $E_1 = 0.11\,\text{eV}$ and $E_2 = 0.45\,\text{eV}$. At the resonance peak, the coherent superposition of the reflected waves cancels out in both amplitude and phase, making the transmission coefficient equal to one [2]. It is interesting to note that the resonance energies are precisely the quantum well eigenenergies [53]. In the next section, we derive the Breit-Wigner approximation to compute the $\mathbf{T}(E)$. This approximation

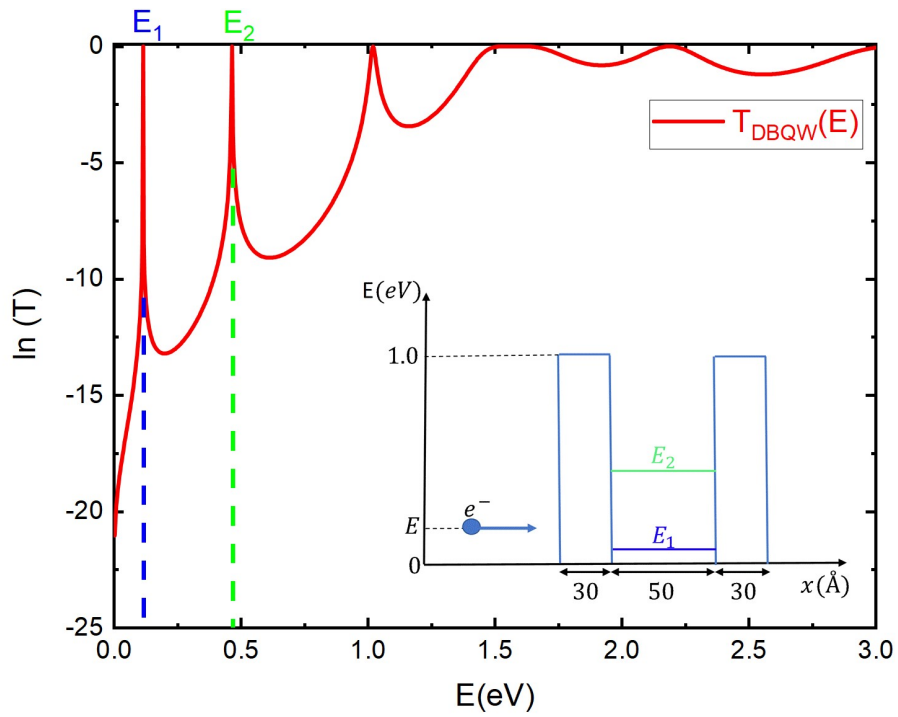

Figure 2.10: Tunneling coefficient as a function of the electron energy for a DBQW with $L_b = 30\,\text{Å}$, $L_w = 50\,\text{Å}$, $m_b^* = 0.15m_0$, $m_w^* = 0.067m_0$ and $V_0 = 1.0$ eV.

is used in our work as an ingredient element to develop an analytical current density expression for RTD structures.

2.5.1 Breit-Wigner Approximation

The Breit-Wigner approximation was proposed in a seminal article entitled *Capture of Slow Neutrons* published, in 1936, by physicists G. Breit and E. Wigner [62]. In this paper, Breit and Wigner investigated the phenomenon of neutron absorption by atomic nuclei after a neutron-nucleus collision. [62]. In this regard, the authors proposed the existence of quasi-stationary states, i.e., resonant energy levels. Then, they derived an approximate expression for the decay time of these states [62]. This formalism can also be applied to the specific case of DBQW structure [3], [18], [53].

In Eq. (2.49), if we consider the infinite well approximation, it is possible to demonstrate that $\theta = -\pi/2$ [3], [53]. Thereby,

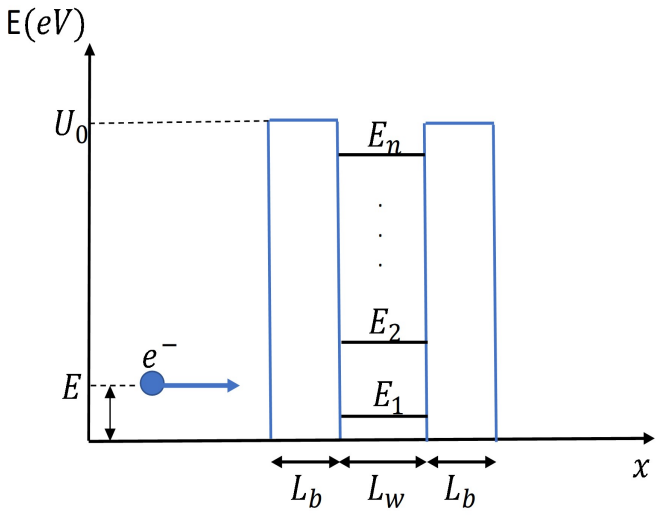

Figure 2.11: Schematic illustration of the resonant levels, E_n, in the quantum well.

$$\cos^2\left(kL_w + \frac{\pi}{2}\right) = \sin^2\left(kL_w\right).$$

At resonance, it is necessary that $E \rightarrow E_n$, and consequently, $\mathbf{T}_{DBQW}(E) \rightarrow 1$. Then, $\sin^2\left(kL_w\right) \rightarrow 0$, where n is the index for the eigenenergies, as illustrated in Fig. (2.11). Therefore, we can write

$$\sin^2\left(kL_w\right) \approx \left[\left(k - k_n\right)L_w\right]^2, \tag{2.50}$$

where k is given by

$$k - k_n = \frac{\sqrt{2m_w^* E_n}}{\hbar}\left(\sqrt{\frac{E}{E_n}} - 1\right). \tag{2.51}$$

We can write the electron energy around the resonant energy levels as $E = E_n + \epsilon$, hence, we have

$$\sqrt{\frac{E}{E_n}} = \sqrt{\frac{E_n + \epsilon}{E_n}} = \sqrt{1 + \frac{\epsilon}{E_n}} = \sqrt{1 + \delta}, \tag{2.52}$$

where $\delta = \epsilon / E_n$. One can rewrite Eq. (2.51) as

$$k - k_n = \frac{\sqrt{2m_w^* E_n}}{\hbar}\left(\sqrt{1 + \delta} - 1\right),$$

assuming small δ, we can approximate $\sqrt{1+\delta} \approx 1 + \delta/2$, thus

$$k - k_n \approx \frac{\sqrt{2m_w^*}}{\hbar}\frac{\sqrt{E_n}}{2}\left(\frac{E-E_n}{E_n}\right),$$

hence

$$\begin{aligned}
\left[(k-k_n)\,L_w\right]^2 &\approx \left\{\left[\frac{\sqrt{2m_w^*}}{\hbar}\frac{\sqrt{E_n}}{2}\left(\frac{E-E_n}{E_n}\right)\right]L_w\right\}^2, \\
\left[(k-k_n)\,L_w\right]^2 &\approx \left[\frac{m_w^* L_w^2}{2\hbar^2}\frac{(E-E_n)^2}{E_n}\right].
\end{aligned} \tag{2.53}$$

Therefore, combining Eq. (2.53) with Eq. (2.49), the Breit-Wigner approximation for the tunneling coefficient is given by

$$\mathbf{T}_{DBQW}(E) \approx \frac{\frac{2\mathbf{T}_1^2\hbar^2 E_n}{4\mathbf{R}_1^2 m_w^* L_w^2}}{\frac{2\mathbf{T}_1^2\hbar^2 E_n}{4\mathbf{R}_1^2 m_w^* L_w^2} + (E-E_n)^2} \tag{2.54}$$

Writing Eq. (2.54) in the usual Lorentzian form, one can define the resonance linewidth as

$$\Gamma = \sqrt{\frac{2\mathbf{T}_1^2\hbar^2 E_n}{\mathbf{R}_1^2 m_w^* L_w^2}}$$

hence, rewriting Eq. (2.54):

$$\mathbf{T}_{DBQW}(E) \approx \frac{(\Gamma/2)^2}{(\Gamma/2)^2 + (E-E_n)^2} \tag{2.55}$$

In case of unequal barriers, using the same formalism described in this section, it is possible to derive a Lorentzian approximation similar to Eq. (2.55) [3]. To do so, we start by defining $\mathbf{T}_L = \mathbf{T}_L(E_n)$ and $\mathbf{T}_R = \mathbf{T}_R(E_n)$ as the tunneling coefficients of the left and right barriers in respect to the well, respectively. Following the same procedure, the tunneling coefficient for asymmetric barriers, in the Breit-Wigner approximation, is

$$\mathbf{T}_{DBQW}(E) = \frac{\Gamma_L\Gamma_R}{\Gamma_e^2}\frac{(\Gamma_e/2)^2}{(\Gamma_e/2)^2 + (E-E_n)^2}, \tag{2.56}$$

where Γ_L and Γ_R are the left and right barrier resonance linewidths, respectively:

$$\Gamma_L = \sqrt{\frac{2\mathbf{T}_L^2\hbar^2 E_n}{(1-\mathbf{T}_L)^2 m_w^* L_w^2}},$$
$$\Gamma_R = \sqrt{\frac{2\mathbf{T}_R^2\hbar^2 E_n}{(1-\mathbf{T}_R)^2 m_w^* L_w^2}},$$

the equivalent resonance linewidth is given by $\Gamma_e = (\Gamma_L + \Gamma_R)/2$. Note that if $\Gamma_L = \Gamma_R$ Eq. (2.56) becomes Eq. (2.55).

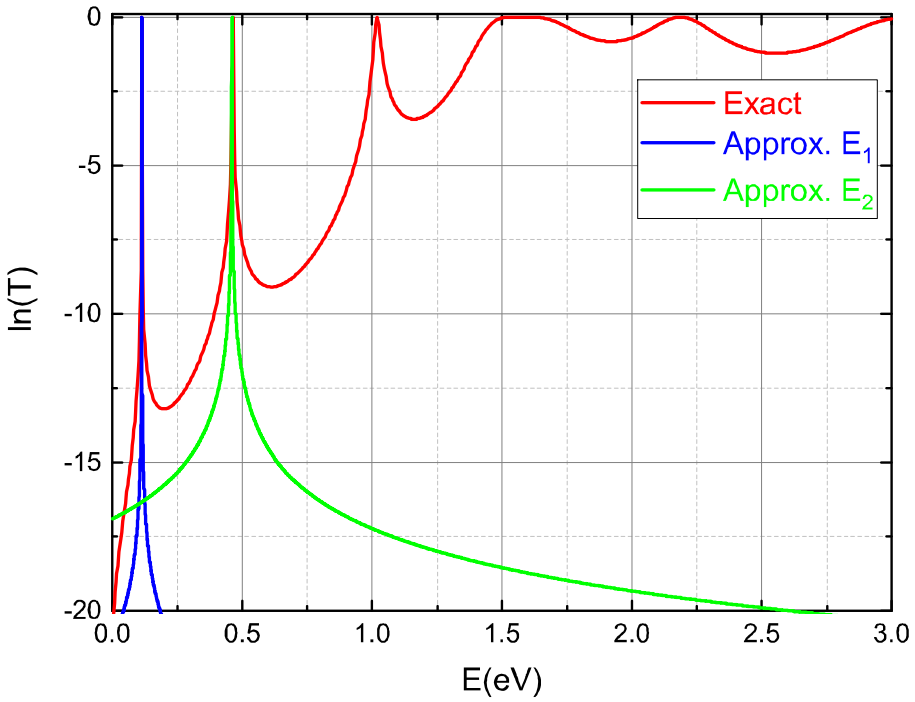

Figure 2.12: Tunneling coefficient for a DBQW. The energy levels were exactly calculated using Eq. (2.49) and using the Breit-Wigner approximation for the resonance energies, $E_1 = 0.11\,\mathrm{eV}$ and $E_2 = 0.45\,\mathrm{eV}$.

Fig. (2.12) shows the tunneling coefficient as a function of kinetic energy for the case illustrated in Fig. (2.10), calculated exactly using Eq. (2.49) and using the Breit-Wigner approximation, Eq. (2.55). From Fig. (2.12), it is possible to identify the resonance energies $E_1 = 0.11\,\mathrm{eV}$ and $E_2 = 0.45\,\mathrm{eV}$. As it can be seen in Fig. (2.12), for $E < U_0$, effectively, the tunneling occurs around the resonance levels. Therefore, the Breit-Wigner approximation shows a good agreement when the electrons kinetic energy, E, is within the resonance linewidth Γ. On the other hand, for kinetic energy outside the resonance width, it can be seen from Fig.

(2.12) that the tunneling coefficient does not provide a good agreement with the exact solution. However, in these regions, the magnitude of $\mathbf{T}_{DBQW}(E)$ is negligible and, therefore, the Breit-Wigner approximation presents a good agreement for the regions of interest [3], [53]. Although the Breit-Wigner approximation offers a satisfactory agreement within the resonance linewidth, in order to use this approximation is necessary to compute the values of the quantum well eigenenergies. However, for a finite rectangular quantum well, the energy levels are obtained through the solution of transcendental equations, which, by definition, has no analytical solutions [1], [54]. To address this problem, in the next chapter, we propose accurate approximate analytical solutions to determine the energy levels in the finite rectangular potential wells.

Chapter 3

Analytical Expressions for Eingenenergy Levels in Finite Rectangular Quantum Wells

This chapter presents original accurate analytical expressions to compute the eigenenergies for finite rectangular quantum wells. Specifically, we propose a novel approximation method to calculate the roots of trigonometric transcendental equations by means of a Taylor series dynamic expansion approach. The expressions are validated against numerical solutions of the energy levels transcendental equations. As a result, an agreement greater than 99% is achieved for the solution space investigated. In addition, we derived useful analytical expressions for nanoelectronics and optoelectronics design purposes. As we will demonstrate in the following chapters, the proposed expressions are helpful in formulating a fully analytical model for the RTD.

3.1 Introduction

As discussed in the previous Chapter, computing the resonant tunneling transmission coefficient by means of the Breit-Wigner approximation requires the value of the finite quantum well eigenergies. In this regards, the classic example found in quantum mechanics textbooks is the infinite rectangular potential well, which has an explicit analytical expression for calculating

the eigenenergies [54]. However, in realistic quantum devices, the infinite well approximation does not provide a good agreement with the experimental results, being necessary to consider the quantum well with finite barrier height [1]. However, for finite quantum wells, the solution of the Schrödinger equation can only be obtained through transcendental equations [1], which do not have an explicit analytical solution. Usually, its solution is determined by numerical techniques, such as Newton-Raphson method [1], [53].

Moreover, in the compact modeling scope, numerical solutions [63]- [64] are not always suitable due to the prohibitive computational effort demanded, especially, when it is necessary to simulate hundreds of thousands of these devices simultaneously, which often occurs in integrated circuits design. Other alternatives, based on infinite series expansion [65]- [67], Green functions [68] and Cauchy-Riemann method [69] are rather complex. Additionally, most of the literature does not consider different effective masses and/or asymmetric wells, which is fundamental to accurate describe semiconductor quantum well devices [70], [71].

Following the discussion in the previous paragraphs, we develop an analytical method providing compact expressions for the computation of finite quantum well eigenenergies. As compact expressions of this nature are not widely found in the literature, we carry out a detailed calculations to find these eigenenergies, aiming to achieve an accuracy level suitable for compact modeling applications.

3.2 Symmetric Finite Square Quantum Well

3.2.1 Theoretical Background

In semiconductor devices, one-dimensional quantum wells are defined as thin layered structures with different bandgaps, where charge carriers, electrons or holes, are confined due to quantum mechanical effects [72]. As shown in Fig. (3.1), a typical symmetric quantum well (SQW) consists of two potential barriers of the same height (regions I and III) and a thin layer of narrower bandgap — the well — where the carriers are confined in the x-direction. The potential energy profile $U(x)$ is given by

$$U(x) = \begin{cases} 0, & x \leq |L_w/2|\,, \\ U_0, & x > |L_w/2|\ . \end{cases} \tag{3.1}$$

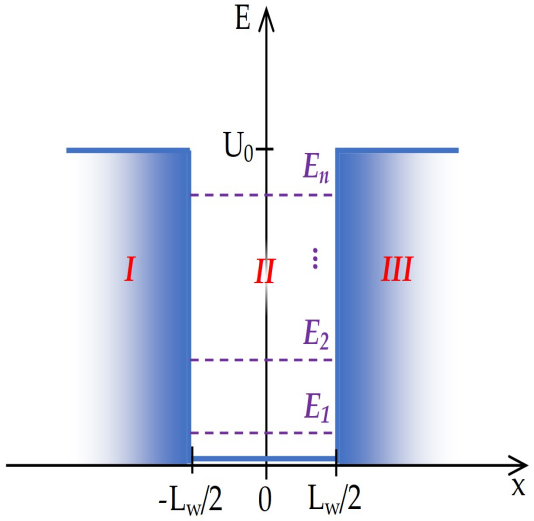

Figure 3.1: Schematic illustration of a typical layered semiconductor structure comprising a rectangular quantum well of width L_w and symmetric potential barriers of height U_0. The terms E_n represent the energy levels.

As usual, Schrödinger one-dimensional equation for this structure is

$$-\frac{\hbar^2}{2m_i^*}\frac{d^2\Psi_i(x)}{dx^2} + U(x)\Psi_i(x) = E\Psi_i(x),\ i = 1, 2, 3 \tag{3.2}$$

where m_i^* is the carrier effective mass in region i, $\hbar$ is the reduced Planck constant, $\Psi_i(x)$ is the wave function in region i and E is the energy of the carrier ($E < U_0$). The solution of Eq. (3.2) in regions I and III is in the form plane waves: $\Psi_1(x) = Ae^{k_1 x}$ and $\Psi_3(x) = Be^{-k_1 x}$, where A and B are normalization constants, and the wave vector k_1 for both regions is

$$k_1 = \sqrt{\frac{2m_b^*(U_0 - E)}{\hbar^2}}, \tag{3.3}$$

where m_b^* is the effective carrier mass at the potential barriers. The solution to the Schrödinger equation in region II is

$$\Psi_2(x) = C\cos(k_2 x) + D\sin(k_2 x) \tag{3.4}$$

where C and D are normalization constants, and the wave vector is $k_2 = \left(\sqrt{2m_w^* E}\right)/\hbar$, where m_w^* is the carrier effective mass at the potential well.

The usual boundary conditions — also know as BenDaniel-Duke boundary conditions — at the interface of two semiconductor materials, i and j, are [71]:

$$\begin{aligned} \Psi_i(x) &= \Psi_j(x) \\ \frac{1}{m_i^*}\frac{\partial}{\partial x}\Psi_i(x) &= \frac{1}{m_j^*}\frac{\partial}{\partial x}\Psi_j(x). \end{aligned} \tag{3.5}$$

Assuming constants A and B different from zero, these boundary conditions yield a transcendental equations known in the literature as odd-parity equation:

$$\frac{m_w^*}{m_b^*}k_1 = k_2 \tan\left(\frac{k_2 L_w}{2}\right), \tag{3.6}$$

similarly, assuming constants C and D different from zero, yields another transcendental equations known in the literature as even-parity equation:

$$-\frac{m_w^*}{m_b^*}k_1 = k_2 \cot\left(\frac{k_2 L_w}{2}\right). \tag{3.7}$$

Defining ξ as the parameter that encompasses the physical parameters of the well:

$$\xi = \frac{L_w}{2\hbar^2}\sqrt{2m_w^* U_0}, \tag{3.8}$$

we can write

$$\eta = \frac{k_2 L_w}{2} = \frac{L_w}{2\hbar^2}\sqrt{2m_w^* E}, \tag{3.9}$$

Hence, Eqs. (3.6) and (3.7) can be written as

$$\tan(\eta) = \alpha_m \sqrt{\frac{\xi^2}{\eta^2} - 1}, \tag{3.10}$$

$$\cot(\eta) = -\alpha_m \sqrt{\frac{\xi^2}{\eta^2} - 1}, \tag{3.11}$$

where $\alpha_m^2 = m_w^*/m_b^*$ is the parameter accounting for the differences in effective masses along the structure.

Under the parabolic band approximation, the eigenenergy levels are calculated using the expression $E_n = k_n^2\hbar^2/(2m_w^*)$ [72], where k_n is the wave vector associated with each state in the well region. Then, we have

$$E_{sy,n} = \frac{2\hbar^2}{m_w^* L_w^2}\eta_n^2, \quad n = 1, 2, 3, ...N_{sy}, \tag{3.12}$$

where n corresponds to the n-th energy level of a set of N_{sy} allowed energy levels in the finite well.

As seen in Eq. (3.12), the energy levels of a symmetric quantum well, $E_{sy,n}$, are obtained as function of η_n. In other words, they depend on finding the roots of Eqs. (3.10) and (3.11). The traditional approaches to compute these energy levels rely on graphical methods [73], [74] or numerical methods [63], [64]. As stated before, neither of them can be considered suitable for compact modelling, which requires simplified analytical expressions. Other approaches available in the literature [65]- [68] are too complex for compact modeling. Many of them do not provide explicit analytical expressions and/or do not take into account the effective mass differences of realistic structures. In an attempt to solve these shortcomings, in this work, we present a novel method to obtain the energy levels, $E_{sy,n}$, with closed-form and high-accurate analytical expressions, which are well suited for compact modelling in the semiconductor industry. To do so, in the next sub-section we focus on solving Eqs. (3.10) and (3.11).

3.2.2 Analytical Approximate Solution for SQW

To obtain a general method for computing any allowed energy levels for a wide range of physical parameter values, U_0, m_w^* and m_b^*, we split the solution into two parts, whether or not the condition $\eta/(\alpha_m\xi) \ll 1$ is met.

Condition $\eta/(\alpha_m\xi) \ll 1$ is satisfied:

Initially, to achieve a more concise formulation, we combine the odd and even parity equations into a single general formulation. To do so, it is enough to recognize that

$$\tan\left(\eta + \pi/2\right) = -\cot\left(\eta\right),$$

in such way that, we can combine Eqs. (3.10) and (3.11) to provide:

$$\tan\left(\eta + \frac{(n+1)\pi}{2}\right) = \alpha_m \sqrt{\frac{\xi^2}{\eta^2} - 1}. \tag{3.13}$$

Also, we know that $\tan(\eta + (n+1)\pi/2) \longrightarrow \infty$ when $\eta \longrightarrow n\pi/2$. Therefore, due to this asymptotic behavior, it is difficulty to elaborate an accurate and low-complexity analytical approximation for $\tan(\eta)$, $\forall \eta \in \mathbb{R}$. Therefore, the approximation proposed in this section is restricted for $\eta/\left(\alpha_m \xi\right) \ll 1$, which is equivalent to say that $\tan(\eta) \longrightarrow +\infty$.

We start by applying the trigonometric identity:

$$\tan^2\left(\eta\right) = \sec^2\left(\eta\right) - 1$$

in Eq. (3.13). Thus,

$$\sec^2\left(\eta + \frac{(n+1)\pi}{2}\right) = \frac{\alpha_m^2 \xi^2}{\eta^2}\left[1 + \left(\frac{\eta}{\alpha_m \xi}\right)^2 \left(1 - \alpha_m^2\right)\right]. \tag{3.14}$$

Once we are considering only the cases in which $\eta/\left(\alpha_m \xi\right) \ll 1$, we can neglect the term $\left(\eta/\left(\alpha_m \xi\right)\right)^2 \left(1 - \alpha_m^2\right)$, yielding

$$\sec^2\left(\eta + (n+1)\pi/2\right) = \frac{\alpha_m^2 \xi^2}{\eta^2}.$$

then,

$$\eta + \frac{(n+1)\pi}{2} = \arccos\left(\frac{\eta}{\alpha_m \xi}\right). \tag{3.15}$$

Next, we expand $\arccos(\phi)$ in a Taylor series, holding the first three terms, to obtain

$$\arccos(\phi) \simeq \pi/2 - \phi - \phi^3/6.$$

This approximation is accurate for $\phi \ll 1$. From Eq. (3.15), we have that $\phi = \eta/\left(\alpha_m \xi\right)$. Thus, the approach is accurate as long as $\eta/\left(\alpha_m \xi\right) \ll 1$. Replacing the approximation in Eq. (3.15) and rearranging the terms, we have

$$\frac{\eta^3}{6\alpha_m^3\xi^3} + \left(1 + \frac{1}{\alpha_m\xi}\right)\eta + \frac{n\pi}{2} = 0. \tag{3.16}$$

Rewriting Eq. (3.16) in the form $c\eta^3 + b\eta + a = 0$ and defining the constants $a = n\pi/2$, $b = [1 + 1/(\alpha_m\xi)]$ and $c = 1/(6\alpha_m^3\xi^3)$, we obtain a third-degree polynomial equation with one real root and two imaginary roots. Solving for the real root, we get

$$\eta_n = \frac{\zeta_0}{6c} - \frac{2b}{\zeta_0}, \tag{3.17}$$

where

$$\zeta_0 = \sqrt[3]{12\sqrt{3(27a^2 + 4b^3)} + 108ac^2}. \tag{3.18}$$

In the next section, we propose our solution for the cases in which the condition $\eta/\left(\alpha_m\xi\right) \ll 1$ is no longer met.

Condition $\eta/\left(\alpha_m\xi\right) \ll 1$ is not satisfied:

When the condition $(\eta/\alpha_m\xi) \ll 1$ is not satisfied, the third order Taylor series expansions of $\arccos(\phi)$ does not lead to an accurate solution. The most obvious approach would be increase the accuracy by making use of higher order terms in the expansion. Nonetheless, this would lead to a greater complexity in finding the roots of the polynomial. As an alternative approach, we proceed by expanding both sides of the Eq. (3.13) around a chosen optimal point. Naturally, the accuracy of the approximate solution depends on whether the expansion point is close enough to the exact solution, which varies accordingly to the different physical parameters. Thus, instead of carrying out the expansion around a fixed point, we set a dynamic expansion point, η_{expan}, which is a function of the these parameters, to assure that the relative error of the approximation is as small as possible. As it will be shown next, η_{expan} is obtained from a mapping

$$\begin{aligned} \mathbf{M}_{sy} : \mathbb{R}^+ &\longrightarrow \mathbb{R}^+ \\ \xi &\longmapsto \eta_{\text{expan}} \end{aligned} \tag{3.19}$$

where the subscript sy refers to the symmetric quantum well case. The mapped value obtained from $\mathbf{M}_{sy}(\xi)$ is the dynamic expansion point, i.e., $\eta_{\text{expan}} = \mathbf{M}_{sy}(\xi)$. This approach allows for

lower degree polynomials in Taylor series expansion, significantly reducing the effort on finding the roots, while assuring great accuracy. In fact, as we will demonstrate later, a simple linear expansion is enough to ensure high accuracy for the whole interval. In this work, we refer to this approach as the Mobile Expansion Point Method (MEPM).

To establish how many terms are necessary in the expansion, a graphical analysis is carried out. Hence, we start by defining functions for both sides of the transcendental equation. For the specific case of the symmetric potential well, from Eq. (3.13), we set the left-hand side (LHS) as $L_{sy}(\eta)$ and the right-hand side (RHS) as $R_{sy}(\eta)$. Thus,

$$L_{sy}(\eta) = \tan\left(\eta + \frac{(n+1)\pi}{2}\right), n = 1, 2, 3, ...N_{sy} \tag{3.20}$$

$$R_{sy}(\eta) = \alpha_m \sqrt{\frac{\xi^2}{\eta^2} - 1}, \tag{3.21}$$

Next, we graphically analyze $L_{sy}(\eta)$ and $R_{sy}(\eta)$, as shown in Fig. (3.2). The points of intersection between the curves are the roots of Eq. (3.13).

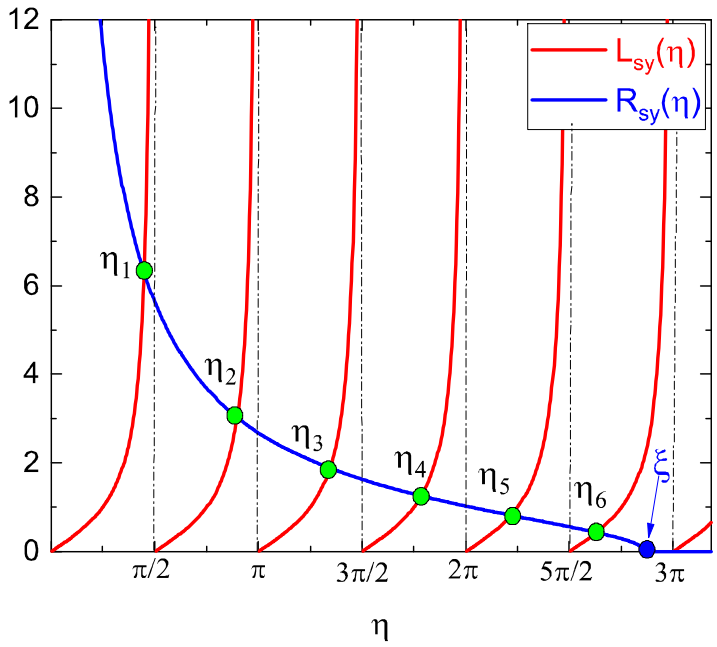

Figure 3.2: Left-hand side (red curves), $L_{sy}(\eta)$, expressed by Eq. (3.20) and right-hand side (blue curve), $R_{sy}(\eta)$, from Eq (3.21). The intersection between the blue and red curves yields the root of the transcendental equation, Eq. (3.13), η_n. The position ξ corresponds to $R_{sy}(\eta) = 0$.

By varying the physical parameters and analyzing the behavior of $L_{sy}(\eta)$ and $R_{sy}(\eta)$, we chose to carry out a parabolic expansion for $L_{sy}(\eta)$ and linear expansion for $R_{sy}(\eta)$, both around η_{expan}. Then, for $L_{sy}(\eta)$ we have

$$L_{sy,app}(\eta) = \sum_{j=0}^{2} \frac{L_{sy}(\eta)^{(j)}(\eta_0)}{j!}(\eta-\eta_{\text{expan}})^j = \zeta_1+(1+\zeta_1^2)(\eta-\eta_{\text{expan}})+\zeta_1(1+\zeta_1^2)(\eta-\eta_{\text{expan}})^2 \ ,$$

where $\zeta_1 = \tan(\eta_{\text{expan}} + (n+1)\pi/2)$.

Similarly, for $R_{sy}(\eta)$ we have

$$R_{sy,app}(\eta) = \sum_{j=0}^{1} \frac{R_{sy}(\eta)^{(j)}(\eta_0)}{j!}(\eta-\eta_{\text{expan}})^j = \zeta_2 + \zeta_3(\eta-\eta_{\text{expan}}), \tag{3.22}$$

where,

$$\begin{aligned} \zeta_2 &= \alpha_m\sqrt{-\frac{\eta_{\text{expan}}^2-\xi^2}{\eta_{\text{expan}}^2}}, \\ \zeta_3 &= \frac{\alpha_m\xi\zeta_2}{\eta_{\text{expan}}(\eta_{\text{expan}}^2-\xi^2)}. \end{aligned} \tag{3.23}$$

Equating both sides and solving for the real root, we obtain

$$\eta_n = \frac{\omega_1+\sqrt{\omega_2+\omega_3}}{\omega_0}, \tag{3.24}$$

where the constants ω_0, ω_1, ω_2 and ω_4 are given by

$$\begin{aligned} \omega_0 &= 2\zeta_1(1+\zeta_1^2) \\ \omega_1 &= \omega_0\eta_{\text{expan}} - 1 + \zeta_3 - \zeta_1^3, \\ \omega_2 &= 1 - 2(\zeta_1^2+\zeta_3+\zeta_3\zeta_1^2) + \zeta_3^2, \\ \omega_3 &= \ \ 4\zeta_1(\zeta_2+\zeta_1^2\zeta_2) - 3\zeta_1^4. \end{aligned}$$

Fig. (3.3) graphically illustrates, for the fundamental state, the regions in which the solution of the transcendental equation, Eq. (3.13), is obtained by the approximation for $\arccos(\phi)$ and by the MEPM.

In the next section, we discuss a simple way to build a proper mapping function to obtain $\eta_{\text{expan}} = \mathbf{M}_{sy}(\xi)$, which is the cornerstone in our methodology.

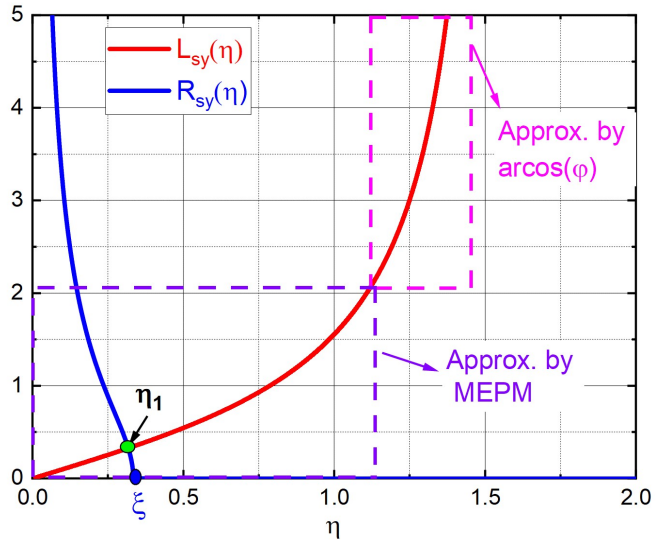

Figure 3.3: Illustration of the application regions of the approximation given by arccos and the MEPM approximation for the ground state.

Building the mapping function $\mathbf{M}_{sy}$

To build the mapping function $\mathbf{M}_{sy}(\xi)$, initially, we plot the fundamental state η_1 as function of ξ. By inspection of Fig. (3.2), one can see that η_1 tends to $\pi/2$ as $\xi \longrightarrow \infty$. Similarly, it is easy to see that the solutions to the higher-order states η_n tends to $n\pi/2$ as $\xi \longrightarrow \infty$. Therefore, for the eigenvalues of Eq. (3.13), we have $\eta_n \in [(n-1)\pi/2, n\pi/2))$. Hence, any function that approximates the curve for $\eta_1(\xi)$ and whose limit tends to $\pi/2$ under the condition $\left|(\eta_1 - \eta_{\text{expan}})/\eta_1\right| \ll \epsilon$ will work as a proper mapping function for the ground state in our approach. Obviously, the proposed solution for η_n will demonstrate better agreement when $\epsilon \longrightarrow 0$. For the sake of clarity, we summarize the above discussion in mathematical notation. In doing so, the mapping function for the symmetrical quantum well must meet these two criteria:

Criterion 1 $|(\eta_n(\xi) - \mathbf{M}_{sy}(\xi))/\eta_n(\xi)| < \epsilon$ *for* $\epsilon = 0.1$ *with* $\alpha_m \in (0.1, 1)$, $\xi \leq \xi_{\max} = 20$

Criterion 2 $\mathbf{M}_{sy}(\xi) \longrightarrow \frac{\pi}{2}$ *when* $\xi \longrightarrow \xi_{\max}$

where $\xi_{\max}$ is the maximum value of ξ in which the condition $\eta/(\alpha_m \xi) \ll 1$ is not satisfied, determined by the minimization of the relative error. Note that the mapping function does not need to meet Criterion 1 for all ξ values, but only for those under the condition $\xi \leq \xi_{\max}$, since

we are dealing with the case where $\eta/\alpha_m\xi \ll 1$ is not met. The value of $\xi_{\max}$ was defined evaluating the overall relative error of our proposition. In addition, our experience indicates that ϵ does not need to be extremely small, given that the mapping function provides only a pointer to the vicinity of the solution. Then, the following mapping function for the ground state is proposed:

$$\mathbf{M}_{sy}(\xi) = \sqrt{\alpha_m}\xi\left(1 - \frac{1}{2}\sum_{j=1}^{2}\exp\left(-\frac{a_i}{\sqrt{\alpha_m}\xi}\right)\right),\ a_i \in \mathbb{R}, \tag{3.25}$$

where coefficients a_i are determined by minimizing the relative error. Hence, in order to obtain the optimized a_i coefficients, we employ nonlinear regression, with R-square 99.8%. Thus, for $\eta_1(\xi)$ with $m_w^* = 0.067m_0$ and $m_b^* = 0.11m_0$, where m_0 is the resting electron mass [75], [76], we obtain $a_1 = 2.45$ and $a_2 = 0.70$. Nonetheless, we should point out that values for a_i are derived only as an illustration of our method. The final expressions for energy levels already provide the optimized mapping function constants for a broader range of typical semiconductors physical parameters. Therefore, it is needless to re-define the mapping function for each different application.

The exact solution for $\eta_1(\xi)$ and the mapping function $\mathbf{M}_{sy}(\xi)$ are shown in Fig. (3.4) for different masses ratios, expressed by the parameter $\alpha_m = \sqrt{m_w^*/m_b^*}$, exhibiting an excellent agreement. Since ξ is a function of m_w^*, L_w and U_0, we demonstrate by this analyses that the proposed mapping function is robust concerning the variation of the QW parameters.

In principle, for each energy level, it would be necessary to define a new mapping function, which it is certainly impractical. However, taking advantage of the properties of the trigonometric functions in the transcendental equations, we can employ Eq. (3.24) to compute any energy level. To do so, we shift ξ and $\mathbf{M}_{sy}(\xi)$ by multiples of $\pi/2$ to the interval of interest to compute η_n, i.e., shifting both ξ and $\mathbf{M}_{sy}(\xi)$ to the interval $((n-1)\pi/2, n\pi/2)$. Since ξ is greater than η_n (see Fig. (3.2)) and $\mathbf{M}_{sy}(\xi)$ was defined for the ground state, i.e., limited to $\pi/2$, they must shift in the opposite direction to the interval $((n-1)\pi/2, n\pi/2)$. To obtain the smallest possible error, we propose a similar mapping function for even values of n, only adjusting the coefficients a_i. Proceeding as before, we obtain the mapping relation for all allowed levels of the symmetric well:

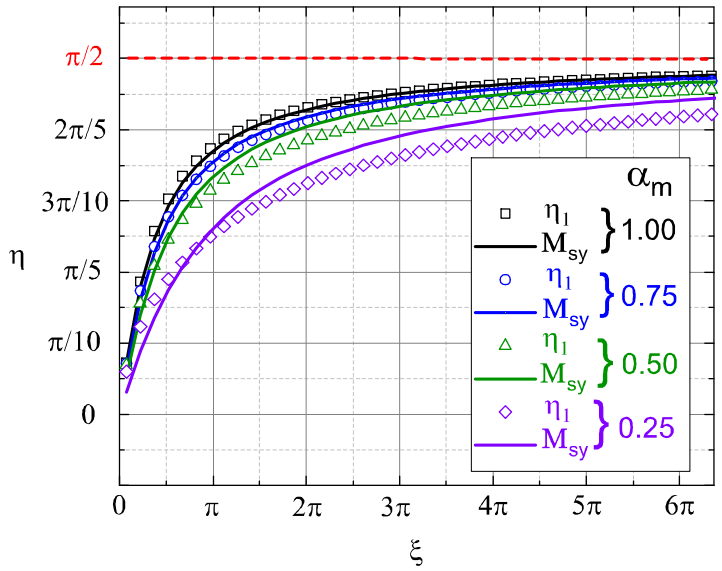

Figure 3.4: Solid colored curves represent the mapping function, $M_{sy}(\xi)$, while symbols represent the solution for the ground state, $\eta_1(\xi)$, for different α_m^2 values.

$$\mathbf{M}_{sy}(\xi) = \begin{cases} p(n) + \frac{\lambda}{2}(2 - e^{-(1.45\delta(n-1)+1)/\lambda} - e^{-0.7/\lambda}), n = 1, 3, 5, ... \\ p(n) - \frac{\pi}{2} + \frac{\lambda}{2}(2 - e^{-5/\lambda} - e^{-1.5/\lambda}), n = 2, 4, 6, ... \end{cases} \tag{3.26}$$

where, $p(n) = (n-1)\,\pi/2$. In Eq. (3.26), $\delta(n-1)$ is the discrete Dirac delta function ($\delta(n-1)$ returns 1 when $n = 1$ and 0 otherwise). The parameter λ is just the value of ξ shifted to the interval of interest to calculate the respective eigenvalue. Thereby, keeping in mind that for each interval of size $\pi/2$ there is only one eigenvalue, we have

$$\lambda = \begin{cases} \left[\left(\sqrt{\alpha_m}\right)^{\delta(n-1)}\right] \xi - p(n), \; n = 1, 3, 5, ... \\ \xi - p(n) - \frac{\pi}{2}, \; n = 2, 4, 6, ... \end{cases} \tag{3.27}$$

Through an inspection of the relative error for $\mathbf{M}_{sy}(\xi)$ we notice that α_m has great impact on the solution for the ground state η_1. Also from the Fig. (3.4), for $\xi < \pi/2$, the tested values for α_m impact more the curve shape for $\eta_1(\xi)$ when $\xi \longrightarrow 0$ than when $\xi \longrightarrow \infty$. Nevertheless, the same analysis performed for the other energy levels does not show a strong dependence of $\eta_n(\xi)$ on α_m for the assessed values. By means of this investigation, the term $\left(\sqrt{\alpha_m}\right)^{\delta(n-1)}$ in Eq. (3.27) when $n = 1$ leads to Eq. (3.25). Ultimately, to determine for which value of ξ the condition $\eta/\left(\alpha_m \xi\right) \ll 1$ no longer holds, we set the threshold value of ξ

considering the minimization of the relative error for different values of physical parameters.

Finally, from Eqs. (3.17) and (3.24), we write Eq. (3.28) that summarizes all possible values of η, providing all allowed energy levels in a one-dimensional finite rectangular quantum well:

$$\eta_n = \begin{cases} \zeta_0/(6c) - 2b/\zeta_0, & \xi \geq \left(\frac{n}{2} + 2\right)\pi \\ \omega_0^{-1}\left(\omega_1 + \sqrt{\omega_2 + \omega_3}\right), & \xi < \left(\frac{n}{2} + 2\right)\pi \end{cases} \tag{3.28}$$

By analyzing Fig. (3.2), it is possible to determine the minimum condition for the curves to intersect each other at the interval $((n-1)\pi/2, n\pi/2)$ for a given n. Hence, it is straightforward that, for the n level, we have $\xi \geq (n-1)\pi/2$ in order to get an eigenvalue in $((n-1)\pi/2, n\pi/2)$. In this way, replacing the expression for ξ defined in Section (3.2.1), we can determine the minimum width so that the symmetric well presents a bound state for the nth energy level:

$$L_{Wsy,\min}(n) = \frac{\pi\hbar(n-1)}{\sqrt{2m_w^* U_0}}. \tag{3.29}$$

For instance, to build a symmetric quantum well with semiconductor parameters $U_0 = 0.3\,\mathrm{eV}$ and $m_w^* = 0.067m_0$ with at least 4 allowed energy levels, the minimum width obtained by setting $n = 4$ in Eq. (3.29) is $L_{Wsy,\min} = 129.75$ Å. As it can be seen from Eq. (3.29), m_b^* does not alter the minimum length for a given energy level, albeit affects its magnitude. Another important relation for engineering purposes is set between the energy level E_n and the width of the well. Thus, combining Eqs. (3.10) and (3.11), and using the relationship:

$$\arctan(\eta) + \arctan\left(\frac{1}{\eta}\right) = \frac{\pi}{2}$$

we can write

$$L_{Wsy,n}(E_n) = \frac{2\hbar}{\sqrt{2m_w^* E_n}}\left[\frac{(n-1)\pi}{2} + \arctan\left(\alpha_m\sqrt{\frac{U_0}{E_n} - 1}\right)\right]. \tag{3.30}$$

We readily point out that the expression obtained in Eq. (3.30) is similar to the result from [77], except for the mass ratio parameter α_m (included by the application of the boundary conditions), which they do not take into account. As an example, consider the design of a semiconductor structure with $U_0 = 0.5\,\mathrm{eV}$, $m_w^* = 0.067m_0$ and $m_b^* = 0.1m_0$. As a requirement, energy level 2 must be $0.2\,\mathrm{eV}$. Through Eq. (3.30), we have $L_{Wsy,2}(E_2 = 0.2\,\mathrm{eV}) = 79.50$ Å.

Finally, examining Fig. (3.2), we have that the number of states allowed in the symmetrical well is

$$N_{sy} = \left\lfloor \frac{2\xi}{\pi} \right\rfloor + 1 \tag{3.31}$$

where $\lfloor z \rfloor$ is the floor function defined as the first integer smaller than z (for instance, $\lfloor 3.37 \rfloor = 3; \lfloor 5 \rfloor = 4$) [78]. In the next section, we address the asymmetric quantum well case following the same strategy developed for the symmetric case.

3.3 Asymmetric Finite Square Quantum Well

3.3.1 Theoretical Background

Fig. (3.5) shows a schematic illustration of an asymmetric rectangular quantum well (ASQW), where the left barrier is lower than the right barrier. For this particular case, the electrical potential energy can be written as

$$U(x) = \begin{cases} U_1, & x < 0 \\ 0, & 0 \leq x \leq L_w \\ U_2, & x > L_w \end{cases}, \tag{3.32}$$

where U_1 and U_2 are the height of the left and right potential energy barrier, respectively, with $U_1 < U_2$.

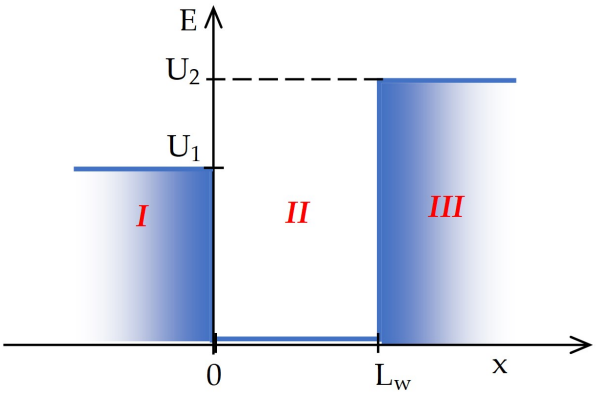

Figure 3.5: Schematic illustration of a typical asymmetric rectangular quantum well of width L_w potential barriers with heights U_1 and U_2.

For regions I and III, the solutions for Schrödinger equation are of the form $\Psi_1(x) = C_1 e^{k_1 x}$ and $\Psi_3(x) = C_3 e^{-k_3 x}$, respectively, where C_1 and C_3 are normalization constants. The wave vectors are $k_1 = \sqrt{2m^*_{b1}(U_1 - E)/\hbar^2}$ and $k_3 = \sqrt{2m^*_{b2}(U_2 - E)/\hbar^2}$, where m^*_{b1} and m^*_{b2} are the effective masses in regions I and III, respectively, and E is the kinetic energy, with $E < U_1$. In the same way, the solution for Schrödinger equation in the well is $\Psi_2(x) = C\cos(k_2 x) + D\sin(k_2 x)$,where C and D are normalization constants and the wave vector is $k_2 = \sqrt{2m^*_w E/\hbar^2}$. Also, one can rewrite $\Psi_2(x)$ as $\Psi_2(x) = C_2\sin(k_2 x + \theta)$. Applying the boundary conditions at $x = 0$ and $x = L_w$, after some algebraic manipulation, we obtain

$$\cot(\theta) = \beta_m \sqrt{\frac{\varsigma_1^2}{\varphi^2} - 1}, \tag{3.33}$$

$$\cot(\varphi + \theta) = -\mu_m \sqrt{\frac{\varsigma_2^2}{\varphi^2} - 1}, \tag{3.34}$$

with $\varsigma_1 = (L_w/\hbar)\sqrt{2m^*_w U_1}$, $\varsigma_2 = (L_w/\hbar)\sqrt{2m^*_w U_2}$and $\varphi = k_2 L_w$. The ratios between the effective masses are $\beta_m^2 = m^*_w/m^*_{b1}$ and $\mu_m^2 = m^*_w/m^*_{b2}$.

Similar to the symmetric case, it is necessary to solve the system formed by two transcendental equations, in order to find the eigenenergies of the asymmetric well. The energy levels are given by

$$E_{asy,n} = \frac{\hbar^2}{2m_w^* L_w^2}\varphi_n^2, \;\; n = 1, 2, 3, ...N_{asy}, \tag{3.35}$$

where φ_n are the solutions obtained by solving the coupled Eqs. (3.33) and (3.34), n corresponds to the nth energy level of a set of N_{asy} allowed energy levels and the subscript asy refers to the asymmetric case. In the next section, we present our solution for Eq. (3.33) and (3.34), based on whether the condition $C_{\max} \ll 1$ is satisfied, where we define $C_{\max}$ as

$$C_{\max} = \max\left\{\frac{\varphi}{\beta_m \varsigma_1}, \frac{\varphi}{\mu_m \varsigma_2}\right\}.$$

The reason for us to adopt this strategy defined by $C_{\max}$ will be clarified in the next section.

3.3.2 Approximate Analytical Solution for ASQW

Once more, to obtain a general method for computing any allowed energy levels for a wide range of physical parameter values, U_1, U_2, m_w^*, m_{b1}^* and m_{b2}^*, we divide the solution in two parts. In this case, the solution is based on whether the condition $C_{\max} \ll 1$ is satisfied.

Condition $C_{\max} \ll 1$ is satisfied:

Proceeding in the same way as in Section (3.2.2) and using the trigonometric identity $\cot^2(A) = \csc^2(A) - 1$, we have for Eq. (3.33):

$$\theta = \arcsin\left(\frac{\varphi}{\beta_m \varsigma_1}\right) + t\pi, \; t \in \mathbb{Z}. \tag{3.36}$$

Similarly, for Eq. (3.34), we have

$$\varphi + \theta = m\pi - \arcsin\left(\frac{\varphi}{\mu_m \varsigma_2}\right), \; m \in \mathbb{Z}. \tag{3.37}$$

Since t and m are both integer numbers, then $m - t$ is also an integer number, thereby, one can write $n = m - t$. Replacing Eq. (3.36) in Eq. (3.37) we have a general transcendental equation for the asymmetric well:

$$\varphi = n\pi - \arcsin\left(\frac{\varphi}{\beta_m \varsigma_1}\right) - \arcsin\left(\frac{\varphi}{\mu_m \varsigma_2}\right). \tag{3.38}$$

Employing a third order Taylor approximation, we have $\arcsin(\phi) \approx \phi + \phi^3/6$. Therefore, the general transcendental equation is approximated to

$$d\varphi^3 + e\varphi - f = 0, \tag{3.39}$$

where

$$\begin{aligned} d &= \frac{1}{6\beta_m^3\varsigma_1^3} + \frac{1}{6\mu_m^3\varsigma_2^3}, \\ e &= 1 + \frac{1}{\beta_m\varsigma_1} + \frac{1}{\mu_m\varsigma_2}, \\ f &= n\pi. \end{aligned} \tag{3.40}$$

Solving Eq. (3.39) and choosing the real root, we have

$$\varphi_n = \chi_1 - \frac{e}{3d\chi_1}, \tag{3.41}$$

where

$$\chi_1 = \sqrt[3]{\sqrt{\left(\frac{f}{2d}\right)^2 + \left(\frac{e}{3d}\right)^3} + \frac{f}{2d}}. \tag{3.42}$$

Again, as discussed in the case of the symmetrical well, the solution is obtained in two parts. The proposed solution for Eq. (3.38) is accurate if $\arcsin(\phi)$ can be approximated to a third order polynomial. Thus, we need to meet $\{\varphi/\beta_m\varsigma_1, \varphi/\mu_m\varsigma_2\} \ll 1$, which implies that $\max\{\varphi/\beta_m\varsigma_1, \varphi/\mu_m\varsigma_2\} \ll 1$, leading to $C_{\max} \ll 1$. In the next section we propose a solution for the cases where the condition $C_{\max} \ll 1$ is not met.

Condition $C_{\max} \ll 1$ is not satisfied:

To combine Eqs. (3.33) and (3.34) in a single expression for the transcendental equations, we employ the trigonometric identity:

$$\cot(\varphi + \theta) = \frac{\cot(\varphi)\cot(\theta) - 1}{\cot(\varphi) + \cot(\theta)}. \tag{3.43}$$

Replacing the terms $\cot(\varphi)$ and $\cot(\varphi+\theta)$ in Eq. (3.43) for the Eqs. (3.33) and (3.34), respectively, and isolating the term $\cot(\varphi)$, we have

$$\cot(\varphi) = \frac{1-\mu_m\beta_m\sqrt{\frac{\varsigma_1^2}{\varphi^2}-1}\sqrt{\frac{\varsigma_2^2}{\varphi^2}-1}}{\beta_m\sqrt{\frac{\varsigma_1^2}{\varphi^2}-1}+\mu_m\sqrt{\frac{\varsigma_2^2}{\varphi^2}-1}}. \tag{3.44}$$

To perform a graphical analysis, we define two functions of φ representing the left- and right-hand sides of the Eq. (3.44). Hence, let $L_{asy}(\varphi)$ be the LHS of Eq. (3.44) and $R_{asy}(\varphi)$ be the RHS of Eq. (3.44). Fig. (5.5) shows the curves of $L_{asy}(\varphi)$ and $R_{asy}(\varphi)$, where the intersection points φ_n are the roots of Eq. (3.44). For the asymmetric well case, we have $\varphi_n \in [(n-1)\pi, n\pi)$. Fig. (5.5) it also shows the position of ς_1. In our case, $U_1 < U_2$ implies that $\varsigma_1 < \varsigma_2$. Note that, for $\varphi > \varsigma_1$, the RHS of Eq. (3.44) belongs to the complex plane, $\mathbb{C}$. Therefore, the variable that determines the existence of a real solution for Eq. (3.44) is ς_1.

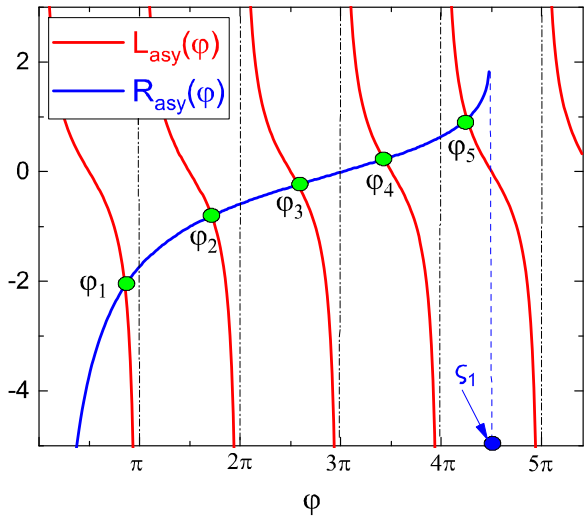

Figure 3.6: Left-hand side (blue curve), $L_{asy}(\varphi)$, and right-hand side (red curve), $R_{asy}(\varphi)$ of Eq (3.44). The intersection between the curves yields the root of the transcendental equation, φ_n.

Employing the same strategy developed in Section (3.2.2), we expand $L_{asy}(\varphi)$ and $R_{asy}(\varphi)$ in a Taylor series around φ_{expan}. Thus, by means of a graphical analysis of Eq. (3.44), shown in Fig. (5.5), we conclude that a simple linear expansion around φ_{expan} for both $L_{asy}(\varphi)$ and $R_{asy}(\varphi)$ is enough to provide high accuracy. Hence, for $L_{asy}(\varphi)$ we have

$$L_{asy,app}(\varphi) = \varepsilon + \left(-1-\varepsilon^2\right)\left(\varphi - \varphi_{\text{expan}}\right)$$

where $\varepsilon = \cot\left(\varphi_{\text{expan}}\right)$. By the same token, expanding $R_{asy}\left(\varphi\right)$ around φ_{expan}, we obtain:

$$R_{asy,app}\left(\varphi\right) = g + hl\left(\varphi - \varphi_{\text{expan}}\right),$$

where the constants are

$$\begin{aligned} g &= \frac{1-\gamma_1\gamma_2}{\gamma_1+\gamma_2}, \\ h &= \frac{\gamma_1\Gamma_2+\gamma_2\Gamma_1}{\gamma_1+\gamma_2}, \\ l &= g\left(\Gamma_2-\Gamma_1\right), \end{aligned} \tag{3.45}$$

with

$$\begin{aligned} \gamma_1 &= \beta_m\sqrt{\frac{\varsigma_1^2}{\varphi_{\text{expan}}^2}-1}, \\ \gamma_2 &= \mu_m\sqrt{\frac{\varsigma_2^2}{\varphi_{\text{expan}}^2}-1}, \\ \Gamma_1 &= \frac{\gamma_1\varsigma_1^2}{\varphi_{\text{expan}}\left(\varsigma_1^2-\varphi_{\text{expan}}^2\right)}, \\ \Gamma_2 &= \frac{\gamma_2\varsigma_2^2}{\varphi_{\text{expan}}\left(\varsigma_2^2-\varphi_{\text{expan}}^2\right)}. \end{aligned} \tag{3.46}$$

Next, we can write an approximation for Eq. (3.44) equating both sides and isolating φ:

$$\varphi_n = \frac{\varepsilon - g}{\varepsilon^2 + hl + 1} + \varphi_{\text{expan}}\,. \tag{3.47}$$

It is worth mentioning that a linear approximation on both sides of Eq. (3.44) was only possible due to our strategy of expanding transcendental equations around a movable point described through the mapping function $\mathbf{M}_{asy}(\varsigma_1)$. In contrast, in a conventional approaches, a second order polynomial approximation for $\cot(\varphi)$ around $\varphi = 0$ in Eq. (3.44) would result in a 4th-order polynomial equation, making the solution very laborious, with no guarantee of satisfactory agreement for the entire range of interest.

Building the mapping function $\mathbf{M}_{asy}$

To determine the mapping function, we proceed just as before in the Sec. (3.2.2). Initially, we plot the fundamental state φ_1 as a function of ς_1. From Fig. (5.5), it is seen that φ_1 tends to π as $\varphi_1 \longrightarrow \infty$. By the same token, from Fig. (5.5), the solutions to the other eigenstates φ_n tends to $n\pi$ as $\varsigma_1 \longrightarrow \infty$, hence, $\varphi_n \in [(n-1)\pi, n\pi)$. Therefore, any function that approximates the behavior for $\varphi_1(\varsigma_1)$ and whose limit tends to π under the condition $\left|(\varphi_1 - \varphi_{expan})/\varphi_1\right| \ll \epsilon$ will work as a mapping function for the ground state. Again, we summarize this arguments in mathematical notation. For this case, the mapping function must meet these two criteria:

Criterion 3 $|(\varphi_n(\varsigma_1) - \mathbf{M}_{asy}(\varsigma_1))/\varphi_n(\varsigma_1)| < \epsilon$ *with* $\epsilon = 0.1$, *for* $\beta_m, \mu_m \in (0.1, 1)$ *and* $\varsigma_1 \leq \varsigma_{\max}$.

Criterion 4 $\mathbf{M}_{asy}(\varsigma_1) \longrightarrow n\pi$ *with* $\varsigma_1 \longrightarrow \varsigma_{\max}$.

where $\varsigma_{\max}$ is the maximum value ς_1 from which the condition $C_{\max} \ll 1$ is not met. Notice that the mapping function does not need to meet Criterion 1 for all ς_1 values, but only for those under the condition $\varsigma_1 \leq \varsigma_{\max}$, concerning the case where $C_{\max} \ll 1$ is not satisfied. The value of $\varsigma_{\max}$ was defined evaluating the overall relative error of our proposition. Again, ϵ does not need to be extremely small, once the mapping function provides only a pointer to the vicinity of the solution instead of the solution itself. Then, the following mapping function for the ground state is proposed:

$$\mathbf{M}_{asy}(\varsigma_1) = b_0 - \sum_{i=1}^{2} b_i \exp\left(-\frac{\sqrt[4]{\beta_m}\varsigma_1}{z_i}\right), \; b_i, z_i \in \mathbb{R}. \tag{3.48}$$

The coefficients b_i and z_i are determined by minimizing the relative error. To obtain the optimized b_i and z_i coefficients, we performed a fitting curve procedure by means of nonlinear regression with the obtained R-square equal to 99.8%. To do so, we computed $\varphi_1(\varsigma_1)$ for the following parameters: $m_w^* = 0.067m_0$, $m_{b1}^* = 0.09m_0$ and $m_{b2}^* = 0.15m_0$ where m_0 is the resting electron mass [75], [76]. For this set of parameters, we obtain $b_0 = 2.9$, $b_1 = 1.59$, $b_2 = 1.37$, $z_1 = 1.42$ and $z_2 = 6.69$. As before, the values for b_i and z_i are defined only once in the derivations steps of our method. Again, the final expressions for the energy levels will

provide the optimized mapping function constants for a broad range of typical semiconductor's physical parameters.

To evaluate the accuracy of our proposed mapping function, we compare the exact solution for $\varphi_n(\varsigma_1)$ and the mapping function $\mathbf{M}_{asy}(\varsigma_1)$ with different masses ratios, expressed by the parameter $\beta_m^2 = m_w^*/m_{b1}^*$. As it can be seen in Fig. (3.7), the mapping function provides an excellent agreement. In addition, since ς_1 is a function of m_w^*, L_w and U_1, we demonstrate that the proposed mapping function is robust concerning the variation of the physical parameters.

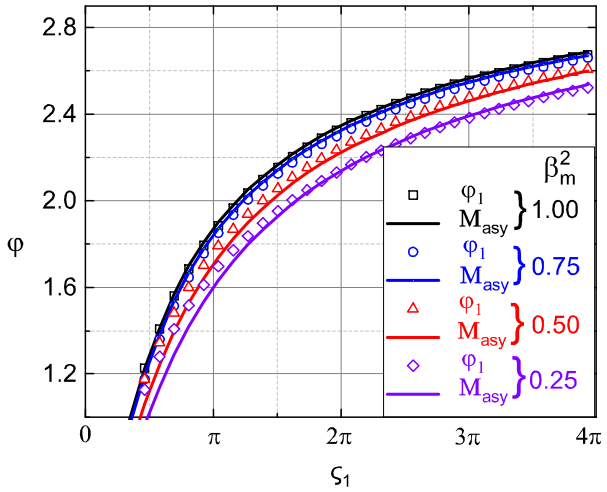

Figure 3.7: Solid curves represent the mapping function, $M_{asy}(\varsigma_1)$, while symbols represent the exact solution for the ground state, $\varphi_1(\varsigma_1)$, for different β_m^2 values.

Again, taking advantage of the periodicity of the trigonometric functions involved in the transcendental equation, we can employ Eq. (3.48) to compute any energy level simply by shifting ς_1 and $\mathbf{M}_{asy}(\varsigma_1)$ by multiples of π to the interval where it is desired to compute φ_n, in this case shifting both to the interval $[(n-1)\pi, n\pi)$. Also, since ς_1 is greater than φ_n (see Fig. (5.5)) and $\mathbf{M}_{asy}(\varsigma_1)$ was defined for the ground state, i.e., limited to π, these two factors must shift opposite directions in order to reach the interval $[(n-1)\pi, n\pi)$. To minimize the relative error, we propose a similar mapping function for $n > 1$, adjusting only the coefficients b_i and z_i. Proceeding in the same manner as in the case $n = 1$, we obtain the mapping relation for all allowed levels of the asymmetric well:

$$\mathbf{M}_{asy}(\varsigma_1) = \begin{cases} 2.9 - 1.59e^{-\left(\sqrt[4]{\beta_m}\right)\varsigma_1/1.42} - 1.37e^{-\left(\sqrt[4]{\beta_m}\right)\varsigma_1/6.69}, n = 1 \\ s + 5.79 - 15.13e^{-(\varsigma_1 - s)/1.05} - 2.91e^{-(\varsigma_1 - s)/6.41}, \ n > 1 \end{cases} \tag{3.49}$$

where, $s = (n-2)\pi$. Again, the optimized expansion point is obtained simply by setting $\varphi_{\text{expan}} = \mathbf{M}_{asy}(\varsigma_1)$.

The limit value at which the condition $C_{\max} \ll 1$ is not met was determined by minimizing the relative error against the numerical solution for the Eqs. (3.41) and (3.47). This analysis was carried out covering a wide range of physical parameters found in the semiconductor heterostructures used in electronic devices.

As such, Eq. (3.50) summarizes all possible values of φ_n, describing all allowed energy levels in a one-dimensional finite asymmetric rectangular quantum well potential:

$$\varphi_n = \begin{cases} \chi_1 - \frac{e}{3d\chi_1}, & \varsigma_1 \geqslant 15 + (n-1)\pi, \\ \frac{\varepsilon - g}{\varepsilon^2 + hl + 1} + \varphi_{\text{expan}}\,, & \varsigma_1 < 15 + (n-1)\pi, \end{cases} \tag{3.50}$$

Unlike the symmetric case, depending on the physical parameters, there may be no solution for Eq. (3.44), i.e., an absence of bound energy levels in the asymmetric well. By analyzing the graphical behavior of the curves $L_{asy}(\varphi)$ and $R_{asy}(\varphi)$, we can determine the minimum condition for which Eq. (3.44) allow a solution. To do so, setting $\varphi = \varsigma_1$, we have that a solution for the ground state exists only when

$$\cot(\varsigma_1) \leq \left(\mu_m \sqrt{\frac{U_2}{U_1} - 1}\right)^{-1}, \varsigma \leq \pi/2 \tag{3.51}$$

Similarly, we can determine the minimum width of the well so the n-th energy level is a bound state:

$$L_{Wasy,\min}(n) = \frac{\hbar}{\sqrt{2m_w^* U_1}} \left\{ (n-1)\pi + \operatorname{arccot}\left[\left(\mu_m \sqrt{\frac{U_2}{U_1} - 1} \right)^{-1} \right] \right\}, \tag{3.52}$$

From Eq. (3.44) we can also compute the exact width of the asymmetric well for a given energy level E_n, a very useful expression for engineering design purposes:

$$L_{Wasy,n}(E_n) = \frac{\hbar}{\sqrt{2m_w^* E_n}} \left\{ n\pi + \operatorname{arccot}\left[\frac{E_n - \beta_m \mu_m \sqrt{U_1 - E_n}\sqrt{U_2 - E_n}}{\sqrt{E_n}\left(\beta_m \sqrt{U_1 - E_n} + \mu_m \sqrt{U_2 - E_n}\right)} \right] \right\} \tag{3.53}$$

Note that Eqs. (3.52) and (3.53) are exact solutions without any kind of approximation employed. Finally, we also express how many energy levels are allowed for a given asymmetric quantum well with width L_w:

$$N_{asy} = \left\lfloor \frac{1}{\pi} \left\{ \varsigma_1 - \operatorname{arccot} \left[\left(\mu_m \sqrt{\frac{U_2}{U_1} - 1} \right)^{-1} \right] \right\} \right\rfloor + 1. \tag{3.54}$$

If we set $U_2 = U_1$ in Eq. (3.52), it becomes Eq. (3.29), as expected. Also, if $U_2 = U_1$ in Eq. (3.51), there will always be at least the ground state. Additionally, $U_2 = U_1$ implies that $N_{asy} = N_{sy}$, since in this case we have $\varsigma_1 = 2\xi$.

As a final note, we mention that it is possible to use the expressions originally developed for the asymmetric quantum well to compute energy levels of the symmetric case by setting $U_2 = U_1$. However, we cannot guarantee the same level of accuracy since the mapping functions were optimized for each specific case.

3.4 Results and Discussion

3.4.1 Results for SQW

We start validating our expressions in comparison to the exact numerical solution. The validation is carried out in terms of ξ, initially considering $\alpha_m = 1$. Indeed, since ξ encompasses the quantum well physical parameters, by contrasting our results with the exact solution, as function of ξ , we validate the proposed expressions for a wide range of quantum well structures. Fig. (3.8) shows the odd mode eigenenergies E_1, E_3, E_5 and E_7 as function of ξ, numerically calculated (considered in this work as an exact solution) and using the analytical expression given by Eq. (3.28). As can be seen, the proposed expressions offer an excellent agreement with the exact solution. Fig. (3.9) shows the relative error of the odd-mode eigenenergies of Fig. (3.8). The maximum error is less than 1%.

Fig. (3.10) show the even mode eigenenergies E_2, E_4, E_6 and E_8 as function of ξ, numerically calculated (symbols) and using the analytical expression proposed by Eq. (3.28) (solid lines). Again, the proposed model displays an excellent agreement to the exact solution. Fig. (3.11) shows the relative error of the even mode eigenenergies plotted in Fig. (3.10). As it can be seen the maximum error is less than 1%.

In addition, to validate our solution for the symmetrical rectangular well, we used a semiconductor structure with the following physical parameters $U_0 = 0.5\,\mathrm{eV}$, $m_w^* = 0.067m_0$,and

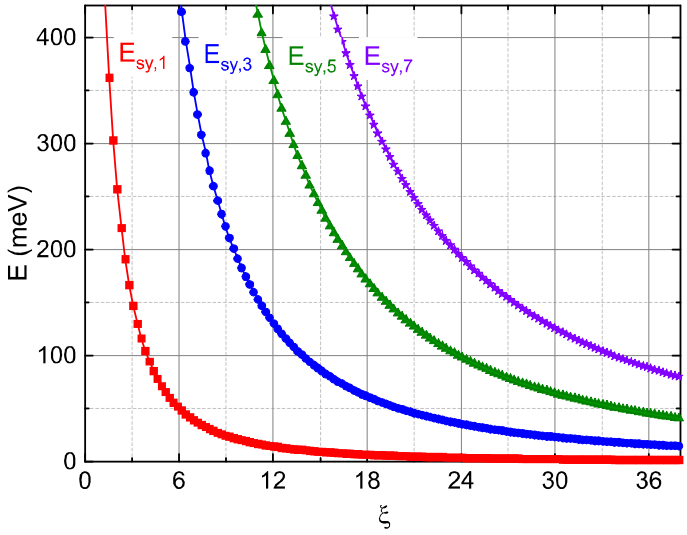

Figure 3.8: Odd mode eigenenergies E_1, E_3, E_5 and E_7 as a function of ξ, numerically calculated (symbols) and using the analytical model proposed by Eq. (3.28) (solid lines).

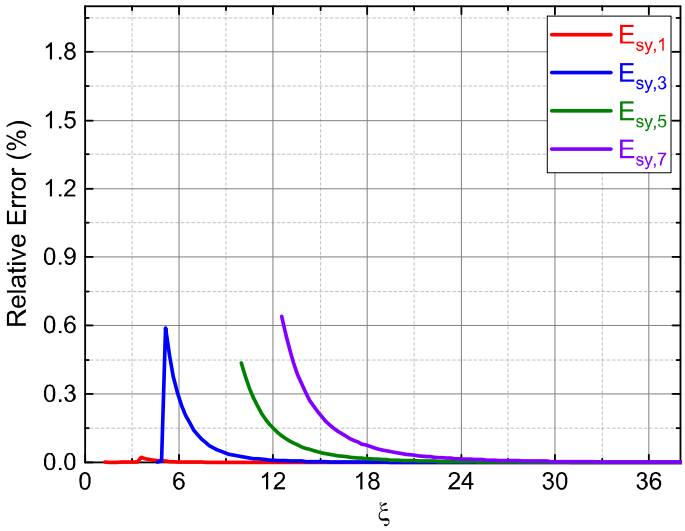

Figure 3.9: Relative error for the odd mode eigenenergies.

$m_b^* = 0.11m_0$, being these values typically found in realistic semiconductor devices (e.g., devices employing AlGaAs heterostructres) [75]- [76], [79]. Fig. (3.12) shows the position of the first three energy levels as function of the width of the well, L_w, obtained numerically by solving Eq. (3.13), and analytically through our expression, Eq. (3.28). We obtained excellent results, in fact, as it can be seen from Fig. (3.12), the curves are visually indistinguishable.

Fig. (3.13) shows the relative error of the proposed model in respect to the numerical

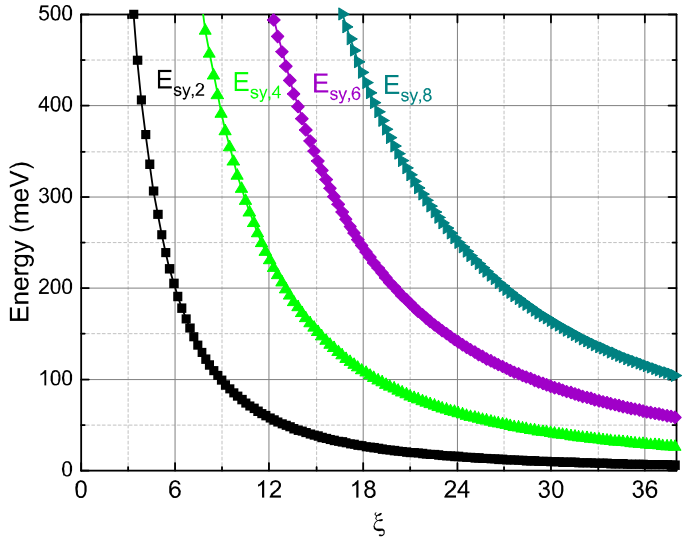

Figure 3.10: The eigenenergies, even mode, E_2, E_4, E_6 and E_8 as function of ξ, numerically calculated (symbols) and using our analytical expressions (solid lines).

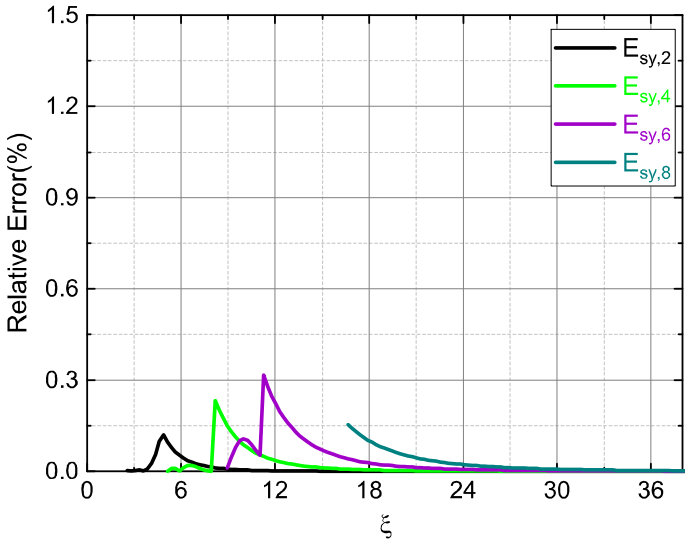

Figure 3.11: Relative error for the even mode eigenenergies.

solution. The relative error is less than 1% for the three energy levels. Finally, to evaluate the robustness of the model for different semiconductor structures, the relative error for different effective masses ratio was also analyzed. Fig. (3.12) shows the relative error for the ground state, $E_{sy,1}$, for $\alpha_m^2 = 0.25$, 0.5, 0.75 and 1. For semiconductors devices, in general, $m_b^* \geq m_w^*$. Hence, the range of analysis for m_w^*/m_b^*, performed in this work, comprises most of the practical cases in nanoelectronics and optoelectronics [75]. As depicted in Fig. (3.14), the

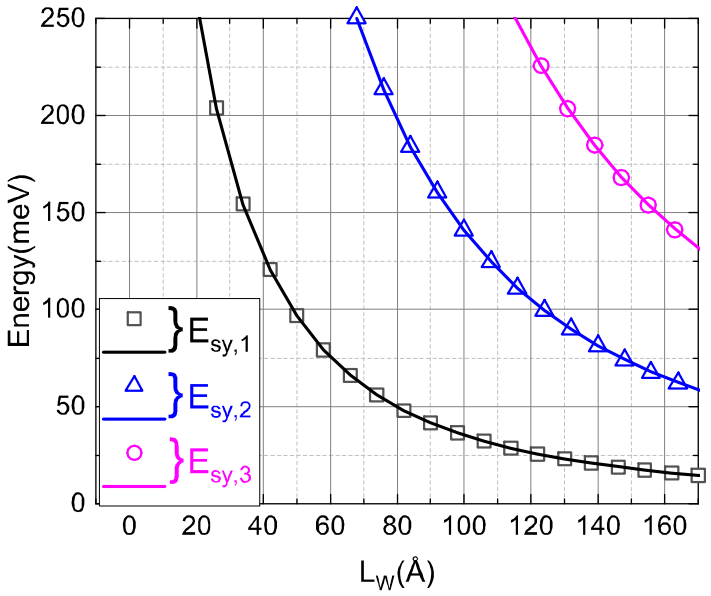

Figure 3.12: Energy levels $E_{sy,1}$, $E_{sy,2}$ and $E_{sy,3}$ as function of L_w.

relative error for all tested values of α_m^2 is below 1%. Notice that, in Fig. (3.13), the relative error curves for the levels $E_{sy,2}$ and $E_{sy,3}$ start from a certain length of the well L_w for which the bound state do exist. These minimum length values can be calculated analytically by Eq. (3.29).

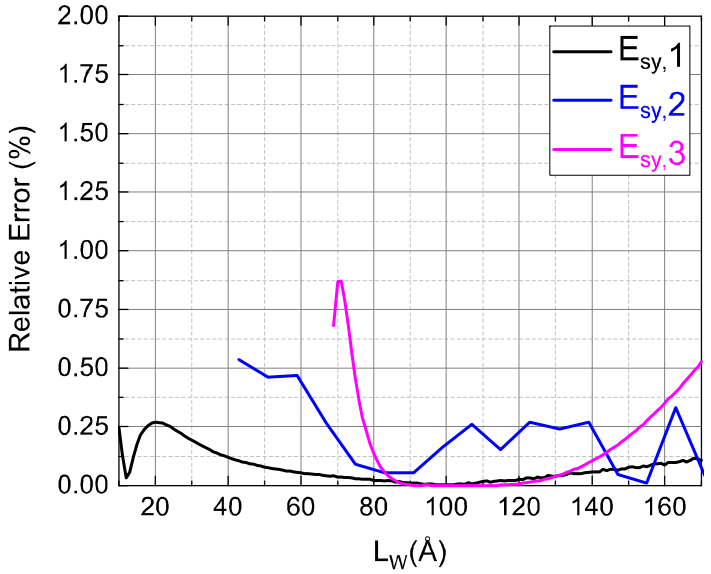

Figure 3.13: Relative error of our proposed model with respect to the exact solution are smaller than 1% for energy levels $E_{sy,1}$, $E_{sy,2}$ and $E_{sy,3}$.

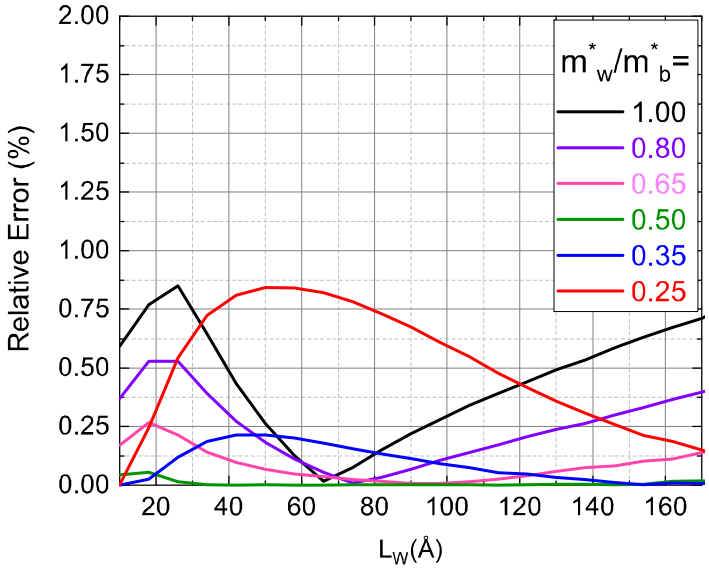

Figure 3.14: Evaluation of our proposed solution regarding different electron effective masses in the potential barrier and the quantum well. This ratio is expressed by $\alpha_m^2 = m_w^*/m_b^*$. All curves are for the ground state, $n = 1$, and $\alpha_m^2 = 0.25, 0.35, 0.50, 0.65, 0.80, 1.00$. For all evaluated values of α_m^2 the relative error is below 1%.

3.4.2 Results for ASQW

In the same way, to check the accuracy of the analytical model for the asymmetric case, we consider an asymmetric rectangular well with $U_1 = 0.2$ eV, $U_2 = 0.5$ eV, $m_w^* = 0.085m_0$, $m_{b1}^* = 0.15m_0$ and $m_{b2}^* = 0.3m_0$ [75]. Fig. (3.15) shows the position of the first three energy levels of the asymmetric well as a function of the width L_w, obtained numerically by solving Eq. (3.44), and analytically through our expression, Eq. (3.50). Again, excellent agreement is obtained. Fig. (3.16) shows the relative error as a function of the width of the well. The relative error for all energy levels evaluated is below 1%. The minimum values of L_w for $E_{asy,2}$ and $E_{asy,3}$ can be calculated using Eq. (3.52).

Fig. (3.17) shows the relative error for the ground state for different values of $\beta_m^2 = m_w^*/m_{b1}^*$ and $\mu_m^2 = m_w^*/m_{b2}^*$ to investigate the accuracy of the expressions for different semiconductor structures. Note that the relative error for all cases addressed are below 1%, showing that the expressions are capable of computing energy levels correctly, regardless of the semiconductor structure. Finally, Fig. (3.18) shows an analysis performed for the asymmetric well model regarding the difference between the barriers heights, $\Delta U = U_2 - U_1$ $(U_2 > U_1)$. Thus,

it was possible to determine that the proposed solution provides a relative error of less than 1% for the fundamental state, even in an unusual case when $\Delta U = 2.0$ eV.

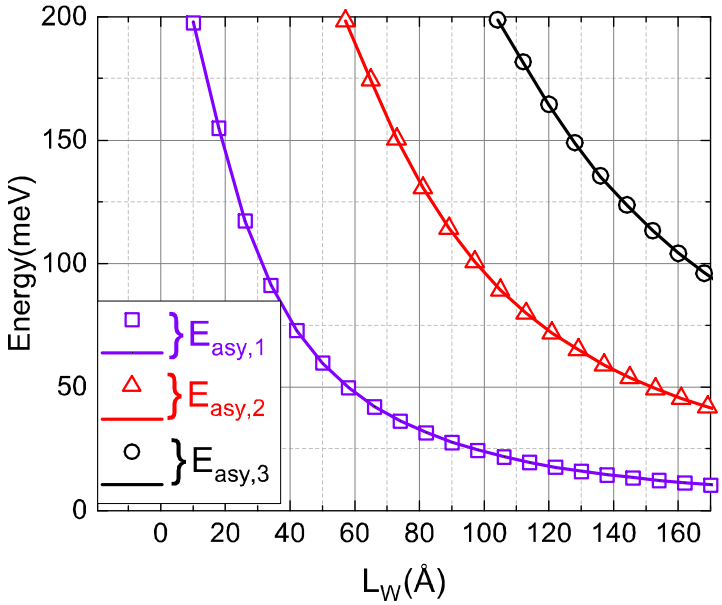

Figure 3.15: Energy levels $E_{asy,1}$, $E_{asy,2}$ and $E_{asy,3}$ as a function of L_w for the asymmetrical quantum well. Comparing our analytical expressions (solid lines) with numerical exact solutions (symbols), we obtain excellent agreement.

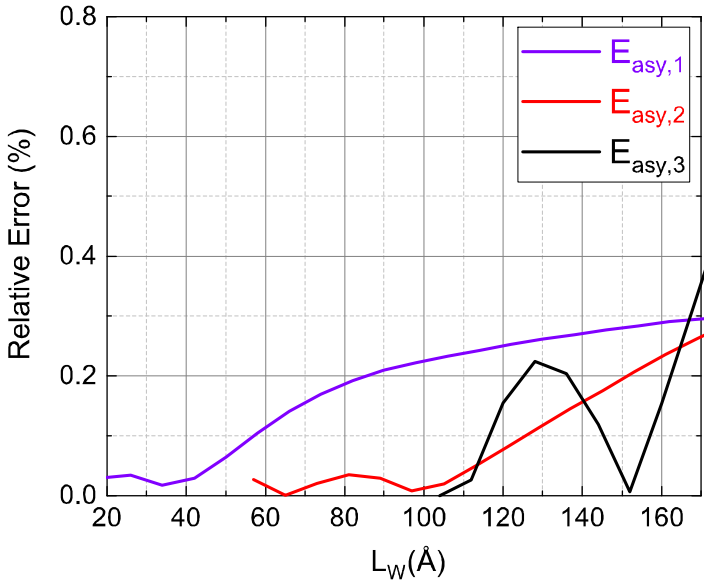

Figure 3.16: Relative errors of our proposed model with respect to the exact solution are smaller than 1% for energy levels $E_{asy,1}$, $E_{asy,2}$ and $E_{asy,3}$.

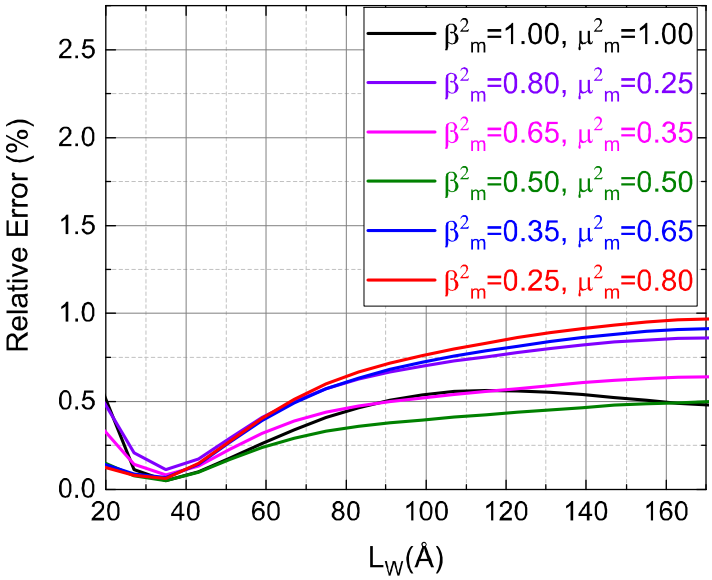

Figure 3.17: Evaluation of our proposed solution regarding the electron effective masses ratios between the potential barrier and the quantum well. This ratio is expressed by $\beta_m^2 = m_w^*/m_{b1}^*$ and $\mu_m^2 = m_w^*/m_{b2}^*$. Relative errors for the ground energy level, $n = 1$, for all evaluated values of β_m^2 and μ_m^2 are below 1%.

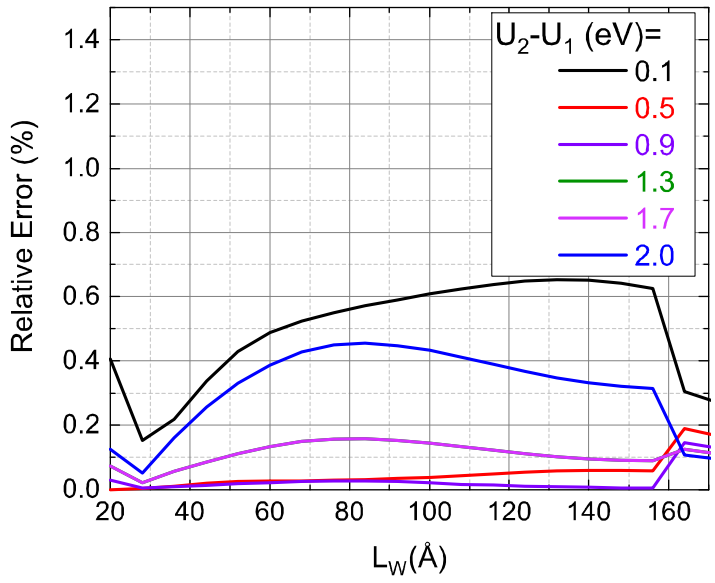

Figure 3.18: Evaluation of our proposed solution regarding difference in barriers height. For all evaluated values of $U_2 - U_1$ the relative error is below 1%.

3.5 Comparison Between Symmetric and Asymmetric Solutions

Concerning the accuracy of the model, an important question that arises is if the solution originally proposed for the symmetric well can be used for asymmetric well. To address this, we evaluate the relative error of the solution proposed for the symmetric quantum well employed in the asymmetric quantum well. Specifically, we evaluate the solution as a function of the quantum well width, for a set of the difference between the barriers heights ($\Delta U = U_2 - U_1$), the results are consolidated in Fig. (3.19).

As it can be seen from Fig. (3.19), for a quantum well with $L_w = 40$ Å and a small asymmetry of 0.2 eV, the relative error is higher than 10%. Therefore, depending on the accuracy level required and the amount of asymmetry, it is more advantageous to use the model proposed for asymmetric quantum well than the symmetric version.

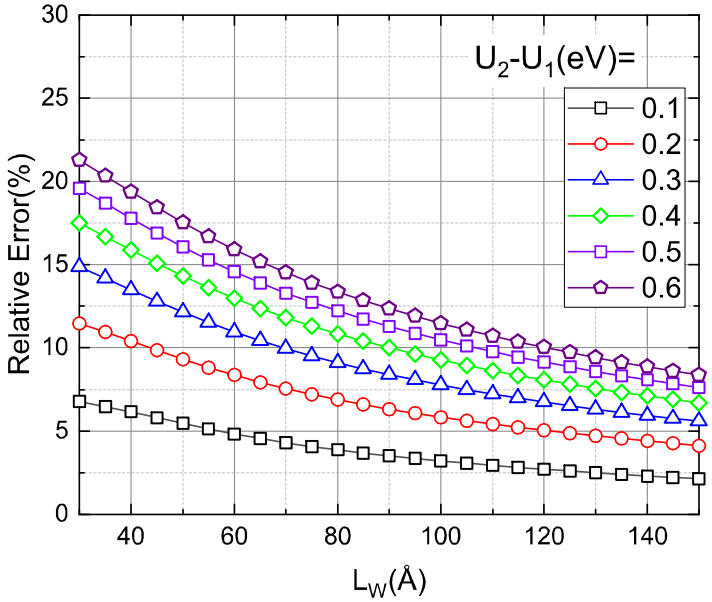

Figure 3.19: Evaluation of the solution proposed for the symmetric quantum well employed in the asymmetric quantum well, regarding difference in barriers height, $U_2 - U_1$.

In this Chapter, we presented a novel method to calculate energy levels in quantum wells, addressing requirements in semiconductor device compact modelling. Our approach is based on a Taylor series expansion technique around a variable optimized expansion point, obtained by mapping functions, to find the roots of transcendental equations. We highlight

that this approach is a general method that can also be applied in other problems involving transcendental equations. The Appendix contains a step-by-step tutorial with instructions on how to apply the method to solve other transcendental equations.

By using the analytical expressions for the position of the eigenenergies in the finite rectangular quantum well developed in this chapter, one can now develop then the Breit-Wigner expression in a purely analytical and explicit form.

The model described in this chapter is summarized in reference [80]. In addition, a different method for determining the energies of rectangular quantum wells was published at [81].

In the next chapter, we outline the charge transport dynamics in RTDs.

Chapter 4

Charge Transport in Resonant Tunneling Diodes

This chapter initially introduces the fundamentals of electronic transport dynamics in RTDs. Specifically, we highlighted the origin of the negative differential resistance (NDR) in the device. Next, the pioneering Tsu-Esaki transport formalism is outlined [31]. We also discuss the popular Schulman's empirical analytical model [82]- [83]. Finally, we discuss the relevant scattering mechanisms present in RTDs.

4.1 Introduction

Fundamentally, the RTD consists of a heterostructure forming a region of double potential barrier, as schematically illustrated in Fig. (4.1). The quantum well width is small enough so that to allow spatial quantization effects. Consequently, the electron momentum in the direction perpendicular to the potential barriers becomes quantized, producing a sequence of two-dimensional subbands associated with the eigenstates, $|\mathbf{k}\rangle$, in the quantum well region. Therefore, there is a two-dimensional (2D) density of states in the quantum well [51].

As illustrated in Fig. (4.1), the energy level E_1 corresponds to the lowest resonant energy level in the quantum well. As shown in Chapter 2, the transmission coefficient profile has a peak at E_1. In fact, the transmissivity is unitary when barriers are identical. In addition, there is a finite lifetime, τ_1, associated with this energy level. Consequently, E_1 has an associated

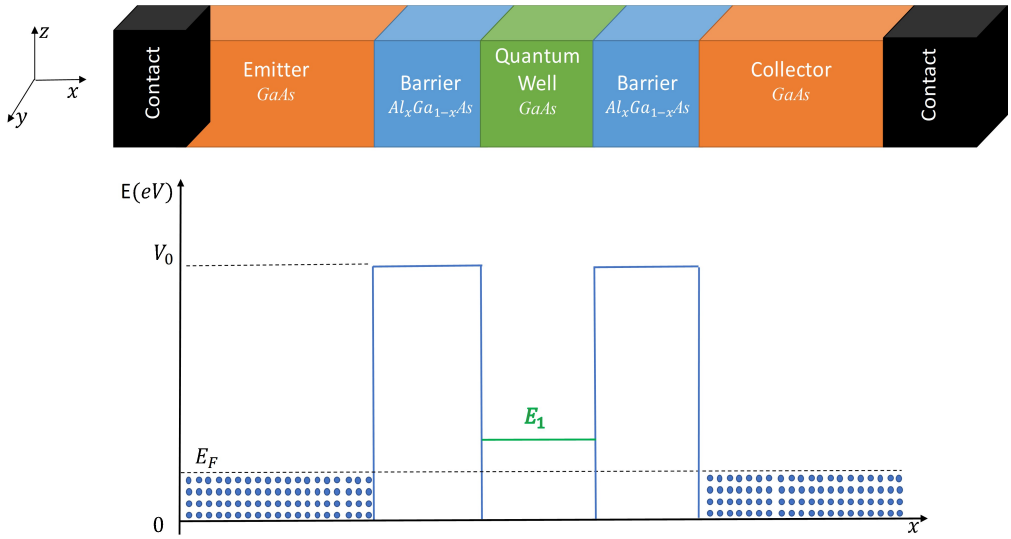

Figure 4.1: **Top:** Schematic illustration of the RTD layer structure. **Botton:** Schematic of the conduction band profile containing the double potential barrier region. E_F refers to the Fermi energy level.

resonance linewidth, Γ_1. The resonance linewidth is inversely proportional to the lifetime i.e. $\propto \hbar/\tau_1$ [53]. As seen earlier, depending on the geometrical parameters, the well can have higher energy levels with their respective resonance linewidths, Γ_i, where i accounts for the i–*th* subband.

As shown in Fig. (4.1), the double barrier structure is surrounded by layers of strongly doped (n-type) GaAs acting as low resistance emitter and collector contacts. With applied bias to the emitter and collector contacts, the emitter Fermi energy level is eventually aligned with the resonant energy level, E_1, in the well. Under this condition, a large current density flows through the barriers due to the increase in the transmission coefficient i.e., a greater number of electrons flow from the emitter region to the collector region. Under higher voltage conditions, the well resonant energy level is below the Fermi energy level, thereby suppressing the supply of electrons. As a result, a sharp decrease in current density occurs. In addition, as a direct consequence of increasing applied voltage, the NDR region emerges, as shown in the **I–V** curve in Fig. (4.3). Moreover, with more than one resonant energy level in the well, additional peak and valley regions will be present in the **I–V** characteristic curve [61].

The electron experiences a change in dimensionality when crossing the potential barriers. Specifically, the dimensionality changes from the three-dimensional state density (3D), in the emitter region, to the two-dimensional state density (2D), in the quantum well region, 3D→2D.

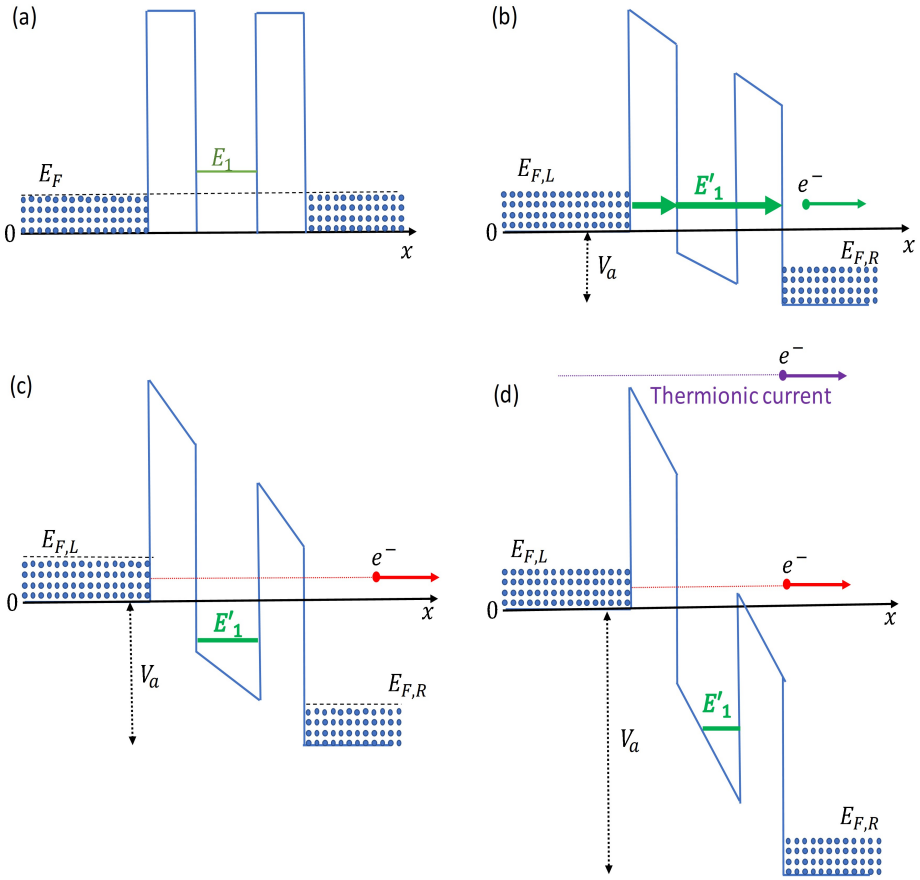

Figure 4.2: Conduction band profile of a typical RTD. Part (a) shows a schematic of the conduction band in absence of applied voltage and part (b) at the resonance condition. Part (c) illustrates the contribution of inelastic processes. Part (d) illustrates the off-resonance condition and the thermionic contribution to the current density.

To elucidate this mechanism, Fig. (4.4) contains a schematic illustration of the conduction band profile in the x-direction, in the absence of an applied bias. Also, Fig. (4.4) shows a schematic illustration of the emitter Fermi sphere in **k**-space, at low-temperature limit. In the equilibrium condition, as it can be seen in Fig. (4.4-b), the wave vector k_x is equal to k_1. In other words, the resonant energy level is outside of the emitter Fermi sphere. Therefore, in this condition, there is no resonant current through the potential barrier [51].

As discussed in Chapter 2, quantum tunneling occurs at resonant energy levels. In the example illustrated in Fig. (4.5-a), this process is indicated by the green arrow. As it can be noted, there is an emitter electron with kinetic energy E'_1 coincident with the resonant energy.

The resonant current is composed mainly of electrons with energy within the resonant en-

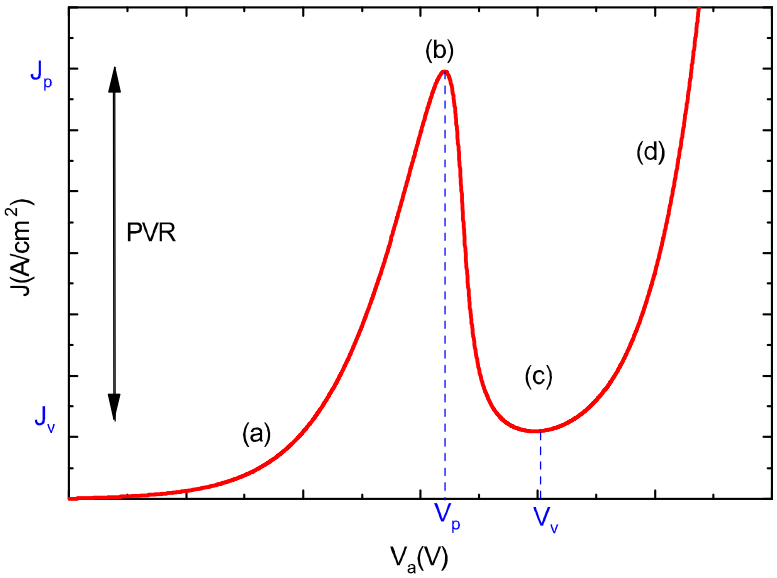

Figure 4.3: The **I–V** characteristic curve of a RTD. J_p and J_v are the peak and valley current density, respectively. V_p and V_v account for the peak and valley voltage positions, respectively. Additionally, it is possible to identify in the figure the corresponding regions, (a), (b), (c) and (d), illustrated in Fig. (4.2).

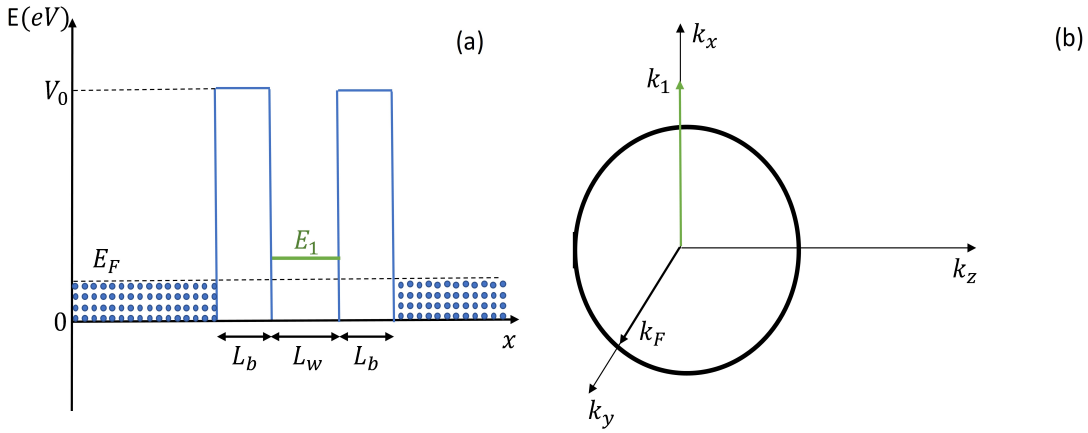

Figure 4.4: Part (a) shows the conduction band of an RTD in thermodynamic equilibrium. The resonant subband E_1 is illustrated in the well above the Fermi level. Part (b) shows the Fermi sphere of the emitter and the quantum well wavevector position, $k_x = k_1$. In this condition, ideally, there is no resonant current.

ergy width, Γ_1**.** Also, the resonant current is proportional to the disk area in **k**-space, Λ, which results from the intersection between the Fermi sphere with the plane parallel to the interface $x - y$, sectioning the sphere at the point $k_x = k_1'$. Thus, any electron with a parallel wave vector component obeying the relation: $k_{\|} \in \Lambda$ contributes to the resonant current density [51].

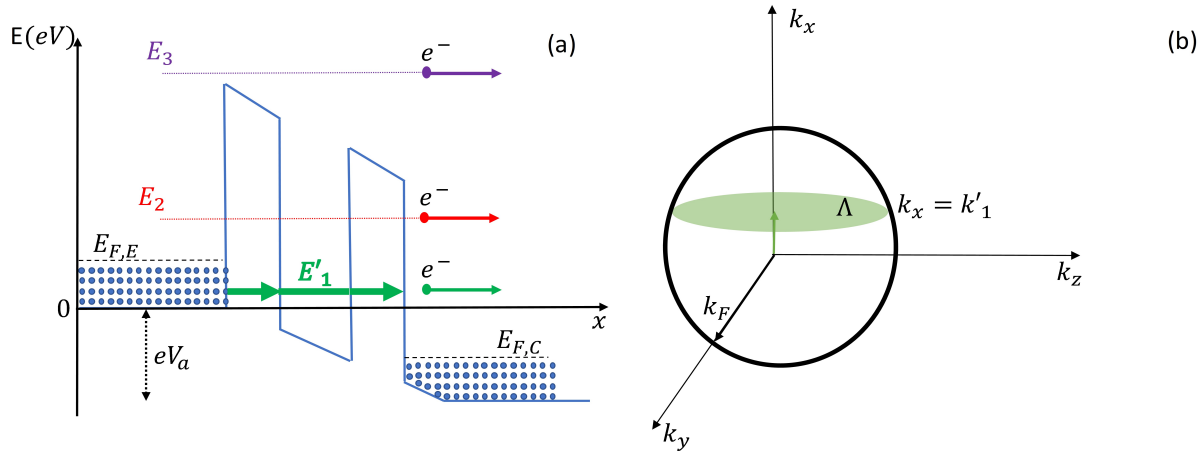

Figure 4.5: Part (a) shows the RTD conduction band under applied voltage V_a. Electrons with energy E'_1 (resonance energy under applied external voltage) tunnel through the resonant subband in the well. There is a slight possibility of electrons with energy E_2 tunnel through the potential barrier. Electrons can overcome the potential barrier by thermionic emission, process depicted by electrons with energy E_3. (b) shows the emitter Fermi sphere, sectioned by the plane parallel to the barriers at the point $k_x = k'_1$.

This process is illustrated in Fig. (4.5-b). In addition to the transport through resonant energy levels, other mechanisms also contribute to the current density. For instance, an electron with energy below the resonant level can absorb a phonon and, sequentially, tunnel through the resonant level [51], [53]. Similarly, an electron with initial energy greater than the resonant level can interact with the lattice vibration emitting a phonon and tunneling through the resonant level. Additionally, electrons with sufficiently high energy can overcome the potential barriers through thermionic emission, as it is also indicated in Fig. (4.5-a). Also, there is still a minor but non-zero probability that electrons with kinetic energy different from the resonant level can tunnel because of the broadening of resonant energy level. This mechanism has an important contribution to the valley current, by electrons with energy E_2, as illustrated in Fig. (4.5-a).

As argued by Luryi [32], during quantum tunneling the kinetic energy is conserved, leading to $E_{3D} = E_{2D}$ [32]. Fig. (4.6) contains a schematic illustration of the RTD conduction band and the density of state in each region.

Considering the effective mass approximation, the total electron energy, at the emitter contact, can be written as

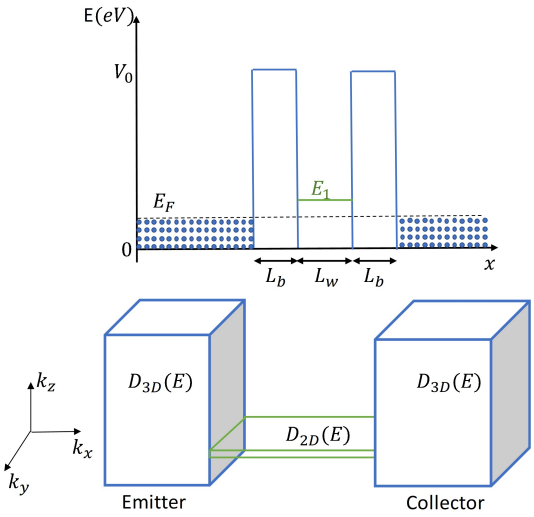

Figure 4.6: Top: A schematic illustration of the double potential barrier structure. Bottom: The figure shows the density of 3D states in the emitter and collector and the 2D density in the quantum well.

$$E_{3D} = E_C + \frac{\hbar^2 k_x^2}{2m_x^*} + \frac{\hbar^2 k_\parallel^2}{2m_\parallel^*}, \tag{4.1}$$

the plane wave vector, parallel to the barriers, is $k_\parallel = \sqrt{k_y^2 + k_z^2}$, where m_x^* is the electron effective mass in the x-direction. The $m_\parallel^*$ term refers to the electron effective mass in the parallel plane. The term E_C represents the bottom of the conduction band.

The total energy in the quantum well is given by

$$E_{2D} = E_n + \frac{\hbar^2 k_\parallel^2}{2m_\parallel^*}, \tag{4.2}$$

where E_n is the energy associated with the n-*th* subband in the quantum well. As discussed earlier, during quantum tunneling, there is a dimensionality reduction, but the electron tunneling do not perceive any potential change in the parallel y- and z-directions. In other words, the momentum in the parallel plane is conserved [32], [51]. However, the momentum in the x-direction, in the quantum well, is quantized.

For instance, consider E_1' (for $n = 1$ under applied bias), tunneling is only possible for electrons possessing momentum satisfying $k_x = k_1'$. Hence, by equating Eqs. (4.1) and (4.2), we have $k_1'^2 = 2m_w^*(E_1' - E_C)/\hbar^2$. Therefore, for $E_C = E_1'$, corresponding to $k_1' = 0$, the electric current density reaches its maximum value [51].

Carrier scattering mechanisms arise from crystal lattice vibrations, impurities, interface roughness, and carrier-carrier interactions. Thus, many scattering events can take place during the tunneling process. Also, impurities in the quantum well can generate additional states in the well, working as traps for the conducting electrons, thereby affecting the **I–V** characteristics. Finally, in addition to the processes described above, there are also the hysteresis effects caused by the intrinsic and extrinsic bistability of the device. These processes can significantly affect device properties, making it difficult to develop a model to accurately reproduce experimental data [51].

One of the first experimental investigations of resonant tunneling in double barrier semiconductor heterostructure was carried out by Chang, Esaki and Tsu, in 1974 [84]. When investigating an RTD device formed by the GaAs/$Al_{0.7}Ga_{0.3}As$ material system, the authors observed small peaks in the output current around the quantum well eigenenergies position, characterizing the resonant tunneling process [84]. However, the investigation was conducted under a low-temperature regime. The difficulty in clearly observing the NDR in RTDs, as compared with Esaki diodes, is due to the challenge in achieving low concentrations of unwanted impurities with the technology available at that time. Only after the 1980s, the quality of epitaxial growth improved significantly, making it possible to observe resonant tunneling in epitaxial layers of the III-V materials group.

For most applications, NDR devices should have a high peak current and a low valley current. Therefore, a figure of merit for RTDs is the peak-to-valley current ratio (PVCR), which is the relation between the resonance peak current and the valley current, as illustrated in Fig. (4.3).

In this context, one of the first observations of the NDR region in RTD, at room temperature, was reported in 1985 [85]- [87], for a device composed of GaAs/AIGaAs heterojunctions. For this device, an approximate PVCR of 4:1 was measured. With the maturing of the epitaxial growth technology, it was possible to manufacture devices with better performance, such as using the InGaAs/AlAs material system [88], where the PVCR is in the order of 30:1 at room temperature and 60:1 at cryogenic temperature [89]. Additionally, resonant tunneling has also been observed in many other material systems, e.g., GaAsP/GaAs [90], InP/InGaAs [91], p-type GaAs/AIGaAs [92], AlSb/lnAs [93], HgTe/HgCdTe [94], Si/Ge_xSi_{1-x} [95]- [96], amorphous

a-Si/SbN, [97], AlGaN/GaN [98], Graphene Nanoribbon RTDs [99]- [100] and, more recently, GaN/AlN [101].

4.2 Quantization in RTDs

For the semiconductor heterostructure present in RTDs, one can describe the conduction band quantization by solving the three-dimensional Schröedinger equation given by

$$\hat{\mathbf{H}} \left| \Psi(x,y,z) \right\rangle = E \left| \Psi(x,y,z) \right\rangle , \tag{4.3}$$

where $|\Psi(x,y,z)\rangle$ is the eigenstate of the system wave function and $\hat{\mathbf{H}}$ is the Hamiltonian operator written in terms of the kinetic energy operators $\mathbf{K}$, and the electron potential $\mathbf{V}$, as $\hat{\mathbf{H}} \equiv \mathbf{K} + \mathbf{V}$ [1]. Assuming quantization in the x-direction, one can write

$$\left[-\frac{\hbar^2}{2} \frac{\partial}{\partial x} \frac{1}{m^*(x)} \frac{\partial}{\partial x} - \frac{\hbar^2}{2m_{\|}^*} \nabla_{\mathbf{r}}^2 + V_{ef}(x) \right] \Psi(\mathbf{r}, x) = E \Psi(\mathbf{r}, x) , \tag{4.4}$$

where $m^*(x)$ is the electron effective mass in the x-direction, perpendicular to the interface while $m_{\|}^*$ represents the electron effective mass parallel to the interface. The term $\mathbf{r}$ is the position vector parallel to the interface and $\Psi(\mathbf{r}, x)$ is the wave function.

Assuming $\Psi(\mathbf{r}, x)$ varies slowly with respect to the dimensions of the crystal unit cell, the eigenvalues of the Hamiltonian operator are the system energy levels [53]. Then, assuming an parabolic energy approximation, we can write $m^*(x)$ as a constant m_x^*:

$$\frac{1}{m_x^*} = \frac{1}{\hbar^2} \frac{\partial^2 E(k_x)}{\partial k_x^2}. \tag{4.5}$$

In Eq. (4.4) $V_{ef}(x)$ is the approximate effective potential, considering the isotropic crystal and ignoring the stress at the heterostructure interface, we have

$$V_{ef}(x) = \frac{\Delta E_c(x)}{e} - V(x) + V_{xc}(x) , \tag{4.6}$$

where ΔE_C is the discontinuity in the conduction band caused by the joining of materials with different bandgaps, and $V(x)$ is the Hartree term. The exchange correlation term among the free carriers is $V_{xc}(x)$ [53].

The Poisson equation is given by

$$\frac{d}{dx}\left(\kappa\left(x\right)\frac{d}{dx}\right)V\left(x\right)=\frac{\rho\left(x\right)}{\epsilon_0}, \tag{4.7}$$

where $\kappa\left(x\right)$ is the dielectric constant as a function of the position and $\rho\left(x\right)$ is the charge density in the structure.

Assuming that the variation of the electric potential occurs only in the x-direction, it is possible to solve Eq. (4.4) using the method of separation of variables. To do so, one can write $\Psi\left(\mathbf{r},x\right)=\Theta(\mathbf{r})\Upsilon(x)$, considering $\Theta(\mathbf{r})$ as a plane wave:

$$\Psi\left(\mathbf{r},x\right)=\Theta(\mathbf{r})\Upsilon(x)=\frac{1}{\sqrt{A}}e^{i\mathbf{k}_{\parallel}\cdot\mathbf{r}}\Upsilon_n(x), \tag{4.8}$$

where A is the normalization factor obtained by

$$\langle\Theta(\mathbf{r})|\Theta(\mathbf{r})\rangle=\int_{-\infty}^{+\infty}\Theta^*(\mathbf{r})\Theta(\mathbf{r})d^2\mathbf{r}=1. \tag{4.9}$$

In the x-direction the one-dimensional Schrödinger equation is

$$\left[-\frac{\hbar^2}{2m_x^*}\frac{d^2}{d^2x}+V_{ef}(x)\right]\Upsilon(x)=E_n\Upsilon(x), \tag{4.10}$$

we can write the total kinetic energy as

$$E_{n,\,k_{\parallel}}=E_n+\frac{\hbar^2k_{\parallel}^2}{2m_{\parallel}^*}.$$

As usual, the density of ionized donors is given by

$$N_d^+(x)=\frac{N_d(x)}{1+g.e^{(E_F-E_d)/k_BT}}, \tag{4.11}$$

where $N_d(x)$ represents the density of impurities donors and g accounts for the degeneracy factor. For fermions, by the Pauli exclusion principle, we have $g=2$. Also, E_d is the donor energy level, E_F is the Fermi energy level and k_B is the Boltzmann constant. The electron density can be found through the relation

$$n_i=\int_0^{\infty}D\left(E\right)f\left(E\right)dE, \tag{4.12}$$

where $D(E)$ is the density of states and $f(E)$ represents the Fermi-Dirac statistics:

$$f(E) = \frac{1}{1 + \exp\left[\left(E - E_F\right)/k_B T\right]}, \tag{4.13}$$

for a two-dimensional system, the density of states is given by

$$D(E) = \frac{m_{\|}^*}{\pi\hbar^2}, \tag{4.14}$$

replacing Eqs. (4.13) and (4.14) in Eq.(4.12), one obtain

$$n_i = \frac{m_{\|}^*}{\pi\hbar^2}\int_{E_i}^{\infty} \frac{1}{1 + \exp\left[\left(E - E_F\right)/k_B T\right]} dE. \tag{4.15}$$

Thus, for quantized heterostructures once the subbands have been determined, the free electron density distribution $n(x)$ can be calculated through the expression

$$n(x) = \sum_i \Upsilon_i^*(x)\Upsilon_i(x)n_i = \sum_i \left|\Upsilon_i(x)\right|^2 n_i, \tag{4.16}$$

replacing Eq. (4.15) in Eq.(4.16), yields

$$n(x) = \frac{m_{\|}^*}{\pi\hbar^2} k_B T \sum_i \left|\Upsilon_i(x)\right|^2 \ln\left[1 + \exp\left(\left(E_F - E_i\right)/k_B T\right)\right], \tag{4.17}$$

The charge density can then be written as

$$\rho(x) = -e\left(N_d^+(x) - N_a^-(x) - n(x) + p(x)\right), \tag{4.18}$$

where e is the electron elementary charge, $N_a^-(x)$ is the ionized acceptors density, $n(x)$ is the free electrons density, given by Eq. (4.16), and $p(x)$ the hole density. In the n-type devices investigated in this work, we can neglect $p(x)$, since it is very small compared to the other charges in Eq. (4.18). Additionally, the energy in the i-*th* subband E_i, and its respective wave functions $\Upsilon_i(x)$ are obtained by solving Eq. (4.4). Therefore, the Schrödinger and Poisson equations form a system of coupled differential equations, which is usually solved self-consistently.

However, in this work, to obtain an analytical model, we assume a low charge density in the quantum well region. Thus, we neglect the Hartree, $V(x)$, and the correlation, $V_{xc}(x)$, electric potential terms. With these considerations, determining the eigenenergies in the finite quantum well becomes a one-dimensional problem already addressed in Chap. (3), where an original analytical solution is provided.

4.3 Tsu-Esaki Carrier Transport Formalism [31]

This section describes the pioneering current density formalism proposed by Tsu-Esaki in 1973 in [31]. Originally, the authors considered a finite superlattice formed of N potential barriers composed by the GaAs/$Al_{0,5}Ga_{0,5}$As heterostructure [31]. In this formalism, the coherent transverse transport of electrons is considered, i.e., it is assumed that the electron coherence length is of the order of the structure width, including the barriers. Thus, it is considered that the electron traverses the potential barriers without loss of phase coherence (purely elastic collisions) [31]. Additionally, in the Tsu-Esaki formalism, the following considerations and simplifications are assumed [31], [58]:

1. Conservation of transverse momentum during tunneling;
2. Electric field evenly distributed in the structure;
3. Space charge formation across the structure is negligible;
4. The existence of load sources or sinks along the structure is disregarded;
5. Effective mass approximation;
6. Current density is composed of electrons;
7. Rectangular potential barriers;

For the RTD illustrated in Fig. (4.1), as discussed previously, it is possible that electrons in the emitter region tunnel into the collector region through the double barrier. Likewise, there is a possibility that electrons in the collector can tunnel into the emitter region through the barriers. Considering the effective mass approximation, one can write

$$E\left(\mathbf{k}\right)=\frac{\hbar^2\left|\mathbf{k}\right|^2}{2m^*}\equiv\frac{\hbar^2k_x^2}{2m_x^*}+\frac{\hbar^2k_y^2}{2m_y^*}+\frac{\hbar^2k_z^2}{2m_z^*},$$

where the wave vector is $\mathbf{k}=k_x\mathbf{x}+k_y\mathbf{y}+k_z\mathbf{z}$. As discussed in the section (4.1), the conservation of the parallel moment is assumed. Then, one can write $\mathbf{k}_{\|}=\mathbf{k}_r=k_y\mathbf{y}+k_z\mathbf{z}$. Taking the bottom of the conduction band as a reference ($E_C=0$), the total kinetic energy can be written as

$$E\left(\mathbf{k}\right) = E_x + E_{\parallel} = \frac{\hbar^2 k_x^2}{2m_x^*} + \frac{\hbar^2 k_{\parallel}^2}{2m_{\parallel}^*}, \tag{4.19}$$

The current density in the RTD can be written as the difference between the current density flowing from the emitter to the collector, $J_{L\to R}$ and the current density from collector to emitter, $J_{R\to L}$. Thus, the current density in the RTD is

$$J = J_{L\to R} - J_{R\to L}.$$

Taking into account the perpendicular velocity of the electron, v_x, the transmission probability coefficient $\mathbf{T}$, the density of states (DOS) in the emitter and collector and the Fermi-Dirac distribution, $f\left(\mathbf{k}\right)$, one can write

$$\begin{aligned} dJ_{L\to R} &= -ev_x\left(\mathbf{k}\right) D_L(k_x)\mathbf{T}(k_x, V_a) f_L\left(\mathbf{k}\right)\left(1 - f_R\left(\mathbf{k}\right)\right)dk_x, \\ dJ_{R\to L} &= -ev_x\left(\mathbf{k}\right) D_R(k_x)\mathbf{T}(k_x, V_a) f_R\left(\mathbf{k}\right)\left(1 - f_L\left(\mathbf{k}\right)\right)dk_x, \end{aligned} \tag{4.20}$$

where the terms $\left(1 - f_R\left(\mathbf{k}\right)\right)$ and $\left(1 - f_L\left(\mathbf{k}\right)\right)$ represent the number of states available in the collector and emitter, respectively.

The density of states $D(k_x)$ is given by

$$D(k_x) = \int_0^{\infty}\int_0^{\infty} D(k_x, k_y, k_z)dk_y dk_z, \tag{4.21}$$

where $D(k_x, k_y, k_z)$ is the three-dimensional density of states in k-space. For simplicity, consider the free electron in a cube of side L, thus, the quantization steps for the three directions are

$$\delta k_x = \delta k_y = \delta k_z = \frac{2\pi}{L},$$

in k-space, the 3-D density of states can be written as

$$D(k_x, k_y, k_z) = 2\frac{1}{\delta k_x \delta k_y \delta k_z}\frac{1}{L^3} = \frac{2}{\left(2\pi\right)^3}, \tag{4.22}$$

where the factor 2 in Eq. (4.22) accounts for the Pauli exclusion principle.

The group velocity of electrons in the semiconductor can be written as $\mathbf{v}_g(\mathbf{k}) = \frac{1}{\hbar}\boldsymbol{\nabla}_k E(\mathbf{k})$. For the one-dimensional case, the velocity x-direction is

$$v_x(\mathbf{k}) = \frac{1}{\hbar}\frac{\partial E(\mathbf{k})}{\partial k_x} = \frac{1}{\hbar}\frac{\partial}{\partial k_x}\left(\frac{\hbar^2 k_x^2}{2m_x^*}\right) = \frac{\hbar k_x}{m_x^*}, \tag{4.23}$$

in addition, one can take advantage of the relation: $v_x dk_x = \frac{1}{\hbar}dE_x$. Then, one can write Eq. (4.20) as

$$dJ_{L\to R} = -e\int_0^\infty\int_0^\infty \frac{2}{(2\pi)^3}dk_y dk_z \mathbf{T}(E_x, V_a) f_L(\mathbf{k})\left(1 - f_R(\mathbf{k})\right)\frac{1}{\hbar}dE_x, \tag{4.24}$$

$$dJ_{R\to L} = -e\int_0^\infty\int_0^\infty \frac{2}{(2\pi)^3}dk_y dk_z \mathbf{T}(E_x, V_a) f_R(\mathbf{k})\left(1 - f_L(\mathbf{k})\right)\frac{1}{\hbar}dE_x, \tag{4.25}$$

rearranging

$$dJ_{L\to R} = -\frac{e}{4\pi^3\hbar}\int_0^\infty\int_0^\infty \mathbf{T}(E_x, V_a) f_L(E)\left(1 - f_R(E)\right)dE_x dk_y dk_z,$$

$$dJ_{R\to L} = -\frac{e}{4\pi^3\hbar}\int_0^\infty\int_0^\infty \mathbf{T}(E_x, V_a) f_R(E)\left(1 - f_L(E)\right)dE_x dk_y dk_z.$$

The total current density is

$$\begin{aligned} J &= J_{L\to R} - J_{R\to L} = -\frac{e}{4\pi^3\hbar}\int_0^\infty \mathbf{T}(E_x, V_a)dE_x \int_0^\infty\int_0^\infty f_L(E)\left(1 - f_R(E)\right)dk_y dk_z + \\ &+\frac{e}{4\pi^3\hbar}\int_0^\infty \mathbf{T}(E_x, V_a)dE_x \int_0^\infty\int_0^\infty f_R(E)\left(1 - f_L(E)\right)dk_y dk_z, \end{aligned}$$

finally, rearranging

$$J = \frac{e}{4\pi^3\hbar}\int_0^\infty \mathbf{T}(E_x, V_a)dE_x \int_0^\infty\int_0^\infty \left[f_L(E) - f_R(E)\right]dk_y dk_z. \tag{4.26}$$

The integration in energy E_x goes from 0 to ∞ because electron tunneling below the bottom of the conduction band falls into the bandgap. In addition, the tunneling is considered to be symmetric, accordingly, $\mathbf{T}(E_x)$ is the same for left-to-right as well as right-to-left incident electrons.

Starting by making a change of coordinates, from Cartesian to Polar, and knowing that $k_{\parallel}dk_{\parallel} = \frac{m_{\parallel}^{*}}{\hbar^2}dE_{\parallel}$, one can write

$$\begin{aligned}\int_0^{\infty}\int_0^{\infty}\left[f_L\left(E\right)-f_R\left(E\right)\right]dk_y dk_z &= \int_0^{\infty}\int_0^{2\pi}\left[f_L\left(E\right)-f_R\left(E\right)\right]k_{\parallel}dk_{\parallel}d\phi, \\ &= 2\pi\frac{m_{\parallel}^{*}}{\hbar^2}\int_0^{\infty}\left[f_L\left(E\right)-f_R\left(E\right)\right]dE_{\parallel}.\end{aligned} \tag{4.27}$$

Combining Eq. (4.27) and Eq. (4.26), yields:

$$\begin{aligned}J &= \frac{em_{\parallel}^{*}}{2\pi^2\hbar^3}\int_0^{\infty}\mathbf{T}(E_x,V_a)\left[\int_0^{\infty}\left[f_L\left(E\right)-f_R\left(E\right)\right]dE_{\parallel}\right]dE_x, \\ J &= \frac{em_{\parallel}^{*}}{2\pi^2\hbar^3}\int_0^{\infty}\mathbf{T}(E_x,V_a)\left[\int_0^{\infty}f_L\left(E\right)dE_{\parallel}-\int_0^{\infty}f_R\left(E\right)dE_{\parallel}\right]dE_x,\end{aligned} \tag{4.28}$$

for the emitter and collector, the Fermi-Dirac statistic is $f_L\left(E\right)$ and $f_R\left(E\right)$, respectively, being described as:

$$f_L\left(E\right) = \frac{1}{1+\exp\left[\left(E_x+E_{\parallel}-E_F\right)/k_BT\right]}, \tag{4.29}$$

$$f_R\left(E\right) = \frac{1}{1+\exp\left[\left(E_x+E_{\parallel}-\left(E_F-eV_a\right)/k_BT\right]\right.}, \tag{4.30}$$

knowing that

$$\int\frac{dy}{1+\exp\left(y\right)} = \ln\left(\frac{1}{1+\exp\left(-y\right)}\right)+K_0,$$

one gets

$$\int_0^{\infty}f_L\left(E\right)dE_{\parallel} = k_BT\ln\left[1+\exp\left(\left(E_F-E_x\right)/k_BT\right)\right], \tag{4.31}$$

$$\int_0^{\infty}f_R\left(E\right)dE_{\parallel} = k_BT\ln\left[1+\exp\left(\left(E_F-E_x-eV_a\right)/k_BT\right)\right], \tag{4.32}$$

where K_0 is an arbitrary constant. Substituting Eqs. (4.31) and (4.32) in Eq. (4.28) and performing some algebraic manipulations, finally, one obtains the Tsu-Esaki current expression [31]:

$$J = \frac{em_{\parallel}^{*}k_BT}{2\pi^2\hbar^3}\int_0^{\infty}\mathbf{T}(E_x,V_a)\ln\left[\frac{1+\exp\left(\left(E_F-E_x\right)/k_BT\right)}{1+\exp\left(\left(E_F-E_x-eV_a\right)/k_BT\right)}\right]dE_x. \tag{4.33}$$

Originally, Tsu and Esaki used the transfer matrix method to calculate the transmission coefficient $\mathbf{T}(E_x, V_a)$ for the N-barriers case. Therefore, in principle, the current density in the Tsu-Esaki formalism must be calculated numerically. Also, when proposed, the formalism of Tsu and Esaki [31] did not consider the difference in the effective mass of the electron in the different semiconductor layers, barriers and the well. Such analysis was carried out later, in 1998, by Schulman in [83].

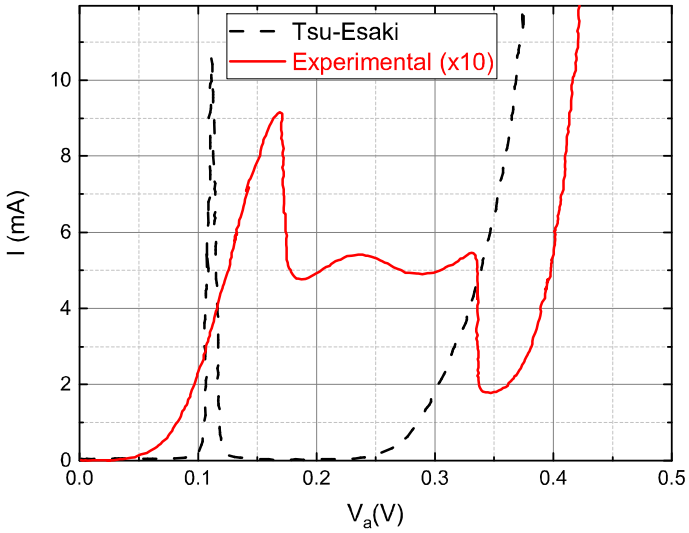

Figure 4.7: I-V curve obtained experimentally and numerically by using the formalism of Tsu and Esaki [31], for a double potential barrier RTD, with $L_b = 85$ formed by the alloy $Al_{0,35}Ga_{0,65}As$, and the quantum well formed by GaAs with $L_w = 50$ measurements, the curves were obtained with $T = 77$ K [102]

Fig. (4.7) shows a comparison between the I-V curve obtained experimentally [102] and by the Tsu and Esaki formalism for a double potential barrier RTD. The $Al_{0.35}Ga_{0.65}As$ barriers have a width of 85 Å, while the GaAs quantum well is 50 Å wide. The curves were obtained at 77 K [102]. As it can be seen, there is no agreement between the current density calculated from the Tsu-Esaki model and the experimental curve. The peak and the valley voltage bias and the PVRC do not agree with the experimentally measured values. The peak and valley current density calculated using the Tsu-Esaki model is ten times higher for the measured peak and

three times smaller for the measured valley [102]. This discrepancy is because the model does not take into account the inelastic phonon scattering mechanisms present in RTDs, and the accumulation and depletion regions formed in the emitter and collector regions, respectively. [103]. Additionally, in the experimental curve, it can be noticed a voltage range where the increase of the applied voltage does not cause significant variation in the current density, appearing as a "shoulder," a plateau. This effect is mainly due to the intrinsic and extrinsic bistability present in bulk RTDs [104] - [106]. Finally, the Tsu-Esaki original model also fails because it does not consider the voltage drop in the GaAs well region, assuming a constant voltage drop in the barrier region. Thus, the model erroneously predicts the first resonance peak at $eV_a = 2E_1$ [31].

The Tsu-Esaki model correctly predicts the general shape of the **I–V** curve, encompassing the current peak and valley and, consequently, the NDR range. However, due to the simplifications and approximations assumed, it completely fails to describe the current density in real RTD devices [58]. Several models have been proposed in the literature to address these inaccuracies [51]. Among these, models modifying the Tsu-Esaki formalism to derive analytical expressions as well as models based in numerical approaches.

In general, numerical models can take into account effects generally neglected in analytical models, such as inelastic scattering effect, non-parabolicity of the band diagram, space-charge builf-up, self-consistent calculations, interface traps, among other considerations [51]. Among the numerical models found in the literature one can mention models based on non equilibrium Green's function (NEGF) [107]- [109], Wigner transport equation [110]- [112], Bhom's formalism [113] and method based on the R-matrix formalism [114]. Among the models mentioned, those that present lower computational effort albeit still providing excellent agreement with experimental data are the models based on the NEGF formalism and the R-matrix, since, in general, the Wigner-Eisenbud [115], and Bhom formalisms rely on Monte-Carlo techniques [112].

In this context, G. Klimeck, using NEGF, developed a device simulator called NEMO (Nano Electronics Modeling Tools) capable of describing the **I–V** characteristics of nanodevices [**?**]. The nanoHUB.org [116] is an OpenSource tool that employs a free NEMO version. The site provides free nanoscale transport simulation programs that run in the cloud and are accessible through a standard web browser [116]. In addition to NEMO, there are commercial TCAD (Technology Computer-Aided Design) platforms for simulating quantum devices, such as Sen-

taurus from Synopsis® and Atlas from Silvaco® [117]. These tools are very useful for validating compact analytical models.

Numerical simulations accurately describe the physical behavior of manometric scale devices [51]. However, it is necessary to deal with the complexity of numerical codes, very long simulation times and stringent requirements for memory storage and computational capacity. In addition, the results are often difficult to interpret.

For engineering purposes, compact analytical models are desired, as they capture the most relevant physical mechanisms governing the carrier transport in quantum devices, in a simple and fast way, being a useful tool for circuit design. In this regard, most models are focused on SPICE implementations, therefore relying on purely empirical fitting parameters [118]- [122]. They are essentially behavioral device models, suitable for circuit simulation but unable to predict the relationship between the RTD layer structure and its electrical output characteristics, a crucial step for device optimization. Such predictive capability is the domain of physics-based models. However, the literature concerning physics-based models for RTDs is quite limited. Indeed, the most well-known physics-based analytical model for the **I–V** characteristics of RTDs is the model proposed by Schulman and co-workers [82], which was recently revisited by [123]. The next section describes the analytical formula for current density in double potential barrier RTDs proposed by Schulman [82].

4.4 Schulman's Model [82]

In 1986, Coon and Liu [124], proposed a model, based on the Tsu-Esaki formulation, for the negative resistance at the temperature limit 0 K. Later, in 1993, Chang *et al.* [118], starting from the expression proposed by Coon and Liu, replaced the original physical parameters by fitting parameters, which allowed to extend the formalism to cover room temperatures. In 1995, Yan *et al.* [120], proposed a fully empirical model in which the **I–V** curve characteristic of the RTD is divided into three parts: before the peak voltage, from the peak voltage to the valley voltage and beyond the valley voltage. Yan *et al.* model is completely empirical, not based on device physics. Finally, in 1996, Schulman proposes to modify the Coon and Liu model, including the essential characteristics of non-zero temperature and the Fermi-Dirac statistic. In

the article [82] Schulman derives an analytical expression for the voltage-current characteristic of the RTD based on Tsu-Esaki formalism [82].

Schulman starts by proposing to compute the transmission coefficient $\mathbf{T}(E_x, V_a)$, originally calculated using MMT, by using the Breit-Wigner approximation (derived in Chapter 2)

$$\mathbf{T}(E_x, V_a) = \frac{(\Gamma_n/2)^2}{(\Gamma_n/2)^2 + (E_x - E_n)^2}, \tag{4.34}$$

where Γ_n and E_n accounts for the n–*th* level resonance linewidths and resonant energy in the well, respectively.

Calculations show that Γ_n is of the order of a few meV, even for thin barrier widths [125], which is much less than k_BT for room temperature. Schulman noticed that, for small Γ_n, the transmission coefficient becomes negligible, except when the kinetic energy E is close to the resonant level E_n. Thus, Schulman proposed the approximation $E_x = E_n - eV_a/2$. In doing so, the logarithmic term in Eq. (4.33) can be placed outside the current integral to provide:

$$J = \frac{em_{\parallel}^* k_B T \Gamma_n}{4\pi^2\hbar^3} \ln\left[\frac{1+\exp\left(\left(E_F - E_n + eV_a/2\right)/k_BT\right)}{1+\exp\left(\left(E_F - E_n - eV_a/2\right)/k_BT\right)}\right]\left[\frac{\pi}{2} + \arctan\left(\frac{E_n - \frac{eV_a}{2}}{\Gamma_n/2}\right)\right]. \tag{4.35}$$

Schulman states that the Eq. (4.35) contains device parameters which can be used as fitting parameters. To fit with experimental data, Schulman proposed:

$$J_1(V_a) = A \ln\left[\frac{1+\exp\left(\left(B - C + n_1 eV_a\right)/k_BT\right)}{1+\exp\left(\left(B - C - n_1 eV_a 2\right)/k_BT\right)}\right]\left[\frac{\pi}{2} + \arctan\left(\frac{C - n_1 eV_a}{D}\right)\right], \tag{4.36}$$

where the physical parameters in Eq. (4.35) are replaced by fitting parameters:

$$\frac{em_{\parallel}^* k_B T \Gamma_n}{4\pi^2\hbar^3} \Rightarrow A,\ E_F \Rightarrow B,\ E_n \Rightarrow C, \text{ and } \Gamma_n/2 \Rightarrow D$$

Eq. (4.36) accounts for the resonant peak current, but it is not capable to reproduce the exponential part of the **I–V** characteristics. To address this problem, an additional term based on conventional diode current-voltage equation is added to Eq. (4.36):

$$J_2(V_a) = H\left(e^{n_1 eV_a/k_BT} - 1\right).$$

Then, Schulman's final expression becomes $J(V_a) = J_1(V_a) + J_2(V_a)$:

$$J(V_a) = A \ln\left[\frac{1+\exp\left(\left(B-C+n_1 eV_a\right)/k_BT\right)}{1+\exp\left(\left(B-C-n_1 eV_a 2\right)/k_BT\right)}\right] \times \\ \times\left[\frac{\pi}{2}+\tan^{-1}\left(\frac{C-n_1 eV_a}{D}\right)\right] + H\left(e^{n_2 eV_a/k_BT}-1\right). \tag{4.37}$$

where H, n_1 and n_2 are fitting parameters.

We should point out that the expression is originally not fully analytical since the resonant energy levels are computed numerically. Additionally, Schulman assumed that quantum tunneling is purely coherent, which is not true in realistic devices. Furthermore, Schulman admitted that the resonant energy levels drop by half the applied voltage ($E_n - eV_a/2$), which is also not always valid, mainly due to the space charge regions. Despite this, the expression derived by Schulman provides the correct lineshape of the resonant current-voltage characteristic.

In [82], Schulman contrasts the model with the experimental results from a RTD composed by the undoped $In_{0.53}Ga_{0.47}As$/AlAs hetrostructure with barrier width of 26 Å, quantum well width of 48 Å and spacer layers of 265 Å. Fig. (4.8) shows a schematic illustration of the RTD considered by Schulman in [82].

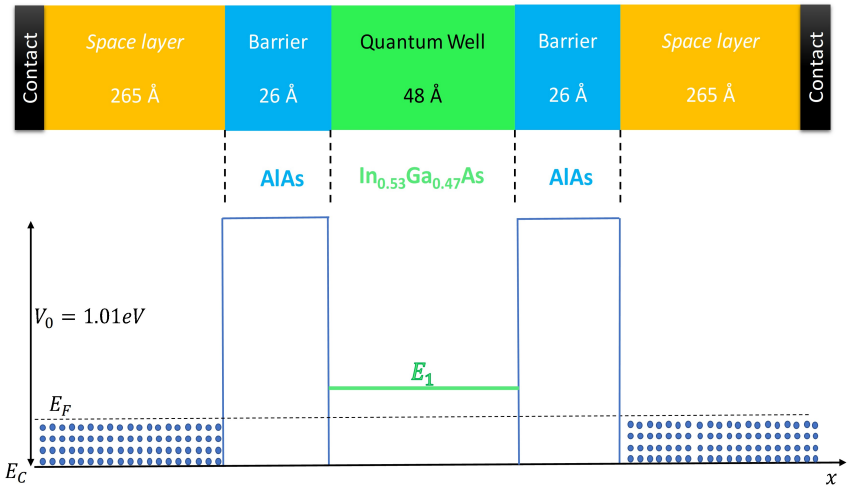

Figure 4.8: Schematic illustration of the device investigated by Schulman in [82].

Fig. (4.9) shows the experimental current density compared to the result provided by the Schulman model. In particular, the fitting parameters used in this validation are; $A = 10^4$, $B = 0.035$, $C = 0.1472$, $D = 0.0052$, $n_1 = 0.115$, $H = 0.1411$ and $n_2 = 0.1201$. As it can be

seen in Fig. (4.9), there is a good agreement. The plateau present in the experimental curve is associated with intrinsic and the extrinsic bistability of the RTD, not modeled by the theoretical Schulman formalism.

Schulman's model, despite based on a compact parametric equation, suitable for a circuit simulator, is composed of several fitting parameters not totally based on physical parameters. Therefore, its accuracy depends on the adjustment of these parameters against the measured data. The work described in [82] is certainly technically sound in terms of the physics of the RTD. However, it can still be considered semi-emprical, since it relies on seven fitting parameters, which have a clear physical meaning but are allowed to vary in order to match theory and experiment. Also, there is no direct correspondence between the model parameters and the device structure regarding the layer thicknesses and compositions, doping levels, etc.

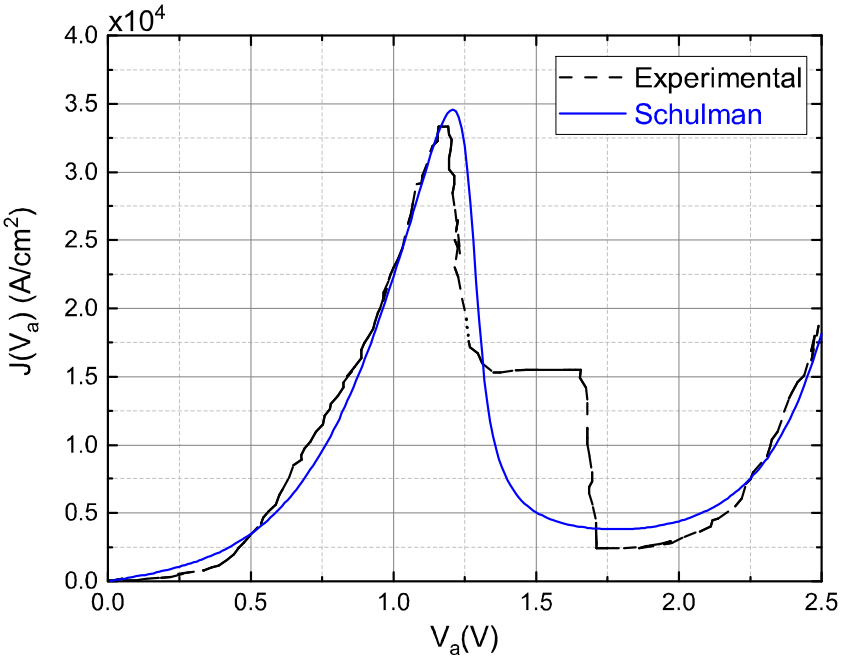

Figure 4.9: Comparison between experimental results and the Schulman model for an RTD with $In_{0,53}Ga_{0,47}As$/AlAs structure [82].

We should point it out that after the Schulman model [82], models such as [121]- [123], [126] can be found in the literature. However, most of these models are not fully analytical and/or do not cover a broad range of temperature and most of than are not predictive. Additionally, many of these models disregard scattering mechanisms in RTDs, preventing an accurate description of the **I–V** characteristics. In this regard, the next section discusses the most relevant

scattering mechanisms present in RTDs.

4.5 Scattering Mechanisms

Several RTD models found in the literature disregard the inelastic scattering effects during electron tunneling, considering a fully coherent current density. In addition, many of these models neglect the formation of the accumulation and depletion regions. Thus, the **I–V** curve provided by these models differs from the experimental data [51]. Therefore, it is necessary to investigate the scattering effects that most impact the tunneling process in RTDs.

In this regard, Tsu-Esaki original formalism neglects the effects of space charge formation in the RTD. Consequently, the potential profile in the double barrier quantum well region, under bias, taken as linear, as illustrated in Fig. (4.2). However, in a more accurate model, the spatial charge distribution in RTDs directly interplays with the electron distribution, giving rise to a non-uniform potential profile [127]- [133]. The charge distribution in biased RTDs, i.e., out of thermodynamic equilibrium, is ruled by energy dissipation processes [53]. Energy dissipation processes, such as LO-phonon emission (optical-longitudinal phonon) [134]- [148], impurity scattering, roughness, and others [103], [149]- [157], lead to charge storage in the quantum well. In this context, inelastic phonon-electron scattering is considered the process that mostly defines the **I–V** characteristic in RTDs [51], [158]. Additionally, inter-band tunneling processes (e.g., $\Gamma - X$) and impurity scattering also affect the transport dynamics in RTD [158].

The Tsu-Esaki formalism [31] assumes that the carriers travel through the device without losing phase coherence. One can argue that this is a plausible assumption since the formalism is only applied in the double barrier section (barriers and well, excluding contacts) with undoped narrow width barriers (although scattering effects, even under these conditions, often become significant [158]). There is also minor scattering contributions from impurities in the strongly doped contact regions, emitter and collector. These regions are often modeled using the semi-classical Thomas-Fermi approximation, in which electrons are assumed to occupy continuous states above the edge of the conduction band [159]- [161]. Thus, in the Thomas-Fermi approach, the electron density $n(x)$ in Eq. (4.18) is computed by taking the difference between the quasi-Fermi level and the conduction band edge [103], [157]. Fully quantum treatment of the contact

regions can be done by adopting a dissipative quantum transport theory such as the Wigner and NEGF transport model [107]- [109], [110]- [112].

In general, the quantum well and potential barrier regions are fabricated to be undoped. Thus, ionized impurity scattering is not expected in the quantum tunneling process. However, donor atoms in adjacent contact regions, emitter and collector, can diffuse to the barrier and well layers during the epitaxial growth process, giving rise to Coulomb scattering centers [149]- [162]. In order to reduce Coulomb scattering, an undoped spacer layer is usually inserted between the contacts and the barriers. Additionally, including spacer layers allows the barriers to sustain symmetry under bias voltage, since most of the bias applied lies over the space layers. As seen in Chapter 2, the asymmetry (is experienced by the electrons at the emitter side) in the conduction band profile degrades the peak of the resonant transmission coefficient, consequently, reducing the resonant tunneling current density [128]- [129]. Fig. (4.10) depicts a schematic illustration of the conduction band profile of an RTD with the inclusion of undoped spacer layers adjacent to the barriers.

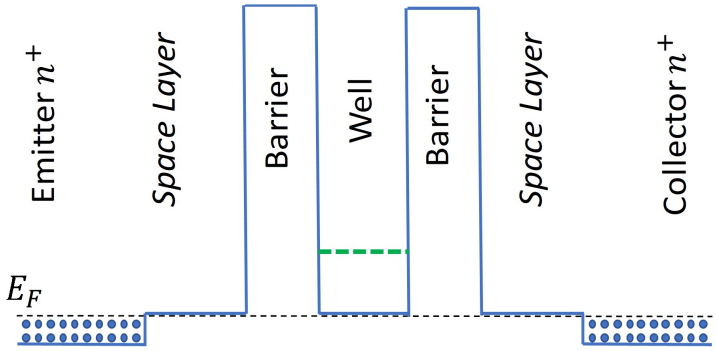

Figure 4.10: Schematic illustration of the conduction band profile of an RTD encompassing double potential barrier, emitter, collector and spacer layer.

The applied external voltage is also distributed in the spacer layer, which is employed because a low doping profile near the resonant tunneling barriers results in a higher PVRC [163]. Thus, in real RTDs, the space charge modifies the electric potential, leading to a region of charge accumulation in the emitter and charge depletion in the collector [164]. Depending on the doping level in the spacer layer, a quasi-triangular quantum well may form a 2DEG region at the emitter [147], [161], as shown in Fig. (4.11-b).

In this context, a widely documented device, which is based on a 2-DEG channel, is the

HEMT (High Electron Mobility Transistor). For instance, consider a HEMT composed by the GaAs/$AI_xGa_{1-x}As$ semiconductor heterostructure with modulated doping, where the GaAs layer is nominally undoped and the $AI_xGa_{1-x}As$ is n-type (to improve mobility and reducing Coulomb scattering, doping occurs at a distance of ~ 100 Å from interface). In thermal equilibrium, to produce a constant Fermi level across the structure, charge transfer occurs across the interface, leading to spatial charge regions on both sides of the junction. Consequently, there is a bending in the conduction band profile [165], [166]. In this case, electrons are transferred from the higher band-gap material to the lower one, forming a region of positive spatial charge due to ionized donors and creating an electron inversion layer in the GaAs side. Specifically, a triangular quantum well is formed at the inversion layer, confining the electrons close to the interface and quantized eigenenergy levels in the well. Thus, a series of subbands are formed, each with a two-dimensional state density of $m^*/\pi\hbar^2$. At low temperatures, electrons occupy only the first subband and hence the electron gas can be considered a quasi two-dimensional where electrons are free in plane parallel to the interface. [167]. In this structure, the electrons are spatially separated from the ionized donor ions, which leads to high electron mobility values ($\mu \gtrsim 10 \times 10^6 \ \ \mathrm{cm}^2/\mathrm{V\,s}$). However, the situation in RTDs is slightly different as the $AI_xGa_{1-x}As$ region is not doped and therefore, there is no 2DEG layer formation in the absence of applied voltage. Nevertheless, bias application produces an accumulation layer adjacent to the potential barrier and two-dimensional states arise at the interface.

As mentioned earlier, the valley current density calculated by the purely coherent model is much smaller than the value measured experimentally (see Fig. (4.7)). Thus, the predicted PVRC ratio is more than an order of magnitude greater than the measured experimental data [51], [102]. This large difference between theoretically calculated and experimentally measured valley current was similarly observed in several RTD structures. Therefore, it cannot be attributed to uncertainty about the material parameters used in the calculations or due to measurement inaccuracies. The excess current observed in the valley region has been attributed to the loss of phase coherence [135], neglected in the coherent tunneling model. One of the main causes of this loss of phase coherence is LO-phonon scattering [134]- [148]. This effect can play an important role even in recently developed RTDs, since the relaxation time of the electrons, due to phonon scattering, is much less than the time required for the electron to cross

the quantum well, the dwell-time, τ_d.

The LO-phonon scattering directly affects the transmission coefficient and the charge distribution in the device. The change in charge distribution results from energy dissipation processes in the well and it is generally investigated using NEGF quantum transport theory [107]- [109]. Other effects of electron-phonon interactions are expected in the charge transport. First, a LO-phonon emission process can create an additional resonant tunneling channel, which appears as a small additional peak in the I-V curve [147]. Second, a LO-phonon scattering can cause a broadening on the transmission peak due to loss of phase coherence. In this framework, Luryi [168] proposed that the NDR would be better described by a sequential process rather than the coherent resonant process. In this approach, the electrons first tunnel from the emitter to the quantum well and subsequently from the well to the collector. Between these two steps, electron phase memory can be completely lost due to the scattering processes [162], [169].

4.5.1 Sequential Tunneling

The formalism described in this section, closely follows reference [158] and it is presented here for completeness.

The transfer matrix method, used in the Tsu-Esaki formalism, can be applied in any heterostructure to describe purely coherent resonant tunneling. However, in a sequential approach, as demonstrated by Weil and Vinter [169], the Hamiltonian transfer method is more suitable, as it allows the direct evaluation of scattering effects such as electron-phonon and electron-electron interactions. The Hamiltonian transfer formalism was originally proposed by Bardeen, in 1961 [170]. Since then, it has been successfully applied to describe several phenomena such as tunneling in superconductor-metal interfaces and the inelastic scattering processes in resonant tunneling devices [138]- [146], [153]- [154], [171]. Fig. (4.12) shows a schematic illustration of the sequential tunneling process in which the electron tunnels through the left barrier to the quantum well, undergoes an energy relaxation process, and then, sequentially, tunnels from the quantum well to the collector through the right barrier.

As described in [158], the double potential barrier structure is divided into three regions; E (emitter), W (well) and C (collector). The transfer of electrons between these regions can be described using tunneling Hamiltonians across each potential barrier, as illustrated in Fig.

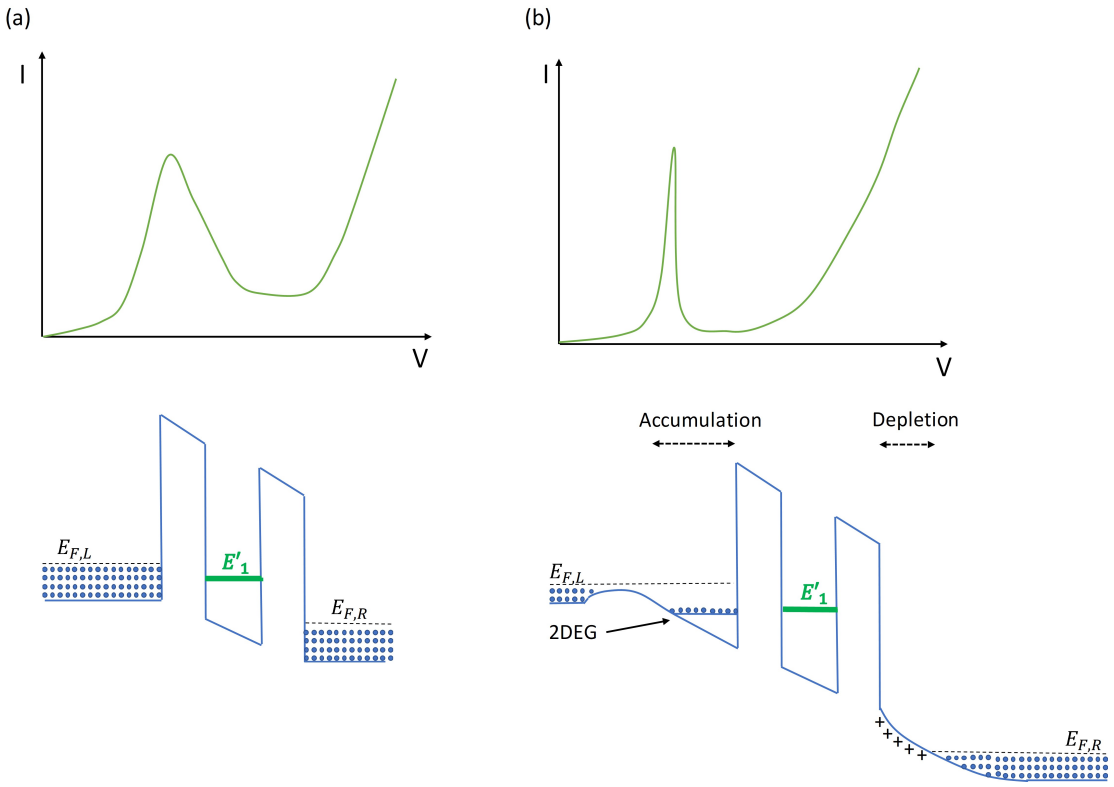

Figure 4.11: Schematic diagram illustrating the difference between resonant tunneling through a double potential barrier structure with an 3-D density of states emitter, linear potential profile (a) and two-dimensional self-consistently calculated potential profile (b). The resonance width in the case of the 3D emitter is larger than that of the 2D emitter.

(4.12). Thus, the total Hamiltonian of the system H_T can be written as

$$H_T = H_e^0 + H_w + H_c^0, \tag{4.38}$$

where, the Hamiltonian in the well is

$$H_w = H_w^0 + H_{ew} + H_{cw} + H_s, \tag{4.39}$$

The terms H_e^0, H_w^0 and H_c^0 are the Hamiltonians of the emitter, well and collector, respectively. The terms H_e^0, H_w^0 and H_c^0 can be written as [158]:

$$
\begin{aligned}
H_e^0 &= \sum_{\mathbf{k}_\parallel^e, k_x^e} \left(E_{\mathbf{k}_\parallel^e} + E_{k_x^e} \right) a^\dagger_{\mathbf{k}_\parallel^e, k_x^e} a_{\mathbf{k}_\parallel^e, k_x^e}, \\
H_c^0 &= \sum_{\mathbf{k}_\parallel^c, k_x^c} \left(E_{\mathbf{k}_\parallel^c} + E_{k_x^c} \right) a^\dagger_{\mathbf{k}_\parallel^c, k_x^c} a_{\mathbf{k}_\parallel^c, k_x^c}, \\
H_w^0 &= \sum_{\mathbf{k}_\parallel^w} \left(E_{\mathbf{k}_\parallel^w} + E_{k_x^0} \right) a^\dagger_{\mathbf{k}_\parallel^w, k_x^0} a_{\mathbf{k}_\parallel^w, k_x^0},
\end{aligned}
$$

where $\mathbf{k}_\parallel$ and k_x are, respectively, the parallel and longitudinal component of the wave vector, $\mathbf{k}$. The term k_x^0 is the wave vector of the resonant energy in the well. $a_\mathbf{k}$ and $a^\dagger_\mathbf{k}$ are the usual electron creation and annihilation operators, respectively [1], [54].

H_{ew} and H_{cw} are the tunneling terms of the emitter-well and collector-well comprising the Hamiltonian of the well region H_w in Eq. (4.39). It is possible to write H_{ew} and H_{cw} as [158]:

$$
\begin{aligned}
H_{ew} &= \sum_{\mathbf{k}_\parallel^e, k_x^e, \mathbf{k}_\parallel^w} \left\{ V\left(\mathbf{k}_\parallel^e, k_x^e; \mathbf{k}_\parallel^w, k_x^0\right) a^\dagger_{\mathbf{k}_\parallel^e, k_x^e} a_{\mathbf{k}_\parallel^w, k_x^0} + H.c. \right\}, \\
H_{cw} &= \sum_{\mathbf{k}_\parallel^c, k_x^c, \mathbf{k}_\parallel^w} \left\{ V\left(\mathbf{k}_\parallel^c, k_x^c; \mathbf{k}_\parallel^w, k_x^0\right) a^\dagger_{\mathbf{k}_\parallel^c, k_x^c} a_{\mathbf{k}_\parallel^w, k_x^0} + H.c. \right\},
\end{aligned}
$$

where $V\left(\mathbf{k}_\parallel^e, k_x^e; \mathbf{k}_\parallel^w, k_x^0\right)$ and $V\left(\mathbf{k}_\parallel^c, k_x^c; \mathbf{k}_\parallel^w, k_x^0\right)$ are the elements of the tunneling matrix between the emitter and the well and between the collector and the well. The term H_s represents other interactions which electrons can undergo during tunneling, such as phonon scattering, electron-electron interaction, and scattering due to impurities.

In this formalism, the transmission coefficient in the well can be written using the Green's function [158]:

$$
G_w = \frac{1}{E(\mathbf{k}_\parallel^e, k_x^e) - i\delta - H_w}, \tag{4.40}
$$

where δ is an infinitesimal increment of energy. Then, one can write the tunneling coefficient as

$$
\mathbf{T}(\mathbf{k}_\parallel^\mathbf{e}, k_x^e) = -\sum_{\mathbf{k}_\parallel^e, k_x^e} \mathrm{Im} \left\langle \mathbf{k}_\parallel^c, k_x^c \right| H_{ew} G_w H_{cw} \left| \mathbf{k}_\parallel^e, k_x^e \right\rangle, \tag{4.41}
$$

after some algebraic manipulation, as proposed in [158], one obtain

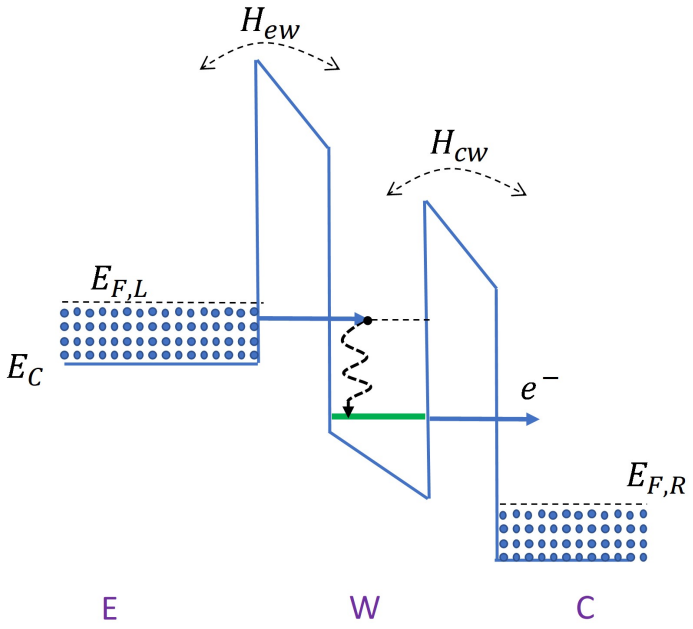

Figure 4.12: Illustration of sequential tunneling assisted by some energy relaxation process. The terms H_{ew} and H_{cw} are the tunneling terms of the emitter-well and collector-well, respectively.

$$\mathbf{T}(\mathbf{k}_{\parallel}^{\mathbf{e}},k_x^e) = -\sum_{\mathbf{k}_{\parallel}^e,k_x^e}\sum_{\mathbf{k}_{\parallel}^w} \mathrm{Im}\,\frac{\left\langle \mathbf{k}_{\parallel}^c,k_x^c\right|\,H_{cw}\left|\mathbf{k}_{\parallel}^w,k_x^0\right\rangle \left\langle \mathbf{k}_{\parallel}^w,k_x^0\right|\,H_{ew}\left|\mathbf{k}_{\parallel}^e,k_x^e\right\rangle}{E(\mathbf{k}_{\parallel}^e,k_x^e)-E(\mathbf{k}_{\parallel}^w,k_x^0)-\Sigma_w\left(\mathbf{k}_{\parallel}^e,k_x^e,E(\mathbf{k}_{\parallel}^e,k_x^e)\right)}, \tag{4.42}$$

where Σ_w is the electron self-energy (the energy that a particle has as a result of changes that it causes in its environment, e.g., due to the semiconductor crystal lattice) in the well due to tunneling and interactions with the lattice. Assuming the terms H_{ew} and H_{cw} conserving the momentum, it is possible to make $V\left(\mathbf{k}_{\parallel},k_x;\mathbf{k}_{\parallel}^w,k_x^0\right) = V_{k_x}$ therefore, one can simplify Eq. (4.42) to [158]:

$$\mathbf{T}(\mathbf{k}_{\parallel}^{\mathbf{e}},k_x^e) = -\,\mathrm{Im}\,\frac{\Gamma}{E(\mathbf{k}_{\parallel}^e,k_x^e)-E(\mathbf{k}_{\parallel}^w,k_x^0)-\Sigma_w\left(\mathbf{k}_{\parallel}^e,k_x^e,E(\mathbf{k}_{\parallel}^e,k_x^e)\right)},$$

where Γ is the intrinsic broadening of the resonant state, approximately

$$\Gamma \approx \sum_{k_x^e} |V_{k_x}|^2\,\delta\left(k_x^e-k_x^0\right).$$

When electrons do not interact with the lattice, that is, $H_s = 0$, it is possible to substitute Σ_w

for $-i\Gamma$ thus, using perturbation theory [1], the lowest order term of the probability coefficient, $\mathbf{T}^{(0)}(\mathbf{k}_{\parallel}^{\mathbf{e}},k_x^e)$ can be simplified to [158]:

$$\mathbf{T}^{(0)}(\mathbf{k}_{\parallel}^{\mathbf{e}},k_x^e)=\mathbf{T}^{(0)}(E_{k_x^e})=\frac{\Gamma^2}{\left(E_x^e-E_x^0\right)^2+\Gamma^2}, \tag{4.43}$$

In this condition, the tunneling current can be written as

$$J=\frac{em_{\parallel}^*}{2\pi^2\hbar^3}\int_0^{\infty}\mathbf{T}(\mathbf{k}_{\parallel},k_x)\left[\int_0^{\infty}\left[f_L\left(E\right)-f_R\left(E\right)\right]dE_{\parallel}\right]dE_x. \tag{4.44}$$

Note that Eq. (4.44) is reduced to the Tsu-Esaki formalism in the absence of scattering. However, in the Hamiltonian transfer approach, scattering effects can be incorporated into current density through the Hamiltonian H_s [158].

4.5.2 Phonon Scattering

As mentioned earlier, interactions between electrons and LO-phonons are, in general, the most important energy dissipation process in polar semiconductor systems such as RTDs. Electrons in double barrier RTDs can emit or absorb phonons during the resonant tunneling process [134]- [148]. As this is an inelastic scattering process, momentum is not conserved. The resonant tunneling assisted by LO-phonons is illustrated schematically in Fig. (4.13).

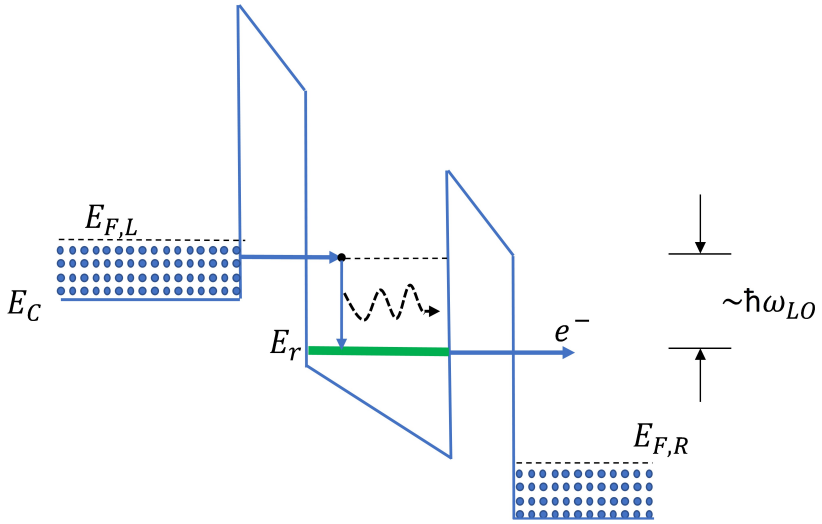

Figure 4.13: Schematic illustration of resonant tunneling assisted by LO-phonons. The term $\hbar\omega_{LO}$ refers to the phonon energy.

The probability of phonon emission is relatively small compared to the main resonant tunneling process. However, the result can be directly seen in the **I–V** characteristic at low temperatures by the presence of a small lateral peak along the main resonant peak [134]- [148]. Additionally, there is a broadening in the resonant linewidth and an increase in the valley current.

In this context, resonant tunneling assisted by LO-phonons was experimentally observed by Goldman *et al.* [104]. In [104], the authors observed a small peak in the valley region a 4.2 K with a magnitude of about 4% in relation to the main peak. Chevoir and Vinter [135] theoretically demonstrated the existence of a small peak, in the **I–V** curve, confirming the observations of Goldman *et al.* [104].

The scattering rate due to phonon emission can be calculated by Fermi's Golden Rule [1]:

$$W(i \rightarrow f) = \frac{2\pi}{\hbar} \left| \langle f | \, H_{e-ph} | i \rangle \right|^2 \delta \left(E_i - E_f - \hbar\omega_{LO} \right),$$

where the Hamiltonian H_{e-ph} describes the electron LO-phonons interaction in a semiconductor. The term $\hbar\omega_{LO}$ denotes the energy of the LO-phonon, where $|i\rangle$ represents the initial state with an electron and $|f\rangle$ the final state with an electron and an emitted phonon. The Hamiltonian which describes the electron-phonon interaction is known as the Fröhlich Hamiltonian [153]- [154]. In the well, the Fröhlich Hamiltonian can be written as [140]- [141]:

$$H_{e-ph} = H_{Fr} = \sum_{\mathbf{q}_{\|}} \frac{\gamma}{\sqrt{AL_e}} \frac{e^{i\mathbf{q}_{\|}\cdot\mathbf{r}_{\|}}}{\left[q_{\|}^2 + \left(n\pi / L_w \right)^2 \right]^{1/2}} \sin\left(\frac{n\pi}{L_w} x \right) \left[a_n \left(\mathbf{q}_{\|} \right) + a_n^{\dagger} \left(-\mathbf{q}_{\|} \right) \right] \quad (4.45)$$

where γ is the coupling constant [140]- [141]. The term AL_e refers to the effective volume of the emitter, where L_e is the effective length of the emitter and A is the cross-section of the plane parallel to the barriers y-z.

In Eq. (4.45) $\mathbf{q}_{\|}$ is the wave vector of the phonon emitted in the parallel plane, $a_n \left(\mathbf{q}_{\|} \right)$ and $a_n^{\dagger} \left(\mathbf{q}_{\|} \right)$ is the photon creation and annihilation operators, respectively. n is the number of phonons allowed in the confinement layer. The excess in current density due to LO-phonon scattering can be calculated as [140]- [141]:

$$J = \frac{1}{A} \int e\mathbf{W} \left(\mathbf{k} \right) g_e \left(\mathbf{k} \right) f_e \left(E((\mathbf{k})) \, d\mathbf{k} \right. \quad (4.46)$$

where $g_e(\mathbf{k}) = 2AL_e/(2\pi)^3$ is the density of states in the emitter $f_e(E((\mathbf{k}))$ is the emitter Fermi-Dirac distribution, $\mathbf{W}(\mathbf{k}) = \Sigma_f W(i \rightarrow f)$ is the total phonon emission rate per electron for a given initial state with the wavevector $\mathbf{k}$. The term Σ_f accounts for the summation of the final states with longitudinal confinement energy equal to the resonant energy level E_r. Note that $g_e(\mathbf{k})\, f_e(E((\mathbf{k}))$ is the number of electrons per unit volume in $\mathbf{k}$-space that tunnel with the emission of phonons with the rate of phonon emission per electron given by $\mathbf{W}(\mathbf{k})$ [140]. Thus, writing the Hamiltonian for electron-phonon interaction, one can apply the Hamiltonian transfer method to compute the current density in the RTD within the sequential tunneling formalism.

Alternatively, Büttiker [172] proposed a phenomenological model that allows the inclusion of scattering effects in the transmission coefficient. In [172], Büttiker calculated the transmission coefficient across a double barrier structure in the presence of a phase randomization reservoir connected to the well. For this, Büttiker extended the Breit-Wigner formula to the sequential tunneling regime, introducing an additional factor to express the incoherent scattering in the original Breit-Wigner formula (derived in Chapter (2)) . For the particular case of symmetric barriers, Büttiker proposes

$$\mathbf{T}(E_x, V_a) = \frac{\Gamma}{\Gamma_T} \frac{\Gamma_T^2}{\Gamma_T^2 + (E_x - E_r)^2}, \tag{4.47}$$

where Γ_T is the total resonance width, composed of a purely coherent intrinsic width, Γ, and the extrinsic width due to scattering, Γ_s .Thus, $\Gamma_T = \Gamma + \Gamma_s$. The dwell-time can be calculated from the intrinsic resonance width as $\tau_d = \hbar/\Gamma$ [172]. By the same token, the phase coherence break time, τ_s, induced by scattering, can be calculated as $\tau_s = \hbar/\Gamma_s$. Eq. (4.47) shows that the relationship between Γ_s and Γ (equivalent to τ_s/τ_d) is an important parameter to provide a boundary between the purely coherent tunneling regime and the sequential tunneling regime. In the sequential regime we have $\Gamma_s/\ \Gamma\ > 1$ the peak value of the transmission coefficient decreases and the transmission peak becomes broader, when compared with the purely coherent tunneling model.

Moreover, as proposed by Mizuta *et al*. [173], the resonance width due to LO-phonon scattering can be estimated through the moment relaxation time, τ_m, calculated by expression [173], [174]:

$$\frac{1}{\tau_m} = \alpha\omega_{LO}\left(\frac{\hbar\omega_{LO}}{E_r}\right)^{1/2} N_{\mathbf{q}}\left\{\ln\left|\frac{a+1}{a-1}\right| + \exp\left(\frac{\Lambda}{T}\right)\ln\left|\frac{1+b}{1-b}\right|\right\}, \tag{4.48}$$

where α is the Fröhlich polar constant given by

$$\alpha = \frac{e^2\sqrt{m_x^*}}{4\sqrt{2}\pi\epsilon_0\hbar\sqrt{\hbar\omega_{LO}}}\left(\frac{1}{\kappa_{opt}} - \frac{1}{\kappa}\right),$$

and κ_{opt} and κ are the dielectric optical (high frequency) and static constants, respectively. The parameter N_q is the average number of phonons in mode **q** given by the Bose-Einstein thermal distribution [174]:

$$N_{\mathbf{q}} = \frac{1}{\exp\left(\Lambda/T\right) - 1}$$

the parameters a and b are defined as

$$a = \left(1 + \frac{\hbar\omega_{LO}}{E_r}\right)^{1/2}$$

$$b = \mathrm{Re}\left(1 - \frac{\hbar\omega_{LO}}{E_r}\right)^{1/2}$$

The term Λ refers to the Debye temperature, which indicates the approximate temperature limit below which quantum effects can be observed [174]. The Debye temperature can be calculated as $\Lambda = \hbar\omega_{LO}/k_B$ [75], [174]. Γ_s can be estimated from the moment relaxation time, such as $\Gamma_s \approx \hbar/\tau_m$. As demonstrated by Mizuta *et al*. [173], the approximation for Γ_s by means of the moment relaxation time, τ_m, provides satisfactory agreement with experimental data.

In addition, the Hamiltonian transfer method can be used to compute scattering effects due to impurities in undoped regions (double barrier and well), as proposed in [153]- [155]. Likewise, from a phenomenological point of view, one can estimate the broadening in the resonance width due to impurities, Γ_{imp}. However, because of the technological maturity of epitaxial growth technique and the insertion of long undoped spacer layers between the double barrier and the doped regions, the excess broadening due to impurities can be neglected [156]. Therefore, scattering due to LO-phonons can be considered the leading broadening resonance linewidth and degrading the PVRC in RTDs.

Despite advances in the compact modeling of RTD I–V characteristics, through an extensive literature review, we identified the need for fully analytical compact models relying on device physics and capable of accurately reproducing RTD I-V characteristics. Aiming to fill this gap, the next chapter presents a compact model describing RTDs 2D-2D and 3D-2D I–V characteristics. The models are based on the device physics and allow the computation of electrical characteristics as a function of physical parameters and geometric dimensions, with a reduced number of fitting parameters, maintaining a compact, fully analytical, and explicit form, which allows easy introduction into a circuit simulator.

Chapter 5

Analytical Physics-Based Models for the I–V Characteristics of 2D-2D and 3D-2D RTDs

In this Chapter, we develop a fully analytical model for the I-V characteristics of 2D-2D and 3D-2D RTDs. Starting from the Tsu-Esaki formalism, we consider the overall electrical potential distribution in the device layer structure, including the space charge region in the emitter layer. Additionally, we also take into account the scattering experienced by electrons during tunneling process through the double barrier region. These additional features greatly improve the accuracy of the proposed models when compared with others approaches reported in the literature. The device models is fully physics-based, allowing the computation of the I-V curve accordingly to the geometry and device structure of the RTD. The models are fully analytical and explicit, thereby well suited for circuit simulator environment. The models are validated against experimental and numerical data from several distinct RTDs structures, providing excellent agreement.

5.1 Model for the I–V Characteristics of 2D-2D RTD

5.1.1 Electric Field and Potential Distribution Model

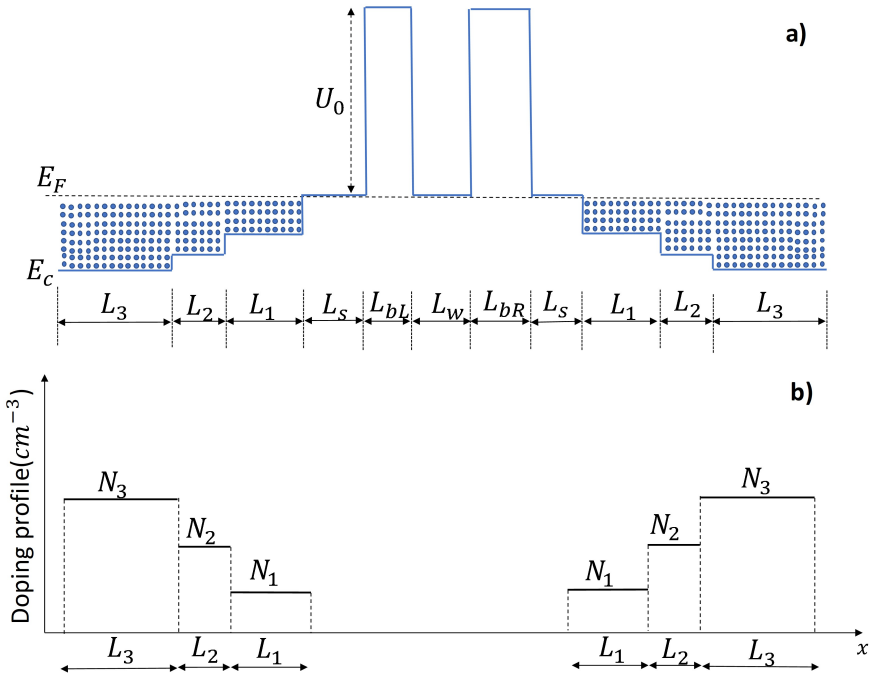

Figure 5.1: Schematic illustration of an arbitrary double barrier RTD structure. **Part (a):** schematic illustration of the RTD conduction band profile. **Part (b):** RTD doping distribution generalized as piecewise uniform.

For the 2D-2D RTD, we consider an arbitrary heterostructure, schematically depicted in Fig. (5.1). To provide a generalized model, we assumed a piecewise uniform doping distribution, as it is usually employed in realistic devices. The self-consistent solutions of the Schrödinger and Poisson equations, under the application of an external electric field, indicate the formation of space charge in the emitter and collector regions [127], [159]. Specifically, for the emitter region both theoretical calculations and experimental demonstrations, considering weakly doped RTD space layers, show an accumulation space charge formation. This accumulation layer is characterized by a two-dimensional electron gas (2-DEG) with quantized energy levels [79], [157], [175].

In this section, for the electrostatic analysis, we follow the approach proposed by Leadbeater [164] to compute the 2-DEG electron concentration, n_a, at the emitter, and next, the electric field

and potential distributions, in terms of n_a.

Accumulation Layer

We start by considering the electrical potential distribution in a set of distinct regions, namely: the potential energy drop in the accumulation layer eV_{ac} (the voltage drop at the emitter taken from the Fermi level to the interface with the left barrier); in the double barrier region eV_{db} (left barrier, rectangular quantum well and right barrier); in the spacer layer eV_s and the depletion region eV_d (the voltage drop in the collector in the depletion region). Fig. (5.2) shows a schematic illustration of the potential double barrier region in the unperturbed condition, Fig. (5.2-a), and under an applied bias voltage (V_a), Fig. (5.2-b).

Under external bias, a fraction of the carriers from the two-dimensional accumulation layer continuously tunnel through the left barrier to reach the well. Meanwhile, the empty states in the 2D accumulation region are replenished with electrons from the 3D region of the emitter, in such way that there is a steady supply of electrons to ensure current continuity across the device.

In the approach proposed by Leadbeater [164], the Fang-Howard variational method [176] is used to compute the potential drop in the accumulation region. In this framework, the one-dimensional variational Fang-Howard wavefunction is

$$\Psi_{ac}(x) = \begin{cases} -2\left(\frac{a}{2}\right)^{3/2} x \exp\left(\frac{ax}{2}\right), & x < 0 \\ 0, & x \geq 0 \end{cases} \tag{5.1}$$

where the subscript "ac" refers to the accumulation region. In this case, the origin, $x = 0$, is placed in the interface between the accumulation region and the left barrier with respect to the rectangular quantum well.

The total energy of the system can be expressed as $\langle E \rangle = \left\langle \Psi_{ac} | \hat{\mathbf{H}} | \Psi_{ac} \right\rangle$, where $\hat{\mathbf{H}}$ is the Hamiltonian operator. As usual, the variational parameter, a, is determined by minimizing $\langle E \rangle$, hence, given by:

$$\langle a \rangle = \frac{\left\langle \Psi_{ac} | \hat{\mathbf{H}} | \Psi_{ac} \right\rangle}{\langle \Psi_{ac} | \Psi_{ac} \rangle}$$

Considering the 2D charge density as $\rho_{ac}(x) = -en_a \left|\Psi_{ac}(x)\right|^2$, we have:

$$\nabla^2 V_e(x) = \frac{-\rho_{ac}(x)}{\kappa_e \epsilon_0}, \tag{5.2}$$

where $V_e(x)$ it is the conduction-band profile in the emitter accumulation layer and κ_e is the emitter dielectric constant. In this approach, the band-bending is due only to n_a, the free electron charge confined in the quasi-triangular well at the emitter side. Contributions from electrons at the 3D bulk region of the emitter as well as from fixed ionized atoms are neglected. The conduction band away from the interface is considered as reference: $E_c = 0$. In the accumulation region, the band bending due to 2D electrons in the quasi-triangular well, solving Poisson's equation, is [164]:

$$V_e(x) = \frac{e n_a e^{ax}}{2\kappa_e \epsilon_0 a} \left(a^2 x^2 - 4ax + 6\right), \ \ (0, -\infty) \tag{5.3}$$

Hence, the voltage drop in the accumulation region is given by $V_e(0)$ [164]:

$$V_e(0) = V_{ac} = \left(\frac{72 e \hbar^2 n_a^2}{11 m_e^* \kappa_e^2 \epsilon_0^2}\right)^{1/3}, \tag{5.4}$$

In our model, the eigenenergy levels in the quasi-triangular quantum well can be easily calculated using the expression [53]:

$$E_{ac,m} = \left[\frac{3\pi e \left\langle F_e \right\rangle}{2}\left(m - \frac{1}{4}\right)\right]^{2/3} \left(\frac{\hbar^2}{2m_e^*}\right)^{1/3}, \tag{5.5}$$

where $m = 1, 2, 3, ...$, is the eigenstate index, $E_{ac,m}$ is the eigenenergy associated with the m*th* two-dimensional subband in the quasi-triangular quantum well. The electric field in the accumulation region is given by $F_e(x) = -\nabla V_e(x)$, yielding

$$F_e(x) = -\frac{e n_a \left(a^2 x^2 - 2ax + 2\right)}{2\epsilon_0 \kappa_e} \exp(ax), \tag{5.6}$$

It should be pointed out that the above formulation takes into account neither the wavefunction penetration into the barrier nor the screening due to 3D-bulk electrons located away from the emitter accumulation region. Therefore, as experimentally observed in [164], this model overestimates the binding energy in the accumulation region. To overcome this inaccuracy, and seeking to closely match the experimental data, we empirically take the value of the effective electric field in the two-dimensional electron gas at the emitter to be multiplied by a factor α_f in

the form: $\langle F_e \rangle = \alpha \langle \Psi_{ac} | F_e(x) | \Psi_{ac} \rangle$, where the required wavefunction is described by Eq. 5.1 Carrying out the calculation, in our model the effective electric field in the accumulation region is averaged out as $\langle F_e \rangle \approx -\alpha_f e n_a/(2\epsilon_e)$. It is important to note throughout the simulations, for every one of the five RTD devices investigated, we kept $\alpha_f = 1/3$.

Double Barrier Region

Space Charge Buildup

As discussed in Chapter 4, the charge storage in the well is due to electrons from the accumulation region which tunnel into the well through the potential barrier. Hence, the next step in our model to find a mathematical relationship between the charge densities in the emitter n_a and the well n_w. To do so, we modify the approach proposed by Sheard and Toombs to describe the 2D state density case. The authors originally developed a model considering a 3D state density at the emitter region [160].

Under proper bias, one can consider the RTD as two parallel plates capacitors in series, with a negative charge in the emitter $-Q_e$, positive in the collector Q_c and a negative charge $-Q_w$ at the center plate of the device, representing the well [160].

In steady state, the charge density in the well is determined by the balance between the current flowing into and out of the well [160]. We can identify the emitter states by means of its wavevector $\mathbf{k} = (k_x, \mathbf{k}_\perp)$ and the collector states as $\mathbf{p} = (p_x, \mathbf{p}_\perp)$. In the 2D quantum well, the wavevector is represented as $\mathbf{q} = (0, \mathbf{q}_\perp)$, i.e., the longitudinal component of the wavevector is the same for all transverse states, since energy is quantized in this direction. Therefore, we describe tunneling in terms of the transition rate between states $\mathbf{q}$**,** in the quantum well, and the states $\mathbf{k}$**,** at the emitter, $W_{\mathbf{kq}} = (W_{\mathbf{qk}})$. Likewise the transition rate between the states of the well $\mathbf{q}$ and the collector states $\mathbf{p}$, $W_{\mathbf{pq}} = (W_{\mathbf{qp}})$. It is possible to compute the transition probability per unit of time by using Fermi's Golden Rule [1]:

$$W_{WL} = \frac{2\pi}{\hbar} \left| \left\langle \Psi_W | \hat{\mathbf{H}} | \Psi_L \right\rangle \right|^2 \delta(E_W - E_L), \tag{5.7}$$

where $\hat{\mathbf{H}} = H - E_L$, with H being the Hamiltonian of the left potential barrier, E_L is the energy level at the emitter. Ψ_L is the emitter wave function and Ψ_W represents the state in the well. According to Bardeen [170], the matrix element of the transition can be written as

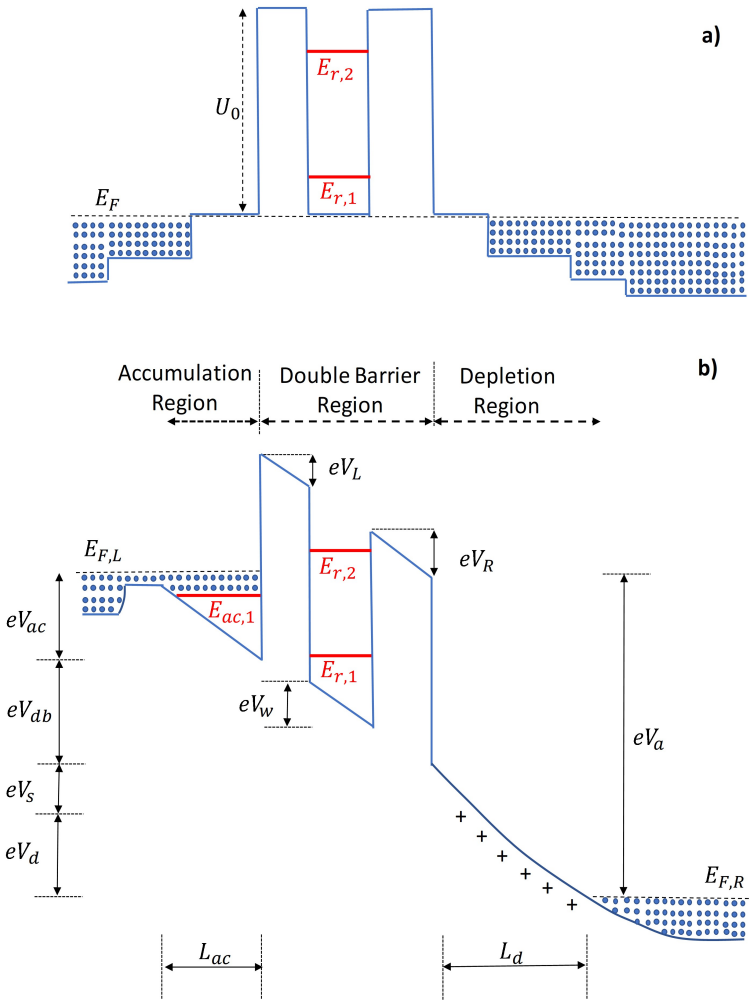

Figure 5.2: Schematic illustration of the conduction-band profile under thermodynamic equilibrium (a) and subjected to an external bias voltage, V_a (b). The voltage drop is distributed in the accumulation layer V_{ac}, in the double barrier region V_{db} and in the depletion region V_d. The figure also shown the extension of the accumulation region L_{ac} and depletion L_d. The term E_{ac} refers to the 2D level at the transmitter and the term E_r the energy levels in the well between the potential barriers.

$$\left\langle \Psi_W|\hat{\mathbf{H}}|\Psi_L \right\rangle = \int_{x_B}^{\infty} \Psi_W^*(H-E_L)\Psi_L d\mathbf{r},$$

where lower limit of integration, x_B, can be defined as any point on the barrier, since $(H-E_L)\Psi_L = 0$ for $x \leq L_b$. Carrying out the calculations, as demonstrated by [160], we have:

$$\left|\left\langle \Psi_W|\hat{\mathbf{H}}|\Psi_L \right\rangle\right|^2 = \frac{\hbar^2 v_L v_w T_L(E_{ac})}{4L_x(L_w + 2/\alpha_M)}\delta_{\mathbf{q}_\perp,\mathbf{k}_\perp} \tag{5.8}$$

where, $v_L = \sqrt{2E_{ac,1}/m_e^*}$ and $v_w = \sqrt{2E_{r,1}/m_w^*}$. $E_{ac,1}$ is the first subband in the accumulation layer at the emitter side and $E_{r,1}$ is the first subband in the quantum well . The parameter α_M is [160]:

$$\alpha_M = \frac{2L_b + L_w + 2L_{ac}}{a_0}\frac{\mathbf{T}_L}{\mathbf{T}_L + \mathbf{T}_R},$$

where a_0 represents the Bohr's radius give by

$$a_0 = \frac{4\pi\kappa_w\epsilon_0\hbar^2}{m_w^* e^2},$$

$\mathbf{T}_L$ and $\mathbf{T}_R$ are the single barrier transmission coefficients relative to the left and right barriers of the well, respectively.

Thus, the rate equations for the states occupation at the emitter $f_\mathbf{k}$ and in the well $f_\mathbf{q}$ (where f is the Fermi-Dirac distribution function) are:

$$\begin{aligned}
\frac{\partial f_\mathbf{k}}{\partial t} &= -\sum_{\mathbf{k},\mathbf{q}}(f_\mathbf{k} - f_\mathbf{q})W_{\mathbf{kq}}, \\
\frac{\partial f_\mathbf{q}}{\partial t} &= -\sum_{\mathbf{q},\mathbf{k}}(f_\mathbf{q} - f_\mathbf{k})W_{\mathbf{qk}} - \sum_{\mathbf{q},\mathbf{p}}(f_\mathbf{q} - f_\mathbf{p})W_{\mathbf{qp}}.
\end{aligned}$$

In steady-state, we have $\partial f_\mathbf{q}/\partial t = 0$. Therefore, the equilibrium condition is

$$\sum_{\mathbf{q},\mathbf{k}}(f_\mathbf{k} - f_\mathbf{q})W_{\mathbf{qk}} - \sum_{\mathbf{q},\mathbf{p}}(f_\mathbf{q} - f_\mathbf{p})W_{\mathbf{qp}} = 0 \tag{5.9}$$

Assuming momentum conservation in the plane perpendicular to the barriers, we have $\mathbf{k}_\perp = \mathbf{q}$ and $\mathbf{p}_\perp = \mathbf{q}$. Additionally, assuming a narrow resonance linewidth, taking into account only the first subband in the emitter and in the well, and considering energy conservation, yields:

$$\frac{\hbar^2 k_0^2}{2m^*} + \frac{\hbar^2 k_\perp^2}{2m^*} = E_{r,n}(V_a) + \frac{\hbar^2 q_\perp^2}{2m^*}, \tag{5.10}$$

likewise, the condition for tunneling from the collector to the well is

$$\frac{\hbar^2 p_0^2}{2m^*} + \frac{\hbar^2 p_\perp^2}{2m^*} = V_a - E_{r,n}(V_a) + \frac{\hbar^2 q_\perp^2}{2m^*}, \tag{5.11}$$

where $k_x = k_0$ and $p_x = p_0$ correspond to the wavevectors at the emitter and the collector in resonant tunneling, respectively. The term $E_{r,n}(V_a)$ refers to the resonant energy levels in the well, under applied bias. Hence, Eq. (5.9) at resonance, for the 2D-2D case, is

$$\sum_{\mathbf{q},\mathbf{k}} W_{\mathbf{qk}}(f_{k_x,\mathbf{k}_\perp} - f_{\mathbf{q}})\delta_{\mathbf{k}_\perp,\mathbf{q}}\delta_{k_x,k_0} - \sum_{\mathbf{q},\mathbf{p}} W_{\mathbf{qp}}(f_{\mathbf{q}} - f_{\mathbf{p}})\delta_{\mathbf{p}_\perp,\mathbf{q}}\delta_{p_x,p_0} = 0 \tag{5.12}$$

when there are no occupied states in the collector with the same energy level of the quantum well, we have $f_{\mathbf{p}} = 0$. Thus, isolating $f_{\mathbf{q}}$ in Eq. (5.9), one can compute the charge stored in the well as $Q = eA\sum_{\mathbf{q}} f_{\mathbf{q}}$, where A is the interface area, yielding:

$$Q = e\frac{\sum_{\mathbf{q},\mathbf{k}} f_{\mathbf{k}} W_{\mathbf{qk}}}{\sum_{\mathbf{q},\mathbf{k}} W_{\mathbf{qk}} + \sum_{\mathbf{q},\mathbf{p}} W_{\mathbf{qp}}} = e\sum_{\mathbf{q},\mathbf{k}} \frac{f_{\mathbf{k}} W_{\mathbf{qk}}}{\tau_L^{-1} + \tau_R^{-1}} \tag{5.13}$$

where $\tau_L^{-1} = \sum_{\mathbf{q},\mathbf{k}} W_{\mathbf{qk}}$ and $\tau_R^{-1} = \sum_{\mathbf{q},\mathbf{p}} W_{\mathbf{qp}}$ [160]. In a sequential tunneling framework, the transmission rates $W_{\mathbf{qk}}$ and $W_{\mathbf{qp}}$ are obtained using Eqs. (5.7) and (5.8). Therefore, $\sum_{\mathbf{q},\mathbf{k}} W_{\mathbf{qk}} = (v_w/2L_W)\,\mathbf{T}_L = \nu\mathbf{T}_L$. Similarly, for the collector side, we have $\sum_{\mathbf{q},\mathbf{p}} W_{\mathbf{qp}} = \nu\mathbf{T}_R$, where ν is the classical attempt ratio [160]. In addition, $\sum_{\mathbf{q}} f_{\mathbf{q}}$ accounts for the number of charge stored in the well, that is, Q_w/e. By the same token, $\sum_{\mathbf{k}} f_{k_x,\mathbf{k}_\perp}$ is the number of states at the emitter with $k_x = k_0$. Summarizing:

$$G(V_a) = \begin{cases} (k_F^2 - k_0^2)/2\pi, 0 < k_0 < k_F \\ 0, \quad otherwise \end{cases} \tag{5.14}$$

Hence, one can rewrite Eq. (5.12) as

$$\nu T_L\left(eG(V_a) - Q_w\right) - \nu T_R Q_w = 0 \tag{5.15}$$

thus, the charge in the well is given by

$$Q_w = \frac{\mathbf{T}_L}{\mathbf{T}_L + \mathbf{T}_R}\left[\frac{k_F^2 - k_0^2}{2\pi}\theta(k_0^2 - k_F^2)\theta(k_0^2)\right] \tag{5.16}$$

where $\theta()$ is the step function.

Meanwhile, Sheard and Toombs [160] proposed the expression (5.16) considering a 3D density of states at the emitter. In other words, there is no formation of quantized energy levels at the emitter. On the other hand, for our specific case, where quantization occurs in the accumulation layer, the charge is proportional to the wavevector of the subbands. Therefore, we can rewrite Eq. (5.16) considering a 2D charge densities $Q_w = en_w$ and $Q_a = en_a$ [160]:

$$n_w = n_a \frac{\mathbf{T}_L}{\mathbf{T}_L + \mathbf{T}_R}\theta(k_0^2 - k_{\max}^2)\theta(k_0^2). \tag{5.17}$$

Finally, to obtain a more compact form, we can simplify Eq. (5.17) by using a Lorentizian approximation to describe the resonant energy levels in the quantum well, as proposed by [159], yielding:

$$n_w \cong n_a \frac{\mathbf{T}_L}{\mathbf{T}_L + \mathbf{T}_R}\left(\frac{1}{\pi}\frac{\Gamma_\Delta^2/4}{\Gamma_\Delta^2/4 + (E_{ac,m} - E_{r,n})^2}\right) = n_a \Lambda_w \tag{5.18}$$

Electrostatic Analysis

As discussed in the previous section, in the RTD the barriers are undoped and at the resonance condition a charge density, n_w, is stored in the quantum well. Also, since the resonance linewidth is narrow, results: $n_a \gg n_w$. To account for the band bending due to the charge in the QW, the charge distribution is given by $\rho_w(x) = -en_w\left|\Psi_w(x)\right|^2$, while the Poisson equation is written as

$$\nabla^2 V_{well}(x) = -\frac{\rho_w(x)}{\epsilon_w}. \tag{5.19}$$

Throughout the derivations, ϵ_b and ϵ_w are the permittivity constants in the barrier and in the well, respectively. L_w is the width of the rectangular quantum well and the terms L_{bL} and L_{bR} are the widths of the QW barriers to the left and right of the well, respectively.

In order to compute the wavefunction, required to calculate the charge distribution $\rho_w(x)$, we consider the first energy subband, $E_{r,1}$. In a first approximation, we assume the equilibrium condition, i.e., an absence of the electric field applied to the structure. Then, the problem

reduces to the solution of the Schrödinger equation for the rectangular finite well under unequal effective masses of the barriers and well regions (see Chapter 3).

For the quantum well, the electric potential is $U(x) = 0$ for $x \leq |L_w/2|$ and $U(x) = U_0$ otherwise. Consider the index $i = 1, 2, 3$, representing the left barrier, quantum well and right barrier regions, respectively. Placing the origin, $x = 0$, at the center of well, for left and right barriers regions, the solutions for Schrödinger equation are $\Psi_1(x) = Ae^{k_1 x}$ and $\Psi_3(x) = Be^{-k_1 x}$, respectively, where A and B are normalization constants. By the same token, the solution for Schrödinger equation in the well is

$$\Psi_2(x) = C\cos(k_2 x) + D\sin(k_2 x),$$

where C and D are normalization constants.

Applying the BenDaniel-Duke [177] boundary conditions at $x = -L_w/2$ and $x = L_w/2$, after some algebraic manipulation, we obtain

$$(A + B)e^{-k_1 L_w/2} = 2C\cos\left(k_2 L_w/2\right), \tag{5.20}$$

$$(B - A)e^{-k_1 L_w/2} = 2D\sin\left(k_2 L_w/2\right). \tag{5.21}$$

As the potential barriers have equal height, U_0, we can assume that $A = B$, that is, the probability of the electrons entering the barrier from the left of the well is equal to the one entering from the right of the well. Hence, from Eq. (5.21) results in $D = 0$. Again, considering $A = B$, from Eq. (5.20) we have a relation between A and C:

$$A = Ce^{-k_1 L_w/2}\cos\left(k_2 L_w/2\right). \tag{5.22}$$

Applying the normalization condition, $\int_{-\infty}^{\infty} |\Psi_i(x)|^2\, dx$, we have

$$\int_{-\infty}^{-L_w/2} \left|Ae^{k_1 x}\right|^2 dx + \int_{-L_w/2}^{L_w/2} |C\cos(k_2 x)|^2\, dx + \int_{L_w/2}^{\infty} \left|Be^{-k_1 x}\right|^2 dx = 1 \tag{5.23}$$

Combining Eq. (5.22) with Eq. (5.23), evaluating Eq. (5.23) and isolating C we have

$$C = \left[\frac{2k_1 k_2}{L_w k_1 k_2 + 2k_2\cos^2\left(k_2 L_w/2\right) + k_1\sin\left(k_2 L_w\right)}\right]^{\frac{1}{2}}, \tag{5.24}$$

by making $C = \sqrt{\upsilon}$ in Eq. (5.24) we have υ as:

$$\upsilon = \frac{2k_1k_2}{L_wk_1k_2 + 2k_2\cos^2(k_2L_w/2) + k_1\sin(k_2L_w)}$$

Hence, the wavefunction in the well is given by

$$\Psi_w(x) = \sqrt{\upsilon}\cos(k_2x),\ x \in (-L_w/2,\ L_w/2) \tag{5.25}$$

where the wave vectors are given by $k_1 = (1/\hbar)\sqrt{2m_b^*(U_0 - E_{r,1})}$ and $k_2 = (1/\hbar)\sqrt{2m_w^*E_{r,1}}$, m_b^* and m_w^* are the effective masses of the particle in the barrier region and in the well region, respectively.

Then, the Poisson equation for the well is written by taking $\rho_w(x) = -en_w\left|\Psi_w(x)\right|^2$, to provide $\nabla^2V_{well}(x) = -\rho_w(x)/\epsilon_w$. Solving the Poisson equation by setting $V_{well}(0) = 0$ and imposing continuity of the electric field displacement vector, $\mathbf{D} = \epsilon\mathbf{F}$, at the well/left barrier interface, at the emitter side of the RTD, $F_w(-L_w/2) = (\epsilon_b/\epsilon_w)F_{bL}$, yields:

$$V_{well}(x) = \frac{en_w\upsilon}{4\epsilon_w}\left(x^2 + \frac{\sin^2(k_2x)}{k_2^2}\right) + \left[\frac{en_a}{\epsilon_w} + \frac{en_w\upsilon}{4\epsilon_w}\left(\frac{\sin(L_wk_2)}{k_2} + L_w\right)\right]x, \tag{5.26}$$

Note that, since the barrier is undoped, the electric field across the left potential barrier is constant, $F_{bL} = (en_a)/\epsilon_b$, resulting from imposing the continuity of the $\mathbf{D}$ vector at the emitter/left barrier: $\epsilon_eF_e{=}\epsilon_bF_{bL}$ with F_e given by Eq. (5.6). Therefore, the voltage drop at the left potential barrier is $V_L = L_{bL}F_{bL}$.

Using Eq. (5.26), the voltage drop in the well, $V_w = V_{well}(L_w/2) - V_{well}(-L_w/2)$, is

$$V_w = \frac{en_aL_w}{\epsilon_w} + \frac{en_wL_w\upsilon}{4\epsilon_w}\left(\frac{\sin(L_wk_2)}{k_2} + L_w\right). \tag{5.27}$$

It is also worth noting that, when there is no space charge stored in the well, i.e., $n_w = 0$, the voltage drop $V_w = (en_aL_w)/\epsilon_w$. This result is expected since the barriers are undoped and the only electric charge in the double-barrier RTD is n_a, the charge in the emitter accumulation layer. Again, imposing the continuity of the $\mathbf{D}$ vector at the interface between the well and the right potential barrier, we have that the electric field at the right barrier is given by $F_{bR} =$

$(\epsilon_w/\epsilon_b)F_w(L_w/2)$. The electric field in the well is obtained by $F_w(x) = -\nabla V_{well}(x)$. Thus, as the barrier layers are undoped, the voltage drop in the right barrier is simply given by $V_R = L_{bR}F_{bR}$. Therefore, the total voltage drop in the double barrier configuration $V_{db} = V_L + V_w + V_R$ is obtained by adding up the voltage drop in the two potential barriers and the quantum well, yielding

$$\begin{aligned} V_{db} &= en_a\left(\frac{L_{bL}+L_{bR}}{\epsilon_b}+\frac{L_w}{\epsilon_w}\right)+\frac{en_w\upsilon\sin\left(L_wk_2\right)}{4k_2}\left(\frac{L_{bR}}{\epsilon_b}+\frac{L_w}{\epsilon_w}\right) \\ &+\frac{en_wL_{bR}\upsilon\left(\sin\left(L_wk_2\right)+L_wk_2\right)}{4k_2\epsilon_b}+\frac{en_wL_w\upsilon}{4}\left(\frac{L_{bR}}{\epsilon_b}+\frac{L_w}{\epsilon_w}\right). \end{aligned} \tag{5.28}$$

Finally, again applying the continuity of the $\mathbf{D}$ vector, we can calculate the voltage drop in the spacer layer placed between the right barrier and the collector as, $V_s = (\kappa_b/\kappa_c)\,F_{bR}L_S$:

$$\begin{aligned} V_s &= \frac{en_wL_S\upsilon\left(\sin\left(L_wk_2\right)+L_wk_2\right)}{4k_2\epsilon_c}+\frac{en_aL_S}{\epsilon_c} \\ &+\frac{en_wL_S\upsilon\sin\left(L_wk_2\right)}{4k_2\epsilon_c}+\frac{en_wL_SL_w\upsilon}{4\epsilon_c}, \end{aligned} \tag{5.29}$$

where ϵ_c is the permittivity constant of the collector semiconductor material and L_S is the width of the undoped spacer layer.

Collector Depletion Region

From the charge neutrality condition, following the approach proposed by [160], we have $Q_c = Q_e + Q_w$, where the negative electronic charge at the emitter, $Q_e = en_a$, and at the quantum well, $Q_w = en_w$, is balanced by the positive ionized charge at the depleted collector, Q_c. In other words, the charge neutrality condition can be rewritten as $n_t = n_a + n_w$, where n_t is the total ionized charge (per unit area) in the depletion region, which is a function of the applied voltage. Then, taking Fig. (5.2-a) as a reference for a generic multiple-layer in a staircase doping profile, we discuss three distinct bias conditions:

$$\begin{aligned} &Case\,1 \quad n_t < N_1L_1, \\ &Case\,2 \quad N_1L_1 < n_t < N_1L_1 + N_2L_2, \\ &Case\,3 \quad n_t > N_1L_1 + N_2L_2. \end{aligned} \tag{5.30}$$

It should be pointed out that the resulting expressions can be readily generalized for larger a number of layers, if needed, depending on the bias conditions as well as parameters including layer thickness and doping density.

Case 1 $n_t < N_1 L_1$

For the solution of the Poisson equation in the collector depletion region, we set the origin $x = 0$ at the interface between the spacer layer and the collector layer, of doping density N_1(see Fig. (5.2-a)). Hence, under the total depletion approximation, the Poisson equation becomes $\nabla^2 V_c(x) = -\left(eN_1\right)/\epsilon_c$ for $0 < x < \lambda_{d1}$, where λ_{d1} is the depletion region width. Integrating twice with respect to x yields

$$V_c(x) = -\frac{eN_1}{2\epsilon_c}x^2 + K_1 x + K_2,$$

where K_1 and K_2 are arbitrary constants to be determined by the boundary conditions. For simplicity, at the origin, we impose $V_c(0) = 0$ and, consequently, $K_2 = 0$. Next, considering an abrupt transition at the edge of the space charge region, the electric field in the collector, $F_c(x) = -\nabla V_c(x)$, is set to zero at $x = \lambda_{d1}$, yielding $K_1 = \left(eN_1\lambda_{d1}\right)/\epsilon_c$. To determine λ_{d1}, we employ the charge neutrality condition:

$$-en_a - en_w + eN_1\lambda_{d1} = 0. \tag{5.31}$$

From Eq. (5.18), $n_w = n_a\Lambda_w$. Then, the total negative charge is

$$n_t = n_a + n_w = n_a\left(1 + \Lambda_w\right). \tag{5.32}$$

By making $\zeta_a = 1 + \Lambda_w$ we have $n_t = n_a\zeta_a$, yielding $\lambda_{d1} = \left(n_a\zeta_a\right)/N_1$. Therefore, the voltage drop due to the space charge formation in the collector is

$$V_d = V_c(\lambda_{d1}) = \frac{e\zeta_a^2 n_a^2}{2\epsilon_c N_1}. \tag{5.33}$$

Case 2 $N_1L_1 < n_t < N_1L_1 + N_2L_2$

For this case, the depletion region width is greater than the width of the first section of the collector region, of doping level N_1. Hence, we have $L_1 < L_d < L_1 + L_2$, where L_d is the depletion region width, defined as $L_d = L_1 + \lambda_{d2}$, λ_{d2} defined as the depletion layer extension into layer L_2.

Fig. (5.3) shows a schematic illustration of the conduction band and the charge density profile for this case.

As in the previous case, we start by solving the Poisson equation:

$$\frac{d^2V_c(x)}{d^2x} = \begin{cases} -eN_1/\epsilon_c, 0 < x < L_1, \\ -eN_2/\epsilon_c, L_1 < x < L_1 + \lambda_{d2}, \end{cases} \tag{5.34}$$

Again, we set $V_{c,1}(0) = 0$. In addition, the electric field at edge of the depletion region, $x = L_1 + \lambda_{d2} = L_d$ is equal to zero. Imposing charge neutrality across the device, after some algebraic manipulation, the total voltage drop becomes

$$V_d = \frac{e\left(n_a\zeta_a - L_1N_1\right)^2}{2\epsilon_cN_2} + \frac{eL_1n_a\zeta_a}{\epsilon_c} - \frac{eL_1^2N_1}{2\epsilon_c}. \tag{5.35}$$

Case 3 $n_t > N_1L_1 + N_2L_2$

Although the expressions above can be easily generalized for increasing number of layers, care should be taken if the doping level becomes very high (see Fig. (5.2-a) for N_3). In the case of strong doping, the electrostatic screening effect becomes relevant and reduces the accuracy of the depletion approximation. An improved approximation is achieved by using the Thomas-Fermi screening formulation [160], [164]. In this case, an expression for voltage drop in the depletion region is given by [164]:

$$V_d = \frac{e}{\epsilon_c}\left[\left(n_a\zeta_a - \frac{N_1L_1}{2}\right)L_1 + \left(n_a\zeta_a - N_1L_1 + \frac{N_2L_2}{2}\right)L_2 + \left(n_a\zeta_a - N_1L_1 + N_2L_2\right)L_{TF}\right], \tag{5.36}$$

where the Thomas-Fermi length is written as:

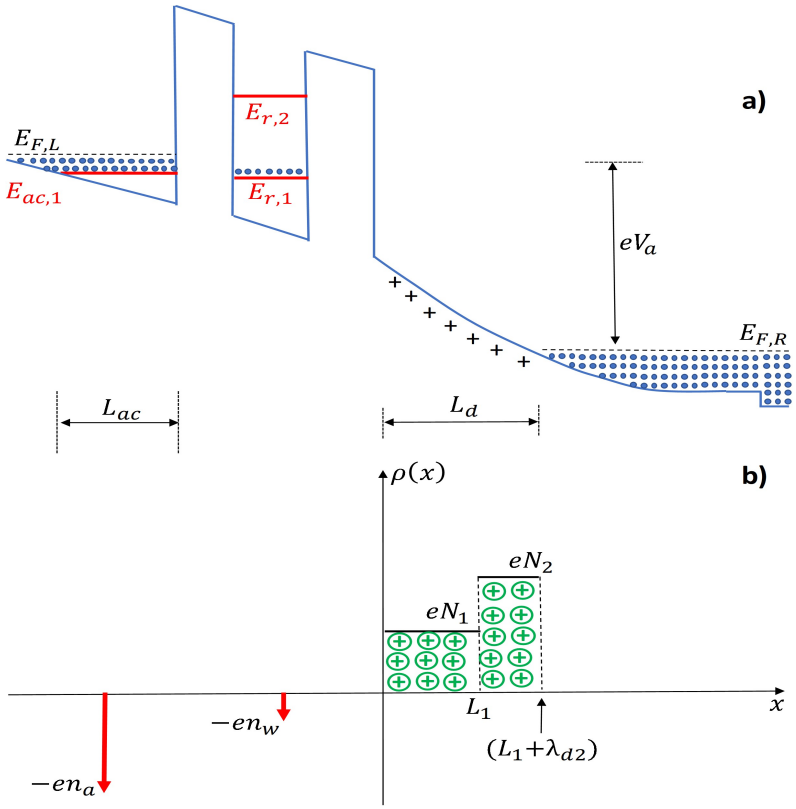

Figure 5.3: **Part (a)**: schematic illustration of the conduction band profile under the application of external bias, V_a.**Part (b):** schematic illustration of charge density profile for the case where the condition $N_1L_1 < n_t < N_1L_1 + N_2L_2$ is met.

$$L_{TF} = \left(\frac{\epsilon_c \hbar^2 \sqrt[3]{\pi^4}}{e^2 m_w^* \sqrt[3]{3N_3}} \right)^{\frac{1}{2}}. \tag{5.37}$$

Considering all the three sets of results discussed above, it is possible to write the voltage drop in the depletion region in a generic polynomial form:

$$V_d = A_d n_a^2 + B_d n_a + C_d, \tag{5.38}$$

where the constants A_d, B_d and C_d are:

$$A_d = \begin{cases} \frac{e\zeta_a^2}{2\epsilon_c N_1}, n_t \leq N_1L_1, \\ \frac{e\zeta_a^2}{2\epsilon_c N_2}, N_1L_1 < n_t \leq N_1L_1 + N_2L_2, \\ 0, n_t > N_1L_1 + N_2L_2, \end{cases}$$

$$B_d = \begin{cases} 0, n_t \leq N_1 L_1, \\ \frac{eL_1\zeta_a}{\epsilon_c} - \frac{eL_1N_1\zeta_a}{\epsilon_c N_2}, N_1L_1 < n_t \leq N_1L_1 + N_2L_2, \\ \frac{e\zeta_a}{\epsilon_c}\left(L_1 + L_2 + L_{TF}\right), n_t > N_1L_1 + N_2L_2, \end{cases}$$

$$C_d = \begin{cases} 0, n_t \leq N_1 L_1, \\ \frac{eL_1^2N_1^2}{2\epsilon_c N_2} - \frac{eL_1^2N_1}{2\epsilon_c}, N_1L_1 < n_t \leq N_1L_1 + N_2L_2, \\ \frac{e}{\epsilon_c}\left[-\frac{N_1L_1^2}{2} + \left(\frac{N_2L_2}{2} - N_1L_1\right)L_2\right. \\ \left. + \left(N_2L_2 - N_1L_1\right)L_{TF}\right], n_t > N_1L_1 + N_2L_2. \end{cases}$$

Then, having written the electrical potential distribution throughout the RTD structure as a function of electronic concentration n_a, next, we derive an expression to analytically compute the dependence of n_a as a function of the applied voltage V_a.

5.1.2 Analytical Approximation for Sheet Density $n_a(V_a)$

The diagram of Fig. (5.2-b), yields the straightforward relation

$$V_a = V_{ac} + V_{db} + V_s + V_d. \tag{5.39}$$

Replacing each respective voltage drop in Eq. (5.39) for their expressions in terms of the emitter charge density obtained in the previous sub-sections, yields

$$c_1 n_a^{2/3} + c_2 n_a^2 + c_3 n_a + c_4 = 0, \tag{5.40}$$

where the constants are

$$c_1 = \left(\frac{72e\hbar^2}{11m_e^*\epsilon_e^2}\right)^{1/3}, \; c_2 = A_d, \tag{5.41}$$

$$\begin{aligned} c_3 &= e\left(\frac{L_{bL}+L_{bR}}{\epsilon_b} + \frac{L_w}{\epsilon_w} + \frac{L_S}{\epsilon_c}\right) + \frac{e\Lambda_w \upsilon \sin\left(L_w k_2\right)}{4k_2}\left(\frac{L_{bR}}{\epsilon_b} + \frac{L_w}{\epsilon_w} + \frac{L_S}{\epsilon_c}\right) \\ &\quad + \frac{e\Lambda_w \upsilon\left(\sin\left(L_w k_2\right) + L_w k_2\right)}{4k_2}\left(\frac{L_{bR}}{\epsilon_b} + \frac{L_S}{\epsilon_c}\right) + \frac{e\Lambda_w L_w \upsilon}{4}\left(\frac{L_{bR}}{\epsilon_b} + \frac{L_w}{\epsilon_w} + \frac{L_S}{\epsilon_c}\right) + B_d, \\ c_4 &= C_d - V_a. \end{aligned} \tag{5.42}$$

To analytically find the roots of Eq. (5.40), it is necessary to eliminate the $2/3$ power dependency of n_a. The usual procedure is to express the equation in terms of $n_a^{2/3}$ and raise both sides of the equation to the third power, resulting in a sixth degree polynomial equation, which is quite cumbersome to handle. Instead, in order to find an approximation for the roots of Eq. (5.40), we expand the term $n_a^{2/3}$, in a Taylor series around the carrier density $n_{at} = E_F m^* / (\hbar^2 \pi)$, which is the maximum value for the carrier density in the accumulation layer, in the low-temperature limit.

Therefore, expanding $n_a^{2/3}$ up to the second order and replacing the expansion in Eq. (5.40):

$$d_2 n_a^2 + d_1 n_a + d_0 = 0, \tag{5.43}$$

where

$$\begin{aligned} d_2 &= c_2 - \frac{c_1}{9\,(n_m)^{\frac{4}{3}}} \\ d_1 &= c_3 + \frac{8c_1}{9\,(n_m)^{\frac{1}{3}}} \\ d_0 &= c_4 + \frac{2c_1\,(n_m)^{\frac{2}{3}}}{9} \end{aligned}$$

Solving Eq. (5.43) and choosing the positive root, one gets

$$n_a = \left| \frac{-d_1 + \sqrt{-4d_0 d_2 + d_1^2}}{2d_2} \right|, \tag{5.44}$$

where we take the absolute value of n_a to avoid unphysical mathematical solutions.

It is worth mention that, in order to evaluate the constants in Eqs. (5.41) and (5.42), it is necessary to have a first estimation for the depletion region width, or, in order words, the value of the total charge density $n_t = n_a + n_w$. To do so, it is enough to recognize that the resonance linewidth is quite narrow, is such way that $n_a \gg n_w$ out of resonance. Then, in a first approximation, $n_w = 0$ yielding $n_t = n_a$ with the depletion width restrict to condition 1, i.e., $n_t < N_1 L_1$. Then, it is possible to estimate the initial value of n_a using Eq. (5.44) and update the value of n_t, to compute A_d, B_d and C_d. Next, n_a is self-consistently recalculated through Eq. (5.44) to obtain a more accurate approximation. Finally, each term of the potential distribution

described in the previous sections is analytically computed and the process is repeated for the following bias point. In addition, under applied external voltage, in our model, the resonant energy level is approximated as

$$E_{r,n}(V_a) \approx E_{r,n}^{(0)} - e(V_{ac} + V_L + V_w/2) - E_{r,n}^{(2)}, \tag{5.45}$$

where $E_{r,n}^{(0)}$ is the resonant energy level in the quantum well in equilibrium, i.e., in the absence of an electrical field. To enhance accuracy, the term $E_{r,n}^{(2)}$ in Eq. (5.45) is the second order correction (first order correction vanishes due to symmetry) mostly due to the quantum Stark effect [2]. The Stark effect correction is analytically estimated by evaluating $E_{r,n}^{(2)} = e\,\langle \Psi_w | V_{well}(x) | \Psi_w \rangle$, with $\Psi_w(x)$ given by Eq. (5.25) and $V_{well}(x)$ given by Eq. (5.26):

$$\langle \Psi_w | V_{well}(x) | \Psi_w \rangle = \left(\frac{\upsilon^2 e n_w}{288 k_2^2 \epsilon_w} \right) \sum_{j=1}^{6} S_j, \tag{5.46}$$

where the terms S_j are:

$$\begin{aligned}
S_1 &= 3L_w^3 k_2^3 - 9L_w k_2 + 9L_w^2 k_2^2 \sin(L_w k_2), \\
S_2 &= 12 L_w k_2 \left[-2\cos^3\left(\frac{L_w k_2}{2}\right) + 3\cos^2\left(\frac{L_w k_2}{2}\right) \right], \\
S_3 &= -18\cos^2\left(\frac{L_w k_2}{2}\right) \sin(L_w k_2), \\
S_4 &= 8\cos\left(\frac{L_w k_2}{2}\right) \sin(L_w k_2), \\
S_5 &= -9\sin(L_w k_2) + 32\sin\left(\frac{L_w k_2}{2}\right).
\end{aligned}$$

5.1.3 Validation of the approximation for $n_a(V_a)$

To evaluate the accuracy of the proposed model for compute n_a, we used experimental data gathered from [164]. This device is referred to as RTD# 1 with the main physical parameters summarized in Table 5.1. Fig. (5.4) depicts a comparison between the experimental results extracted from [164] (symbols) and the results provided by our model (solid red curve). As it can be seen from Fig. (5.4), an excellent agreement with experimental data is observed. In addition, consistent with the experimental data, our model can also describe the drop in the magnitude of n_a, which occurs at resonance due to space charge buildup in the quantum well.

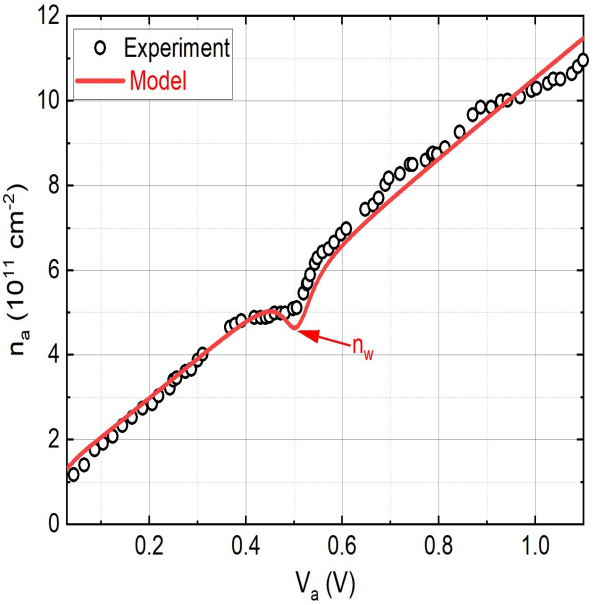

Figure 5.4: 2D electron sheet density in the emitter, n_a, obtained experimentally in [164] (symbols), and computed by the proposed analytical model (solid curve), Eq. (5.44). The figure also indicates the resonant bias point for charge storage in the well, n_w, due to to the resonant tunneling process.

To also validate our approximations for the quantized energy levels in the emitter and in the well, as a function of the bias voltage, we used the self-consistent solution reported on [161]. Fig. (5.5) compares the values of $E_{r,1}$, $E_{ac,1}$ and $E_{ac,2}$, with respect to the Fermi level and as a function of the applied bias, obtained through the self-consistent numerical solution [161], as well as analytically, by our model through the expressions Eq. (5.5) and Eq. (5.45). As it can be seen from Fig. (5.5), our model provides a very close agreement to the numerical solution.

We also compared our results with the experimental data reported in [178], for the eigenenergies levels under bias applied. Fig. (5.6) depicts the eigenenergies values $E_{r,1}$and $E_{ac,1}$ in respect to the Fermi level, as function of applied bias, comparing the experimental results from [178] (symbols) to the results provided by our model (solid lines) through expressions Eq. (5.45) and Eq. (5.5). Again, our model shows an excellent agreement to experimental data.

5.1.4 Tunneling Transmission Coefficient

As shown in Chapter 4, the PVCR of the RTD characteristic curve at resonance is much smaller than predicted by the idealized Tsu-Esaki model. The main cause for this reduction

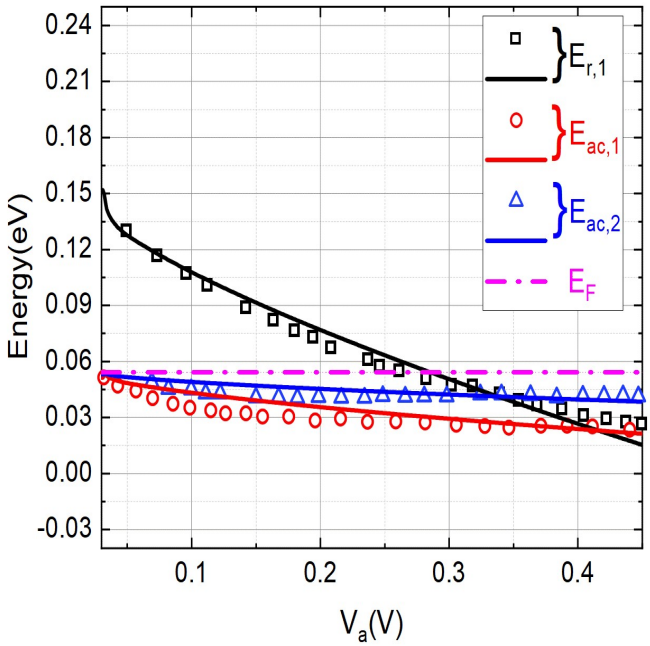

Figure 5.5: Self-consistent numerical solution for the eigenstates, $E_{ac,1}$ (circles), $E_{ac,2}$ (triangles), of the accumulation layer formed in the emitter, as well as for the first subband level in the quantum well, $E_{r,1}$ (squares), under the applied bias. The potential energy reference is the Fermi level position, obtained from [161]. The solid curves represent the solution computed analytically by our model for $E_{ac,1}$, $E_{ac,2}$ and $E_{r,1}$. The Fermi energy level position, E_F, is also shown (Dash-Dot symbols).

on the PVCR is the loss of the phase coherence in the resonant tunneling, caused by intrasubband scattering mechanisms, in particular the interaction between electrons and longitudinal optical phonons (LO-phonons) in the current transport process [135]- [148]. For double-barrier RTDs, the tunneling transmission coefficient is dependent both on the applied voltage as well as scattering mechanisms. To account for both effects and describe the additional broadening due to phonon scattering, we used the Lorentzian approximation proposed by Büttiker [172]:

$$\mathbf{T}_n(E,V_a) = \frac{\Gamma_L\Gamma_R}{(\Gamma_L+\Gamma_R)}\left(\frac{\Gamma_T}{\Gamma_T^2/4+(E-E_{r,n}(V_a))^2}\right). \tag{5.47}$$

In the equation above $\mathbf{T}_n(E,V_a)$ is the electronic transmission coefficient for an electron in the n-*th* subband of the quantum well (QW), E is the incident kinetic energy for the electron while $E_{r,n}(V_a)$ refers to the n-*th* eigenenergy in the quantum well under the applied voltage V_a. Γ_L and Γ_R account for the left and right barrier intrinsic resonance linewidths, respectively. The use of distinct values for the barriers of each side of the well allows the modeling of asymmetric

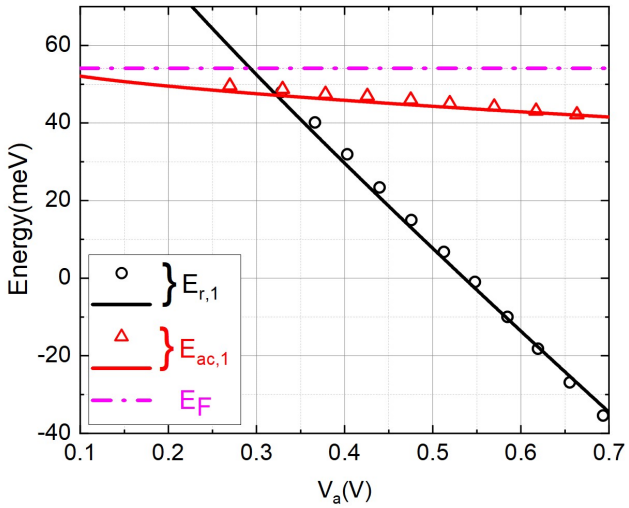

Figure 5.6: Symbols indicate the experimental data obtained from [178] for the eigenstates, $E_{ac,1}$ (circles) of the accumulation layer in the emitter and the first subband in the quantum well , $E_{r,1}$ (triangles), with respect to the Fermi level, under applied bias. The solid curves show the solution computed by our model. The Fermi energy level position, E_F, is also indicated (Dash-Dot symbols).

QWs, if required. Then, the term Γ_T refers to the total resonance linewidth given by $\Gamma_T = \Gamma_L + \Gamma_R + \Gamma_s$, where $\Gamma_s \approx 2\hbar/\tau_s$ is the linewidth due to scattering by LO-phonons and τ_s is momentum relaxation time given by Eq. (4.48) [179]. As demonstrated by Mizuta *et al.* [173], the approximation for Γ_s, shows good agreement with experimental data.

Next, the left and right intrinsic resonance linewidths are

$$\Gamma_{L,\,R} = \frac{v_w \hbar \mathbf{T}_{L,\,R}(E_{ac,m}, V_a)}{2L_w},$$

with the electron velocity in the well $v_w = \sqrt{2E_{r,n}/m_w^*}$ [172]. Finally, in our proposition, we used the WKB approximation (Eq. (2.45)) to calculate the tunneling transmission coefficient $T_{L,\,R}(E_{ac,m}, V_a)$ for a single potential barrier case as a function of applied bias, as

$$\mathbf{T}_{L,\,R}(E_{ac,m}, V_a) = \exp\left\{-\frac{4L_{bL,\,bR}\sqrt{2m_b^*}}{3\hbar e V_{L,\,R}}\left[(U_{L,R})^{3/2} - (U_{L,R} - eV_{L,\,R})^{3/2}\right]\right\}, \qquad (5.48)$$

where, from Fig. (5.2), the effective left-barrier height under applied bias, assuming an energy level $E_{ac,m}$, is $U_L = U_0 - E_{ac,m}$, while for the right side $U_R = U_L - eV_L - eV_w$.

5.1.5 2D-2D Current Density Model

For small values of Γ_T, the transmission coefficient becomes negligible, except when electron kinetic energy is aligned to one of the resonant levels in the well, $E_{r,n}$. Hence, under an applied bias voltage, we approximate $E_x \approx E_{r,n}(V_a)$ where E_x is kinetic energy component related to the electron velocity in the x-direction and $E_{r,n}(V_a)$ is given by Eq. (5.45). Accordingly, the logarithmic part of Eq. (4.33) can be taken out of the integral [82]. Also, it is considered that the emitter eigenenergy, $E_{ac,m}$, in the quasi-triangular well has linewidth Γ_Δ, comparable to the LO-phonon's linewidth, i.e., $\Gamma_\Delta \simeq \Gamma_s$, which is fair approximation for RTDs [164], [178]. Then, replacing the term $\mathbf{T}(E_x, V_a)$ in Eq. (4.33) by means of the Büttikir approximation provided by Eq. (5.47) and replacing E_x in Eq. (4.33) for Eq. (5.45), it becomes possible to integrate Eq. (4.33) from $(E_{ac,m} - \Gamma_\Delta/2)$ up to $(E_{ac,m} + \Gamma_\Delta/2)$, to finally write a generalized expression for the the resonant current density, as given by

$$\begin{aligned} J(V_a) &= \frac{em_e^* k_B T}{\pi^2 \hbar^3} \left(\frac{\Gamma_L \Gamma_R}{\Gamma_L + \Gamma_R} \right) \sum_m \sum_n \ln \left(\frac{1 + \exp\left[\left(E_{ac,m} - E_{r,n}(V_a) \right) / k_B T \right]}{1 + \exp\left[\left(E_{ac,m} - E_{r,n}(V_a) - eV_a \right) / k_B T \right]} \right) \\ &\quad \times \left[\arctan\left(\frac{E_{ac,m} + \Gamma_\Delta/2 - E_{r,n}(V_a)}{\Gamma_T/2} \right) - \arctan\left(\frac{E_{ac,m} - \Gamma_\Delta/2 - E_{r,n}(V_a)}{\Gamma_T/2} \right) \right], \end{aligned} \tag{5.49}$$

where the summations in Eq. (5.49) describe the contribution of all energy levels in the quasi-triangular well as well as in the rectangular QW in the active region of the RTD. The complete scheme for obtaining the 2D-2D current density in RTD is summarized in the flowchart depicted in Fig. (5.7).

In next section, the model is applied to a series of devices experimentally demonstrated in the literature.

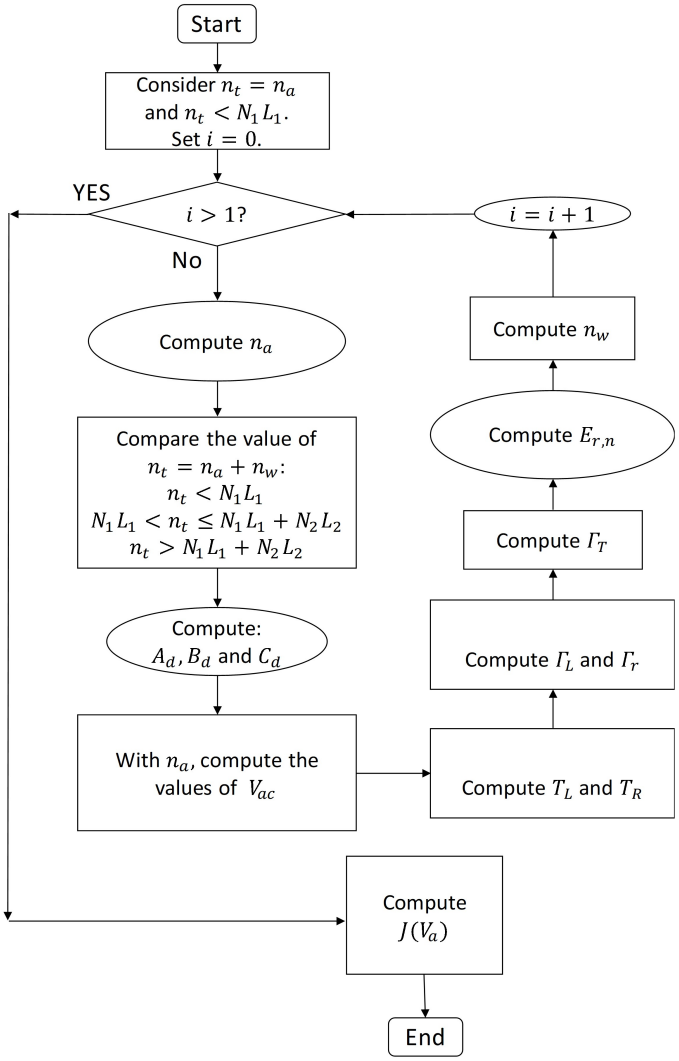

Figure 5.7: Flowchart of the proposed model to calculate the current density for the 2D-2D RTD.

5.1.6 Results and Discussion for 2D-2D Model

In order to validate our model, we contrasted the results obtained from Eq. (5.49) to experimental data extracted from five RTD structures reported in the technical literature. To ensure the comparison with true 2D-2D based RTDs, we restricted ourselves to experimental data in which the nature of quantized emitter was experimentally verified. Table 5.1 describes the layer structure, including thickness, material composition and nominal doping levels, operating temperature, and mesa configuration, of the five RTDs used to validate our compact model. The double barrier region in all the structures in Table 5.1 are undoped. The nominal doping levels

Table 5.1: The composition, nominal doping levels, relevant structures geometrical dimensions and operating temperatures of five RTD's structures used to validate our model.

Structure	RTD#1 [164]	RTD#2 [147]	RTD#3 [147]	RTD#4 [178]	RTD#5 [180]
T	$77\,\mathrm{K}$	$4\,\mathrm{K}$	$4\,\mathrm{K}$	$4.2\,\mathrm{K}$	$2\,\mathrm{K}$
[Al]	$x = 0.4$	$x = 0.4$	$x = 0.4$	$x = 0.31$	$x = 0.35$
Mesas	$\pi \times 10^{-8}\,\mathrm{m}^2$	$\pi \times 10^{-8}\,\mathrm{m}^2$	$4\pi \times 10^{-8}\,\mathrm{m}^2$	$60 \times 60\text{-}\mu\,\mathrm{m}^2$	$500\mu\,\mathrm{m} \times 600\mu\,\mathrm{m}$
(N_3, L_3)	$2 \times 10^{18}, 2\ \mu\mathrm{m}$	$2 \times 10^{18}, 2\ \mu\mathrm{m}$	$2 \times 10^{18}, 0.5\ \mu\mathrm{m}$	$1 \times 10^{18}, 0.3\ \mu\mathrm{m}$	$1 \times 10^{18}, 0.3\ \mu\mathrm{m}$
(N_2, L_2)	$2 \times 10^{16}, 500$ Å	$2 \times 10^{16}, 500$ Å	$1 \times 10^{17}, 500$ Å	$1 \times 10^{16}, 600$ Å	$1 \times 10^{16}, 600$ Å
(N_1, L_1)			$1 \times 10^{16}, 500$ Å		
L_s	25 Å	25 Å	33 Å		
L_{bL}	56 Å	56 Å	111 Å	100 Å	100 Å
L_w	50 Å	117 Å	58 Å	50 Å	50 Å
L_{bR}	56 Å	56 Å	83 Å	100 Å	100 Å
L_s	25 Å	25 Å	33 Å		
(N_1, L_1)	$2 \times 10^{16}, 500$ Å	$2 \times 10^{16}, 500$ Å	$1 \times 10^{16}, 500$ Å	$1 \times 10^{16}, 600$ Å	$1 \times 10^{16}, 600$ Å
(N_2, L_2)	$2 \times 10^{18}, 0.5\ \mu\mathrm{m}$	$2 \times 10^{18}, 0.5\ \mu\mathrm{m}$	$1 \times 10^{17}, 500$ Å	$1 \times 10^{18}, 0.3\ \mu\mathrm{m}$	$1 \times 10^{18}, 0.3\ \mu\mathrm{m}$
(N_3, L_3)			$2 \times 10^{18}, 2\ \mu\mathrm{m}$		

are in unit of cm^{-3}. For all devices used in this work the emitter and collector are composed of n-GaAs material. The barriers and the well are composed of $\mathrm{Al}_x\mathrm{Ga}_{1-x}\mathrm{As}$ and GaAs undoped semiconductors, respectively.

The electronic effective masses and the dielectric constants in the alloy $\mathrm{Al}_x\mathrm{Ga}_{1-x}\mathrm{As}$, as well the theoretical value of U_0, were obtained from [75]. Also, for GaAs, the effective masses is $m^*_{GaAs} = 0.067m_0$, where m_0 is the rest mass, and the theoretical value of the LO-phonon energy is $\hbar\omega_{LO} = 36.25\ m\,\mathrm{eV}$ [75]. In all devices used to validate our model it was enough to consider only the first energy level both in the emitter quasi-triangular quantum well at the emitter side and in the rectangular quantum well, i.e., $m = n = 1$ in our model.

For the device RTD#1 the experimental data is obtained from [164] and the main features of the device are summarized in Table 5.1. As it can be seen from Fig. (5.8), the **I-V** characteristic provided by our model display an excellent agreement with the experimental findings. To

achieve this agreement, a minimal adjustment in the width of the potential barriers, concerning their nominal value, was necessary. Specifically, the adjusted value was 58.5 Å, relatively to the nominal value of 56 Å. The difference, of the order of few Bohr radii, is within the uncertainty range of all major epitaxial growth techniques.

For RTD#2 the experimental data is obtained from [147] and the main features of the device are summarized in Table 5.1. As it can be seen from Fig. (5.9), the **I-V** characteristic described by the proposed model presents a quite good agreement with the experimental data. This turn, to achieve the agreement, a small adjustment in the width of the quantum well was necessary. The value used in our model was 112 Å (only 5 Å difference from the nominal value). In addition, we assumed an unintentional doping level of $n = 10^{15}\ cm^{-3}$ for the GaAs spacer layer of 25 Å, which was nominally undoped.

For RTD#3, we used the experimental data from another RTD described in [147] and the main features of this device are summarized in Table 5.1. As it can be seen from Fig. (5.10), the **I-V** characteristic described by the proposed model presents an excellent agreement with the experimental data. To achieve this result, a small adjustment in some nominal parameters were necessary, namely: $L_w = 56.5$ Å, $L_{bL} = 110.5$ Å and $n = 0.85 \times 10^{16}\ cm^{-3}$. Again, all three are small deviations from the nominal values, well within the fabrication tolerances of established epitaxial growth techniques.

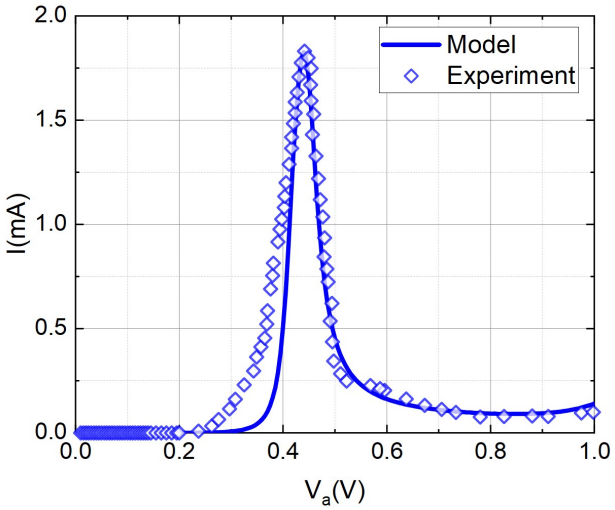

Figure 5.8: Comparison between the **I–V** curves obtained by the proposed 2D-2D current density model (solid curve) and the experimental curve (symbols) of the RTD #1 [164]. Data was measured at 77 K.

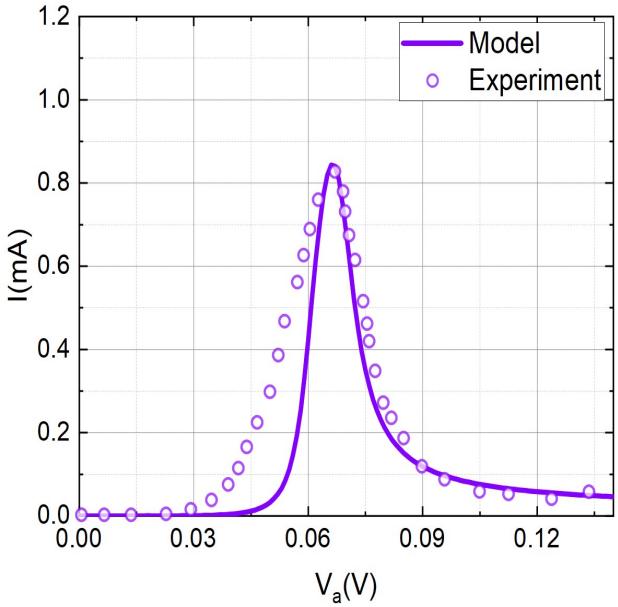

Figure 5.9: Comparison between the **I–V** curves obtained by the proposed 2D-2D current density model (solid curve) and the experimental curve (symbols) of the RTD #2 [147]. Data were measured at 4 K.

For RTD#4, the experimental data is obtained from [178] and the main features of the device are summarized in Table 5.1. As it can be seen from Fig. (5.11), the **I-V** characteristic described by the proposed model presents an excellent agreement with the experimental data. Once again, a small adjustment in the width of the potential barriers, relatively to the nominal value, was necessary. The value used in our calculation was 103 Å, an increase of only 3 Å.

Finally, for RTD#5, the experimental data is obtained from [180] and the main features of RTD#5 are summarized in Table 5.1. The model correctly predicts the PVCR ratio and the peak current position, as it can be seen from Fig. (5.12). In order to obtain this agreement, only a minor adjustment in the width of the quantum well, from the nominal value of 50 Å (see Table 5.1) to 48 Å, was necessary. However, the shoulder-like shape in the **I-V** curve around 0.5 V, as well as the fluctuations registered in the valley region, are not captured by the model. This is because these anomalies have been associated to an intrinsic bistability effect as well as the charge feedback mechanism between the emitter and well, which sometimes arises at resonance [164], [160]. Neither one of those undesired effects were accounted for in our model Also, it should be pointed out that the only broadening mechanism included in our model is the scattering for LO-phonons. Therefore, the observed discrepancy between theory

and experiment also means that other broadening mechanisms play an important role in the shaping of the **I-V**curve for this particular device.

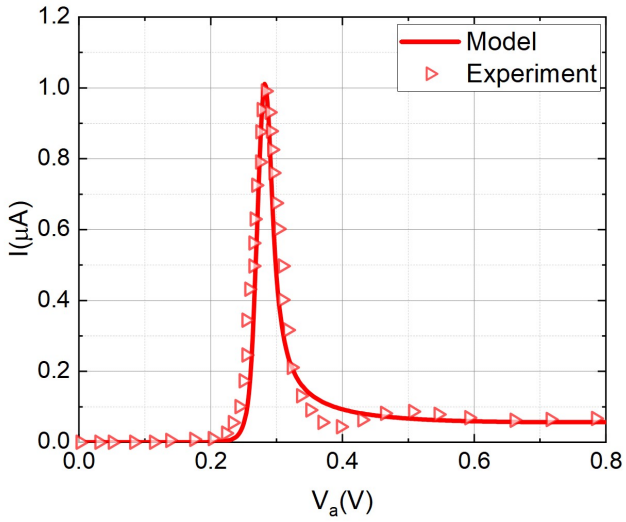

Figure 5.10: Comparison between the **I–V** curves obtained by the proposed 2D-2D current density model (solid curve) and the experimental curve (symbols) of the RTD #3. [147]. Data was measured at 4 K

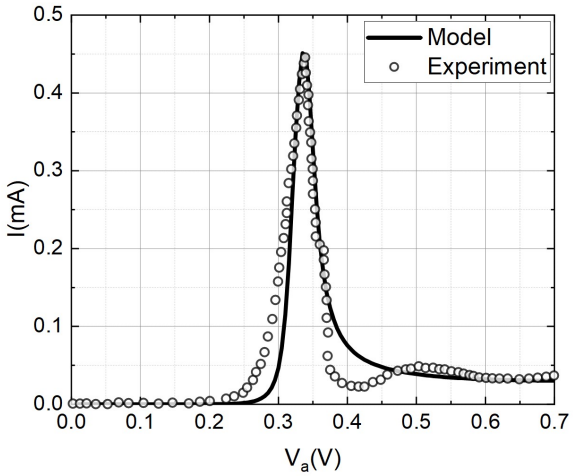

Figure 5.11: Comparison between the **I–V** curves obtained by the proposed 2D-2D current density model (solid curve) and the experimental curve (symbols) of the RTD #4 [178]. Data was measured at 4.2 K.

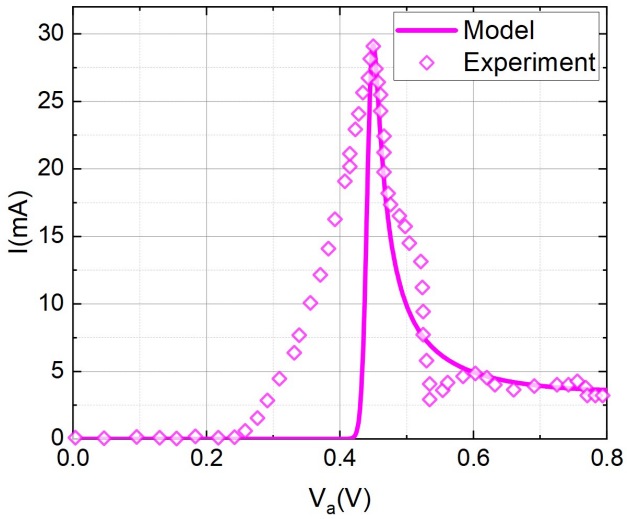

Figure 5.12: Comparison between the **I–V** curves obtained by the proposed 2D-2D current density model (solid curve) and the experimental curve (symbols) of the RTD #5. [180]. Data was measured at 2 K.

5.2 Model for the I–V Characteristics of 3D-2D RTD

5.2.1 Electric Field and Potential Distribution Model

Similarly to Section 5.1, we start by considering the electrical potential distribution across the device. Fig. (5.13-a) shows a schematic illustration of the potential double barrier region in equilibrium. Fig. (5.13-b) shows a schematic illustration of the double barrier potential RTD structure under an applied bias voltage (V_a). Fig. (5.13-c) shows a schematic illustration of the charge density distribution within the structure.

As pointed out n the discussion of the 2D-2D model, obtaining a reliable physics-based model is necessary to accurately describe the electric field distribution across the structure, giving raise to an accumulation region at the emitter layer and a depletion region at the collector layer. Depending on the thickness of these spacer layers and the operating temperature, a quasi-triangular quantum well may form at the emitter, yielding a 2DEG. This energy-level quantization feature usually occurs in very low-temperature regimes, as Section 5.1 illustrates. On the other hand, for the 3D-2D case, we now derive a model to describe the case where there is no quantum well at the emitter region. Therefore, the model in the present sub-section considers the resonant current density as 3D-2D (three-dimensional emitter to a 2DEG quantum

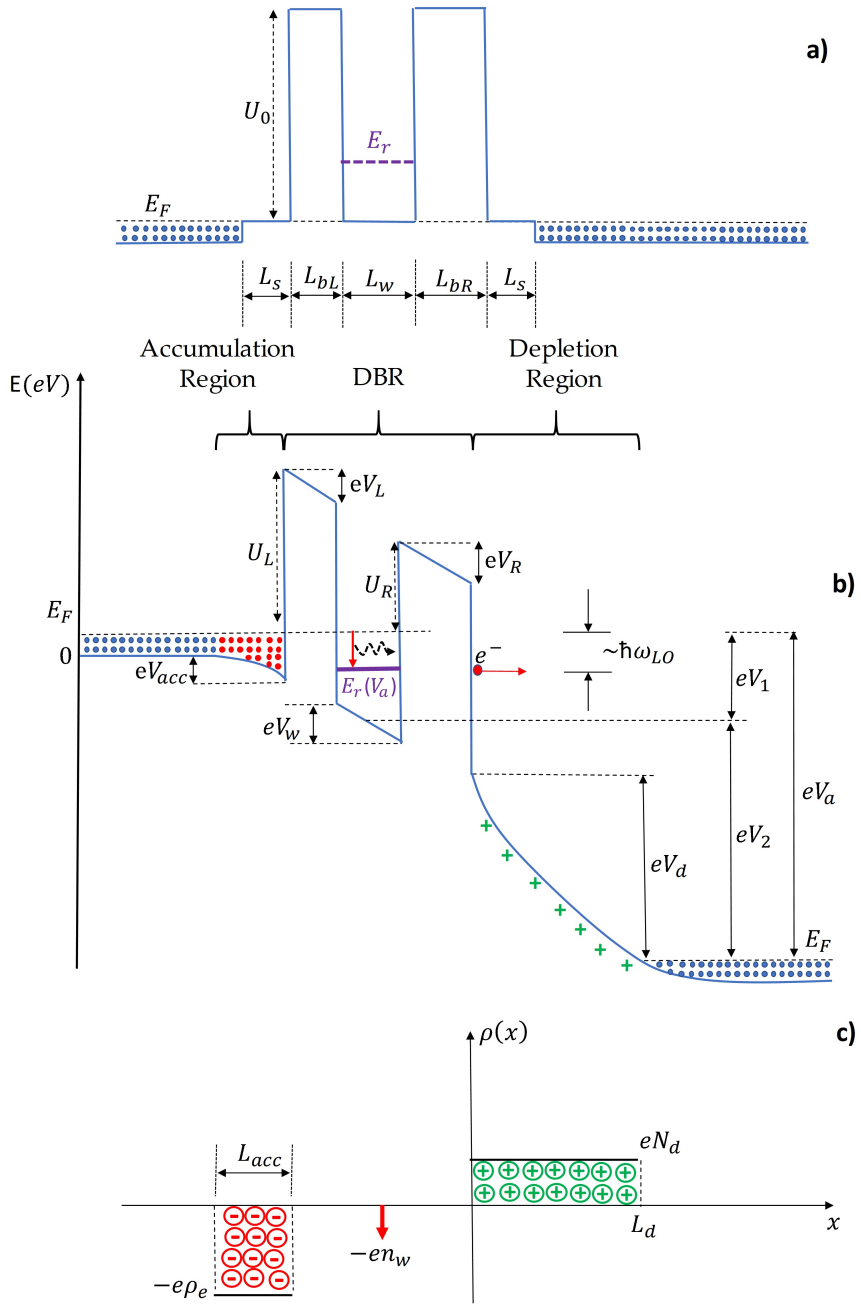

Figure 5.13: Part (a) shows a schematic illustration of an arbitrary double barrier potential RTD structure; (b) the same conduction-band profile subjected to an external bias voltage, V_a; and (c) the corresponding charge-density distribution.

well).

The starting point is to compute the space charge formation along the device. To do so, the electric potential distribution is calculated in a set of distinct regions as schematically illustrated

in Fig. (5.13-b). Since there is no quantization at the emitter side, our approach to describe the electric potential distribution in 3D-2D RTDs differs slightly from the 2D-2D model.

Under bias, Sheard and Toombs [160] argue that the RTD is electrostatically equivalent to a pair of identical parallel plate capacitors in series with a negative charge $-Q_w$ on the center plate, representing the quantum well. To improve their approach, we consider the RTD as two distinct capacitors in series: C_1 and C_2. This consideration is more realistic because it takes into account charge storage in the quantum well. Hence, unlike [160], the absolute value of the space charge in the emitter, $|Q_e|$, is different from the space charge in the collector, $|Q_c|$. A schematic illustration of the charge distribution is presented in Fig. (5.13-c).

Next, we determine the voltage drop in the accumulation region at the emitter, V_{acc}. To do so, we assume a uniform charge density as a function of the applied voltage, $\rho_e(V_a)$. Therefore, we can write $|Q_e(V_a)| = e\rho_e(V_a)L_{acc}$ (per unit area), where L_{acc} is an effective value that accounts for the accumulation region width. Then, Poisson's equation is taken as:

$$\nabla^2 V_e(x) = \frac{e\rho_e}{\epsilon_e}, \tag{5.50}$$

and the electric field at this layer is given by $F_e(x') = -\nabla V_e(x)$, where $x = 0$ is placed at the left-hand side of the left barrier. To solve the Poisson equation, we use the traditional boundary conditions, i.e., imposing $V_e(0) = 0$ and $F_e(-L_{acc}) = 0$, thereby considering an abrupt transition at the edge of the quasi-neutral zone. Thus, the voltage drop in the accumulation region is given by

$$V_{acc} = \frac{e\rho_e L_{acc}^2}{2\epsilon_e} = \frac{Q_e L_{acc}}{2\epsilon_e}. \tag{5.51}$$

Assuming a high electronic concentration in the accumulation region, we estimate L_{acc} using the Thomas-Fermi screening theory [160]:

$$L_{acc} = \left(\frac{\epsilon_e \hbar^2}{e^2 m_e^*} \sqrt[3]{\frac{\pi^4}{3N_d}} \right)^{\frac{1}{2}}. \tag{5.52}$$

The electric field at the interface between the accumulation region and the potential-barrier layer is $|F_e(0)| = Q_e/(\epsilon_0 \kappa_e)$. By imposing the continuity of the electric displacement vector (**D**) at this interface, $\epsilon_e \mathbf{F}_e(0) = \epsilon_{bL}\mathbf{F}_{bL}$, we obtain the electric field at the left-barrier layer as $|F_{bL}| = Q_e/\epsilon_{bL}$, where ϵ_{bL} is the electric permittivity at the left-barrier layer. Since

the potential-barrier layer is undoped, the voltage drop is simply given by $V_L = |F_{bL}|\, L_{bL} = (Q_e L_{bL})\,/\epsilon_{bL}$.

The next step in our model is to find a mathematical expression for the charge stored in the quantum well. This charge storage results from the steady-state carrier from the accumulation region (tunneling through the potential barrier). In our work, we modify the expression provided by [160], originally proposed for the low temperature limit (0 K), to account for the finite temperature effects. The authors used a rate-equation approach to relate the electronic charge at the emitter to the stored charge in the rectangular quantum well. Their expression accounts for energy and momentum conservation, and the final result is weighted by $T_L/(T_L + T_R)$, where T_L and T_R are the single-barrier transmission coefficients relative to the left- and right-barrier, respectively [160]. The derivation of this expression is outlined in Sec. 5.1.1. We consider the 2-DEG charge density in the quantum well as $|Q_w| = en_w$, where n_w is the sheet carrier density in the well. Hence, taking only the first subband in the quantum well, we have

$$n_w \approx \frac{T_L}{T_L + T_R} \int_{E_1}^{\infty} g_{2D} f\,(E - E_F)\, dE, \tag{5.53}$$

where g_{2D} is the two-dimensional effective electron density of states (DoS), and f is the Fermi-Dirac distribution. Therefore, the charge in the quantum well can be estimated by

$$Q_w \approx \frac{e m_w^* k_B T}{\pi \hbar^2} \frac{T_L}{T_L + T_R} \ln\left\{1 + \exp\left(\frac{E_F - E_n(V_a)}{k_B T}\right)\right\}, \tag{5.54}$$

where m_w^* is the effective mass of the electron in the quantum-well.

To account for the voltage drop in the quantum well due to charge storage, we take $\rho_w(x') = -en_w\,|\Psi_w(x')|^2$. Consequently, Poisson's equation is given by $\nabla^2 V_{well}(x') = -\rho_w(x')/\epsilon_w$. Proceeding as outlined in Section 5.1.1, the required wave function, neglecting the shallow penetration in the barriers, is

$$\Psi_w(x') = \left(\frac{2}{L_w + (q_1)^{-1}\sin(q_1 L_w)}\right)^{\frac{1}{2}} \cos(q_1 x'), \tag{5.55}$$

where L_w is the width of the rectangular quantum well. In this case, the reference, $x' = 0$, is placed at the center of the quantum well. The wave vector associated with the lowest subband

is $q_1 = (1/\hbar)\sqrt{2m_w^* E_1}$, where the energy level E_1 is computed analytically by our model described in Chapter 3.

To solve the Poisson equation, we set $V_{well}(0) = 0$. Then, by imposing continuity of $\mathbf{D}$ at the quantum-well/left-barrier interface, we have:

$$V_{well}(x') = \frac{Q_w}{2q_1\epsilon_w}\left(\frac{\sin^2(q_1x') + q_1^2x'^2}{q_1L_w + \sin(q_1L_w)}\right) + \left(\frac{Q_e}{\epsilon_w} + \frac{Q_w}{2\epsilon_w}\right)x', \tag{5.56}$$

valid for $-L_w/2 \leq x' \leq L_w/2$. Hence, the voltage drop in the quantum well, $V_w = V_{well}(L_w/2) - V_{well}(-L_w/2)$, is

$$V_w = \frac{Q_eL_w}{\epsilon_w} + \frac{Q_w}{\epsilon_w}\frac{L_w}{2}. \tag{5.57}$$

Inspecting the contribution of Q_w to Eq. (5.57), in a similar fashion to [160], we can understand this result as if the electrons in the quantum well are effectively described as a charge sheet of infinitesimal thickness located at $x' = 0$. By knowing the position of the common plate capacitor ($x' = L_w/2$), one can determine the capacitances and their respective voltage drops. Hence, the voltage drops across the emitter and collector capacitors are $V_1 = Q_e/C_1$ and $V_2 = Q_c/C_2$, respectively (see Fig. (5.13-b)). The geometric capacitances (per unit area) are:

$$\frac{1}{C_1} = \frac{L_{acc}}{\epsilon_e} + \frac{L_{bL}}{\epsilon_{bL}} + \frac{L_w}{2\epsilon_w}, \tag{5.58}$$

$$\frac{1}{C_2} = \frac{L_w}{2\epsilon_w} + \frac{L_{bR}}{\epsilon_{bR}} + \frac{L_d}{\epsilon_c}, \tag{5.59}$$

where κ_e, κ_c, κ_{bR} and κ_w are the dielectric constants at the emitter, collector, right-barrier and quantum-well layers, respectively. The terms L_{bL} and L_{bR} are the widths of the potential-barrier to the left and right sides of the well, respectively. The term L_d is the width of the depletion region.

For the depletion region at the collector layer, we consider the total depletion approximation, with the charge density being $\rho_c = |e|\,N_d$, where N_d is the effective doping concentration. Thus, we can write the depletion charge density as $Q_c = |e|\,N_dL_d$. The charge neutrality principle requires that $Q_c = Q_e + Q_w$. Therefore, the depletion width is $L_d = (Q_e + Q_w)/eN_d$. Starting by substituting L_d in Eq. (5.59) and noticing that $V_a = V_1 + V_2$, leads to

$$V_a = \frac{Q_e}{C_1} + \frac{Q_e + Q_w}{C_2}$$

and we can write:

$$V_a = aQ_e^2 + bQ_e + c, \tag{5.60}$$

where

$$a = \frac{1}{e\epsilon_c N_d},\ b = \frac{1}{C_1} + \frac{Q_w}{e\epsilon_w N_d} + \eta \text{ and } c = Q_w\eta.$$

$$\eta = \frac{Q_w}{e\epsilon_w N_d} + \frac{L_{bR}}{\epsilon_{bR}} + \frac{L_w}{2\epsilon_w}.$$

By solving Eq. (5.60) and choosing the positive root, we have:

$$Q_e(V_a) = -\frac{1}{2a}\left(b - \sqrt{4aV_a - 4ac + b^2}\right). \tag{5.61}$$

The electric field at the right-barrier F_{bR} is determined by imposing the continuity of $\mathbf{D}$ at the well/right-barrier interface. Then, the voltage drop is $V_R = |F_{bR}|\, L_{bR}$:

$$V_R = \frac{Q_e L_{bR}}{\epsilon_{bR}} + \frac{Q_w L_{bR}}{\epsilon_{bR}}. \tag{5.62}$$

As observed in real devices, Eq. (5.62) demonstrates that the voltage drops in the potential barriers are unequal even if $L_{bL} = L_{bR}$ given that there is charge stored in the quantum well. Finally, from the band diagram depicted in Fig. (5.13-a), the voltage drop at the depletion region is $V_d = V_a - V_{acc} - V_L - V_w - V_R$.

In addition, under an applied external voltage, the resonant energy level shift is approximated in our model as

$$E_n(V_a) \simeq E_n^{(0)} - eV_1 - E_n^{(2)}, \tag{5.63}$$

where $E_n^{(2)}$ is a second-order correction due to the quantum well electric field generated by the space charge. Again, $E_n^{(2)}$ is essentially the energy level shift caused by the Quantum-Confined Stark Effect [181], given by $E_n^{(2)} = e\,\langle\Psi_w|V_{well}(x)|\Psi_w\rangle$:

$$E_n^{(2)} = \frac{eQ_w}{24\epsilon_w S_0^2 q_1^3}\left\{L_w^3 q_1^3 + 3L_w^2 q_1^2 \sin(L_w q_1) + [12L_w q_1 - 6\sin(L_w q_1)]\cos^2(L_w q_1/2) - 3L_w q_1 - 3\sin(L_w q_1)\right\}, \quad (5.64)$$

where $S_0 = L_w + (q_1)^{-1}\sin(q_1 L_w)$.

To increase accuracy, our 3D-2D RTD model takes T_L and T_R as dependent of $V_L(V_a)$ and $V_R(V_a)$, respectively. Moreover, $V_L(V_a)$ and $V_R(V_a)$ are a function of the charge in the well, Q_w, which in turn is a function of T_L and T_R, i.e., the charge in the well modifies the voltage drop at the barriers. Rigorously, the problem must be solved self-consistently. Alternatively, to avoid numerical procedures, we take $Q_w \ll Q_e$ when out of resonance to obtain an approximate solution in two steps. First, we calculate the voltage drop considering $Q_w = 0$. Then, after estimating the T_L and T_R, we recalculate each voltage drop term taking $Q_w \neq 0$.

5.2.2 3D-2D Current Model

In the resonant model, the transmission coefficient becomes negligible, except when the electron kinetic energy in x-direction, E_x, is aligned with the resonant levels in the quantum well, E_n. Thus, under applied bias, we can make $E_x \approx E_n(V_a)$ with $E_n(V_a)$ given by Eq. (5.63). Accordingly, the logarithmic part of Eq. (4.33) can be pulled out of the integral [82].

The tunneling transmission coefficient is computed by Eq. (5.47) described in Sec. (5.1.4). In the 3D-2D model, we consider an incident electron kinetic energy $E = E_F$, the effective left-barrier height under an applied bias is $U_L(V_a) = U_0 - E_F - eV_{acc}$, and the right-barrier height is $U_R(V_a) = U_L(V_a) - eV_L - eV_w$ (see Fig. (5.13-b)).

Considering Eq. (4.33), we replace the term $\mathbf{T}(E_x, V_a)$ by Eq. (5.47) and E_x in by Eq. (5.63), and integrate from 0 up to ∞ in order to obtain a generalized resonant current expression:

$$J(V_a) = \frac{em_e^* k_B T}{\pi^2\hbar^3}\left(\frac{\Gamma_L\Gamma_R}{\Gamma_L+\Gamma_R}\right)\sum_n \ln\left[\frac{1+\exp\left(\left(E_F - E_n(V_a)\right)/\left(k_B T\right)\right)}{1+\exp\left(\left(E_F - E_n(V_a) - eV_a\right)/\left(k_B T\right)\right)}\right] \times\left[\frac{\pi}{2} + \arctan\left(\frac{E_n(V_a)}{\Gamma_T/2}\right)\right], \quad (5.65)$$

where the summation describes the contribution over all energy levels in the rectangular quantum well.

5.2.3 Model Validation and Discussion for the 3D-2D Model

To validate the proposed framework, we contrast the results obtained through our model with experimental and numerical data gathered from different 3D-2D RTD structures. The electron effective masses, the dielectric constants in the GaAs, AlAs, $Al_xGa_{1-x}As$ and $In_xGa_{1-x}As$ lattices, the theoretical LO-phonon energy value is $\hbar\omega_{LO}$, as well as the theoretical value of U_0, are obtained from [75], [182]. Otherwise mentioned, in all devices investigated, the operating temperature is $T = 300\,\mathrm{K}$.

We start validating our model with the device described in [82], composed by an $In_{0.53}Ga_{0.47}As$/AlAs heterostructure with $L_{bL} = L_{bR} = 2.6\,\mathrm{nm}$ and $L_w = 4.8\ \mathrm{nm}$. For this device we have: $N_d = 1 \times 10^{18}\,\mathrm{cm}^{-3}$and $E_F \approx 35\ m\,\mathrm{eV}$ [82]. As it can be seen from Fig. (5.14), the proposed model presents an excellent agreement with the experimental curve, correctly describing the resonant peak and the approximate magnitude of the current density obtained experimentally. Also, our model correctly predicts the PVCR value, the main figure-of-merit, which characterizes the NDR region. However, to achieve this agreement, we replaced the Q_e parameter in our model for an approximation, $Q'_e = \alpha Q_e$, where α is a fitting parameter. This procedure was done for all evaluated devices. Our calculations revealed that the resonant peak position is very sensitive to the value of Q_e, as it determines the voltage drop across the whole structure. Besides, the α parameter can be justified by our approximation for L_{acc}. Albeit it provides a good quantitative agreement for the accumulation width, in realistic devices, L_{acc} also varies with the applied bias. For this device, we set $\alpha = 0.85$. Also, the barrier width and the doping level were adjusted to 25 Å and $N_d = 0.75 \times 10^{18}\,\mathrm{cm}^{-3}$, respectively. This small adjustment to the barrier width was in the order of a few Bohr radii, within the uncertainty range of the majority of epitaxial growth techniques. As a final remark, we noticed an undesired shoulder-like shape at the valley region around 1.5 V (see Fig. (5.14)). This effect is mostly attributed to the intrinsic/extrinsic bistability and feedback mechanism present in realistic devices [82], [160], which are not included in our compact model.

The next device used in our validation is reported in [183]. It is composed of a double-barrier

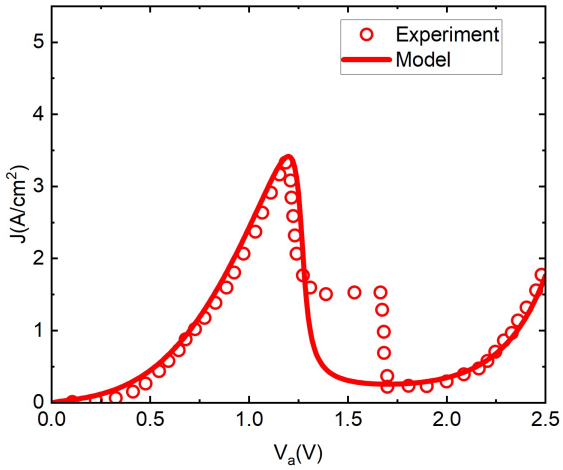

Figure 5.14: Comparison between the **I–V** characteristics obtained by our proposed model (solid line) and the experimental data (symbols) [82].

$In_{0.8}Ga_{0.2}As$/AlAs heterostructure with symmetrical undoped $In_{0.53}Ga_{0.47}As$ space layers. The nominal parameters reported are $L_{bL} = L_{bR} = 1.1\,\text{nm}$, $L_w = 3.5$ nm, $N_d = 3 \times 10^{18}\,\text{cm}^{-3}$and $E_F \approx 55\ m\,\text{eV}$. As demonstrated by the results shown in Fig. (5.15-a), the proposed model correctly predicts the resonant peak characteristics and the PVCR. To achieve such an agreement, we set in our calculations $\alpha = 0.80$. As noted before, our model does not accounts for the hysteresis anomaly around 0.5 V in the experimental curve. We should also point out that AlAs layers have an indirect bandgap, leading to an additional broadening in total resonance linewidth. In our model, we neglect the contribution of carrier tunneling across intra-band channels, such as the $\Gamma - L$ bands tunneling. Nevertheless, even for the indirect bandgap case, our model closely matches the experimental curve with minor adjustments in the nominal parameters.

Next, we compare our results with RTD investigated by Yang *et al*. [184]. This device is composed by a GaAs/AlAs heterostructure, with the nominal parameters reported as $L_{bL} = L_{bR} = 1.7\,\text{nm}$, $L_w = 4.5$ nm, $N_d = 1 \times 10^{18}\,\text{cm}^{-3}$ and $E_F \approx 55\ m\,\text{eV}$. Fig. (5.15-b) shows the analytical and the experimental **I–V** curves. Our model presents a good agreement with the experimental data, correctly describing the characteristic curve, the location of the resonance peak, and the magnitude of the current density. Again, to achieve this result, small adjustments were performed: $N_d = 0.85 \times 10^{18}\,\text{cm}^{-3}$, $L_{bL} = L_{bR} = 1.55\,\text{nm}$ and $\alpha = 0.80$.

The next device is composed by an $Al_{0.33}Ga_{0.67}As$/GaAs heterostructure with $L_{bL} = L_{bR} =$

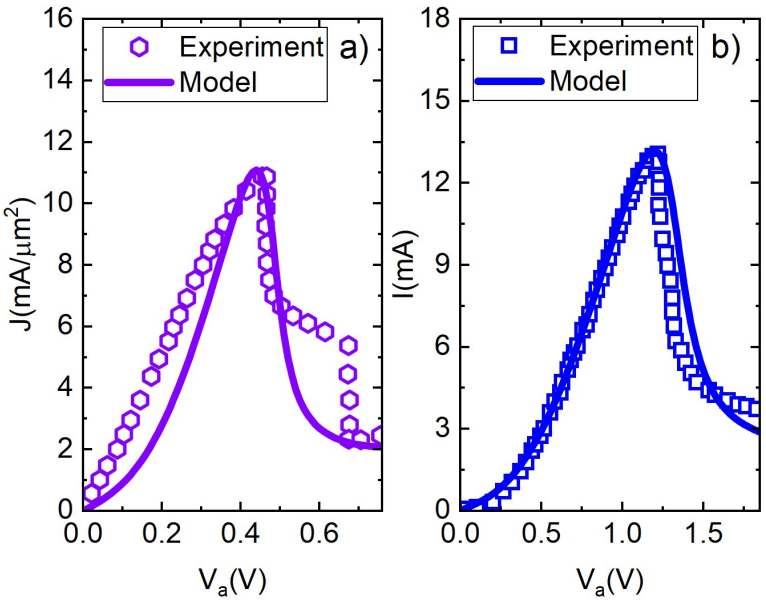

Figure 5.15: Comparison between the **I–V** curves obtained by our proposed model (solid line) and the experimental data (symbols) for (a) RTD reported on [183]; and (b) RTD reported on [184].

3.0 nm and $L_w = 3.0$ nm. For this numerically analyzed device, the nominal parameters are: $T = 77\,\mathrm{K}$, $N_d = 1 \times 10^{18}\,\mathrm{cm}^{-3}$ and $E_F \approx 58\ m\,\mathrm{eV}$ [133]. As it can be seen in Fig. (5.16), the proposed model provides an excellent agreement to the self-consistent calculations. Once more, a small adjustment in a few nominal parameters was necessary: $L_w = 3.15$ nm, $L_{bL} = L_{bR} = 3.3\,\mathrm{nm}$, $N_d = 1.1 \times 10^{18}\,\mathrm{cm}^{-3}$ and $\alpha = 0.95$. Eventually, as the bias increases, the effective right barrier height, $U_R(V_a)$, vanishes, and T_R approaches unity. In this situation, the device behaves as a conventional diode, yielding the characteristic exponential **I–V** current lineshape. It is interesting to observe that, since the effective barrier height in our model also varies accordingly to the applied bias, the model matches the exponential part of the **I–V** curve without any further adjustment. Although our main goal in this work is to model the NDR region, this additional feature is an improvement when compared to the previous model developed in [82], where an additional fitting equation is required.

The next RTD is a device analyzed by ourselves using Silvaco-ATLAS numerical simulator. This TCAD platform is based on a self-consistent electric potential model and NEGF carrier transport formalism. The device is composed by an $Al_{0.5}Ga_{0.5}As/GaAs$ heterostructure with $L_{bL} = L_{bR} = 2.0\,\mathrm{nm}$ and three different quantum-well widths: $L_w \in (2.5, 3.0, 4.0)$ nm. For this device, we have $N_d = 1 \times 10^{18}\,\mathrm{cm}^{-3}$ and $E_F \approx 50\ m\,\mathrm{eV}$. As can be seen from

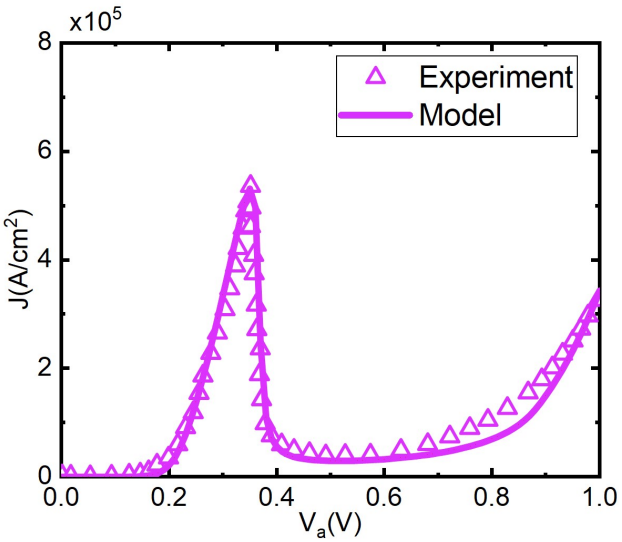

Figure 5.16: Comparison between the **I–V** curves obtained by our proposed model (solid line) and the self-consistent numerical model (symbols) for the RTD evaluated by [133].

Fig. (5.17) the proposed model presents a very close agreement with the simulated results for all three widths investigated. To achieve this agreement, we used $N_d = 1.1 \times 10^{18}\,\mathrm{cm}^{-3}$, $L_{bL} = L_{bR} = 2.15\,\mathrm{nm}$ and $\alpha = 1$ in our calculations

In addition to the **I–V** characteristics, we also validated our expression for the resonant energy level under an applied bias, Eq. (5.45). For this investigation, we set $L_w = 2.0\ \mathrm{nm}$ in the RTD structure. As it can be seen in Fig. (5.18), our expression provides an excellent agreement with TCAD results for the ground energy level as a function of the applied bias. Furthermore, our model correctly predicts energy rise around the resonance peak since we did not neglect the quantum Stark effect in Eq. (5.45). We also validated our expressions to compute the space charge in the quantum well and the accumulation region, given by Eqs. (5.54) and (5.61), respectively. The model is in excellent agreement with the TCAD results, as demonstrated in Fig (5.19). Again, our model correctly predicts the variation of the charge density around the resonance peak for both space charges regions, Q_e and Q_w. Fig. (5.20) shows the respective **I–V** characteristics for comparison. As it can be seen, our model correctly predicts the **I–V** curve profile of the RTD.

It is also possible to evaluate the charge density distribution in the accumulation, double-barrier and depletion regions. As demonstrated in Fig. (5.21), an inspection on the electronic concentration reveals a charge accumulation near the DBR at the emitter side (bright-red color

indicates the high electronic density), and a depletion (blue color) at the collector layer. Fig. (5.21) shows the electronic concentration at the resonant peak ($V_a \simeq 0.67\ V$) and Fig. (5.21) shows the electronic concentration at the valley voltage range ($V_a \simeq 1.2\ V$). The results obtained by Eqs. (5.54) and (5.61) are consistent with the numerical data from the TCAD simulation. Inspecting Fig. (5.21), one can see that the electronic concentration in the quantum well reaches its maximum value at the resonant peak. In contrast, the electronic concentration in the quantum well is significantly reduced at the valley bias range. This behavior is in total accordance with the device theory as well as our analytical predictions.

We also compared our results with the TCAD investigation performed by [185] for nitride-based RTDs. These devices have been attracting a great deal of attention for applications in THz technology and also because of their wide bandgap [185]. The RTD is composed by an $Al_xGa_{1-x}N$/GaN heterostructure with nominal parameters as $L_{bL} = L_{bR} = 1.5\,\mathrm{nm}$, $L_w = 1.5$ nm and $N_d = 1 \times 10^{19}\,\mathrm{cm}^{-3}$. Other relevant physical parameters and a complete description of this device can be found in [185]. We compared our results for two different compositions of the $Al_xGa_{1-x}N$ barrier: $x = 0.1$ and $x = 0.2$. As shown in Fig. (5.4-a), the proposed model presents an excellent agreement with the simulated curve, yielding the same PVCR. Once more, to reach this agreement, we used $\alpha = 1.18$, $L_{bL} = L_{bR} = 1.4\,\mathrm{nm}$ and $L_w = 1.7\ \mathrm{nm}$ in our calculations.

We reinforce that in all devices used to validate our model, the minor fitting performed in our theoretical predictions for Q_e through α parameter does not alter the order of magnitude of Q_e. Furthermore, the fine adjustment performed in some geometric dimensions is within the typical tolerances of most device nanofabrication technologies.

In this Chapter, we developed fully analytical compact models to describe the **I-V** characteristic of 2D-2D and 3D-2D RTDs. The models are based on the Tsu-Esaki formalism but include a complete analysis of the electric field across the device, allowing one to account for the space-charge effects due to the formation of a quasi-triangular well at the emitter side as well as the quantum Stark effect. The proposed model also incorporates an analytical tunneling coefficient, including LO-phonon scattering mechanisms and asymmetrical QW barriers.

The models were validated by comparison to experimental and numerical data obtained from different RTDs described in the literature and numerical simulation performed by means

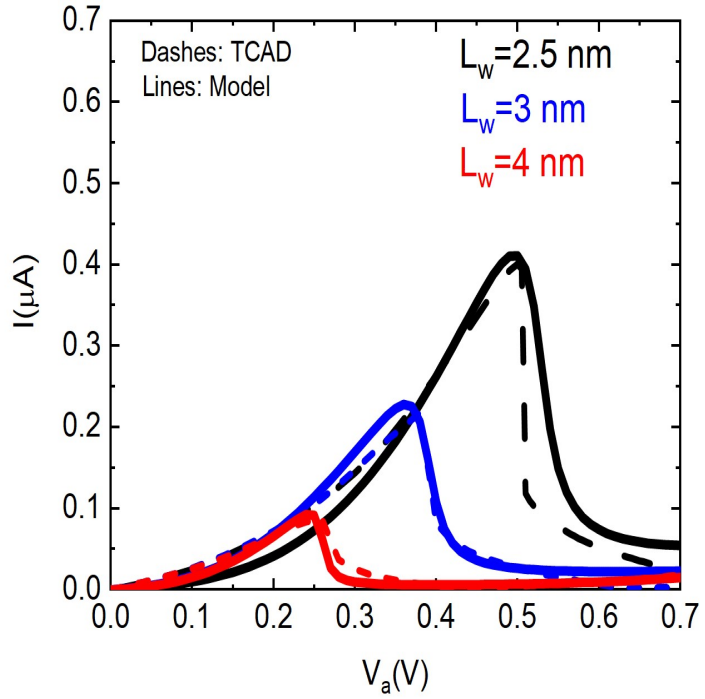

Figure 5.17: Comparison between the **I–V** curves obtained by our proposed model (solid line) and quantum transport TCAD simulations (doted line) performed to investigate the RTD regarding different quantum-well widths.

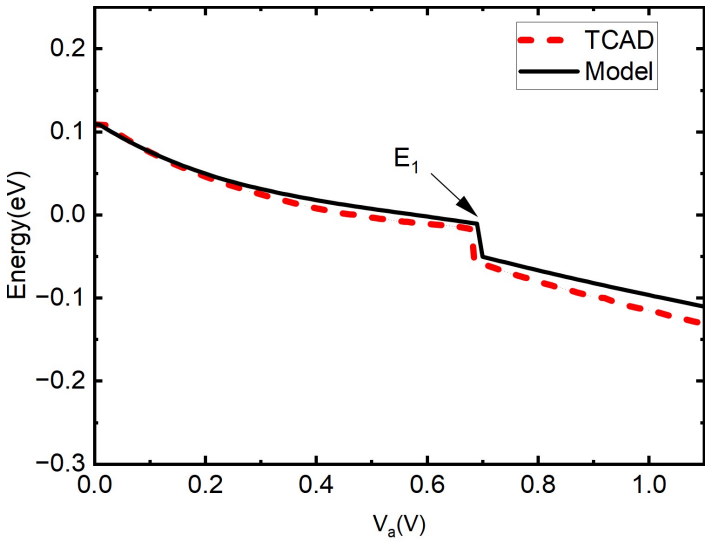

Figure 5.18: Validation of our proposed model (solid lines) against TCAD simulations (dotted line) performed for the RTD with $L_w = 2.0$ nm regarding the fundamental resonant energy level under applied bias.

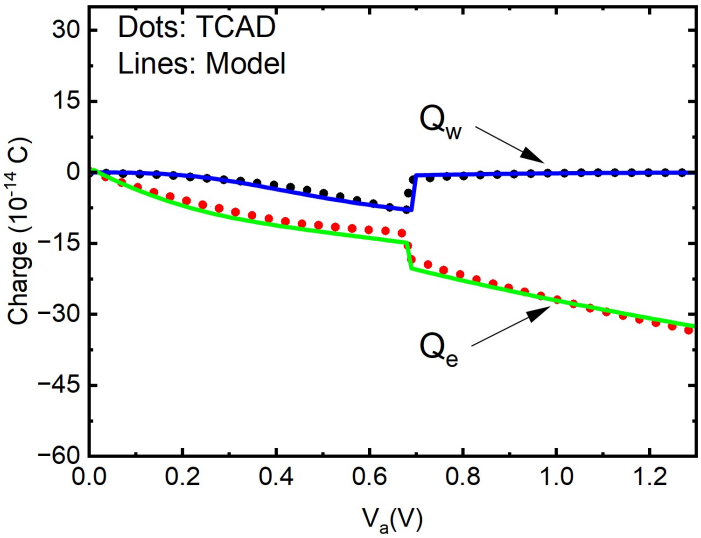

Figure 5.19: Validation of our proposed model (solid lines) against TCAD simulations (dotted line) performed for the RTD with $L_w = 2.0$ nm regarding space-charge density in the quantum-well and the accumulation regions.

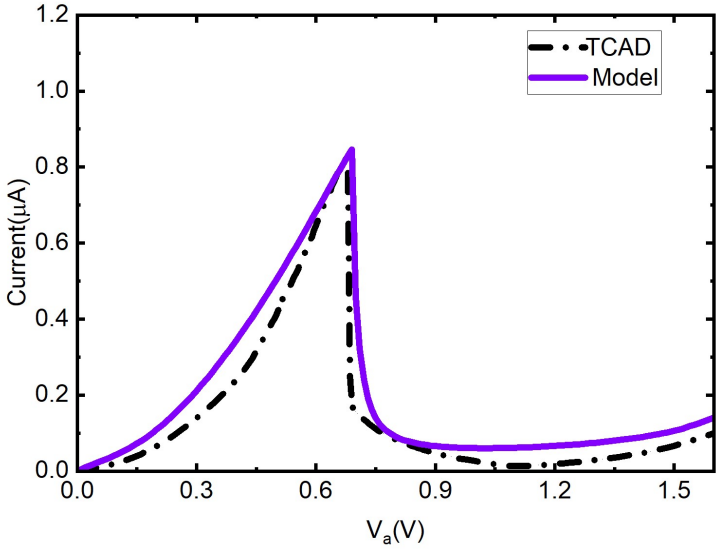

Figure 5.20: Validation of **I–V** characteristics of the proposed model (solid lines) against TCAD simulations (dash_dotted line) performed with $L_w = 2.0$ nm.

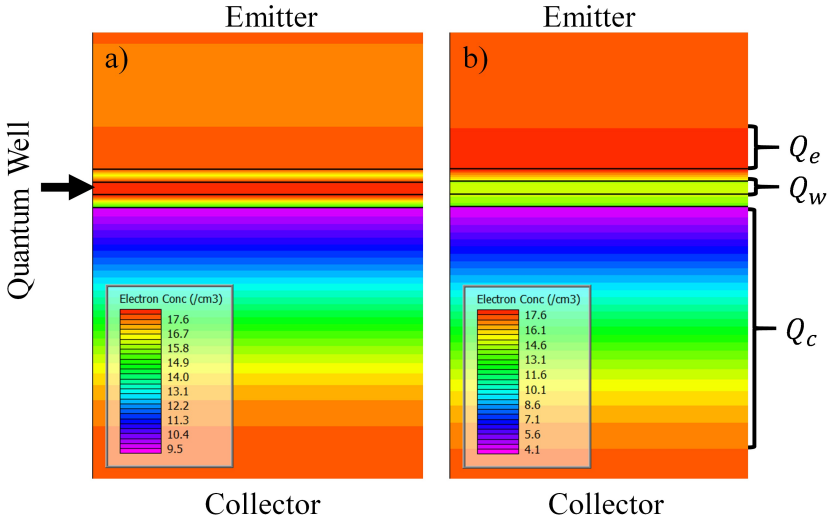

Figure 5.21: Simulated charge-density maps around resonance (left) and the valley voltage ranges (right).

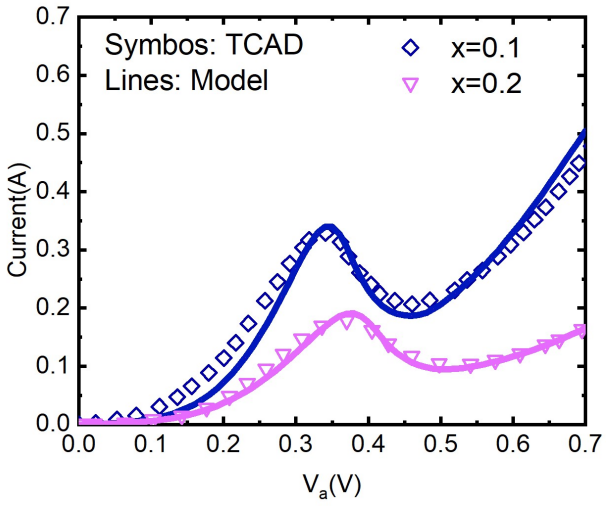

Figure 5.22: Comparison between the **I–V** characteristics obtained by our proposed model (solid line) and the quantum-transport numerical simulation (doted line) for the RTD described in [185].

of TCAD software. The overall agreement in terms of the PVCR and peak current is excellent and the model is capable of reproducing the main features of the **I-V** characteristics for all RTDs, with only minimal adjustments regarding the layer structure and/or doping levels, all changes well below the fabrication tolerances of current epitaxial growth techniques.

The correct modeling of the NDR range, as well as the PVCR, are essential to design RTD oscillators, analog-to-digital converters, frequency dividers/multipliers, and digital circuits employing multiple valued logic [50]. In this regard, we highlight that our model provides an excellent quantitative agreement for both NDR regions for all devices used for validation. We should also note that the proposed model include only direct bandgap contributions only, neglecting small contribution due to other conduction band-minima, such as intra-band tunneling, e.g., $\Gamma - X$ and $\Gamma - L$.

We should also point out that the proposed model for RTD 2D-2D works well for cryogenic temperatures where the energies in the quasi-triangular quantum well in the accumulation region are well-defined, ensuring the 2D nature of the emitter electrons. Hence, for the 2D-2D model, we neglect the small contribution of 3D electrons in the emitter. On the other hand, we validated our model for the RTDs 3D-2D, considering only the contribution of 3D electrons at the emitter side. The 3D-2D model works well for RTDs operating at room temperature. In other words, we did not account for hybrid regimes in intermediate temperatures, with simultaneous contributions 2D-2D and 3D-2D.

We considered the total ionization for the accumulation and depletion regions for both models and the models developed in this work were validated for n-type RTDs. Still, even with the simplifications assumed, the proposed model presents an excellent agreement with validation data, comparable to much more sophisticated numerical approaches.

The results presented in this chapter regarding the 2D-2D model were published at [188]. Also, the initial results for the 3D-2D model can be found at [189]- [190].

Chapter 6

Conclusions and Future Works

In this thesis, we focused on modeling the I-V characteristics of RTDs. We provided a brief account of the historical context in which the resonant tunneling concept was conceived. In Chapter 2, we reviewed useful analytical expressions for computing the quantum tunneling transmission coefficient across rectangular potential barriers, with and without applied bias.

As a required step, to obtain an analytical model it is necessary to determine the energy levels in the finite-height quantum well present in the RTD structure. However, to determine these energy levels it is necessary to solve transcendental equations that do not have an exact analytical solution. Therefore, approximate analytical solutions were developed for symmetric and asymmetric rectangular quantum wells, demonstrating excellent agreement when contrasted against the exact solution. Next, a literature review of carrier transport in RTDs was carried out, where the challenges in developing compact models for I-V characteristics were identified. Additionally, the main scattering mechanisms in RTDs were discussed, in order to incorporate their effects into the proposed model.

In Chapter 5, we developed a fully analytical model for the I-V characteristics of 2D-2D and 3D-2D RTDs. In particular, depending on the thickness of these spacer layers and the operating temperature, a quasi-triangular quantum well may form at the emitter, yielding a 2DEG. This energy-level quantization feature usually occurs in very low-temperature regimes. In this case, the RTD is named 2D-2D (two-dimensional emitter to a 2DEG quantum well) RTD. On the other hand, for the 3D-2D case, there is no quantum well at the emitter region and the model considers the resonant current density as 3D-2D (three-dimensional emitter to a 2DEG quantum

well). To do so, we started from the Tsu-Esaki formalism and considered the electrical potential distribution in the device layer structure, including the space charge region in the emitter layer.

The models developed combine elements of previous works found in the literature but also add some modifications and original contributions, such as the inclusion of the quantum Stark effect, the dependence of the tunneling transmission on the bias voltage and LO-phonon scattering mechanisms, analytical calculations of eigenenergy levels and the analytical computation of charge densities. These features result in an accurate novel expression to describe I–V characteristic of 2D-2D and 3D-2D RTDs. The models were validated by comparison to numerical results obtained using TCAD simulation and experimental data available from different RTDs described in the literature. The overall agreement is excellent, and the model accurately reproduces the I–V characteristics for all RTDs, with only minimal adjustments regarding a few physical parameters. It is worth noting that all changes well below the fabrication tolerances of current epitaxial growth techniques.

The RTD is a building block for oscillators capable of operating in the THz range, thus making it one of the target candidates for 6G applications. Therefore, in a future work, there is a need for accurate small-signal equivalent circuit modeling. As a first step, in the next Section, we provide our partial results on the analytical modeling for the elements of RTD small-signal equivalent circuits. In addition, future work also includes modeling the I-V characteristics of nanowire RTDs and RTTs (Resonant Tunneling Transistors).

6.1 RTD Equivalent Small-Signal Model

As mentioned in the previous Chapter, the most distinct feature of RTDs is their highly nonlinear I–V characteristics on account of their NDR. This unique behavior enables the development of terahertz oscillators and detectors, and its detailed description depends on different parameters, such as device size, material composition, doping levels, and temperature [35]- [47] . Aiming the design of next-generation transceivers, a reliable compact model must correctly describe the I–V and C–V characteristics in regard to fabrication parameters, without losing track of the underlying physics. To do so, in this section we sketch a fully analytical model for the first-order characteristics of the 3D-2D RTD.

Fig. (6.1) shows the small-signal equivalent circuit model of an RTD [186].

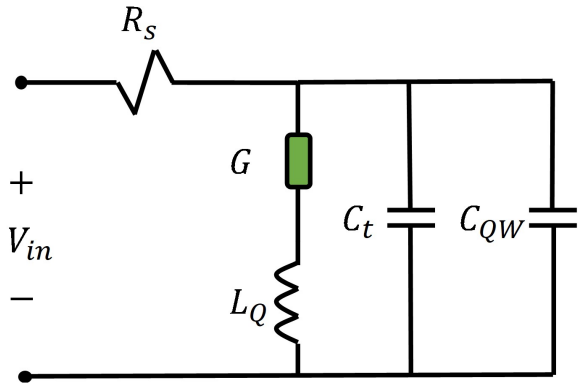

Figure 6.1: RTD equivalent small-signal circuit.

In the circuit, R_S represents the contact and access resistance on accounts of the metal-semiconductor contact resistance and the sheet resistance of the heavily doped semiconductor contacts. G represents the differential conductance (first derivative of the DC I–V curve). L_Q is the tunneling inductance which accounts for the time required for the buildup or decay of the wave function in the quantum well, leading to a delay of current with respect to bias. The capacitance C_t represents the capacitance due to the space charge buildup in both accumulation and depletion regions. C_{QW} represents the quantum capacitance resulting from the charge and discharge of free carriers in the well [186].

We calculate the device conductance and its equivalent capacitance to compute the maximum operating frequency and the associated maximum output power, fundamental features for designing RTD-based oscillators. To find the differential conductance characteristics, we apply the generalized chain rule in Eq. (5.65), yielding:

$$G = \frac{dJ}{dV_a} = \frac{\partial J}{\partial E_n}\frac{\partial E_n}{\partial V_a} + \frac{\partial J}{\partial \Gamma_T}\frac{\partial \Gamma_T}{\partial V_a} + \frac{\partial J}{\partial \Gamma_L}\frac{\partial \Gamma_L}{\partial V_a} + \frac{\partial J}{\partial \Gamma_R}\frac{\partial \Gamma_R}{\partial V_a}. \tag{6.1}$$

First, we notice that the linewidth enhancement factor due to scattering is much more significant than the intrinsic linewidths, i.e., $\Gamma_s \gg \Gamma_R, \Gamma_L$. Since $\Gamma_T = \Gamma_L + \Gamma_R + \Gamma_s$, we have $\Gamma_T \approx \Gamma_s$. In addition, since Γ_s is almost a constant with respect to V_a [187], we can make $\partial\Gamma_T/\partial V_a \approx 0$. Next, following the argument of Coon and Liu [124], as the intrinsic linewidths Γ_L and Γ_R are much smaller than the energy level, we can assume:

$$\left|\frac{\partial \Gamma_L}{\partial V_a}\right|, \left|\frac{\partial \Gamma_R}{\partial V_a}\right| \ll \left|\frac{\partial E_n}{\partial V_a}\right|. \tag{6.2}$$

Therefore, we can approximate Eq. (6.1) to:

$$G \approx \frac{\partial J}{\partial E_n}\frac{\partial E_n}{\partial V_a} \tag{6.3}$$

By evaluating Eq. (6.3), we have the differential conductance as

$$\begin{aligned} G \approx & -\frac{\Gamma_R e^2 \Gamma_L m_e^*}{2}\left\{k_B \Gamma_T T\left(1+\Lambda_1\right)\left(1+\zeta\right)\ln\left(\frac{1+\zeta}{1+\Lambda_1}\right)\right. \\ & -2\left[\frac{\pi}{2}+\arctan\left(\frac{2E_n}{\Gamma_T}\right)\right]\left(\zeta-\Lambda_1\right) \\ & \left.\times\left(E_n^2+\frac{\Gamma_T^2}{4}\right)\right\}\left\{\pi^2\hbar^3\sqrt{4aV_a-4ac+b^2}\right. \\ & \left.\times\left(1+\zeta\right)\left(1+\Lambda_1\right)\left(E_n^2+\frac{\Gamma_T^2}{4}\right)C_1\left(\Gamma_L+\Gamma_R\right)\right\}^{-1}, \end{aligned} \tag{6.4}$$

where

$$\begin{aligned} \Lambda_1 &= \exp\left(\left(E_F - E_n(V_a) - eV_a\right)/\left(k_B T\right)\right), \\ \zeta &= \exp\left(\left(E_F - E_n(V_a)\right)/\left(k_B T\right)\right). \end{aligned}$$

Off resonance, there is no space charge buildup in the well and, for constant values of L_{acc} and L_d, the device behaves like a parallel plate capacitor, with the charge accumulated at the emitter plate being proportional to the applied voltage. Hence, in this case, this geometric component of the capacitance is simply given by

$$C_t = \left(\frac{1}{C_1}+\frac{1}{C_2}\right)^{-1} \tag{6.5}$$

The terms C_1 and C_2 are defined in Chapter 5 given by the equations (5.58) and (5.59). By evaluating Eq. (6.5) we have:

$$C_t = (N_d\epsilon_w\epsilon_{bL}\epsilon_{bR}e)\{[(N_d(L_{acc}+L_d)e+Q_e)\epsilon_{bR} + e\epsilon_w N_d L_{bR}]\epsilon_{bL} + e\epsilon_{bR}\epsilon_w N_d L_{bL}\}^{-1} \tag{6.6}$$

Following the approach proposed by R. Lake and J. Yang in [187], a simple expression to compute the quantum capacitance is given by

$$C_{QW} = -\frac{G\hbar}{\Gamma_T} \tag{6.7}$$

Therefore, the overall equivalent capacitance of the RTD can be estimated by

$$C_{eq} = C_t + C_{QW}$$

The tunneling inductance is given by [186]:

$$L_Q = \frac{\Gamma_T}{G\hbar} \tag{6.8}$$

Furthermore, the circuit has a negative differential conductance for frequencies below $f_{\max}$. Hence, the cutoff frequency, i.e., the maximum oscillation frequency, is given by [191]:

$$f_{\max} = \frac{1}{2\pi}\left\{\left[\frac{1}{L_Q C_t}\left(1-\frac{C_t}{2L_Q G^2}\right)\right] x\left[1-\left(1-\frac{GR_S+1}{GR_S\left(C_t/\left(2L_Q G^2\right)-1\right)^2}\right)^{1/2}\right]\right\}^{1/2} \tag{6.9}$$

Finally, the maximum output power of an oscillator can be computed by [126], [192]:

$$P_{\max} = \frac{3}{16}\Delta I\Delta V\left[1-\left(\frac{f}{f_{\max}}\right)^2\right] \tag{6.10}$$

where the NDR is characterized by $\Delta I = I_v - I_p$ and $\Delta V = V_v - V_p$ with I_v, I_p, V_v and V_p representing the peak and valley values for the voltages and currents, respectively. Typically, the equivalent capacitance of RTDs is in the order of a few femtofaradays while the series resistance is about a few ohms [186]. These values assure the THz operating frequency range for RTD-based oscillators.

In a future work, we will contrast the results from the expressions derived in this section with experimental and simulation results from technical literature.

6.2 Nanowire RTD and RTT

In a future work, we will focus on the compact modeling of quantum wire RTDs and RTTs operating in the quasi-ballistic regime. In the quantum wire RTD, the transport carries experience lateral quantum confinement, leading to a collimation effect in these devices and altering their electrical output characteristics. In this context, it is worth mentioning the work of Björk *et al.* [194], in 2002. The authors investigated the electronic properties of heterostructured quantum wires with InAs/InP semiconductor structures. The device possesses a double potential barrier region, resulting in the quantum wire diode with resonant tunneling, as it can be seen schematically in Fig. (6.2). Fig. (6.2) shows a schematic illustration of the device proposed by [194], of radius R_0, with two InP regions of length L_b forming the potential barriers for the resonant structure. The term R_c refers to the conductive radius, i.e., the effective conduction radius of the longitudinal channel, disregarding the lateral depletion region of the RTD.

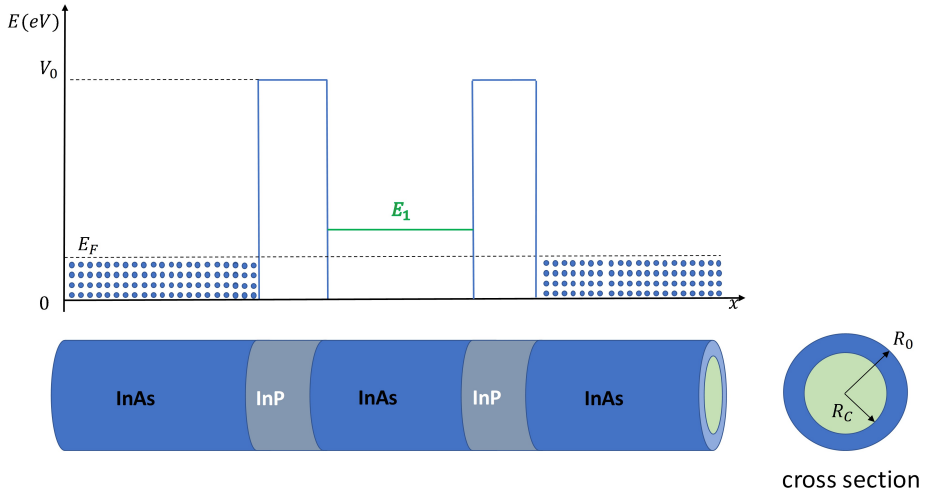

Figure 6.2: Schematic illustration of the quantum wire resonant tunneling diode proposed by Björk et al. [194]. On top, the figure shows a schematic illustration of the conduction band in the longitudinal direction and a cross-section of the device [194].

In 2005, Wensorra *et al.* in [195] proposed a nanocolumn resonant tunneling diode (vertical

quantum wire) formed by AlAs/GaAs semiconductor heterostructure. As reported by Wensorra *et al*., the quantum wire RTD investigated presents an electrons collimation effect due to the lateral confinement of the nanocolumn [195]. Thus, the proposed RTD presents quasi-one-dimensional electron transport in the vertical direction of the nanocolumn.

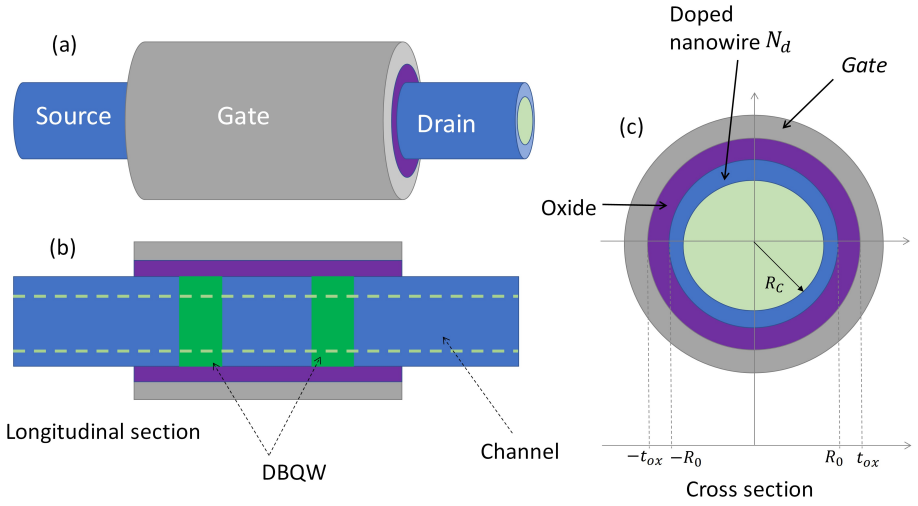

Figure 6.3: (a) Schematic illustration of a quantum wire RTT. (b) a longitudinal section of the device where it can be identified the double potential barrier and the quantum well. (c) a cross-section in the NW-RTT showing the gate electrode, the oxide layer, the depletion region and the conduction channel defined by the conducting radius R_C. The term t_{ox} refers to the width of the oxide.

Another interesting device for modeling is the quantum wire resonant tunneling transistor, NW-RTT. Fig. (6.3) shows a schematic illustration of a quantum wire NW-RTT. The advantage of NW-RTTs is their potential to operate at higher speeds than conventional transistors. In this context, the device proposed by Wensorra *et al.* uses the gate voltage to control the width of the depletion region, consequently controlling the nanocolumn conducting radius and the current density [196]. NW-RTTs provide greater improvement in device performance compared to bulk RTTs [196]. Despite its interesting features, there is a lack of physics-based models for both quantum wire RTDs and RTTs in the literature, which makes these devices an promising topic for future works.

Appendix A

Mapping Function Approximation Method

A.1 Introduction

In the semiconductor industry, there has been a growing demand for fully analytical models to describe the basic electronic circuit components. This demand occurs because, although accurate, numerical models impose challenges, such as very long simulation times and higher requirements for computational capacity. In the scope of today technologies, where it is necessary to simulate integrated circuit design with dozens of millions of transistors, numerical simulations impose great difficulties. In modeling such devices, it is often necessary to solve transcendental equations. However, by definition, these equations do not have a closed-form analytical solution, making them particularly difficult to handle. As a result, most existing formulations in the literature resort to numerical routines like the Newton-Raphson method to tackle these equations.

In this scenario, the present appendix provides a method to write the solution of transcendental equations in terms of analytical expressions. We exemplified the application of the Mapping Function Approximation Method (MFAM) employed in Chapter 3 to compute eigenvalues of the finite square well potential. Here, we split the method in six steps to facilitate understanding.

In short, our method is used to find analytical solutions to transcendental equations by approximating these equations in polynomials using Taylor series expansions. Nonetheless, instead of expanding the transcendental equations in a predetermined fixed point, for instance, the origin of the system, we expand the transcendental equation in a moving point provided by a

"mapping function". In our approach, the moving point varies accordingly to the parameters of the original transcendental equation, in a way that minimizes the relative error.

A.2 Step-by-Step Mapping Function Approximation Method

We begin by applying the MFAM to calculate the approximate roots of an arbitrary transcendental equation, namely,

$$\sqrt[3]{\frac{\kappa\xi\mu^2\eta^2+5\kappa\xi\mu^2\eta+\sqrt[3]{\varepsilon}}{\kappa\xi\mu^2}}+\frac{\sqrt[6]{\varepsilon}}{\sqrt{\kappa\xi}\mu}\left(\eta\right)^{\frac{2}{3}}+\frac{\ln\left(\eta^2+2\phi\right)}{10(-\eta/10-10)}-\frac{\sqrt[3]{\varepsilon/\mu^6}}{\kappa\xi}\left[\ln\left(\eta^2+5\sigma\right)\right]^{\frac{1}{3}}=0. \tag{A.1}$$

Eq. (A.1) could, for instance, represent some physical phenomenon in which the constants κ, ξ, μ, ε, ϕ, and σ are operational and/or physical parameters and η is the variable of interest. In our example, κ, ξ, μ, ε, ϕ, $\sigma \in \mathbb{R}_0^+$. At a first glance, Eq. (A.1) may look cumbersome. However, we demonstrate in the next section that, by applying the MFAM, an approximate solution can be easily found with satisfactory agreement.

A.2.1 STEPS:

1. The first step, if needed, is to rearrange the equation, grouping the transcendental function(s) to one side of the equality. Thus, for Eq. (A.1), we get:

$$\sqrt[3]{\frac{\kappa\xi\mu^2\eta^2+5\kappa\xi\mu^2\eta+\sqrt[3]{\varepsilon}}{\kappa\xi\mu^2}}+\frac{\sqrt[6]{\varepsilon}}{\sqrt{\kappa\xi}\mu}\left(\eta\right)^{\frac{2}{3}}=\frac{\ln\left(\eta^2+2\phi\right)}{10(-\eta/10-10)}+\frac{\sqrt[3]{\varepsilon/\mu^6}}{\kappa\xi}\left[\ln\left(\eta^2+5\sigma\right)\right]^{\frac{1}{3}} \tag{A.2}$$

2. To get a more visually friendly equation, we can define a parameter that encompasses the most relevant aspects of the target equation (not a mandatory step). For Eq. (A.2), we define $\lambda = \sqrt[3]{\varepsilon}/\kappa\xi\mu^2$. Hence, rearranging equation (A.2) and writing as a function of λ, we get

$$\sqrt[3]{\eta^2+5\eta+\lambda}+\sqrt{\lambda}\left(\eta\right)^{\frac{2}{3}}=\frac{\ln\left(\eta^2+2\phi\right)}{\eta+100}+\lambda\left[\ln\left(\eta^2+5\sigma\right)\right]^{\frac{1}{3}}. \tag{A.3}$$

3. The next step is to write each side of Eq. (A.3) as an independent function of η. For this, we call the left-hand side of Eq. (A.3) as $LHS(\eta)$, and the right-hand side as $RHS(\eta)$.

Thus, we have

$$LHS(\eta) = \sqrt[3]{\eta^2 + 5\eta + \lambda} + \sqrt{\lambda}\,(\eta)^{\frac{2}{3}}\,, \tag{A.4}$$

$$RHS(\eta) = \frac{\ln\left(\eta^2 + 2\phi\right)}{\eta + 100} + \lambda\left[\ln\left(\eta^2 + 5\sigma\right)\right]^{\frac{1}{3}}. \tag{A.5}$$

4. In this step, we use what is commonly referred to in the literature as a graphical method (GM) to identify preliminary approximate solutions of Eq. (A.3), needed only to build the mapping function. In this example, the GM consists of plotting the $LHS(\eta)$ and $RHS(\eta)$ curves in the same chart for a set of parameters λ, ϕ and σ. The solution, η, of interest is just the intersection point of the curves. For illustration, Fig. (A.1) shows the $LHS(\eta)$ and $RHS(\eta)$ curves for $\lambda = \lambda_1 = 1000$, $\phi = \phi_0 = 100$ and $\sigma = \sigma_0 = 10$. Next, we plot the $LHS(\eta)$ and $RHS(\eta)$ curves, but in this case, for a different value of the chosen parameter, λ_1, and keeping the same values of ϕ_0 and σ_0. We repeat this process varying λ_i, where $i \in (1, 2, ..., N)$ and N is the number of different values of λ to cover the full application range. Thus, for each value of λ, we build a table relating to the solution, η_0, obtained by identifying the intersection point.

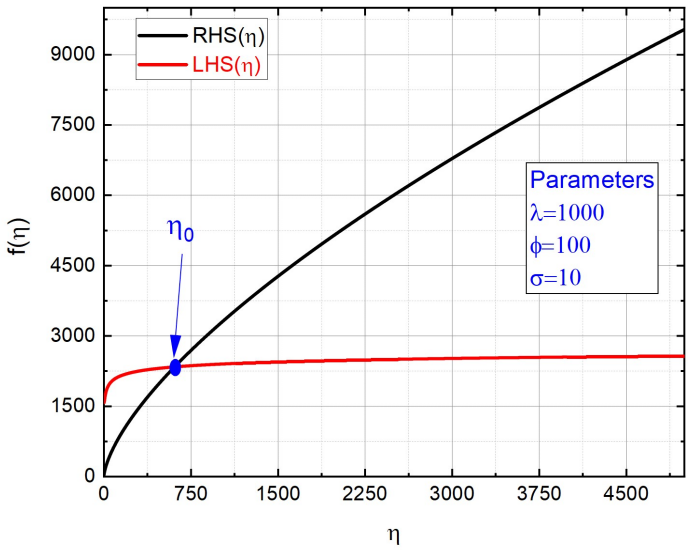

Figure A.1: $LHS(\eta)$ and $RHS(\eta)$ curves for $\lambda = \lambda_1 = 1000$, $\phi = \phi_0 = 100$ and $\sigma = \sigma_0 = 10$. The intersection point η_{ex} is the approximate solution provided by the graphical method.

A judicious choice of ϕ_0 and σ_0, was made in regard to this particular example. Nevertheless, any value of ϕ and σ, in the physical range, can be used.

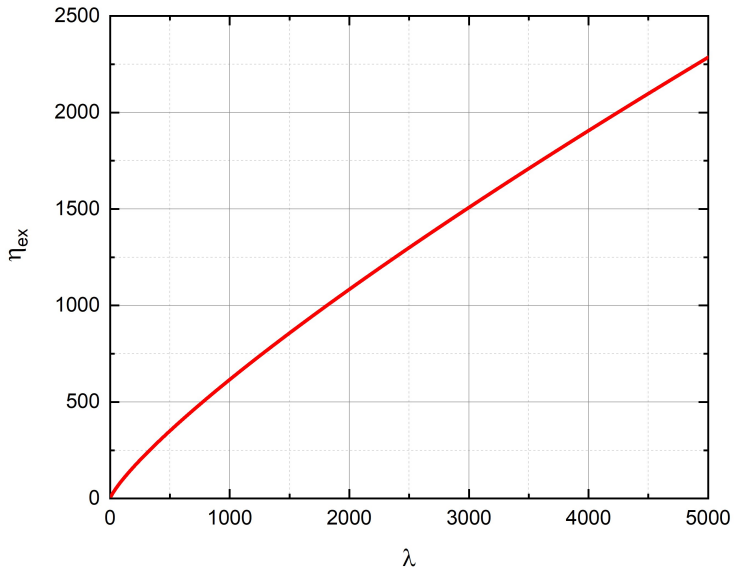

Figure A.2: Solution of Eq. (A.1) as function of λ with $\phi = 100$ and $\sigma = 10$.

5. Next, with the curve shows in the Fig. (A.2), we can use a software platform, such as Origin or Matlab (Curve Fitting Toolbox™), to find the expression of the mapping function which matches the relationship described in Fig. (A.2), with satisfactory agreement. Following the steps above, we get the mapping function

$$\eta_0(\lambda) = c_1 \lambda^{c_2}, \tag{A.6}$$

where, c_1 and c_2 are constants. The Fig. (A.3) shows a picture of the software window used to find the mapping function, Eq. (A.6). In this case, with $\phi = 100$ and $\sigma = 10$ the Origin software automatically adjusted the values of the constants to,

$$\begin{aligned} c_1 &= 2.21915, \\ c_2 &= 0.81452. \end{aligned}$$

In our example, different values of ϕ and σ would result in others values to c_1 and c_2. Nevertheless, despite different choices, the mapping function agrees well with the graphical solution. This happens because, in our method, the point obtained with the mapping

function acts just as a pointer to the vicinity of the root we are seeking. Hence, the mapping function is defined once in our method. On the other hand, if we decide to use the mapping function as a direct solution, the relative error will grow rapidly as we change the input values, as we will show later.

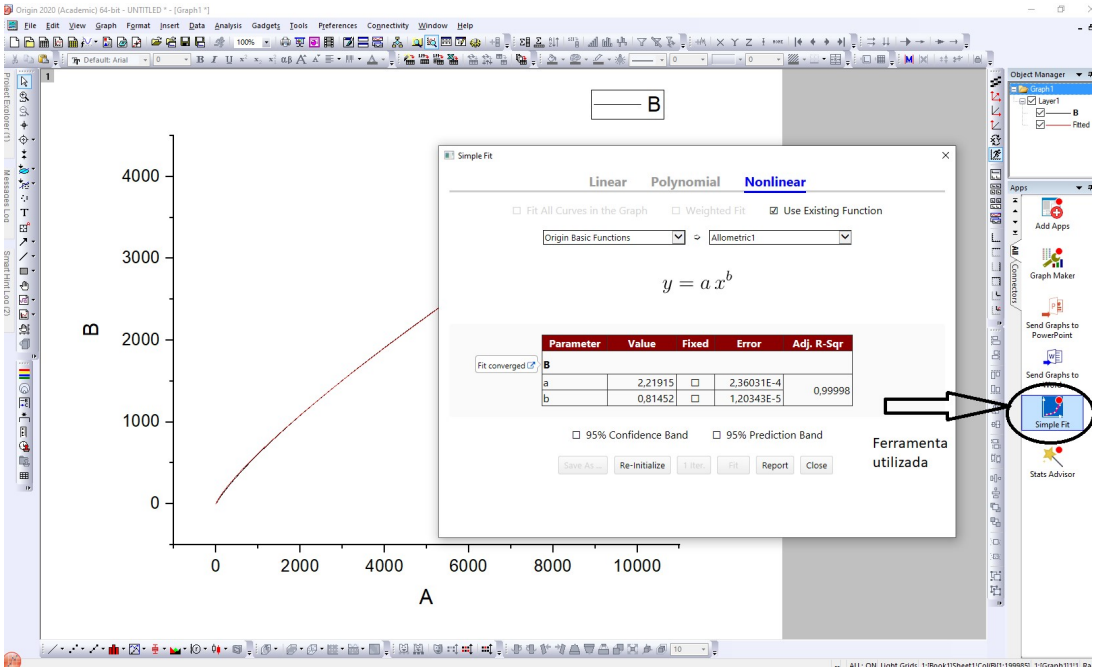

Figure A.3: User interface of Origin software used to find the mapping function.

6. Next, by using Taylor series, we can expand the functions $LHS(\eta)$ and $RHS(\eta)$ into polynomials of low degree around η_0 and, consequently, easily solve Eq. (A.2). To properly choose the polynomial degree, we can go back to the fourth step and analyze the lineshape of the curve of Fig. (A.1) to get a hint of which degree of the polynomial would be more adequate. In our particular case, we choose to expand $LHS(\eta)$ into a second order polynomial and $RHS(\eta)$ into a first order polynomial, thus we have

$$\begin{aligned} LHS(\eta) &\simeq a + b(\eta - \eta_0) + c(\eta - \eta_0)^2, \\ RHS(\eta) &\simeq d + e(\eta - \eta_0), \end{aligned}$$

hence, the approximate Eq. (A.2) becomes

$$a + b(\eta - \eta_0) + c(\eta - \eta_0)^2 = d + e(\eta - \eta_0), \tag{A.7}$$

where the constants from Taylor expansion are

$$
\begin{aligned}
a &= \sqrt[3]{\eta_0^2 + 5\eta_0 + \lambda} + \sqrt{\lambda}\,(\eta_0)^{\frac{2}{3}}\,, \\
b &= \frac{1}{3}\frac{2\eta_0 + 5}{(\eta_0^2 + 5\eta_0 + \lambda)^{2/3}} + \frac{2}{3}\frac{\sqrt{\lambda}\,(\eta_0)^{\frac{2}{3}}}{\eta_0}, \\
c &= \frac{(\eta_0^2 + 5\eta_0 + \lambda)^{\frac{-2}{3}}}{3} - \frac{1}{9}\frac{(2\eta_0 + 5)^2}{(\eta_0^2 + 5\eta_0 + \lambda)^{\frac{2}{3}}} - \frac{1}{9}\frac{\sqrt{\lambda}\,(\eta_0)^{\frac{2}{3}}}{\eta_0^2}, \\
d &= \frac{\ln(\eta_0^2 + 2\phi)}{\eta_0 + 100} + \lambda\left[\ln\left(\eta_0^2 + 5\sigma\right)\right]^{\frac{1}{3}}, \\
e &= \frac{1}{\eta_0 + 100}\left(\frac{2\eta_0}{\eta_0^2 + 2\phi} - \frac{\ln(\eta_0^2 + 2\phi)}{\eta_0 + 100}\right) + \frac{2}{3}\frac{\lambda\eta_0}{(\eta_0^2 + 5\sigma)\left[\ln(\eta_0^2 + 2\phi)\right]^{\frac{2}{3}}},
\end{aligned}
$$

Finally, one of the roots of the resulting polynomial equation, Eq. (A.7), is the solution provided by our method. Thus, by simply solving Eq. (A.7) and choosing the real root, the solution is described as

$$
\eta = \frac{1}{2c}\left(-b + e + 2c\eta_0 + \sqrt{e^2 - 2be - 4ac + 4cd + b^2}\right). \tag{A.8}
$$

A.3 Results

To show the robustness of our method, we can compare our solution, given by Eq. (A.8), with the numerical solution for several values of ϕ and σ. Fig. (A.4) shows the exact and approximate solution for several values of ϕ and σ. As it can be seen, our solution provides a good agreement with the exact solution. Fig. (A.5) shows the relative error of our method for several values of ϕ and σ. The maximum error resulting from our method is around 1.5% for a broad range of λ, ϕ and σ. Note that, even changing the values of ϕ and σ to different values from those which the mapping function was defined, there was no need for any change in our solution, Eq. (A.8).

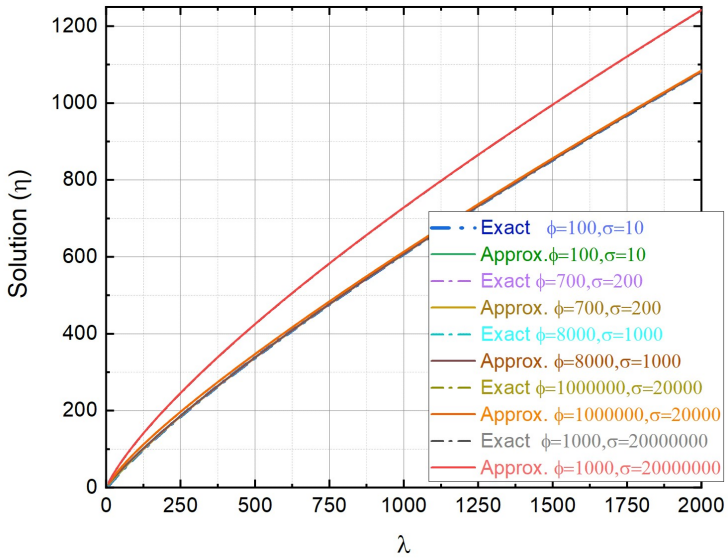

Figure A.4: Exact and the approximate solution for different values of ϕ and σ.

One might think that, instead of expanding the functions $LHS(\eta)$ and $RHS(\eta)$ using Taylor series, the solution could be more easily found just using Eq. (A.6). The problem with this approach is that the function provided by the Origin software, in this case expressed by Eq. (A.6), is set for fixed values of the parameters ϕ and σ (in this case, $\phi_0 = 100$ and $\sigma_0 = 10$). Consequently, by using Eq. (A.6) for different values of ϕ_0 and σ_0, the relative error would certainly increase. Fig. (A.6) shows the relative error obtained using Eq. (A.6), as it can be seen, the relative error is much greater than the value provided by our method. In fact, for some values of λ the relative error observed is more than 100%.

It is possible to improve the accuracy of the solution proposed by our method, for instance, by increasing the degree of the expansion polynomials, $LHS(\eta)$ and $RHS(\eta)$ or improving the mapping function. However, a trade-off must be accomplished because this method aims to provide approximate solutions that are easy to compute, compact, fully analytical, and, at the same time, offer good agreement to exact solutions.

In conclusion, we demonstrated that the method originally proposed to find the finite quantum well problem eigenvalues can also be used to find the roots of other transcendental equations. It is worth to keep in mind that the method described here is an approximation method since transcendental equations, by definition, have no analytical solution. In this sense, the

method can be considered as a tool to obtain analytical expressions for those who work with compact modeling.

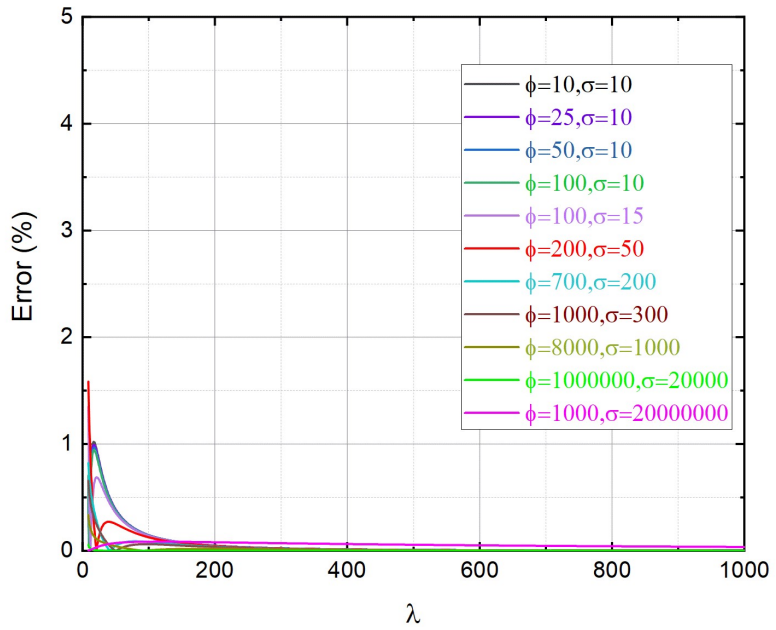

Figure A.5: The relative error for different values of ϕ and σ.

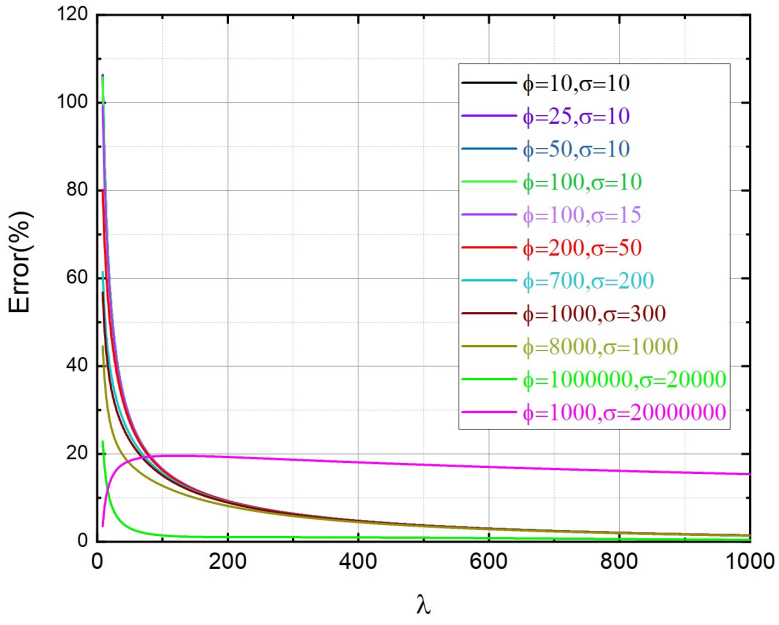

Figure A.6: The relative error obtained using Eq. (A.6).

Reference

[1] K. Brennan, "*The Physics of Semiconductors - with applications to optoelectronics devices*", Cambridge University Press, Cambridge, UK, 1999.

[2] A. F. J. Levi, "*Applied Quantum Mechanics* ", Second Edition. New York. Cambridge University Press, 2006.

[3] Quantum Theory of Tunneling 2nd Edition, 2014 by World Scientific Publishing Co. Pte. Ltd., 2014.

[4] J. Elster and H. Geitel, Bequerel rays, Wied. Ann. vol. 66, 735, 1889.

[5] E. Rutherford, *Radioactive substance emitted from Thorium compounds*, Phil. Mag. vol. 49, p. 1 1900.

[6] Schweidler: E.R. von Schweidler, Premier Congres de Radiologie, Liege, 1905.

[7] F. Hund, *Progress in the classification and theory of molecular spectra*, Part I, Z. Phys. vol. 42, p. 93, 1927.

[8] E. Merzbacher, *The early history of quantum tunneling*, Physics Today, vol. 55, p. 44, 2002.

[9] G. Gamow, *Quantum theory of atomic nucleus*, Z. Phys. vol. 51, p. 204, 1928.

[10] G. Gamow, *Quantum theory of nuclear disintegration*, Nature, vol. 122 p. 805, 1928.

[11] M. Born, *Theory of nuclear disintegration*, Z. Phys. vol. 58, p. 306, 1929.

[12] R.W. Gurney and E.U. Condon, *Quantum theory and radioactive disintegration*, Phys. Rev. vol. 33, p. 127, 1929.

[13] R. Oppenheimer, *Quantum theory of autoelectric field currents*, Proc. Natl. Acad. Sci. vol. 14, p. 363, 1928.

[14] R.W. Gurney, *Nuclear levels and artificial disintegration*, Nature vol. 123, p. 565, 1929.

[15] R.H. Fowler and L. Nordheim, "*Electron Emission in Intense Electric Fields*", Proc. Roy. Soc. A119, p. 173, 1928.

[16] Bo Lojek. "*History of Semiconductor Engineering (1st ed.)*". Colorado Springs, Springer Publishing Company Incorporated, pp 1-31, 2010.

[17] L. Esaki, "*New phenomenon in narrow germanium p-n junctions,*" Phys. Rev., vol. 109, 2, pp. 603-604, 1958.

[18] C. B. Duke, "*Tunneling in solids*", Academic, New York, USA, p.32, 1969.

[19] L. V. Iogansen, "*The Possibility of Resonance Transmission of Electrons in Crystals Through a System of Barriers*" Sovt J. Phys. J. Exptl. Theoret. Phys. (U.S.S.R.) vol. 47, pp. 270-277, 1964.

[20] I. Giaver, "*Energy Gap in Superconductors Measured by Electron Tunneling*", Phys. Rev. Lett. vol. 5, p. 147, 1960.

[21] I. Giaver,"*Electron Tunneling Between Two Superconductors*", Phys. Rev. Lett. vol. 5, p. 464, 1960.

[22] L. Esaki e R. Tsu, "*Superlattice and Negative Differential Conductivity in Semiconductors,*" IBM Journal of Research and Development, vol. 14, pp. 61-65, 1970.

[23] Jean-Pierre Colinge, Chi-Woo Lee, Aryan Afzalian, Nima Dehdashti Akhavan, Ran Yan, Isabelle Ferain, Pedram Razavi, Brendan O'Neill, Alan Blake,Mary White, Anne-Marie Kelleher, BrendanMcCarthy, and RichardMurphy, "*Nanowire transistors without junctions*," Nature Nanotech., vol. 5, pp. 225–229, 2010.

[24] Colinge, J. P and Greer J., "*Nanowire transistors: physics of devices and materials in one dimension,*" Cambridge, United Kingdom, New York, NY : Cambridge University Press, 2016.

[25] Available in https://www.nobelprize.org/prizes/physics/1973/summary/, accessed on 05/02/2024

[26] H. Sakaki, "*Scattering suppression and high-mobility effect of size-quantized electrons in ultrafine semiconductor wire structures,*" Jpn. J. Appl. Phys., vol. 19, pp. L735-L738, 1980.

[27] J. Lee, M. Kim and K. Yang, "*A 1.52 THz RTD Triple-Push Oscillator With uM Level Output Power,*" in IEEE Transactions on Terahertz Science and Technology, vol. 6, no. 2, pp. 336-340, 2016.

[28] K. Ismail, "*Si/SiGe high-speed field-effect transistors," in Electron DevicesMeeting, 1995. IEDM* '95., International, pp. 509–512, 1995.

[29] T. Maekawa, H. Kanaya, S. Suzuki, and M. Asada, "*Oscillation up to 1.92 THz in resonant tunneling diode by reduced conduction loss,*" Appl. Phys. Express, vol. 9, no. 2, Art. no. 024101, 2016.

[30] M. Kim, J. Lee, J. Lee and K. Yang, "*A 675 GHz Differential Oscillator Based on a Resonant Tunneling Diode,*" in IEEE Transactions on Terahertz Science and Technology, vol. 6, no. 3, pp. 510-512, 2016.

[31] R. Tsu e L. Esaki, "*Tunneling in a finite superlattice*", Apply. Phys. Lett., vol. 22, no. 11, pp. 562-564, 1973.

[32] S. Luryi, "*Frequency limit of double barrier resonant tunneling oscillators*," Appl. Phys. Lett., vol. 47, pp. 490–492, Sept. 1985.

[33] P. Roblin and H. Rohdin, "*High Speed Heterostructure Devices: From device concepts to circuit modeling,*" Cambridge University Press, Cambridge, UK, 2002.

[34] J. S. Moon, R. Rajavel, S. Bui, D. Wong, D. H. Chow, "*Room-temperature InAlAs/InGaAs/InP planar resonant tunneling-coupled transistor,*" Appl. Phys. Lett., vol. 87, p. 183110, 2005.

[35] ITU-R, "ITU-R M.2150-0 - Detailed specifications of the terrestrial radio interfaces of International Mobile Telecommunications-2020 (IMT-2020)," 2021.

[36] H.-J. Song and N. Lee, "Terahertz Communications: Challenges in the Next Decade," IEEE Trans. Terahertz Sci. Technol., vol. PP, pp. 1–1, 2021.

[37] T. S. Rappaport et al., "Wireless Communications and Applications Above 100 GHz: Opportunities and Challenges for 6G and Beyond," IEEE Access, vol. 7, pp. 78729–78757, 2019.

[38] D. Cimbri, J. Wang, A. Al-Khalidi, and E. Wasige, "Resonant Tunnelling Diodes High-Speed Terahertz Wireless Communications - A Review," IEEE Trans. Terahertz Sci. Technol., no. XX, pp. 1–1, 2022.

[39] N. Orihashi, S. Suzuki, and M. Asada, "*One THz harmonic oscillation of resonant tunneling diodes,*" Appl. Phys. Lett., vol. **87**, no. 23, (2005).

[40] M. Feiginov, C. Sydlo, O. Cojocari, and P. Meissner, "*Resonant-tunneling-diode oscillators operating at frequencies above 1.1 THz*" Appl. Phys. Lett., vol. 99, Art. no. 233506, 2011.

[41] H. Kanaya, R. Sogabe, T. Maekawa, S. Suzuki, and M. Asada, "*Fundamen-tal oscillation up to 1.42 THz in resonant tunneling diodes by optimized collector spacer thickness*" J. Infrared, Millim., THz Waves, vol. 35, no. 5, pp. 425–431, 2014.

[42] S. Suzuki, M. Shiraishi, H. Shibayama, and M. Asada, "*High-power operation of terahertz oscillators with resonant tunneling diodes using impedance-matched antennas and array configuration*", IEEE J. Sel. Topics Quantum Electron., vol. 19, no. 1, Art. no. 8500108, 2013.

[43] N. Oshima, K. Hashimoto, S. Suzuki and M. Asada, "*Terahertz Wireless Data Transmission With Frequency and Polarization Division Multiplexing Using Resonant-Tunneling-Diode Oscillators*", in IEEE Transactions on Terahertz Science and Technology, vol. **7**, no. 5, pp. 593-598, 2017.

[44] J. Park, J. Lee, K. Lee and K. Yang, "*A 0.71-pJ/b ON-OFF Keying K -Band Oscillator Using an InP-Based Resonant Tunneling Diode*", in IEEE Microwave and Wireless Components Letters, vol. 27, no. 7, pp. 660-662, 2017.

[45] S. Kitagawa, K. Ogino, S. Suzuki, and M. Asada, "*Wide frequency tuning in resonant-tunneling-diode terahertz oscillator using forward biased varactor diode*", Jpn. J. Appl. Phys., vol. **56**, no. 4, p. 40301, (2017).

[46] M. Shiraishi et al., "*High output power (400 μW) oscillators at around 550 GHz using resonant tunneling diodes with graded emitter and thin barriers*", Appl. Phys. Exp., vol. 4, no. 6, p. 64101, 2011.

[47] E. Wasige et al., "*Resonant tunnelling diode terahertz sources for broad band wireless communications*", Proc. SPIE, Terahertz, RF, Millimeter, Submillim.-Wave Technol. Appl. X, vol. 10103, p. 101031J, 2017.

[48] S. Luryi, A. Zaslavsky "*Blue sky in SOI: new opportunities for quantum and hot-electron devices*" Solid-State Electronics vol. 48, 877–885, 2004.

[49] S. Luryi , A. Zaslavsky "*Nonclassical devices in SOI: Genuine or copyright from III–V*" Solid-State Electronics vol. 51, pp. 212–218, 2007.

[50] H.C. Lin, "*Resonant Tunneling Diodes For Multi-Valued Digital Applications*" in Proceedings IEEE Int. Symp. Multiple Valued Logic, pp. 188–195, 1994.

[51] Jian Ping Sun, G. I. Haddad, P. Mazumder and J. N. Schulman, "*Resonant tunneling diodes: models and properties,*" in Proceedings of the IEEE, vol. 86, no. 4, pp. 641-660, April 1998.

[52] Computational Electronics Semiclassical and Quantum device modeling and Simulation, 2010.

[53] D. K. Ferry, S. M. Goodnick, J. Bird. Transport in Nanostructures. 2nd edition. Cambridge University Press: New York. 2009.

[54] Cohen-Tannoudji, C., Diu, B., & Laloë, F. *Quantum mechanics*. New York Wiley, 2005.

[55] Ashcroft, N. and Mermin, N. *Solid State Physics*. Harcourt Brace College Publishers, New York, 1976.

[56] D. Jena, *Physics of semiconductors and nanostructures*. Cornell University, 2017.

[57] Herbert Goldstein, Charles P. Poole, John L. Safko, *Classical Mechanics*, Addison Wesley, 2002.

[58] M. O. Vassell, Johnson Lee, and H. F. Lockwood. "*Multibarrier tunneling in Ga1-xAlxAs/GaAs heterostructures*". J. Appl. Phys. 54, 5206 1983.

[59] K. F. Brennan and C. J. Summers. "*Theory of resonant tunneling in a variably spaced multlquantum well structure: An Airy function approach* " J. Appl. Phys. vol. 51**,** no. 2, 1987.

[60] S. Vatannia e G. Gildenblat, "*Airy's Functions Implementation of the Transfer-Matrix Method for Resonant Tunneling in Variably Spaced Finite Superlattices*", IEEE Journal of Quantum Electronics, vol. 32, no. 6, pp. 1093-1105, 1996.

[61] L. Esaki, *Long journey into tunneling*, Proc. of the IEEE, vol. 62, p. 825, 1974.

[62] Breit, G. Wigner, E. "*Capture of Slow Neutrons"* Phys.Rev. vol. 49**,** pp. 519-531, 1936.

[63] T. L. Li and K. J. Kuhn, "Finite Element Solutions to GaAs-AlAs Quantum Wells with Connection Matrices at Heterojunctions," J. Comput. Phys., vol. 115, no. 2, pp. 288–295, Dec. 1994.

[64] F. Gelbard and K. J. Malloy, "Modeling quantum structures with the boundary element method," J. Comput. Phys., vol. 172, no. 1, pp. 19–39, Sep. 2001.

[65] D. L. Aronstein and C. R. Stroud, "General series solution for finite square-well energy levels for use in wave-packet studies," Am. J. Phys., vol. 68, no. 10, pp. 943–949, Oct. 2000.

[66] D. W. L. Sprung, Hua Wu, and J. Martorell, "A new look at the square well potential," Eur. J. Phys., vol. 13, no. 1, pp. 21–25, Aug. 1992.

[67] B. I. Barker, G. H. Rayborn, J. W. Ioup, and G. E. Ioup, “Approximating the finite square well with an infinite well: Energies and eigenfunctions,” Am. J. Phys., vol. 59, no. 11, pp. 1038–1042, Nov. 1991.

[68] F. M. Andrade, “Exact Green’s function for rectangular potentials and its application to quasi-bound states,” Phys. Lett. Sect. A Gen. At. Solid State Phys., vol. 378, no. 21, pp. 1461–1468, Mar. 2014.

[69] P. Paul and D. Nkemzi, “On the energy levels of a finite square-well potential,” J. Math. Phys., vol. 41, no. 7, pp. 4551–4555, Jul. 2000.

[70] T. L. Li and K. J. Kuhn, “Effects of mass discontinuity on the numerical solutions to Quantum wells using the effective mass equation,” Journal of Computational Physics, vol. 110, no. 2. pp. 292–300, Nov. 1994.

[71] V. A. Singh and L. Kumar, “Revisiting elementary quantum mechanics with the BenDaniel-Duke boundary condition,” Am. J. Phys., vol. 74, no. 5, pp. 412–418, May 2006.

[72] K. F. Brennan, The Physics of Semiconductors - with applications to optoelectronics devices, Cambridge. Cambrige, UK, 1999.

[73] C. D. Cantrell, “Bound-State Energies of a Particle in a Finite Square Well: An Improved Graphical Solution,” Am. J. Phys., vol. 39, no. 1, pp. 107–110, Jan. 1971.

[74] J. V. Mallow, “Simple graphical solution for the finite square well with no change of variables,” Am. J. Phys., vol. 64, no. 8, pp. 1072–1073, Aug. 1996.

[75] S. Adachi, “GaAs, AlAs, and Al_x Ga_{1-x} As: Material parameters for use in research and device applications,” J. Appl. Phys., vol. 58, no. 3, pp. R1–R29, Aug. 1985.

[76] Y. Galvão Gobato et al., “Spin injection from two-dimensional electron and hole gases in resonant tunneling diodes,” Appl. Phys. Lett., vol. 99, no. 23, p. 233507, Dec. 2011.

[77] C. Fouillant and C. Alibert, “A new approach to the symmetric rectangular quantum well: Analytic determination of well width from energy levels,” Am. J. Phys., vol. 62, no. 6, pp. 564–565, Jun. 1994.

[78] R Blümel, "Analytical solution of the finite quantum square-well problem", J. Phys. A: Math. Gen., 38, 42, pp. L673–L678, 2005.

[79] H. V. A. Galeti, Y.G. Gobato, V. O. Gordo, L. F. dos Santos, M.J. S. P. Brasil, V. López-Richard, G. E. Marques, M. Orlita, J. Kunc, D. K. Maude, "Magnetooptical investigation of two-dimensional gases in n-type resonant tunneling diodes," *Semicond. Sci. Technol.,* vol. 27, p. 015018, Dec. 2012.

[80] D. R. Celino, A. M. de Souza, R. A. R. Pereira, and M. A. Romero, “On the Quantum Well Devices Modeling: Analytical Solutions for Energy Levels and Exact Expressions for Design Purposes”, to be published.

[81] Celino, Daniel R., Romero, Murilo A., Ragi, Regiane, "*Accurate and fully analytical expressions for quantum energy levels in finite potential wells for nanoelectronic compact modeling,*" Journal of Computational Electronics, v. 21, p. 1000-1009, 2021.

[82] J. N. Schulman, H. J. De Los Santos and D. H. Chow, "*Physics-based RTD current-voltage equation*", in IEEE Electron Device Letters, vol. **17**, no. 5, pp. 220-222, 1996.

[83] J. N. Schulman, "*Extension of Tsu-Esaki model for effective mass effects in resonant tunneling*", Appl. Phys. Lett. 72, 2829, 1998.

[84] L. L. Chang, L. Esaki and R. L. Tsu, "*A one-dimensional 'superlattice*'" in semiconductors", Appl. Phys. Lett. vol. 24, 1974.

[85] T. J. Shewchuk, P. C. Chapin, P. D. Coleman, W. Kopp, R. Fischer and H. Morkoc, " *Resonant tunneling oscillations in a GaAs-Al(x)Ga(1-x)As heterostructure at room temperature*" Appl. Phys., Lett. vol. 46, 508, 1985.

[86] M. Tsuchiya, H. Sakaki and J. Yoshino, "*Room Temperature Observation of Differential Negative Resistance in an AlAs/GaAs/AlAs Resonant Tunneling Diode*", Jap. J. Appl. Phy,. 24, L466, 1985.

[87] F. Capasso, K. Mohammed and A. Cho, "*Resonant tunneling through double barriers, perpendicular quantum transport phenomena in superlattices, and their device applications*", in IEEE Journal of Quantum Electronics, vol. 22, no. 9, pp. 1853-1869, 1986.

[88] T. Inata, S. Muto, Y. Nakata, S. Sua, T. Fujii and S. Hiyamizu, "*Conduction Band Edge Discontinuity of* $In_{0.52}Ga_{0.48}As/In_{0.52}(Ga_{1-x}Al_x)_{0.4}8As(0 \leq x \leq 1)$ *Heterostructures*", Jap. J. Appl. Phys., 26, L1332, 1987.

[89] T. P. E. Broekaert, W. Lee and C. G. Fonstad, "*Pseudomorphic* $In_{0.53}Ga_{0.47}As/AlAs/InAs$ *resonant tunneling diodes with peak-to-valley current ratios of* 30 *at room temperature*", Appl. Phys. Lett. vol. 53, p. 1545, 1988.

[90] P. Gavrilovic, J. M. Brown, R. W. Kaliski, N. Y. Holonyak Jor., K. Hess, M. J. Ludowise, W. T. Dietze and C. R. Lewis, "*Resonant tunneling in a* $GaAs_{1-x}P_x$*-GaAs strained-layer quantum-well heterostructure*", Sol. State Comm. vol. 52, p. 237, 1984.

[91] T. H. H. Vuong, D. C. Tsui and W. T. Tsang, "*Tunneling in* $In_{0.53}Ga_{0.47}As$*-InP double-barrier structures*", Appl. Phys. Lett. vol. 50, p. 212, 1987.

[92] E. E. Mendez, W. I. Wang, B. Ricco and L. Esaki, "Resonant tunneling of holes in AlAs-GaAs-AlAs heterostructures", Appl. Phys. Lett. vol. 47, p. 415, 1985.

[93] L. F. Luo, R. Beresford and W. I. Wang, "*Resonant tunneling in AlSb/InAs/AlSb double-barrier heterostructures*", Appl. Phys. Lett. vol. 53, p. 2320, 1988.

[94] M. A. Reed, R. J. Koestner and M. W. Goodwin, "*Resonant tunneling through a* $HgTe/Hg_{1-x}Cd_xTe$ *double barrier, single quantum well heterostructure*", Appl. Phys. Lett. vol. 49, p. 1293, 1986.

[95] H. C. Liu, D. Landheer, M. Buchanan and D. C. Houghton, "*Resonant tunneling in* $Si/Si_{1-x}Ge_x$ *double-barrier structure*", Appl. Phys. Lett. vol. 52, p. 1809, 1988.

[96] S. S. Rhee, J. S. Park, R. P. G. Karunasir, Q. Ye and K. L. Wang, "*Resonant tunneling through a* $Si/Ge_xSi_{1-x}/Si$ *heterostructure on a GeSi buffer layer*", Appl. Phys. Lett. vol. 53, p. 204, 1988.

[97] S. Miyazaki, Y. Thara and M. Hirose, "*Resonant tunneling through amorphous silicon–silicon nitride double-barrier structures*", Phys. Rev. Lett. vol. 59, p. 125, 1987.

[98] Bo Gao, Yao Ma, Yang Liu, and Min Gong, "*In□uence of the Heterojunction Spacer on the Performance of AlGaN/GaN/AlGaN Resonant Tunneling Diodes*", IEEE Transactions on Electron Devices, vol. 64, no. 1, 2017.

[99] Arash Yazdanpanah Goharrizi, Milad Zoghi, and Mehdi Saremi, "*Armchair Graphene Nanoribbon Resonant Tunneling Diodes Using Antidote and BN Doping*", IEEE Transactions on Electron Devices, vol. 63, no. 9, 2016.

[100] Milad Zoghi and Arash Yazdanpanah Goharrizi, "*Strain-Induced Armchair Graphene Nanoribbon Resonant-Tunneling Diodes*", IEEE Transactions on Electron Devices, vol. 64, no. 10, 2017.

[101] Huili Grace Xinga, Jimy Encomendero, and Debdeep Jena, "*New Physics in GaN Resonant Tunneling Diodes*" SPIE OPTO, San Francisco, California, UAS, vol. 10918, p. 109180Z-1, 2019.

[102] Hyungmo Yoo, Thesis, "*Effect of Structural Parameters on Resonant Tunneling Diode Performance*", Oregon State University, 1991.

[103] A. Douglas Stone and P. A. Lee, "*Effect of Inelastic Processes on Resonant Tunneling in One Dimension*", Phys. Rev. Lett. vol. 54, 1196, 1985.

[104] Goldman, V. J., Tsui. D. C., Cunninggham, J. E. *"Observation of intrinsic bistability in resonant tunneling structures"*, Phys. Rev. Lett., vol. 58, p. 1256, 1987.

[105] Foster, T. J. et al., *Current bistability in double-barrier resonant tunneling devices*, Phys. Rev. B, vol. 39, p. 6205, 1989.

[106] Berkwotiz, H. L., Lux, R. A., "*Hysteresis predicted in I-V curve of heterojunction resonant tunneling diodes simulated by a self-consistent quantum method*" J. Vac. Sci. Technolo. B, vol. **5**, p. 967, 1987.

[107] Roger Lake, Gerhard Klimeck, R. Chris Bowen, and Dejan Jovanovic, "*Single and multi-band modeling of quantum electron transport through layered semi conductor devices*", Journal of Applied Physics, vol. 15, 1997.

[108] R. Lake, G. Klimeck, D. K. Blanks, "*Interface Roughness and Polar Optical Phonon Scattering in InGaAs/AlAs/InAs RTDs*" Semicond. Sci. Technology, vol 13, pg. A163, 1998.

[109] G. Klimeck, R.C. Bowen, T. Boykin, and T.A. Cwik, "*sp3s Tight-Binding Parameters for Transport Simulations in Compound Semiconductors*" Superlattices and Microstructures, vol. 27, no. 5-6, pp. 519–524, 2000.

[110] W.R. Frensley "*Wigner function model of a resonant tunneling semiconductor device*" Phy. Rev. B vol. 36, pp. 1570 – 1580, 1987.

[111] J. Lee and M. Shin, "*Quantum Transport Simulation of Nanowire Resonant Tunneling Diodes Based on a Wigner Function Model With Spatially Dependent Effective Masses*", in IEEE Transactions on Nanotechnology, vol. 16, no. 6, pp. 1028-1036, Nov. 2017.

[112] Damien Querlioz, Philippe Dollfus, "*The Wigner Monte Carlo Method for Nanoelectronic Devices: A Particle Description of Quantum Transport and Decoherence*", Londres, UK, John Wiley & Sons, Inc. 2010.

[113] X. Oriols, "*Quantum-Trajectory Approach to Time-Dependent Transport in Mesoscopic Systems with Electron-Electron Interactions"*, Phys. Rev. Lett. vol. 98, pp. 066803-066807, 2007.

[114] P. N. Racec, E. R. Racec, H. Neidhardt, "*Evanescent channels and scattering in cylindrical nanowire heterostructures*", Phys. Rev. B, vol. 79, no. 15, p. 155305, 2009.

[115] E. P. Wigner and L. Eisenbud, "*Higher angular momenta and long range interaction in resonance reactions*", Phys. Rev. vol. 72, pp. 29–41, 1947.

[116] Available on https://nanohub.org/resources/rtdnegf accessed on 05/02/2024.

[117] Available on https://www.silvaco.com/services/tcadServices/tcad_services.html accessed on 05/02/2024

[118] C. E. Chang, et al., "*Analysis of heterojunction bipolar transistor/resonant tunneling diode logic for low-power and high-speed digital applications*", IEEE Trans. Electron Devices, vol. 40, pp. 685-691, 1993.

[119] T. Kuo, et al., "*Large-signal resonant tunneling diode model for SPICE3 simulation*", IEDM Tech. Dig., pp. 567-570, 1989.

[120] Z. Yan and M. J. Deen, "*New RTD large-signal DC model suitable for PSPICE*", IEEE Trans. Computer-Aided Des. Integrated Circuits and Systems, vol. 14, no. 2, pp. 167-172, 1995.

[121] Sherif F. Nafea and Ahmed A.S. Dessouki, "*An Accurate Large-signal SPICE Model For Resonant Tunneling Diode*", 22nd International Conference on Microelectronics ICM, Cairo, 2010.

[122] Gary Ternent and Douglas J. Paul, "*SPICE Modeling of the Scaling of Resonant Tunneling Diodes and the Effects Sidewall Leakage*", IEEE Transactions on Electron Devices, vol. 59, no. 12, 2012.

[123] S.L Yadav and H. Najeeb-ud-din. "A simple analytical model for the resonant tunneling diode based on the transmission peak and scattering effect," *J Comput Electron,* vol. 19, pp. 1061–1067, Jun. 2020.

[124] D. Coon and H. Liu, "*Frequency limit of double barrier resonant tunneling oscillators*", Appl.Phys. Lett., vol 49, pp. 94-96, 1986.

[125] D. H. Chow, et al., "*1.7-ps, microwave integrated-circuit-compatible InAs/AlSb resonant tunneling diodes*", Appl. Phys. Lett., vol. 61, pp. 1685-1687, 1992.

[126] D. Wang, J. Su, H. Yi, H. Wang and W. Tan, "Analytical Modeling and Band-Structure Engineering of Resonant Tunneling Diode for Biased Terahertz Detector", *IEEE Transactions on Electron Devices*, vol. 69, no. 3, pp. 994-998, March 2022.

[127] M C Payne, "*Space charge effects in resonant tunnelling*" Semiconductor Science and Technology, vol. 2, p. 797, 1987.

[128] M. Cahay, M. McLennan, S. Datta, and M. S. Lundstrom, "*Importance of space-charge effects in resonant tunneling devices*", Appl. Phys. Lett., vol. 50, no. 10, 1987.

[129] Konstantin S. Grishakov and Vladimir F. Elesin, "*Emitter Spacer Layers In□uence on the Dynamic Characteristics of Resonant-Tunneling Diode*", IEEE Transactions On Electron Devices, vol. 64, no. 7, 2017.

[130] Y. Rajakarunanayake, and T. C. McGill, "Self-consistent solutions of electronic wave functions at GaAs–AlxGa1-xAs interfaces" J. Vac. Sci. Technol. B, vol. 5, no. 4, 1987.

[131] M. L. Leadbeater, E. S. Alves, F. W. Sheard, L. Eaves, M. Henini, O. H. Hughes and G. A. Toombs, "*Observation of space-charge build-up and thermalization in an asymmetric double-barrier resonant tunnelling structure*", J. Phys.: Condens. Matter l, pp. 10605-10611, 1989.

[132] R. Chris Bowen, Gerhard Klimeck, and Roger K. Lake William R. Frensley Ted Moise, "*Quantitative simulation of a resonant tunneling diode*", J. Appl. Phys. vol. 81, no. 7, pp. 3207-3212, 1997.

[133] W. Pötz, "*Self-consistent model of transport in quantum wen tunneling structures*", Journal of Applied Physics, vol. 66, p. 2458, 1989.

[134] V. J. Goldman, D. C. Tsui and J. E. Cunningham, "*Evidence for LO-phonon-emission-assisted tunneling in double-barrier heterostructures*", Phys. Rev., B, vol. 36, p. 7635, 1987.

[135] F. Chevoir and B. Vintor, "*Calculation of phonon-assisted tunneling and valley current in a double-barrier diode*", Appl. Phys. Lett., vol. 55, p. 1859, 1989.

[136] F. Chevoir and B. Vintor, "*Resonant and scattering-assisted magnetotunneling, in Resonant Tunneling in Semiconductors: Physics and applications*", Plenum, New York, 1990.

[137] S. Das Sarma and B. A. Mason, "*Optical phonon interaction effects in layered semiconductor structures*", Ann. Phys., vol. 163, p. 78, 1985.

[138] N. S. Wingreen, K. W. Jacobsen and J. W. Wilkins, "*Resonant tunneling with electron-phonon interaction: An exactly solvable model*", Phys. Rev. Lett., vol. 61, p. 1396, 1988.

[139] W. C. T. F. Zheng, P. Hu, B. Yudanin and M. Lax, "*Model of phonon-assisted electron tunneling through a semiconductor double barrier*", Phys. Rev. Lett., vol. 63, p. 418, 1989.

[140] P. J. Turley and S. W. Teitsworth, "*Electronic wave function and electron-confined-phonon matrix elements in GaAs/$Al_xGa_{1-x}As$ double-barrier resonant-tunneling structures*", Phys. Rev., B, vol. 44, p. 3199, 1991.

[141] P. J. Turley and S. W. Teitsworth, "*Phonon-assisted tunneling due to localized modes in double-barrier structures*", Phys. Rev., B, vol. 44, p. 8181, 1991.

[142] N. Mori, T. Ando, "*Electron-optical-phonon interaction in single and double heterostructures*", Physical Review B, vol. 40, no. 9, 1989.

[143] N. Mori, K. Taniguchi and C. Hamaguchi, "*Effects of electron-interface-phonon interaction on resonant tunnelling in double-barrier heterostructures*", Semicond. Sci. Technol., **7**, B83, (1992).

[144] N. Zou and K. A. Chao, "*Inelastic electron resonant tunneling through a double-barrier nanostructure*", Phys. Rev. Lett, vol. 69, p. 3224, 1992.

[145] A. A. Klochikhin, "*Spectrum of a free polaron and convergence radius in perturbation theory*", Sov. Phys.-Solid State, vol. 21, p. 1770, 1980.

[146] E V Anda and F Flores, "*The role of inelastic scattering in resonant tunnelling heterostructures*", 1. Phys.: Condens. Matter 3, pp. 9087-9101, 1991.

[147] M. L. Leadbeater, E. S. Alves, L. Eaves, M. Henini, and O. H. Hughes, A. Celeste and J. C. Portal, G. Hill and M. A. Pate, "Magnetic field studies of elastic scattering and optic-

phonon emission in resonant-tunneling devices," *Physical Review B,* vol. 39, no. 5, Feb. 1989.

[148] C. J. Goodings, H. Mizuta and J. R. A. Cleaver, "*Electrical studies of charge build-up and phonon-assisted tunnelling in double-barrier materials with very thick spacer layers*", Appl. Phys., vol. 75, p. 363, 1994.

[149] Gu, C. Coluzza, M. Mangiantini and A. Frova, "*Scattering effects on resonant tunneling in double-barrier heterostructures*", Appl. Phys., vol. 65, p. 3510, 1989.

[150] A. F. M. Anwar, R. B. LaComb and M. Cahay, "*In□uence of impurity scattering on the traversal time and current-voltage characteristics of resonant tunneling structures* " Superlattices and Microstructures, vol. 11, p. 131, 1992.

[151] C. J. Arsenault and M. Meunier, "*Proposed new resonant tunneling structures with impurity planes of deep levels in barriers*", Appl. Phys., vol. 66, p. 4305, 1989.

[152] Jin-feng Zhang and Ben-yuan Gu, "*Effects of a localized state inside the barrier on the temporal characteristics of electron tunneling in double-barrier quantum wells*", Phys. Rev., B, vol. 44, p. 8204, 1991.

[153] H. A. Fertig and S. Das. Sarma, "*Elastic scattering in resonant tunneling systems*", Phys. Rev., B, vol. 40, p. 7410, 1989.

[154] H. A. Fertig, Song He and S. Das. Sarma, "*Elastic-scattering effects on resonant tunneling in double-barrier quantum-well structures*", Phys. Rev., B, vol. 41, p. 3596, 1990.

[155] E. Wolak, K. L. Lear, P. M. Pinter, E. S. Hellman, B. G. Park, T. Well, J. S. Harris, Jr and D. Thomas, "*Elastic scattering centers in resonant tunneling diodes*", Appl. Phys. Lett, vol. 53, p. 201, 1988.

[156] T. Nakagawa, T. Fujita, Y. Matsumoto, T. Kojima and K. Ohta, "*Sharp resonance characteristics in triple-barrier diodes with a thin undoped spacer layer*", Jpn. J. Appl. Phys., vol. 26, p. L980, 1987.

[157] J. S. Wu, C. Y. Chang, C. P. Lee, K. H. Chang, D. G. Liu, and D. C. Liou, "*Resonant tunneling of electrons from quantized levels in the accumulation layer of double barrier heterostructures*", Applied Physics Letters vol. 57, p. 2311, 1990.

[158] Hiroshi Mizuta and Tomonori Tanoue, "*The Physics and Applications of Resonant Tunnelling Diodes*", Cambridge University Press, New York, 1995.

[159] T. Fiig, A.P. Jauho, "Self-consistent modelling of resonant tunnelling structures," *Surface Science*, vol. 267, pp. 392-395, Jul. 1992

[160] F.W. Sheard, and G.A. Toombs, "Space charge buildup and bistabi1ity in resonant-tunneling double-barrier structures," *Appl. Phys. Lett.,* vol. 52, no. 15, p. 1228, Apr. 1988.

[161] P. H. Rivera and P. A. Schulz, "*Analysis of the Current-Voltage Characteristics Lineshapes of Resonant Tunneling Diodes*", Brazilian Journal of Physics, vol. 26, no. 1, 1996.

[162] M. Johnson and A. Grincwajg, "*Effect of inelastic scattering on resonant and sequential tunneling in double barrier heterostructures*", Appl. Phys. Lett, vol. 51, p. 1729, 1987.

[163] l. Mehdi, R. K. Mains, and G. I. Haddad, "*Effect of spacer layer thickness on the static characteristics of resonant tunneling diodes*", Appl. Phys. Lett. vol. 51, no. 9, 1990.

[164] Mark Levence Leadbeater, "*Resonant tunnelling in semiconductor heterostructures*", Tese de doutorado, University of Nottingham, 1990.

[165] T. Mimura, S. Hyamizu, T. Fujii e K. Nambu, "*A New Field-Effect Transistor with Selectively Doped GaAs/n-AlGaAs Heterojunction*", Jpn. Appl. Phys. vol. 19, p. 225, 1980.

[166] P. M. Smith, S. M. J. Liu, M. Y. Kao, P. Ho, S. C. Wang, K. H. G. Duh, S. T. Fu, e P. C. Chao, "*W-band high efficiency InP based powerHEMT with 600 GHz fmax*", IEEE Microwave Guided Wave Lett. vol. 5, p. 230, Julho 1995.

[167] T. W. Hickmott, "*Magnetotunneling from accumulation layers in AlGaAs capacitors*", Physical Review B, vol. 32, no., 10, (1985).

[168] S. Luryi, "*Coherent versus incoherent resonant tunneling and implications for fast devices, Superlattices and Microstructures*", vol. 5, p. 375, 1989.

[169] Weil and B. Vinter, "*Equivalence between resonant tunnelling and sequential tunnelling in double-barrier diode*s", Appl. Phys. Lett, vol. 50, p.1281, (1987).

[170] J. Bardeen, "*Tunnelling From a Many-Particle Point of View*", Physical Review Letters, vol. 6, no. 2, 1961.

[171] M C Payne, "*Transfer Hamiltonian description of resonant tunnelling*", Journal of Physics C: Solid State Physics, vol. 19, pp. 1145-1155, 1986.

[172] M. Büttiker, "*Coherent and sequential tunneling in series barriers*", IBM J. Res. Develop. vol., 32, no. 1, 1988.

[173] H. Mizuta, T. Tanoue and S. Takahashi, "*Theoretical analysis of peak-to-valley ratio degradation caused by scattering processes in multi-barrier resonant tunneling diodes"*, Proceedings of IEEE/Cornell Conference on Advanced Concepts in High Speed Semiconductor Devices and Circuits, p. 274, 1989.

[174] K. Seeger, "*Semiconductor Physics An Introduction"*, Springer Series in S. S. Science, New York, 2004.

[175] R. Lassning and W. Boxleitner, "Tunneling From Quasi Two-Dimensional Space Charge Layers," *Solid State Communication*, vol. 64, no. 6, pp. 979-982, May 1987.

[176] F. F. Fang and W. E. Howard, "*Negative Field-Effect Mobility on (100) Si Surfaces*", Phys. Rev. Lett. vol. 16, p. 797, 1966.

[177] V. A. Singh and L. Kumar, "Revisiting elementary quantum mechanics with the BenDaniel-Duke boundary condition," Am. J. Phys., vol. 74, no. 5, pp. 412–418, May 2006.

[178] Y. G. Gobato, F. Chevoir, J. M. Berroir, Y. Guldner, J. Nagle, J. P. Vieren and B. Vinter, "Magnetotunneling analysis of the scattering processes in a double-barrier structure with a two-dimensional emitter," *Physical Review B,* vol. 43, no. 6, Feb. 1991.

[179] H. Sheng, J. Sinkkonen, "Subband Current in Resonant Tunneling Diode," *Superlattices and Microstructures,* vol. 12, no. 4, Aug. 1992.

[180] A. Vercik, Y. G. Gobato, M.J.S.P. Brasil, S. S. Makler, "Kinetics of excitonic complexes on tunneling devices," *Physical Review B,* vol. 71, p. 075310, Feb. 2005.

[181] H. B. de Carvalho, M. J. S. P. Brasil, V. Lopez-Richard, Y. Galvão Gobato, G. E. Marques, I. Camps, L. C. O. Dacal, M. Henini, L. Eaves, and G. Hill, "Electric-field inversion asymmetry: Rashba and Stark effects for holes in resonant tunneling devices", Physical Review B, **74,** 041305 R, 2006.

[182] S. Adachi, "Material parameters of In1-xGaxAsyP1-y and related binaries," es," J. Appl. Phys., vol. 53, no. 12, pp. 8775–8792, Dec. 1982.

[183] Muttlak, S., Abdulwahid, O., Sexton, J., Kelly, M., & Missous, M. InGaAs/AlAs Resonant Tunneling Diodes for THz Applications: An Experimental Investigation. IEEE Journal of the Electron Devices Society, vol. 6, pp. 254-262, 2018.

[184] Long Yang, Steven D. Draving, Dan E. Mars and Mike R. T. Tan, "*A 50 GHz Broad-Band Monolithic GaAdAlAs Resonant Tunneling Diode Trigger Circuit*", IEEE Journal of Solid State Circuits, vol. 29, no. 5, 1994.

[185] Lin'an Yang, Yue Li, Ying Wang, Shengrui Xu, and Yue Hao, "Asymmetric quantum-well structures for AlGaN/GaN/AlGaN resonant tunneling diodes", J. Appl. Phys. vol. 119, pp. 164501, 2016

[186] R. Morariu et al., "Accurate small-signal equivalent circuit modeling of resonant tunneling diodes to 110 GHz," IEEE Trans. Microw. Theory Techn., vol. 67, no. 11, pp. 4332–4340, Nov. 2019.

[187] R. Lake and Junjie Yang, "A physics based model for the RTD quantum capacitance," in IEEE Transactions on Electron Devices, vol. 50, no. 3, pp. 785-789, March 2003.

[188] Daniel R. Celino, Regiane Ragi, Murilo A. Romero, "*Analytical Physics-Based Compact Current-Voltage Model for 2D-2D Resonant Tunneling Diodes,*" IEEE Transactions on Nanotechnology, v. 21, p. 752-762, 2022.

[189] D. R. Celino, A. M. de Souza, C. L. M. P. Plazas, R. Ragi, and M. A. Romero, "*Fully analytical compact model for the I–V characteristics of resonant tunneling diodes,*" in Proc. 35th Symp. Microelectronics Technol., pp. 1–4, 2021.

[190] D. R. Celino, A. M. deSouza, C. L. M. P. Plazas, R. Ragi, and M. A. Romero, "*A physics-based RTD model accounting for space charge and phonon scattering effects,*" J. Integr. Circuits Syst., vol. 17, no. 1, pp. 1–8, 2022.

[191] E. R. Brown, C. D. Parker, T. C. L. G. Sollner; Effect of quasibound-state lifetime on the oscillation power of resonant tunneling diodes. Appl. Phys. Lett. 6 March 1989; 54 (10): 934–936.

[192] V. P. Sirkeli, O. Yilmazoglu, D. S. Ong, S. Preu, F. Küppers and H. L. Hartnagel, "Resonant Tunneling and Quantum Cascading for Optimum Room-Temperature Generation of THz Signals," in IEEE Transactions on Electron Devices, vol. 64, no. 8, pp. 3482-3488, Aug. 2017.

[193] E. R. Brown, J. R. Söderström, C. D. Parker, L. J. Mahoney, K. M. Molvar, "Oscillations up to 712 GHz in InAs/AlSb resonanttunneling diodes", Appl. Phys. Lett. 58, 2291 (1991).

[194] M. T. Björk, B. J. Ohlsson, C. Thelander, A. I. Persson, K. Deppert, L. R. Wallenberg, and L. Samuelson, "*Nanowire resonant tunneling diodes*", Applied Physics Letters, vol. 81, p. 4458, 2002.

[195] Jakob Wensorra, Klaus Michael Indlekofer, Mihail Ion Lepsa, Arno Förster, and Hans Luth, "*Resonant Tunneling in Nanocolumns Improved by Quantum Collimation*", Nano Letters, vol. 5, no. 12, pp. 2470-2475, 2005.

[196] J. Wensorra, M. I. Lepsa, S. Trellenkamp, J. Moers, K. M. Indlekofer, H. Lüth, "*Gate-controlled quantum collimation in nanocolumn resonant tunneling transistors,*" Nanotechnology, vol. 20, p. 465402, 2009.


EESC • USP